



**HAL**  
open science

# Elaboration and study of TiO<sub>2</sub> nanostructures for hydrogen generation via photolysis of water

Daniela d'Elia

► **To cite this version:**

Daniela d'Elia. Elaboration and study of TiO<sub>2</sub> nanostructures for hydrogen generation via photolysis of water. Chemical and Process Engineering. École Nationale Supérieure des Mines de Paris, 2011. English. NNT : 2011ENMP0029 . pastel-00636920

**HAL Id: pastel-00636920**

**<https://pastel.hal.science/pastel-00636920>**

Submitted on 28 Oct 2011

**HAL** is a multi-disciplinary open access archive for the deposit and dissemination of scientific research documents, whether they are published or not. The documents may come from teaching and research institutions in France or abroad, or from public or private research centers.

L'archive ouverte pluridisciplinaire **HAL**, est destinée au dépôt et à la diffusion de documents scientifiques de niveau recherche, publiés ou non, émanant des établissements d'enseignement et de recherche français ou étrangers, des laboratoires publics ou privés.

École doctorale n° 432 : SMI - Sciences des Métiers de l'Ingénieur

## Doctorat ParisTech

# THÈSE

pour obtenir le grade de docteur délivré par

## L'École nationale supérieure des mines de Paris

### Spécialité " Énergétique "

*présentée et soutenue publiquement par*

**Daniela D'Elia**

Le 30 juin 2011

## Elaboration and study of TiO<sub>2</sub> nanostructures for hydrogen generation via photolysis of water

(Elaboration et étude de nanostructures de TiO<sub>2</sub> pour la production d'hydrogène  
par photolyse de l'eau)

Directeurs de thèse : **Jean-François HOCHEPIED & Arnaud RIGACCI**

Co-encadrement de la thèse : **Christian BEAUGER**

### Jury

<b>M. Jean-Christophe VALMALETTE</b>	Professeur, Institut Matériaux Microélectronique et Nanosciences de Provence, Université du Sud Toulon - Var	Président
<b>Mme Corinne CHANEAC</b>	Professeur, Laboratoire de Chimie de la Matière Condensée de Paris, Université Pierre et Marie Curie, Paris VI	Rapporteur
<b>M. Alain PIERRE</b>	Professeur, IRCELYON, Université Claude Bernard Lyon 1	Rapporteur
<b>M. Mourad BENABDESSELAM</b>	Professeur, Laboratoire de Physique de la Matière Condensée, Université de Nice - Sophia Antipolis	Examineur
<b>Mme Valérie SPITZER-KELLER</b>	Docteur HDR, Laboratoire des Matériaux, Surfaces et Procédés pour la Catalyse, Université Louis Pasteur de Strasbourg	Examineur
<b>M. Christian BEAUGER</b>	Docteur HDR, Centre Énergétique et Procédés, Mines ParisTech	Examineur
<b>M. Jean-François HOCHEPIED</b>	Docteur HDR, Centre Énergétique et Procédés, Mines ParisTech	Examineur
<b>M. Arnaud RIGACCI</b>	Docteur, Centre Énergétique et Procédés, Mines ParisTech	Examineur

**MINES ParisTech**

**Centre Énergétique et Procédés**

Rue Claude Daunesse, 06904 Sophia Antipolis Cedex, France



## Table of contents

<b>Introduction.....</b>	<b>8</b>
<b>1. TiO<sub>2</sub>: generalities, water splitting, elaboration and doping.....</b>	<b>13</b>
<b>1.1 Crystal structure.....</b>	<b>13</b>
<b>1.2 Properties.....</b>	<b>16</b>
1.2.1 Electronic structure.....	16
1.2.2 Optical properties.....	17
1.2.3 Photoactivity.....	18
1.2.4 Hydrogen production: water photolysis.....	19
1.2.4.1 Theoretical basis.....	19
1.2.4.2 Notion of efficiency.....	20
1.2.4.3 Potential solutions to improve water splitting efficiency.....	23
1.2.4.4 Testing systems: photoreactors.....	27
<b>1.3 Elaboration methods.....</b>	<b>29</b>
1.3.1 Nanoparticles from precipitation of TiCl <sub>4</sub> .....	30
1.3.2 Nanotubes from Kasuga's method.....	34
1.3.2.1 Preliminary presentation	
1.3.2.2 Synthesis conditions	
1.3.2.3 Morphology classification	
1.3.2.4 Mechanism of formation	
1.3.2.5 Structural hypothesis	
1.3.3 Aerogels and xerogels.....	40
1.3.3.1 General presentation.....	40
1.3.3.2 Sol-gel synthesis.....	42
1.3.3.3 Aging.....	46
1.3.3.4 Drying.....	48

1.3.3.5 Post treatments.....	53
1.3.3.6 Applications.....	54
1.3.3.7 Short overview of the literature on TiO <sub>2</sub> -based aerogels.....	54
<b>1.4 Doping.....</b>	<b>58</b>
1.4.1 Generalities.....	58
1.4.2 Cationic doping : metal doping.....	60
1.4.3 Anionic doping : non metal doping.....	63
<b>1.5 Summary and comments.....</b>	<b>65</b>
<b>2. Samples elaboration and characterization: particles, 1D-structures and aerogels/xerogels.....</b>	<b>67</b>
<b>2.1 Nanoparticles.....</b>	<b>68</b>
2.1.1 Elaboration and samples.....	68
2.1.1.1 Synthesis.....	68
2.1.1.2 Samples.....	71
2.1.2 Characterisations.....	71
2.1.2.1 X-Ray diffraction.....	71
2.1.2.2 Transmission Electron Microscopy.....	73
2.1.2.3 Nitrogen adsorption/desorption .....	77
2.1.3 Discussion.....	81
<b>2.2 1D-structures.....</b>	<b>87</b>
2.2.1 Elaboration and samples.....	87
2.2.1.1 Synthesis.....	87
2.2.1.2 Samples.....	87
2.2.2 Characterizations.....	88
2.2.2.1 X-Ray diffraction.....	88
2.2.2.2 Transmission Electron Microscopy.....	90

2.2.2.3 Nitrogen adsorption/desorption .....	95
2.2.3 Discussion.....	99
<b>2.3 Aerogels and xerogels.....</b>	<b>101</b>
2.3.1 Elaboration and samples.....	101
2.3.1.1 Sol-gel synthesis.....	101
2.3.1.2 Aging and washing.....	102
2.3.1.3 Drying.....	103
2.3.1.4 Calcination.....	104
2.3.1.5 Synoptic view of the elaboration process.....	105
2.3.1.6 Samples.....	106
2.3.2 Characterization.....	107
2.3.2.1 X-Ray diffraction.....	107
2.3.2.2 Transmission Electron Microscopy.....	110
2.3.2.3 Nitrogen adsorption/desorption .....	114
2.3.2.4 Elementary analysis.....	117
2.3.3 Discussion.....	118
<b>2.4 Conclusion.....</b>	<b>122</b>

### **3. Doping : Vanadium doped nanotubes and nitrogen doped aerogels and xerogels.....124**

<b>3.1 Vanadium doped nanotubes.....</b>	<b>125</b>
3.1.1 Elaboration.....	125
3.1.2 Characterizations.....	126
3.1.2.1 X-Ray diffraction.....	126
3.1.2.2 Raman spectroscopy.....	128
3.1.2.3 Transmission Electron Microscopy.....	130
3.1.3 Discussion.....	134

<b>3.2 Nitrogen doped aerogels and xerogels.....</b>	<b>134</b>
3.2.1 Elaboration.....	134
3.2.1.1 Synthesis, drying and calcinations.....	134
3.2.1.2 Samples.....	135
3.2.2 Characterizations.....	137
3.2.2.1 X-Ray diffraction.....	137
3.2.2.2 Raman spectroscopy.....	139
3.2.2.3 Transmission Electron Microscopy.....	140
3.2.2.4 Nitrogen adsorption/desorption .....	142
3.2.2.5 Elementary analysis.....	146
3.2.2.6 X-Rays Photoemission Spectroscopy .....	147
3.2.3 Discussion.....	153
<b>3.3 Conclusions .....</b>	<b>155</b>
<b>4. Evaluation of hydrogen evolution.....</b>	<b>157</b>
<b>4.1 Experimental set-up .....</b>	<b>158</b>
4.1.1. Testing devices and procedure.....	158
4.1.1.1 General description .....	158
4.1.1.2 Description of the ISS testing facility.....	159
4.1.1.3 Description of the LMSPC testing facility.....	160
4.1.2. Samples preparation procedure.....	163
<b>4.2 Properties of the commercial TiO<sub>2</sub> products used as reference .....</b>	<b>163</b>
4.2.1 X-Ray diffraction .....	163
4.2.2 Nitrogen adsorption/desorption .....	164
4.2.3 Transmission Electron Microscopy .....	167
4.2.4 Diffuse reflectance UV-VIS spectroscopy.....	168
<b>4.3 Optical characterization of nanoparticles, nanotubes, aerogels and xerogels samples .....</b>	<b>170</b>

4.3.1 Nanoparticles.....	170
4.3.2 Nanotubes.....	171
4.3.3 Aerogels.....	173
4.3.4 Nitrogen-doped aerogels.....	174
4.3.5 Nitrogen-doped xerogels.....	177
<b>4.4 Hydrogen evolution .....</b>	<b>178</b>
<b>4.4.1 List of the tested samples .....</b>	<b>178</b>
4.4.2.1 Evaluation of nanoparticles .....	179
4.4.2.2 Evaluation of nanotubes.....	180
4.4.2.3 Evaluation of aerogels.....	184
4.4.2.4 Evaluation of Pt-loaded aerogels and xerogels.....	186
4.4.2.5 Discussion.....	189
4.4.2.6 Complementary studies.....	191
<b>4.4.3 Testing of nitrogen-doped samples.....</b>	<b>192</b>
4.4.3.1 Evaluation of aerogels.....	192
4.4.3.2 Evaluation of xerogels.....	192
<b>4.5 Conclusions.....</b>	<b>194</b>
<b>5 General conclusions and some perspectives.....</b>	<b>198</b>
<b>Appendix 1 Vanadium doping: High Temperature X-Rays Diffraction study and photocatalytic tests for hydrogen evolution.....</b>	<b>203</b>
<b>Appendix 2 Characterization techniques.....</b>	<b>209</b>
<b>References.....</b>	<b>219</b>



## Introduction

In the energy field, researchers have to face a major challenge: how to satisfy the worldwide increasing energy demand without increasing greenhouse effect. Nuclear energy can represent a solution thanks its greenhouse free energy production but includes different other important limitations such as accessibility, safety and security, nuclear wastes as well as geopolitics. Renewable energies sources are abundant and clean but energy they provide is most of the time discontinuous. Nowadays, hydrogen-based technologies are considered as the most promising for future clean energy, although scientific research did not find yet satisfactory industrial solutions for its production, storing and use. Hydrogen ( $H_2$ ) is an energy vector and not an energy source: it is not readily available in nature and some energy must be used to produce it. Main  $H_2$  sources are:

- fossil fuels: most of today's  $H_2$  (about 95%) is produced via steam-methane reforming<sup>1</sup>, oil products oxidation or reforming and coal gasification,
- biomass:  $H_2$  is produced using thermochemical and biological processes,
- water<sup>2</sup>:  $H_2$  is produced via water splitting.

Water splitting can be mainly performed via techniques such as electrolysis, chemical/thermochemical  $H_2$  production processes and biophotolysis (by algae). Electrolysis is the most advanced technology but the dissociation of water needs electricity, coming, for example, from nuclear energy. Producing  $H_2$  by water splitting just using directly renewable energy source is still a scientific challenge. Indeed, it may permit to produce  $H_2$  through a perfectly clean process.

The first report on the efficiency of  $H_2$  production from water by photoelectrolysis was published by Fujishima et al. in Nature [Fujishima and Honda, 1972] at the time of the first oil crisis. At this time, the titanium dioxide<sup>3</sup> based photocatalysis drew the attention of many people as one of the most promising catalytic routes for  $H_2$  production. Since then, photocatalytic water splitting has been studied intensively with powdered  $TiO_2$  aqueous suspensions, most of the time with platinum (Pt) deposited on  $TiO_2$  as a cathodic catalyst [Varghese and Grimes, 2008].

The US Department of Energy (DOE) has set the commercialization benchmark of the energy conversion efficiency of water splitting at 10% [Science, 2002].

Three parameters affect strongly energy conversion efficiency from solar energy to  $H_2$  on  $TiO_2$  as follows:

---

<sup>1</sup> So-called SMR.

<sup>2</sup> Water is the most abundant source of hydrogen on the planet.

<sup>3</sup>  $TiO_2$

- inability to use visible light (as band gap of anatase TiO<sub>2</sub> is 3.2 eV, only UV radiations can excite electrons from valence to conduction band),
- fast recombination of photogenerated excitons<sup>4</sup> (charges lifetime must be high enough as compared to characteristic reaction times of radicals formed by TiO<sub>2</sub>),
- fast backward reaction (indeed, the reaction that from H<sub>2</sub> and O<sub>2</sub> gives H<sub>2</sub>O is thermodynamically favoured).

Within this general frame, improving the efficiency of TiO<sub>2</sub> for H<sub>2</sub> generation by water splitting is the general objective of my thesis. This means practically to contribute:

- to expand the photoresponse of the semiconductor in the visible region;
- and/or
- to limit the fast recombination of the photogenerated electron/hole pairs.

For this purpose, I have selected an experimental strategy consisting in elaborating and comparing some different TiO<sub>2</sub> (nano)morphologies and then modifying their properties by doping methods.

In this work, first I have elaborated three significantly different TiO<sub>2</sub> morphologies (slightly elongated nanoparticles, nanotubes and three-dimensional<sup>5</sup> sol-gel networks so-called aerogels or xerogels) in order to check the impact of the respective morphologies on water splitting efficiency.

Later, I have tried to improve the two latter families's materials for H<sub>2</sub> photoproduction through cationic or anionic doping. This technique has been basically selected in order to shift the light absorption of the materials in the visible range.

Finally, I have tested the most promising materials (doped as well as undoped) versus H<sub>2</sub> evolution.

This document gathers the main results I have obtained during my Ph-D and is divided into four chapters.

The first chapter is a short bibliographic review on TiO<sub>2</sub> and some aspects directly related to the investigated field:

---

<sup>4</sup> i.e. electron/hole pairs.

<sup>5</sup> 3D.

- TiO<sub>2</sub> crystal structure, (I have mostly described the allotropic forms prepared in the thesis: anatase, rutile, TiO<sub>2</sub>-B),
- TiO<sub>2</sub> properties (after a short report of the electronic and optical properties, I have described the photocatalytic hydrogen production and the main strategies to improve it),
- the most important elements of the elaboration methods I have selected,
- doping as a general strategy to shift the absorption spectrum of the photocatalysts in the visible range.

The second chapter is devoted to the preparation of the three different TiO<sub>2</sub> morphologies studied within the frame of this work:

- nanoparticles from precipitation of TiCl<sub>4</sub> and NaOH and crystallization in autoclave. (In this part I present the effects of pH and crystallization temperature on the features of the final materials.)
- nanotubes from alkaline hydrothermal transformation of a commercial product followed by ion-exchange treatment and calcinations (Kasuga's method [Kasuga et al., 1998a]). (In this section, I focus on the effect of the calcinations temperature on the structure of photocatalysts.)
- aerogels and xerogels from sol-gel synthesis followed by supercritical or evaporation drying, respectively, and calcinations. (Here the impact of the drying route and, again, the calcinations temperature will be presented.)

In the third chapter, I summarize and discuss results obtained by doping some of the materials presented in the previous chapter. This chapter is divided into two subparts as follows:

- elaboration of vanadium-doped nanotubes. As doping procedure, I have used the wet-impregnation of products by VO(acac)<sub>2</sub><sup>6</sup> followed by calcinations in air. Once prepared, resulting nanotubes are characterized. In order to investigate the influence of vanadium on the structure of the final products, close collaborations with Professor Jean-Christophe Valmalette from Université du Sud Toulon Var<sup>7</sup> to perform Raman Spectroscopy, with Assistant-Professor Yoshikazu Suzuki from Kyoto University<sup>8</sup> to carry out the High Temperature X-Rays diffraction<sup>9</sup> and with Dr Etienne Balan and Amélie Bordage to perform HERFD-XANES<sup>10</sup> have been engaged.

---

<sup>6</sup> Vanadyl acetylacetonate

<sup>7</sup> Institut Matériaux Microélectronique Nanosciences de Provence (IM2NP), UMR CNRS 6242, Toulon.

<sup>8</sup> Institute of Sustainable Science (ISS).

<sup>9</sup> HT-XRD.

<sup>10</sup> Institut de Minéralogie et Physique des Milieux Condensés /University Paris VI

- elaboration of nitrogen-doped aerogels and xerogels<sup>11</sup>.

Since it is suspected that nitrogen could significantly modify the electronic properties of TiO<sub>2</sub>, close collaboration with Dr. Yannick-Fagot Revurat from Nancy University<sup>12</sup> have been engaged on XPS analysis.)

Finally, the fourth chapter gathers results on bandgap evaluation of the different representative undoped materials plus nitrogen-doped aerogels and xerogels together with their hydrogen evolution.

Bandgap characterizations have been realized on the basis of diffuse reflectance measurements performed at Université de Nice – Sophia Antipolis, with the kind agreement of Professor M. Benabdesselam<sup>13</sup>. Hydrogen evolution tests have been made possible thanks to Dr. Nicolas Keller and Dr. Valerie Keller-Spitzer at University Louis Pasteur<sup>14</sup> in Strasbourg as well as Assistant-Professor Yoshikazu Suzuki from Institute of Sustainability Science (ISS) at Kyoto University. Thanks to the unique opportunity to test materials in different laboratories, we could compare two different equipments and conditions for the hydrogen production with the TiO<sub>2</sub>-based materials I have elaborated during my PhD.

---

<sup>11</sup> N-doped aerogels/xerogels.

<sup>12</sup> Institut Jean Lamour (IJL), UMR CNRS 7198, Nancy.

<sup>13</sup> Laboratoire de Physique de la Matière Condensée (LPMC), UMR CNRS 6070, Nice.

<sup>14</sup> Laboratory of Materials, Surfaces and Processes for the Catalysis (LMSPC), UMR CNRS 7515, Strasbourg.



## 1. TiO<sub>2</sub>: generalities, water splitting, elaboration and doping

This chapter is a bibliographic overview, focused on the key points of my thesis in order to support the subsequent experimental choices I have made and presented at the end of this chapter.

This chapter is consequently divided into four main parts as follows.

- In the first part, I describe the crystallographic features of the three allotropic forms of TiO<sub>2</sub> we have considered in this work: anatase, rutile and TiO<sub>2</sub>-B.
- Then, starting from the description of the electronic and optical properties of TiO<sub>2</sub>, I give a short overview of the related mechanism of photoactivity and the processes of hydrogen production through water splitting.
- Later, I detail the elaboration methods we have selected to obtain TiO<sub>2</sub> photocatalysts: precipitation from two solutions of TiCl<sub>4</sub> and NaOH in order to produce nanoparticles, alkaline hydrothermal transformation for nanotubes, sol-gel route for xerogels and aerogels elaboration.
- Finally, I present why we have chosen vanadium and nitrogen to dope our TiO<sub>2</sub>-based materials.

### 1.1 Crystal structures

TiO<sub>2</sub> has 11 allotropic forms: anatase, rutile, brookite, TiO<sub>2</sub>-B (« bronze ») and seven high-pressure phases of TiO<sub>2</sub> [Dubrovinsky et al, 2001]. These latter phases do not occur in nature and they are synthesized by high pressure treatment of anatase or rutile [Kavan et al, 1996]. These “high pressure” forms are expected to have smaller bandgaps but similar chemical characteristics [Mattesini et al, 2004]. Their existence was theoretically predicted and then experimentally proven. Specifically, a form of TiO<sub>2</sub> with the cotunnite structure was prepared at high temperature and pressure and then quenched in liquid nitrogen. It is the hardest known oxide.

Rutile and anatase are the most used TiO<sub>2</sub> forms because they have the highest activities for photocatalytic reactions but the precise reasons for this behavior have not been elucidated in details yet [Fujishima et al, 2008]. Recently, increasing scientific interest is dedicated to TiO<sub>2</sub>-B, because of its use as electrode material in rechargeable lithium-ion battery ([Nuspl et al, 1997], [Armstrong et al, 2004]. Table 1.1 sums up the crystallographic features of anatase, rutile and TiO<sub>2</sub>-B. Figure 1.1 illustrates the structures of anatase and rutile.

Form	a (Å)	b (Å)	c (Å)	$\beta$ (°)	Space group	$\rho_s$ (cm <sup>3</sup> .g <sup>-1</sup> )
Anatase	3,777	3,777	9,501	90	I4 <sub>1</sub> /amd	3,92
Rutile	4,594	4,594	2,9586	90	P4 <sub>2</sub> /mnm	4,25
TiO <sub>2</sub> -B	12,163	3,735	6,513	107,29	C2/m	3,76

Table 1.1 Cell parameters and density of TiO<sub>2</sub> forms.  $\rho_s$  is the skeleton density

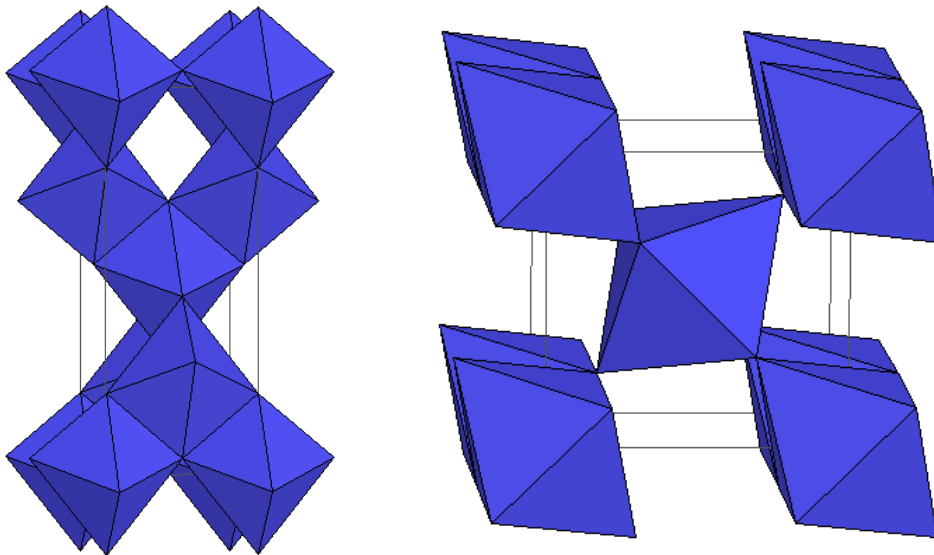
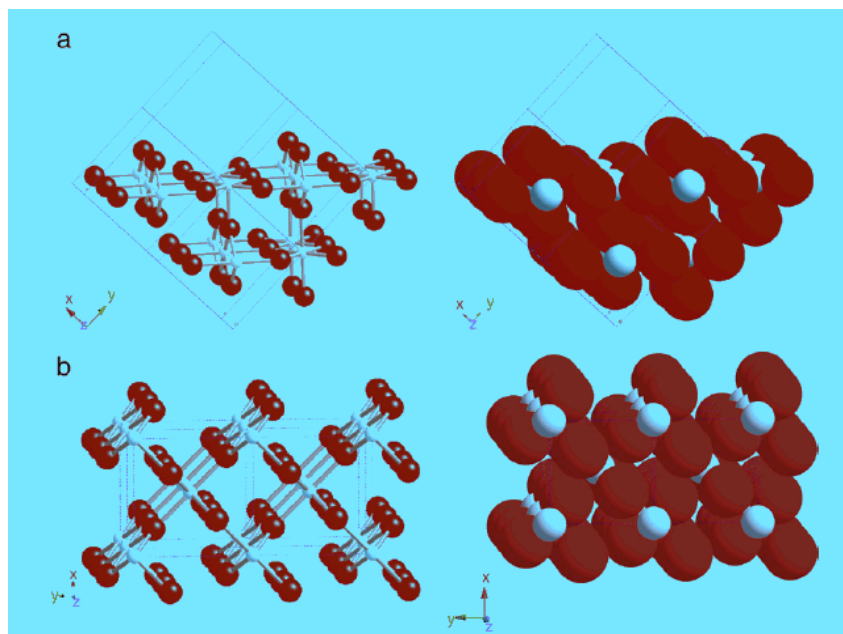


Figure 1.1 Scheme of TiO<sub>6</sub> chains elementary cell: left) anatase and right) rutile

[<http://ruby.colorado.edu/~smyth/min/tio2.html>]

In both structures 3d<sup>0</sup> Ti<sup>4+</sup> cations are at the center of an octahedron of O<sup>2-</sup> ions. In rutile, O<sup>2-</sup> ions build a hexagonal compact stacking, while in anatase a cubic compact stacking. Ti<sup>4+</sup> cations fill half of octahedral sites in both structures. The TiO<sub>6</sub> octahedra are linked sharing edges and corners.

Rutile has three main crystal faces, two are quite low in energy and are thus considered to be important for polycrystalline or powder materials [Ramamoorthy et al., 1994]: (110) and (100) (Fig. 1.2). The (001) face is thermally less stable [Diebold2003].



**Figure 1.2 : Schematic representations of selected low-index faces of rutile: (a) (110) and (b) (100)**  
**[Fujishima et al, 2008]**

The most energetically stable surface is (110), and therefore it has been the most studied. Anatase has two low energy surfaces, (101) and (001) (Figure 1.3), which are common for natural crystals ([Burnside et al., 1998] and [Hengerer et al., 2000]).

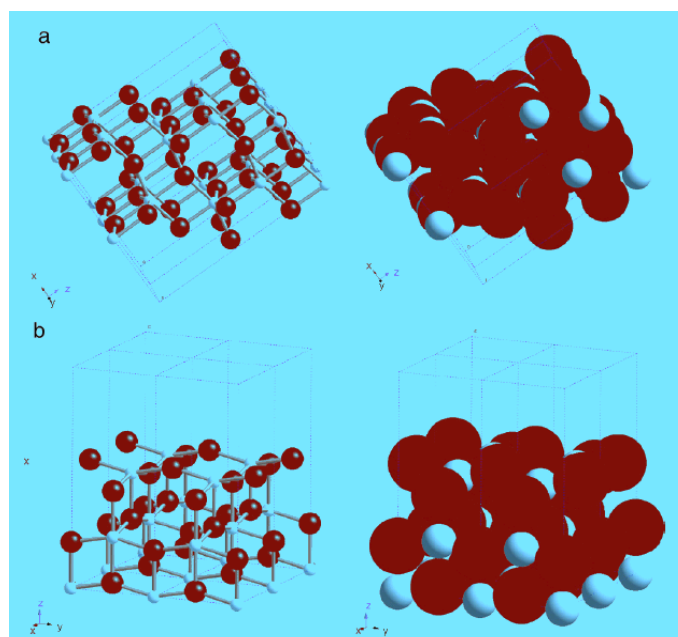


**Figure 1.3. Schematic representations of selected low-index faces of anatase: (a) (101) and (b) (100)**  
**[Fujishima et al., 2008]**

The (101) surface is the most prevalent face for anatase nanocrystals [Shklover et al., 1997].

Anatase is the most stable phase for nanoparticles below 11 nm. For calcinations in the range of 630 – 1050 °C anatase becomes rutile. Rutile is the most stable phase for nanoparticles above 35 nm <sup>[15]</sup>.

In TiO<sub>2</sub>-B, like in other forms of TiO<sub>2</sub>, edges and corners link TiO<sub>6</sub> octahedra [Marchand et al., 1980] (Figure 1.4). Regarding to the other most common forms of TiO<sub>2</sub> (anatase, rutile), TiO<sub>2</sub>-B is characterized by both cationic and anionic vacancies

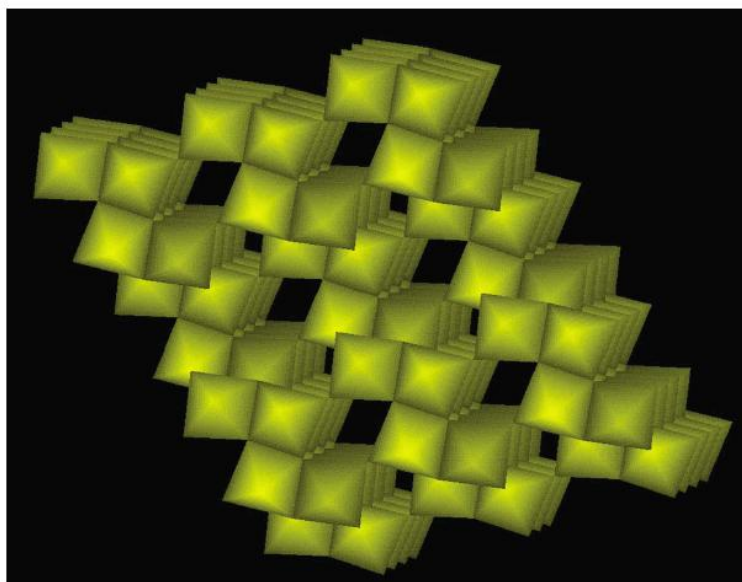


Figure 1.4. Crystal structure of TiO<sub>2</sub>-B [Bruce, 2005]

## 1.2 Properties

### 1.2.1 Electronic structure

TiO<sub>2</sub> is a semiconductor. It is characterized by a gap ranging from 3 to 3.2 eV between the top of the valence band and the bottom of the conduction band<sup>16</sup>. Classically, when TiO<sub>2</sub> is excited by a photon of energy equal or higher than the value of its bandgap, an electron “jumps” from the valence band to the conduction band and creates a hole in the valence band (Figure 1.5). This photogenerated electron-hole pair (so-called exciton) can promote redox reactions. This effect has been called Honda-Fujishima effect, from the names of the first two scientists who discovered it in 1972 [Fujishima and Honda, 1972].

---

<sup>15</sup> In the 11-35 nm range the most stable phase is brookite.

<sup>16</sup> A semiconductor with a large bandgap is an insulator [Shriver and Atkins, 2006].

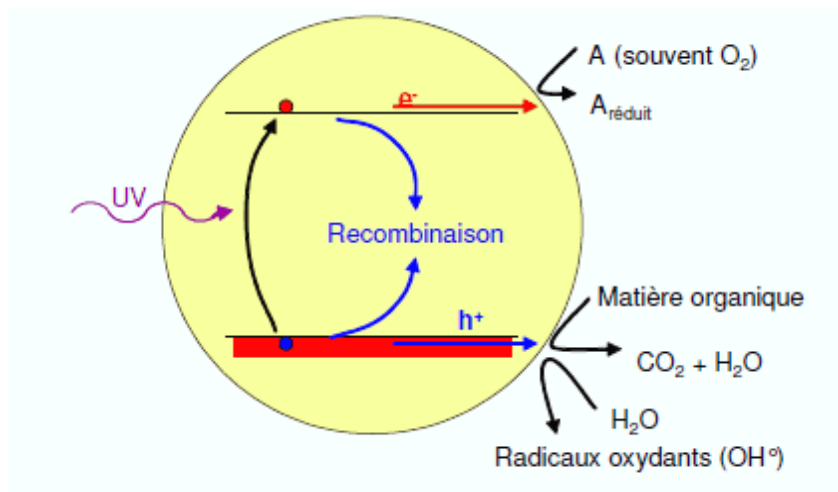
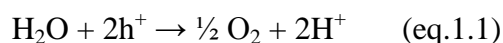


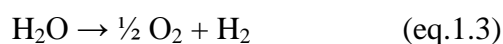
**Figure 1.5. Electronic excitation and photocatalytic process of a semi-conductor under solar irradiation (where,  $e^-$  is the electron and  $h^+$ , the hole, and A is the acceptor) [Hermann, 1999]**

The energetic levels of the valence band are mainly made up of the  $2p$  orbitals of the oxygen atoms, the energetic levels of the conduction band are made up of the  $3d$  orbitals of the titanium atoms. Regarding the three allotropic forms considered in the previous section, bandgap of i) anatase is 3.2 eV, ii) rutile is 3.0 eV and iii)  $\text{TiO}_2\text{-B}$  is 3.22 eV. In 1942 Earle reported that rutile and anatase are n-semiconductors<sup>17</sup> [Earle, 1942].

In a photocatalytic process, the partial reactions induced in water splitting are:



The overall reaction is the water dissociation reaction:



The standard free enthalpy per mole of the reaction (1.3) is  $\Delta_r G^0 = 237.141 \text{ kJ}\cdot\text{mol}^{-1}$ .

### 1.2.2 Optical properties

Using the Planck–Einstein equation, we can calculate the wavelength needed to excite anatase, rutile and  $\text{TiO}_2\text{-B}$ . For anatase the minimum energy required corresponds to a wavelength of 387.5 nm, for rutile 413.3 nm, for  $\text{TiO}_2\text{-B}$  385.1 nm. So anatase and  $\text{TiO}_2\text{-B}$  only absorb UV light, while rutile also absorbs visible light in the violet range.

<sup>17</sup> **n-type semiconductors** are characterised by a conductivity controlled by electrons in the CB.

### 1.2.3 Photoactivity

The Figure 1.6 sums up the most important photocatalytic applications of  $\text{TiO}_2$ .

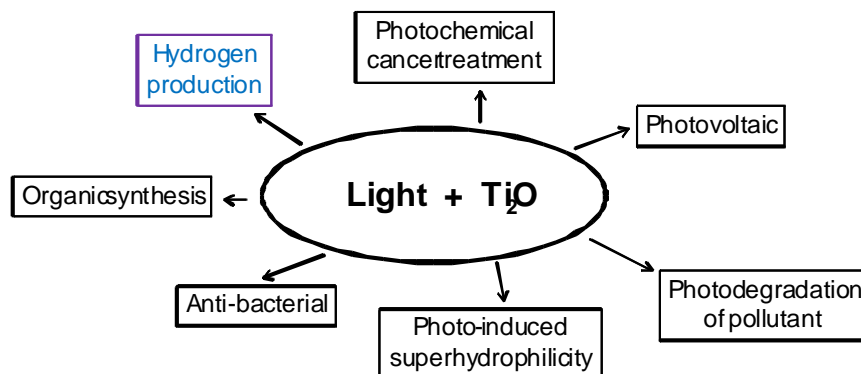


Figure 1.6. Main photocatalytic applications of  $\text{TiO}_2$  [Fujishima et al., 1999]

Among the several applications of  $\text{TiO}_2$ , here below I will only mention the most significant.

In 1972 the Honda-Fujishima effect was first applied by these scientists to the photoelectrochemical splitting of water ( $\text{H}_2\text{O}$ ) to produce hydrogen ( $\text{H}_2$ ) and oxygen ( $\text{O}_2$ ). At the end of 1977, Frank and Bard described the decomposition of cyanide in the presence of  $\text{TiO}_2$  aqueous suspensions [Frank and Bard, 1977]. In the 1980s, degradation of various harmful compounds in both water and polluted air were studied ([Fox and Dulay, 1993] and [Hoffman et al., 1995]). However,  $\text{TiO}_2$  is inadequate to treat huge amount of water and/or air, because light energy density is primarily low, and in addition,  $\text{TiO}_2$  can only use the UV part of the solar spectra as already exposed. Another important application is the degradation of the *Escherichia coli* (E.coli) cells that can completely disappear on  $\text{TiO}_2$  after about one week under a UV irradiation of  $1 \text{ mW}\cdot\text{cm}^{-2}$  [Sunada et al., 1998].

In the last decade research attention was focused on the ability of  $\text{TiO}_2$  to form hydrocarbon compounds starting from  $\text{CO}_2$  [Paulose et al., 2009]. In addition, the increasing worldwide need of energy and ambition to use solar light has led scientific community to re-consider the first application of Honda-Fujishima effect, i.e. the  $\text{H}_2$  production from water splitting [Hashimoto et al., 2005].

Among all the allotropic forms of  $\text{TiO}_2$ , anatase is the most photoactive one, which is probably mainly due to the position of its conduction band (CB) at  $-0.2 \text{ eV}$ , while CB of rutile is located at  $0 \text{ eV}$ . This means that anatase has a higher reducing power.

However, experiments carried out in water solutions demonstrate that for several applications the most active commercial material is actually Degussa P25, a mixture of anatase (80 wt.%) and rutile (20 wt.%).

Traditional theory in photocatalysis assesses that P25 is active because once excited the electron generated in the anatase phase “jumps” to the rutile one. So the combination of rutile and anatase improves the charge separation and, consequently, the photoactivity of the

material ([Hoffmann et al., 1995] and [Fujishima et al., 2000]). Although this statement is commonly accepted by the related scientific community, up to now no researches have been able to deeply explain the high performance of Degussa P25 [Hurum et al., 2003].

In 2003 Hurum et al. [Hurum et al., 2003] criticized this reference theory and proposed a new approach. Hurum and co-workers used the electron paramagnetic resonance (EPR) to characterize the behavior of the excited electrons. They stated that they are first transferred from rutile CB to localized states (traps) having their energy level in the anatase band gap, then to anatase particle surface. Moreover, since rutile is active under visible light, it is able to absorb more photons what contributes to increase the global efficiency.

Figure 1.7 illustrates the two different approaches: the original theory and the Hurum's one. In any case it appears clear that the strength of Degussa P25 is the contact between rutile and anatase that allows charges separation at the interface of the two phases.

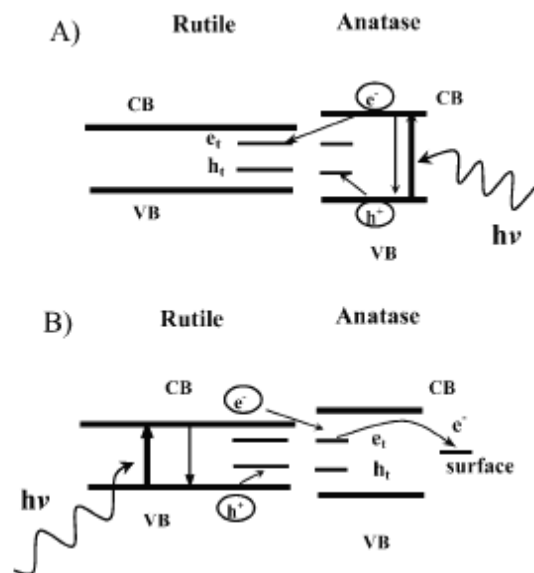


**Figure 1.7. Schematic illustration of charges separation in P25 : A) Original model where charges separation occurs in anatase and rutile acts as electron sink, B) Hurum's model where rutile is the antenna with subsequent charge separation [Hurum et al., 2003].**

## 1.2.4 Hydrogen production: water photolysis

### 1.2.4.1 Theoretical basis

The condition required for semiconductors to be efficient for  $H_2$  production by water photolysis is rather simple: the conduction band level should be more negative than  $H_2$  production level ( $E_{H^+/H_2O} = 0$  eV at pH=0) while the valence band should be more positive than  $H_2O$  oxidation level ( $E_{O_2/H_2O} = 1.23$  eV at pH=0) [Ni et al., 2007]. Several semiconductor

candidates satisfy this requirement: GaP, ZrO<sub>2</sub>, CdS, KTaO<sub>3</sub>, KTa<sub>0.77</sub>Nb<sub>0.23</sub>O<sub>3</sub>, CdSe, SrTiO<sub>3</sub>, TiO<sub>2</sub>, Nb<sub>2</sub>O<sub>5</sub> and ZnO (Figure 1.8). Among all these materials, TiO<sub>2</sub> is the most suitable because it is considered stable against corrosion, it has a quite strong photoactivity, it has a strong chemical stability in various environments and, last but not least, it is abundant and cheap.

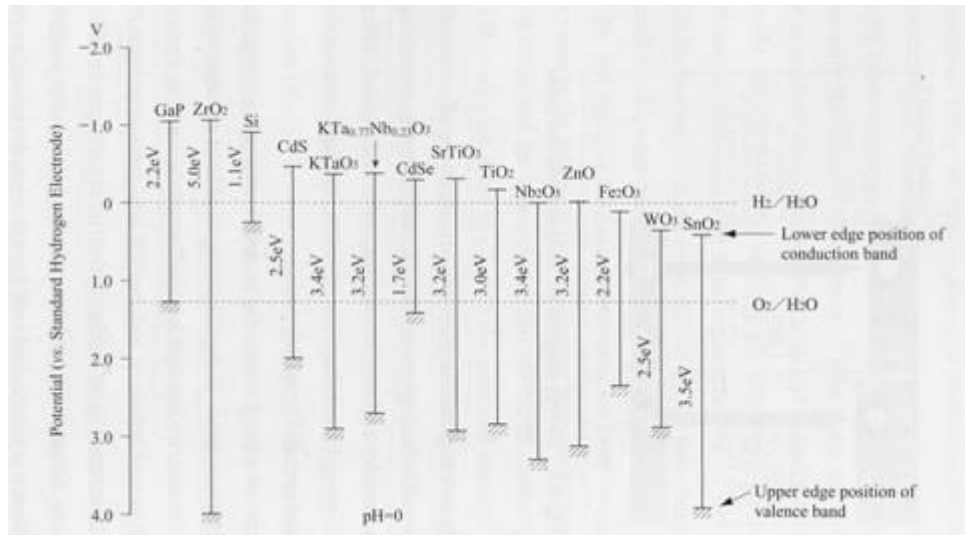


Figure 1.8. Potentials diagram for typical semiconductors. [Fujishima et al., 1999]

Water splitting is a photocatalytic process cycle because it satisfies the three criteria described in 2007 by Emeline et al. [Emeline et al., 2007]:

- The reagent must be adsorbed and the energy of adsorption must not be too high, otherwise the adsorbate molecules will be bound to the surface too strongly, what might prevent their subsequent transformation.
- The activation energy barrier for a surface photoreaction must be lower than the corresponding energy barrier of the thermal dark process.
- The binding energy of the reaction products on the surface must be sufficiently low so that they can easily desorb in ambient conditions. This third point is critical in fulfilling the requirement of chemical restoration of the initial state of the photocatalyst.

Emeline et al. [Emeline et al., 2007] state that water photolysis satisfies these three criteria because:

- The surface of TiO<sub>2</sub> is hydroxylated, which strongly polarizes the adsorbed water molecules, due to charges on the surface. So the reactive state of these water molecules is higher than reactive state of water molecules in liquid phase;
- Adsorbed water molecules are both reduced and oxidized by photogenerated carriers. This proves that the bottom of the conduction band of TiO<sub>2</sub> is lower than reduction potential of water and that the top of the valence band is higher than oxidation potential of water;
- Products of photolysis (O<sub>2</sub> and H<sub>2</sub>) easily desorb from the surface, thus the surface sites return to their hydroxylated state.

### 1.2.4.2 Notion of efficiency

As already said in the introduction, the US DOE set the commercialization benchmark of energy conversion efficiency (ECE) at 10% [Nowotny et al, 2007]. In this case the ECE is defined as the ratio of energy output ( $E_{out}$ ) from the produced hydrogen to the amount of external energy provided to the system (Equation 1.4):

$$\eta = \frac{E_{out}}{E_{in}} \quad \text{eq. 1.4}$$

$E_{out}$  is the energy provided by hydrogen produced by the water splitting, knowing that the enthalpy of the hydrogen oxydoreduction is - 241.84 kJ/mole and the free energy is - 227.968 kJ/mole.  $E_{in}$ , instead, can be calculated by the integration of the spectrum of the irradiation lamp as function of the reactor geometry.

In the case of the photoelectrolysis,  $E_{out}$  and  $E_{in}$  are decomposed in detail in the following equation 1.5:

$$\eta = \frac{j_P(E_{rev}^0 - |E_{app}|)}{I_0} \quad \text{eq. 1.5}$$

where  $j_P$  is the photocurrent density ( $\text{mA}\cdot\text{cm}^{-2}$ ),  $I_0$  is the irradiance of incident light ( $\text{mW}\cdot\text{cm}^{-2}$ ),  $E_{rev}^0$  is the standard reversible potential (which is 1.23V for water splitting reaction),  $|E_{app}|$  is the absolute value of the applied potential which is obtained as follows :

$$E_{app} = (E_{meas} - E_{aoc}) \quad \text{eq. 1.6}$$

where  $E_{meas}$  is the potential at which the photocurrent density was measured,  $E_{aoc}$  is the electrode potential at open circuit condition in the same electrolyte solution under the same illumination intensity at which the photocurrent density was measured ([Nowotny et al, 2007]).

Varghese et al. [Varghese and Grimes, 2008] defined the overall solar energy conversion efficiency of a water photoelectrolysis cell ( $\epsilon_0$ ) as the product of the absorption efficiency ( $\epsilon_g$ ), the quantum efficiency ( $\epsilon_q$ ) and the chemical efficiency ( $\epsilon_c$ ):

$$\epsilon_0 = \epsilon_g \epsilon_q \epsilon_c \quad \text{eq. 1.7}$$

$\epsilon_g$  can be defined as the ratio of the absorbed energy on the incident energy;  $\epsilon_q$  is the ratio of number of excitons on the number of absorbed photons;  $\epsilon_c$  is the fraction of excited state energy converted to stored chemical energy. These three definitions suggest that, in order to improve the efficiency, we can:

- improve the light absorption of the photocatalyst, to increase the adsorbed energy and consequently  $\epsilon_g$ ;
- improve the charge separation, to increase the number of excitons and consequently  $\epsilon_q$ ;
- limit the backward reaction, to increase the excited state energy and consequently  $\epsilon_c$ .

The solid line of the Figure 1.9 shows the profile of the overall solar energy conversion efficiency depending upon the wavelength to excite the semiconductor, under solar light. The maximum of 33% corresponds to a bandgap wavelength of 900 nm, so the bandgap of the semiconductor must be 1.38 eV.

To have at least 10% efficiency the bandgap must be not higher than 2.68 eV, this is why narrowing the TiO<sub>2</sub> bandgap is crucial. Of course, this is an ideal limit. Considering the energy loss ( $E_{\text{loss}}$ ) a smaller bandgap semiconductor is needed. The dotted line of the Figure 1.9 reports the maximum photoconversion efficiencies corresponding to different values of  $E_{\text{loss}}$ . The ideal limit of  $\epsilon_0$  is 30.7% corresponding to a bandgap wavelength of 775 nm (1.6 eV) and  $E_{\text{loss}}$  0.38 eV.  $E_{\text{loss}}$  considers losses due to thermodynamics as well as losses caused by the non-idealities in the conversion process (kinetic losses).

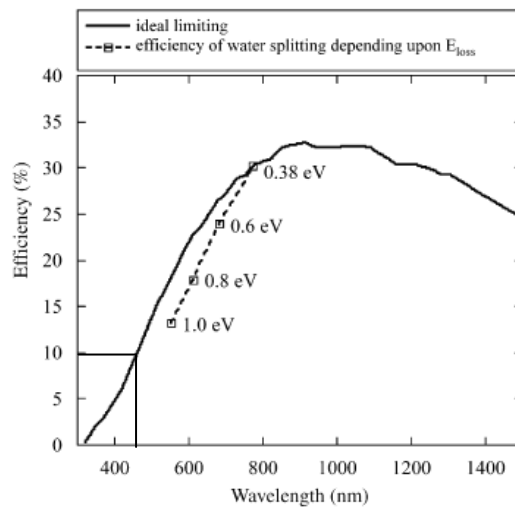


**Figure 1.9. The ideal limiting solar conversion efficiency for single band gap devices. The dotted line shows efficiency of photoelectrolysis cells at different values of  $E_{\text{loss}}$  [Varghese and Grimes, 2008]**

In most of the laboratories, researchers usually use a xenon lamp or a AM1.5 global solar system to simulate the solar spectrum. Simulated spectra often have deviation from the solar spectrum. Murphy et al. [Murphy et al., 2006] correlated the maximum efficiency depending upon semiconductor bandgap under xenon or AM1.5 illuminations (Figure 1.10). For a 10% efficiency bandgap of the semiconductor should be about 2.4 eV.

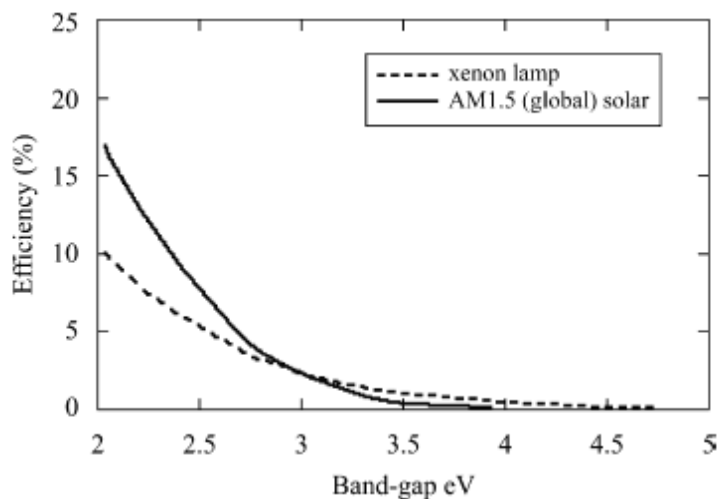


**Figure 1.10. Maximum possible efficiency depending upon semiconductor bandgap, under xenon arc lamp and AM1.5 solar illuminations [Murphy et al., 2006]**

As already stated in the general introduction of this manuscript, the efficiency of a TiO<sub>2</sub>-based water splitting system using solar energy is low due to:

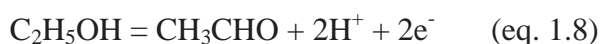
- fast recombination of the photogenerated electrons/holes,
- fast backward reaction between H<sub>2</sub> and O<sub>2</sub> into water,
- and, of course, inability to harvest visible light.

#### 1.2.4.3 Potential solutions to improve water splitting efficiency

Scientists have investigated several techniques to resolve the hardships underlined here-before and enhance the H<sub>2</sub> production. These techniques can play a role in the charge separation (addition of electron donors, noble metal loading, dye sensitization and elaboration of composite semiconductors), on the suppression of the backward reaction (addition of carbonate salts) or on the bandgap reduction (doping and ion implantation). They are listed and briefly commented below.

• **Addition of electron donors**, such as ethylenediamine tetraacetic acid (EDTA), methanol (MeOH), ethanol (EtOH), lactic acid ([Gurunathan et al., 1997], [Lee et al., 2001], [Bamwenda et al., 1995] and [Nada et al., 2005]), in order to improve the charge separation.

Organic compounds donate electrons at the VB<sup>18</sup> to compensate the electron deficiency. For example, for ethanol and methanol, it can be illustrated as follows.



and

---

<sup>18</sup> Valence band.



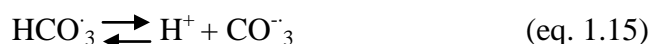
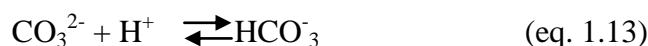
Not only is MeOH a hole scavenger in water splitting mechanism but also an hydrogen source. TiO<sub>2</sub>, in fact, also catalyzes methanol reforming reactions [Galinska and Walendziewski, 2005], [Al-Mazroai et al., 2007], [Jitputti et al., 2008], [Rosseler et al., 2010]:



The last reaction shows that the overall reaction conducts to H<sub>2</sub> and can have CO<sub>2</sub> as a final product if the reaction is complete.

• **Addition of carbonate salts**, in order to suppress the backward reaction. The most efficient one is Na<sub>2</sub>CO<sub>3</sub> [Arakawa and Sayama, 2000].

Photo-generated holes were consumed by reacting with carbonate species to form carbonate radicals as follows.



On the other hand, peroxy carbonates were easily decomposed into O<sub>2</sub> and CO<sub>2</sub>



The evolution of CO<sub>2</sub> and O<sub>2</sub> could promote desorption of O<sub>2</sub> from the photocatalyst surface and thus could minimize the formation of H<sub>2</sub>O through the backward reaction between H<sub>2</sub> and O<sub>2</sub>. Then desorbed CO<sub>2</sub> soon was dissolved and converted into HCO<sub>3</sub><sup>-</sup>, in turn effecting H<sub>2</sub> production.

Addition of the same amount of Na<sub>2</sub>CO<sub>3</sub> and K<sub>2</sub>CO<sub>3</sub> should exhibit comparable photocatalytic influence. However, when Pt-TiO<sub>2</sub> was used as photocatalyst, addition of Na<sub>2</sub>CO<sub>3</sub> was more effective than addition of K<sub>2</sub>CO<sub>3</sub> in terms of H<sub>2</sub> production [Arakawa and Sayama, 2000]. The reason to the above phenomenon remains unknown.

Electrons donors and carbonate salts are consumed during the reaction, so continual addition of electron donors is required to sustain hydrogen production. They are named “sacrificial agents”. This is the limitation of their use.

• **Noble metal loading**, such as Pt, Pd and Au [Bamwenda et al., 1995], [Sakthivel et al., 2004], [Wu and Chen, 2004], [Rosseler et al., 2010].

As the Fermi levels of these noble metals are lower than that of the top of the CB<sup>19</sup> of TiO<sub>2</sub>, photo-excited electrons can be transferred from CB to metal particles deposited on the surface of TiO<sub>2</sub>, while photo-generated VB holes remain on the TiO<sub>2</sub>. These phenomena greatly reduce the possibility of electron-hole recombination, resulting in efficient separation and stronger photocatalytic activity.

• **Doping** (cationic and anionic) [Choi et al., 1994]. The effects of the doping on the photocatalytic activity will be described in a separate paragraph (paragraph 1.4).

• **Dye sensitization** [Dhanalakshmi et al., 2001].

In the dye sensitization technique the sensitizer (and not the semiconductor) is excited by visible light (Figure 1.11). The transfer of electron from the dyes to the semiconductor causes the hydrogen production reactions. Dye sensitization is widely used to utilize visible light for energy conversion. Some dyes having specific redox property and visible light sensitivity can be used in solar cells as well as photocatalytic systems. Adding redox systems or sacrificial reagents, such as I<sub>3</sub><sup>-</sup>/I or EDTA, enables the dye regeneration.

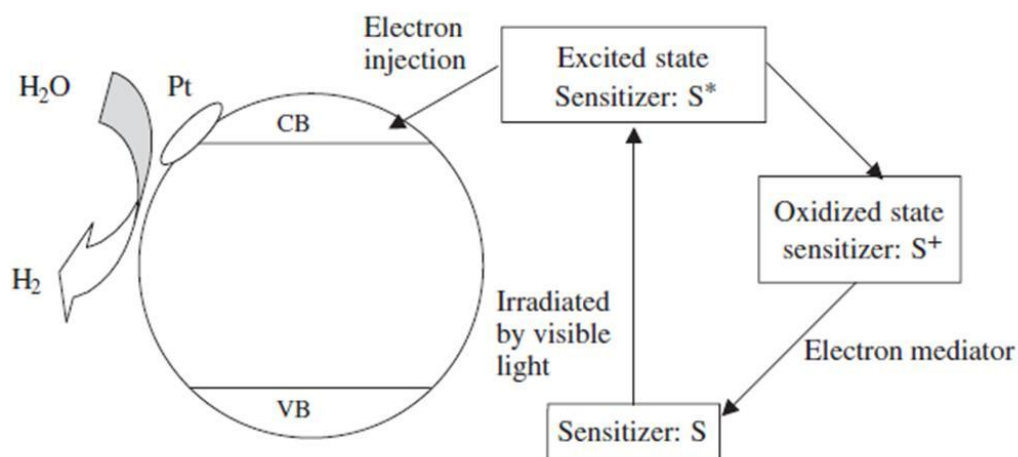


Figure 1.11 : Schematic mechanism of dye-sensitized photocatalytic hydrogen production under visible light irradiation [Ni et al., 2007]

• **Elaboration of composite semiconductors** [So and ans SJ Moon, 2004].

Semiconductor coupling is another method to utilize visible light for hydrogen production. The idea of this technique is the same as the dye sensitization: TiO<sub>2</sub> is not directly excited by light but receives electrons. Following the reference theory explaining the action of the P25

<sup>19</sup> Conduction band.

(and already exposed in part 1.2.3), when a large band gap semiconductor is coupled with a small band gap semiconductor with a more negative CB, CB electrons can be injected from the smaller band gap semiconductor to the larger band gap semiconductor. Thus, a wide electron-hole separation can be achieved as shown in Figure 1.12.

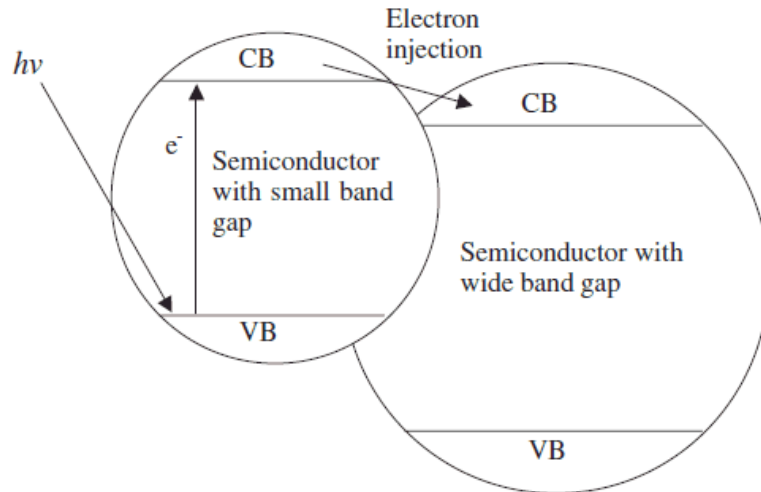


**Figure 1.12 Schematic illustration of the electron injection mechanism in composite semiconductors**  
[Ni et al., 2007]

• **Metal and non-metal ion implantation** [Anpo et al., 2001].

When  $\text{TiO}_2$  is bombarded with high-energy transitional metal ions (accelerated by high voltage), these high-energy ions are injected into the lattice and interact with  $\text{TiO}_2$ . This process modifies  $\text{TiO}_2$  electronic structure and optical response. Through molecular orbital calculations, Yamashita et al. [Yamashita et al., 2001] investigated the effect of the vanadium ( $\text{V}^{5+}$ ,  $\text{V}^{4+}$ ,  $\text{V}^{3+}$ ) implantation on the  $\text{TiO}_2$  matrix. Yamashita found that vanadium cations substitute the  $\text{Ti}^{4+}$  ion and that the mix of  $\text{Ti}(d)$  orbital with metal( $d$ ) orbital of the implanted metal ions leads to bandgap narrowing [Yamashita et al., 2001].

Presently metal ion implanted  $\text{TiO}_2$  is considered to be the most effective photocatalyst for solar energy utilization and is in general referred as the “second generation photocatalyst”.

#### 1.2.4.4 Testing systems: photoreactors

Once elaborated, materials must be tested in a photoreactor. Schematically, the main two features of any photoreactor are the irradiation source and the quartz or borosilicate glass jacket design. Quartz has a high transmission ratio but is quite expensive. On the other hand, borosilicate is less expensive but transparent only in the near-UV domain.

Different types of lamp can be used as irradiation sources. Hg lamp emits mainly UV radiations, whereas xenon lamp emits UV-VIS light and its spectrum is, in the visible range, the most similar to solar one. Figure 1.13 shows the spectra of xenon lamp (with and without filter) and AM1.5 global sunlight. It can be seen that although spectrum of xenon lamp has a profile close to that of AM1.5, its photon flux is greater at short wavelengths.

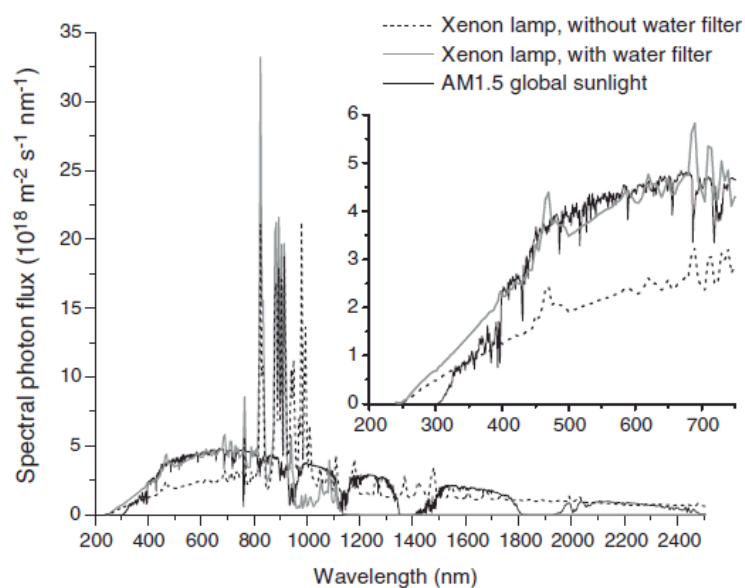


**Figure 1.13.** Spectral photon flux for the xenon lamp, with and without the water filter, compared to the AM1.5 global solar spectrum. The lamp had logged 1250 h of operation when the spectrum was recorded. The inset shows detail of short wavelengths. In all cases, the total irradiance is normalised to  $1000\text{Wm}^{-2}$ . [Murphy et al., 2006]

Photoreactors for water splitting are typically cell systems or suspension systems. If carried out in a cell system (i.e. the semiconductor is coated on an electrode) the hydrogen production is called photoelectrochemical, if semiconductor is dispersed in a reagents solution the process is called photocatalytic [Ashokkumar, 1998].

The most famous cell system is the Honda-Fujishima equipment (Figure 1.14):

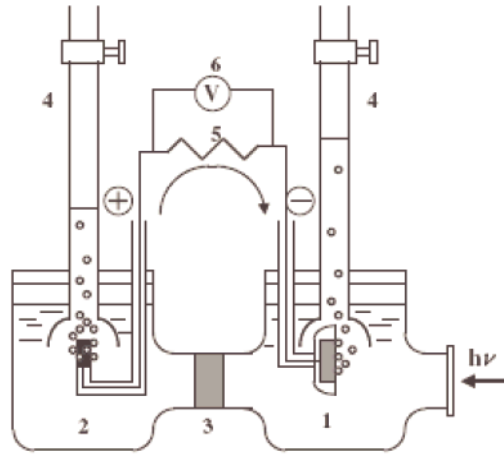


**Figure 1.14. Schematic diagram of photoelectrochemical cell. (1)TiO<sub>2</sub> electrode, (2) platinum black counter electrode, (3) ionically conductor separator, (4) gas burettes, (5) load resistance, (6) voltmeter. [Fujishima and Honda, 1972]**

Working on the efficiency of photocatalysts and of their deposition methods is the key points for improving this equipment.

The second group of hydrogen production photoreactors concerns suspensions. TiO<sub>2</sub> powders are dispersed in aqueous solution in the reactor. Both reduction and oxidation reactions take place on the nanoparticles surface (Figure 1.15):

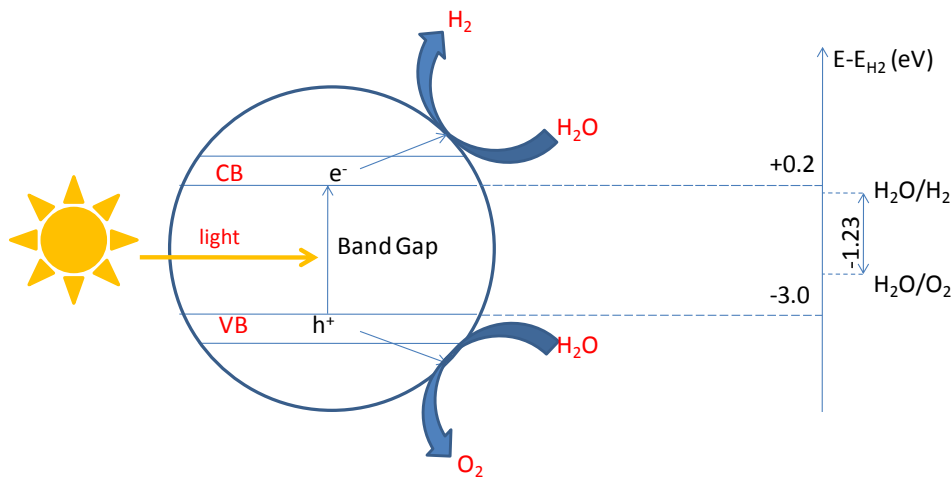


**Figure 1.15. Representation of watersplitting reaction on TiO<sub>2</sub> anatase nanoparticles surface**

Each nanoparticle can be considered as a *mini*-reactor. Advantages of this configuration are the ease of laboratory fabrication and the limitations of energy losses. However, the evolution of hydrogen and oxygen in the same compartment entails the necessity to either use sacrificial agents or separate both gases, to avoid any risk of recombination.

Lamp can be set outside the reactor [Nishijima et al., 2007] as well as inside the reactor [Jitputti et al., 2007], as shown in Figure 1.16.

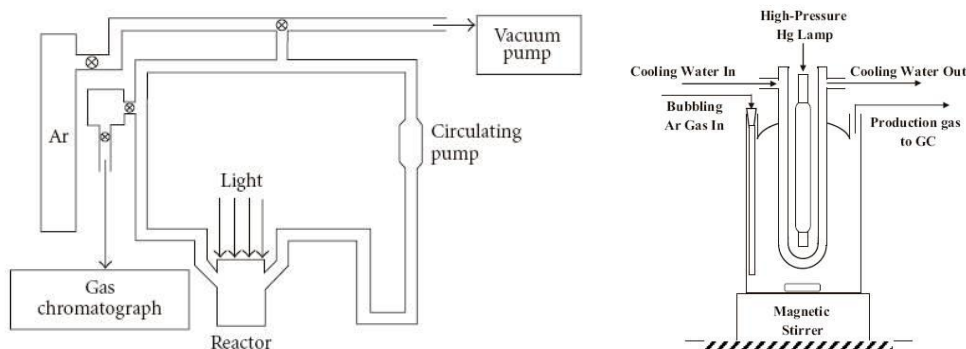


**Figure 1.16.** On the left side, the scheme shows a slurry reactor with an outside lamp [Nishijima et al., 2007] and on the right side, a slurry reactor with an inside lamp [Jitputti et al., 2007]

### 1.3 Elaboration methods

One of the original points of this thesis is the study of the impact of different morphologies on the hydrogen production, keeping constant the crystalline phase. No systematic investigation on this matter had been found in literature at the beginning of my thesis in this direction, and comparing results of different researches can easily lead to misunderstanding, because of the huge amount of variable parameters, like, for example, the testing conditions. In addition I had the great opportunity to use several elaboration techniques and competences within the research center.

Morphology and texture of the material have, as I will “demonstrate” in the following chapters, great impact on charge separation, a crucial point for hydrogen production.

The idea of this study is to synthesize several amorphous materials and crystallize them in a further step. For each morphology, we have selected the following elaboration methods.

1. Precipitation of  $\text{TiCl}_4$  and  $\text{NaOH}$  in order to have an amorphous and reactive precursor for a hydrothermal crystallization at defined temperature and pH. The final materials are slightly elongated nanoparticles;
2. Hydrothermal alkaline process to have lepidocrocite-type sheets, following the preparation method established by Kasuga [Kasuga et al., 1998b]. After the hydrothermal transformation, the product is washed with water. According to the Ma’s work [Ma et al., 2004] single-layer nanosheets of hydrated  $\text{Ti}_{0.91}\text{O}_2$  roll up into sodium titanate nanotubes after washing with  $\text{NaOH}$  water solution. The PhD thesis of Thomas Beuvier correlates the rolling-up of nanosheets to the conditions of the hydrothermal transformation:  $\text{NaOH}$  concentration (pH of the suspension), precursor (raw material), time and temperature. Indeed, once washed with water we can obtain four different morphologies: nanosheets, nanotubes, nanowires and nanofibers. A further acid ion-exchange leads to acidic titanates structures. After calcination we can obtain crystallized objects;

3. Sol-gel route to obtain amorphous and very porous precursors. We have dried our gels following two different processes in order to have two significantly different materials (xerogels or aerogels). Both products have then been crystallized by calcination.

In the following paragraphs I detail these three elaboration methods.

### 1.3.1 Nanoparticles from precipitation of $\text{TiCl}_4$

Several synthesis routes can be used to elaborate  $\text{TiO}_2$  nanoparticles, some of these preparation methods are:

1. Hydrolysis or thermohydrolysis of  $\text{TiCl}_4$  or  $\text{TiCl}_3$ . In order to complete the crystallization, the precipitated is aged for several days or calcined or treated in hydrothermal conditions;
2. Thermal decomposition of a titanium precursor (for example titanium isopropoxide) vapor in a flow reactor system by the metal organic chemical vapor deposition method (MOCVD) [Schleicha and Walter, 1997], [Benfer and Knzinger, 1999];
3. Solution combustion method: a solution of titanyl nitrate and glycine in water heated to  $350\text{ }^\circ\text{C}$ . The solution undergoes dehydration and a spark appears locally, which spreads throughout the mass yielding a voluminous solid product [Nagaveni et al., 2004].

In this thesis I have elaborated  $\text{TiO}_2$  nanoparticles from the precipitation of two solutions of  $\text{TiCl}_4$  and  $\text{NaOH}$  followed by crystallization in autoclave. For this system we have chosen to precipitate under standard conditions of temperature and pressure ( $25\text{ }^\circ\text{C}$  and 1 atm) and pH of the solution 2. In this part we will explain why we have chosen this pH.

The aim of the precipitation of  $\text{TiCl}_4$  was not to directly synthesize well crystallized nanoparticles, but have a reactive precursor for the following hydrothermal transformation in the autoclave. Transformation in autoclave is faster, allows a complete crystallization of the final product and a better control of the agglomerates. In this work the parameters we have changed are temperature and pH of hydrothermal crystallization, and we have kept constant the conditions of precipitation.

Precipitation and crystallization are governed by surface phenomena. In the discussion part of the chapter devoted to the preparation of not-modified nanoparticles, we will use theoretical concepts. Here below I am going to recall the most important ones.

Let us consider the formation of a solid  $A_S$  from solubilized  $A_L$ :  $A_L \rightarrow A_S$

The driving force of the precipitation (and of the crystallization) is the difference of the chemical potentials of the starting solution and the suspension at its equilibrium point:

$$\mu_L - \mu^{eq} = RT \ln(a/a^{eq}) \quad (\text{eq. 1.18})$$

where  $a$  and  $a^{eq}$  are respectively the activities of the solute in the real solution and the activity of the solute at its equilibrium point.

The ratio  $a/a^{eq}$  is the supersaturation ratio ( $S$ ). A low supersaturation ratio ( $1 < S < 10$ ) usually leads to the formation of crystals with characteristic size ranging from micron to millimeter (crystallization), because of the low nucleation rate and a long and significant growth. A high supersaturation ratio ( $S > 10^3$ ) leads to precipitation, because of a high nucleation rates.

In the precipitation process, surface tension has a fundamental role on the features of the final products: size, shape, crystal phase, solubility, nucleation and growth. Surface tension is defined as the energy required to increase the surface area of the condensed phase by a unit amount.

During the precipitation, solid is formed in four steps:

1. Generation of a zero-charge precursor in solution;
2. Formation of nuclei by condensation of zero-charge precursor:

Several kinds of nucleation can occur:

- Primary nucleation: nuclei are directly issued from the starting solution. This nucleation can be:
  - Homogeneous if nuclei are formed in the bulk ;
  - Heterogeneous if nuclei are formed on solid foreign objects (reactors walls, stirrer, solid particles).
- Secondary nucleation: nuclei are issued by attrition from the precipitated phase.

Literature reports several kinetics models that linked the nucleation with the sursaturation and the surface tension. In the classical theory, the variation of the free enthalpy corresponding to the formation of solid germs composed of  $n$  units from a solution is given by the following equation [Nielsen, 1964]:

$$\Delta G = n(\mu_S - \mu_l) + A\gamma \quad (\text{eq. 1.19})$$

where:

- $n$  is the number of monomers of the solid particle, chemical potential of which is  $\mu_S$ ;
- $\mu_l$  is the chemical potential of the particle in the solution;
- $A$  is the surface of the germ ( $\text{m}^2$ );
- $\gamma$  is the solid-liquid surface tension ( $\text{J} \cdot \text{m}^{-2}$ ).

If we suppose that the germ is spherical and composed of  $n$  monomers with  $v$  their molecular volume, we can calculate its radius  $r$  and surface  $A$ :

$$r = \left(\frac{3nv}{4\pi}\right)^{\frac{1}{3}} \quad (\text{eq. 1.20})$$

$$A = n^{2/3}(36\pi v^2)^{1/3} \quad (\text{eq. 1.21})$$

$$\text{So } \Delta G = -nkT \ln S + n^{2/3}(36\pi v^2)^{1/3}\gamma \quad (\text{eq. 1.22})$$

the maximum of  $\Delta G$  corresponds to a critical radius that may be considered as the radius of the nuclei:

$$r^* = \frac{2\gamma.v}{kT \ln S} \quad (\text{eq. 1.23})$$

Furthermore, the nucleation rate  $J$  can be expressed:

$$J = A_1 \exp\left(-\frac{16\pi V_m^2 \gamma_{g,l}^3}{3(KT)^3 \ln^2 S}\right) \quad (\text{e.q. 1.24})$$

Where  $A_1$  is the kinetic coefficient [nb]  $\text{m}^{-3}\text{s}^{-1}$

3. Growth of the germ by :

- a. 2D nucleation on the surface of the particles following the same chemical process (oxolation and/or olation) occurring during the germination. The number of the molecules constituting the germ is:

$$n^{\text{crit}} = \frac{2\lambda}{kT \ln S} \quad (\text{eq. 1.25})$$

where  $\lambda$  is the linear energy (equivalent to surface energy but adapted to 2D nuclei) ( $\text{J}\cdot\text{m}^{-1}$ ).

So the free enthalpy is:

$$\Delta G^{\text{crit}} = \frac{4\lambda^2}{kT \ln S} \quad (\text{eq. 1.26})$$

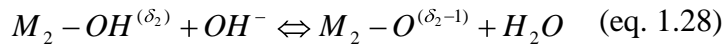
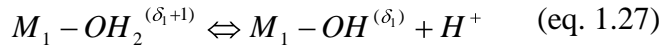
In this case the growing velocity depends on the frequency of the creation of 2D germs.

- b. continuous growth supported on a defect (spiral growth...) or not (K-faces);
- c. oriented attachment.

4. Aging of the particles in suspension, it means an increase of the average size of the particles via Ostwald ripening.

Sursaturation can be evaluated using some models based on the knowledge of the speciation and solubility of the solid phases. Surface tension can also be evaluated using models involving the nature of the faces and surface charge. This surface charge is due to the acid-basic sites, so due to the pH for the (hydr)oxides.

During the precipitation of  $TiCl_4$ , (hydr)oxides are formed. On the oxide surface the charge reversal involves two acid-base couples:



Protonation constants of these two formulas can be evaluated by the MUSIC theory [Hiemstra1989]. When the values of the protonation constants differ of at least 2 or 3 pH units, at  $pH > PZC^{20}$  the negative surface charge is caused by the deprotonation of  $M_2OH$  groups, at  $pH < PZC$  the positive charge is given by the the protonation of  $M_1OH$  groups [Jolivet et al., 2004].

The surface charge of the solid is linked to surface tension. Gibb's law states that the surface tension depends on the adsorption density  $\Gamma$  ( $\text{mol.m}^{-2}$ ) and chemical potentials of species  $i$ :

$$d\gamma = - \Gamma_i d\mu_i \quad (\text{eq. 1.29})$$

Size and shape of nanoparticles depends on interfacial tension between liquid and solid, which can be controlled via pH.

The equation 1.24 shows that when the density of charged surface is high, the interfacial tension is low and the size of nanoparticles decreases. So in order to have small nanoparticles, pH of the solution must be far from the point of zero charge, on condition that we stay in the plateau of low solubility and if we consider isotropic particles. The PZC of  $TiO_2$  is between 5.2 and 7. So we should choice a pH lower than 5.2 or higher than 7.

In the case of  $TiO_2$ , another complication comes from polymorphism. Jolivet and his co-workers establish in several articles [Cassaignon et al., 2007], [Jolivet et al., 2008], [Pottier et al., 2003] the correlation of pH of solution and crystal phase of the final product.

For pH 1-2 rutile phase is formed, for  $2 \leq pH \leq 6$  phase anatase and brookite precipitated, for higher pH product is not crystallized. At pH close to 5 amount of brookite is 20% [Pottier et al., 2003]. Among these three forms of  $TiO_2$ , anatase has the smallest size. Since for our experiments we wanted small particles size to have high solubility for the following crystallization in autoclave, we have chosen pH 2. The Figure 1.17 shows that size of particles

---

<sup>20</sup> The point of zero charge is defined as “pH values for which one of the categories of surface charge is equal to zero, at given ambient temperature, pressure and aqueous solution composition” [Vayssieres, 2007].

increases with the pH. Since PZC of anatase is 5.3, precipitation was achieved for pH lower than PZC.

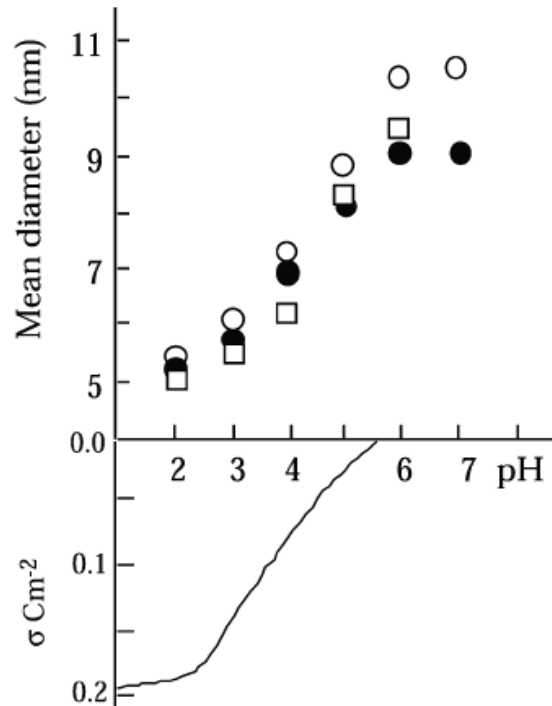


**Figure 1.17.** Average size of anatase particles formed at different pH and ionic strength NaCl (0.5 mol.L<sup>-1</sup>) and aged 24 hours (●) and one week (○) at 60 °C. □ mean particle size at ionic strength NaCl (3 mol.L<sup>-1</sup>) and aged one week at 60 °C. (b) Variation of the electrostatic surface charge density of anatase

## 1.3.2 Nanotubes from Kasuga's method

### 1.3.2.1 Preliminary presentation

1 D TiO<sub>2</sub> morphology has received much attention for its wide range of industrial applications, because of its good electron conduction [Yoshida et al., 2005]. Up to now three are the main methods for preparation of TiO<sub>2</sub> nanotubes:

1. the template method. The method involves the synthesis of the nanotubular structures within the pores of a nanoporous membrane: the pores within these nanoporous membranes act as templates for the synthesis of nanomaterials [Hulteen and Martin, 1997];
2. anodic oxidation. Nanotubes are fabricated by anodic oxidation of a pure titanium sheet in an aqueous solution containing hydrofluoric acid [Gong et al., 2001];
3. wet chemical method. In 1998 Kasuga et al. reported the synthesis of TiO<sub>2</sub> nanotubes via alkaline treatment.

Figure 1.18 illustrates the chronology of synthesis and applications of TiO<sub>2</sub> nanotubular structures:

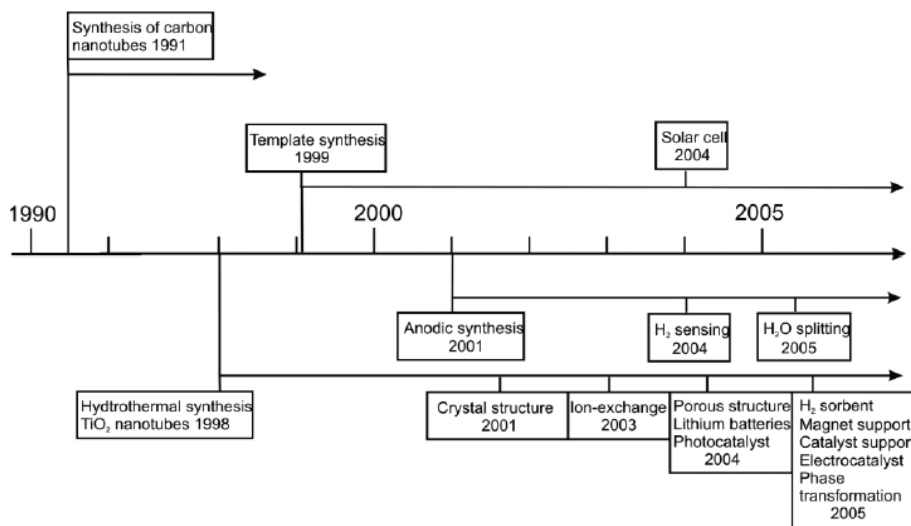


Figure 1.18. Simplified timeline describing the development of TiO<sub>2</sub> nanotubular structure

### 1.3.2.2 Synthesis conditions

The “Kasuga method” [Kasuga et al., 1998a], [Kasuga et al., 1998b] consists of four main steps:

1. Hydrothermal transformation of a precursor of TiO<sub>2</sub> (anatase, rutile or amorphous precipitate) at 110-170 °C for 0.5-6 days in strong basic solution (usually NaOH 8-10 M);
2. Washing with water and ion-exchange treatment with acid (usually HCl or HNO<sub>3</sub>);
3. Drying;
4. Calcination.

Features of the final product mainly depend on the combinations of hydrothermal transformation parameters: nature of the TiO<sub>2</sub> precursor, time and temperature of the hydrothermal transformation, concentration of the basic solution, and molar ratio of TiO<sub>2</sub>/NaOH. Bavykin et al. carried out a study on the effect of hydrothermal conditions on the final properties of TiO<sub>2</sub> nanotubular materials. In this study they changed amount of TiO<sub>2</sub> precursor (0.25-9 g of anatase) and temperature (120-190 °C); they kept constant amount and concentration of NaOH (300 mL 10 M) and time (22 h). Main results of this work are:

1. Increasing the molar ratio of TiO<sub>2</sub>/NaOH leads to an increase of the average pore diameter and a decrease of the specific surface area;

2. Increasing the temperature from 120 to 150 °C leads to an increase of the average pore diameter of TiO<sub>2</sub> nanotubular structures. Materials are hollow;
3. Temperatures above 170 °C cause synthesis of not-hollow structures with a wide size distribution in diameter.

Tsai et Teng [Tsai and Teng, 2004] confirm the result of Bavykin on the increase of the tube diameter with the temperature. Moreover they establish that surface area increases with temperature till 140 °C, while it drops at 150 °C.

So low temperatures should lead to the preparation of photocatalysts with high surface area. However materials issued from hydrothermal transformations at about 120 °C tend to break into nanoparticles during calcinations at 400-500 °C, temperature at which anatase is formed. 150 °C, instead, allows a stabilization of the morphology even after post-heat treatment [Yoshida et al., 2005].

Since we wanted to keep the morphology, we have chosen the following synthesis conditions: anatase commercial nanoparticles (since we have used a protocol established in the literature), 150 °C, 72h in order to have a complete transformation of the precursor, 8 g of TiO<sub>2</sub> on 100 ml NaOH 10 M.

### 1.3.2.3 Morphology classification

Scientific community employs several terms to name TiO<sub>2</sub> 1D nanostructures: nanotubes, nanorods, nanofibers, nanowhiskers, nanobelts and nanocylinders, for example. Bavykin et al. [Bavykin et al., 2006] define four main morphologies: nanosheets, nanotubes, nanowires and nanofibers, as Figure 1.19 sums up:

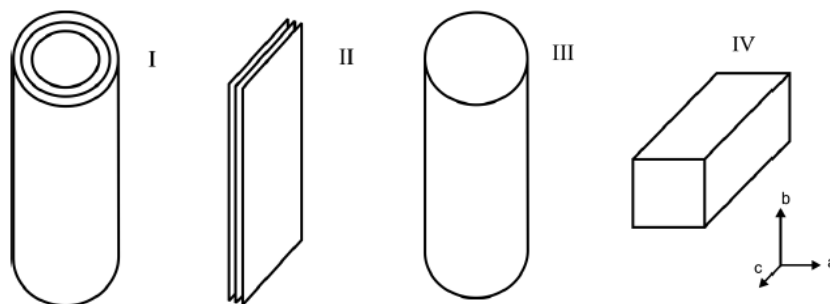


**Figure 1.19. I) Nanotubes, II) Nanosheets, III) Nanorods or nanowires, IV) Nanofibers, nanoribbons or nanobelts. [Bavykin et al., 2006].**

Though, in the literature distinguishing nanowires and nanofibers is still under discussion, and they probably represent a unique morphology.

### 1.3.2.4 Mechanism of formation

Since the first synthesis of titanium oxide nanotubes by Kasuga, several efforts have been done to understand the formation mechanisms of these materials. Scientific debates still go on but two points seem to be widely accepted:

1. Formation of nanosheets during the hydrothermal transformation;
2. Rolling of nanosheets into nanotubes.

Bavykin et al. proposed three mechanisms shown in Figure 1.20:

- a) the helical scrolling of a single-layer nanosheet;
- b) the scrolling of several conjoined nanosheets;
- c) direct production of a multi-walled nanotube.

The first mechanism is the most widely accepted, while the second one the less accepted.

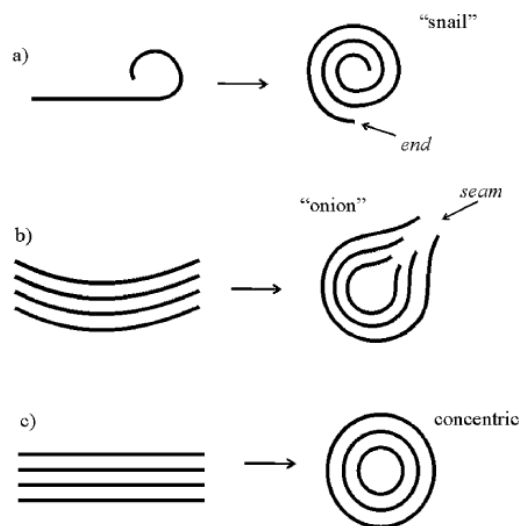


**Figure 1.20. The three possible mechanisms to obtain multi-walls nanotubes [Bavykin et al., 2006]**

Starting from  $\text{Ti}_{0.91}\text{O}_2$  nanosheets, Ma and co-workers demonstrated the direct rolling of nanosheets in nanotubes during the ion intercalation/deintercalation step of the synthesis process [Ma et al., 2004].

Recently, Li et al. [Li et al., 2007] showed that, after 12 h aging in autoclave,  $\text{TiO}_2$  nanoparticles start to exfoliate and a nano-tree structure was clearly observed (Figure 1.21 a)); increasing the hydrothermal time the tree-like structure is developed into layer structure (Figure 1.21 b)); the rolling-up of the layers occurs during the washing treatment, according to Ma's work (Figure 1.22 c)).

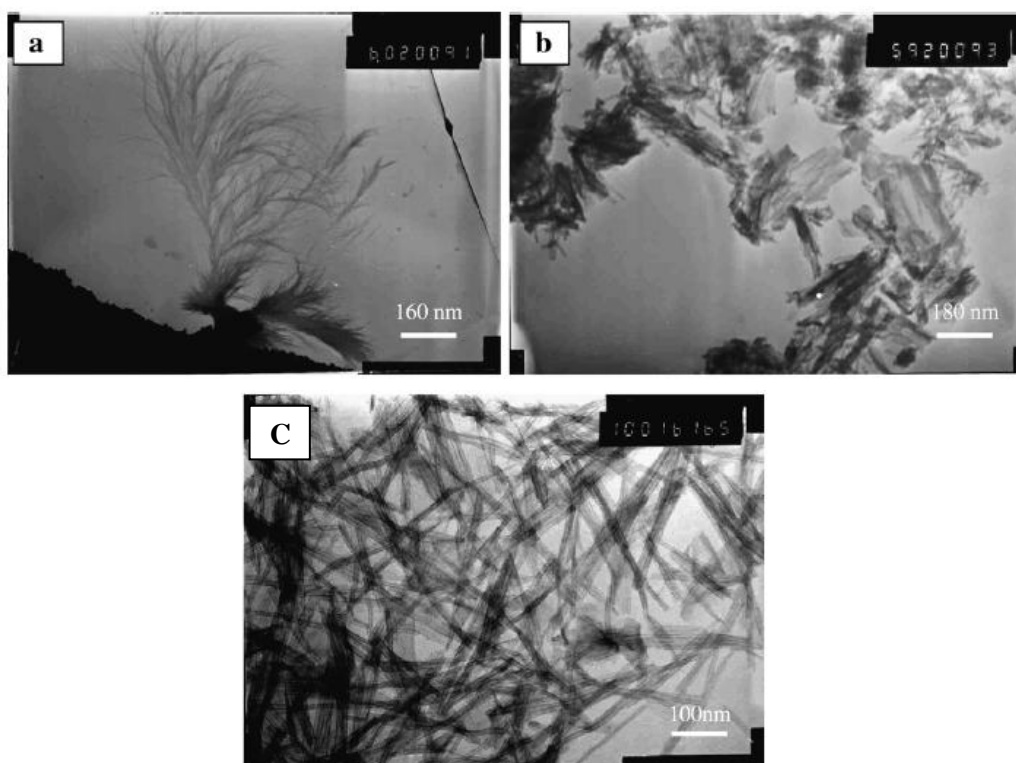


**Figure 1.21.** TEM images of a TiO<sub>2</sub> sample after a alkaline hydrothermal treatment at 130 °C for a) 12 h, b) 24 h, c) 24 h and washing with nitric acid and water

### 1.3.2.5 Structural hypothesis

The first work that reports deep structural investigations of TiO<sub>2</sub> nanotubes appeared in 2001 [Peng et al., 2001]. In this paper, Peng and coworkers used the TEM and HRTEM tools to state that not-calcined nanotubes are not TiO<sub>2</sub> nanotubes but layered H<sub>2</sub>Ti<sub>n</sub>O<sub>2n+1</sub> titanate nanotubes. In 2003 Ma and co-workers [Ma et al., 2003] criticized Peng's theory and proposed a new structural model, based on XRD, electronic diffraction (ED), study on the thermogravimetry (TG) behavior of nanotubes and on the phase obtained with a calcination at 500 °C. Based on XRD patterns, they ascribe the peak at  $2\theta = 9.5^\circ$  not to Na<sub>2</sub>Ti<sub>3</sub>O<sub>7</sub> or H<sub>2</sub>Ti<sub>3</sub>O<sub>7</sub> but to a lepidocrocite<sup>21</sup>-type titanate phase. The formula of this phase is H<sub>x</sub>Ti<sub>2-x/4</sub><sub>x/4</sub>.H<sub>2</sub>O. Based on ED analysis, Ma et al. prove that face-centered rectangular reciprocal cell is the same that the diffraction feature of body-centered H<sub>x</sub>Ti<sub>2-x/4</sub><sub>x/4</sub>.H<sub>2</sub>O, unit cell parameters of which are  $a = 0.3783$  nm and  $c = 0.2978$  nm. H<sub>2</sub>Ti<sub>3</sub>O<sub>7</sub>, instead, has a rectangular unit cell that can not satisfy the face-centered feature, because  $b = 0.375$  and  $c = 0.2978$  nm. Moreover, according to TG studies, nanotubes have a weight loss ~13% after heated to 100 °C. For H<sub>2</sub>Ti<sub>3</sub>O<sub>7</sub>, in the same conditions, weight loss ~7% is expected. Finally, at 500 °C nanotubes

<sup>21</sup> "**lepidocrocite** is a red to reddish brown mineral consisting of iron oxide hydroxide; often found in iron ores together with goethite." Princeton University

phase is anatase. If their structure was  $H_2Ti_3O_7$ , at this temperature their phase would be  $TiO_2$ -B [Feist and Davies, 1992].

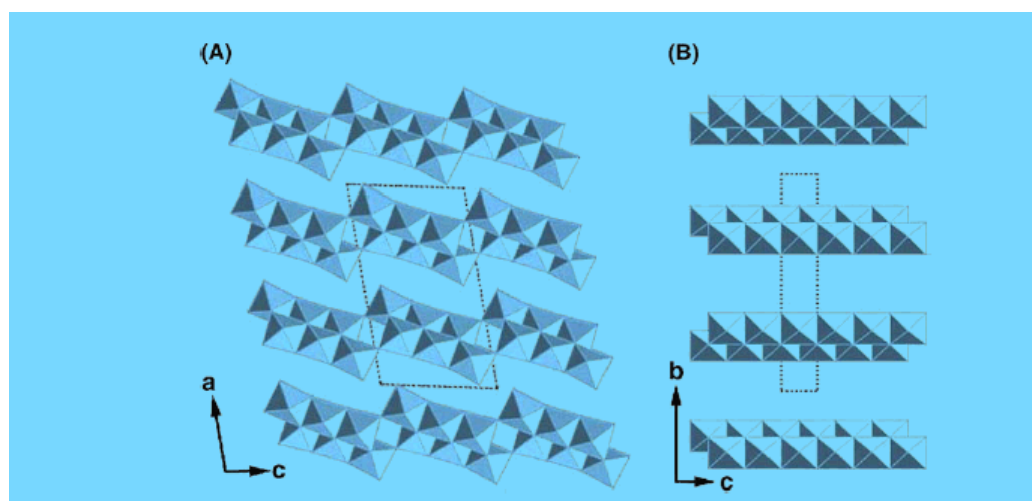


Figure 1.22. (A) titanate model proposed by Peng, and (B) lepidocrocite model proposed by Ma [Ma et al., 2003].

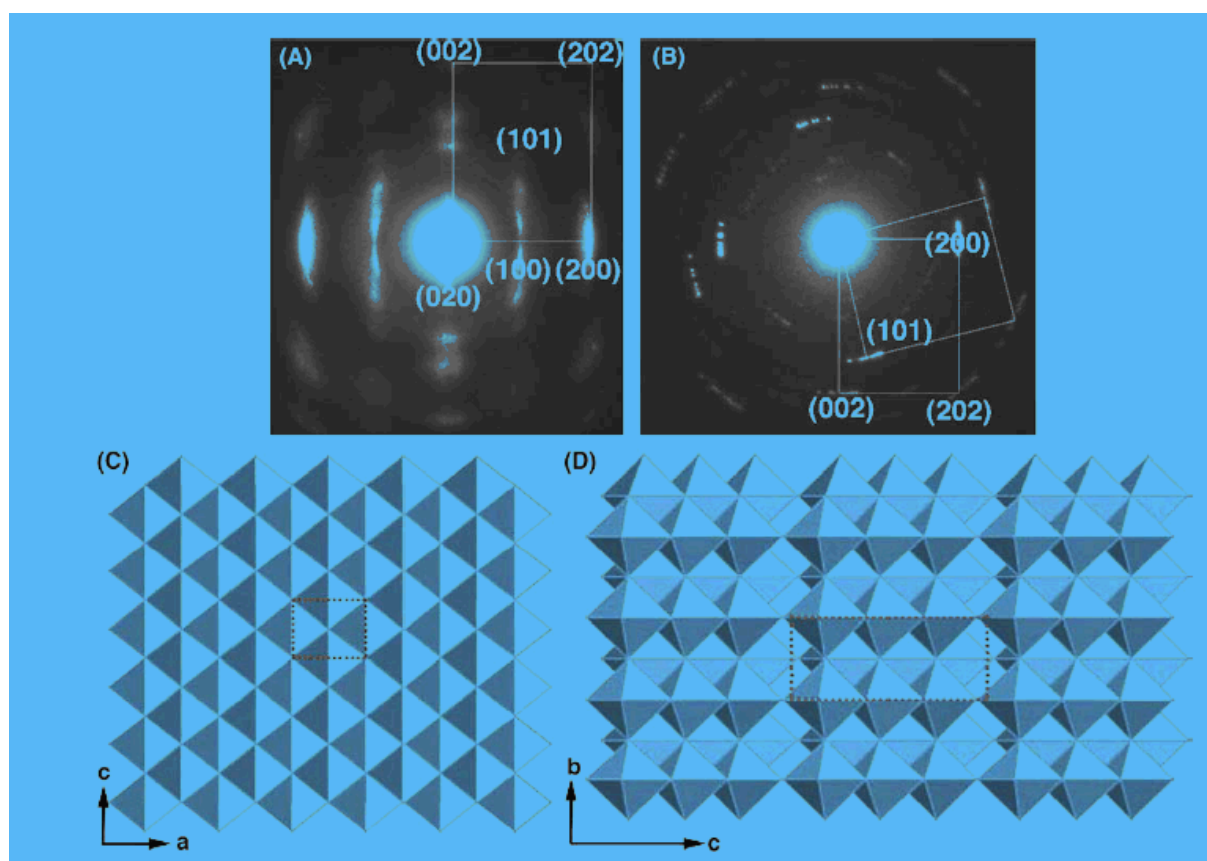


Figure 1.23. (A) Typical ED pattern from nanotubes. The interlayer distance in the walls was measured to be  $\sim 0.8$  nm (Peng measured  $\sim 0.78$  nm). The other spot exhibits a face-centered rectangular reciprocal unit cell ( $a = 0.38$  nm,  $c = 0.30$  nm). (B) Typical sheet-like crystallites. The face-centered reciprocal unit cells appears too. (C, D) The comparison of single sheet structure model of lepidocrocite and titanate models. Only lepidocrocite projects along the normal ( $a = 0.3783$  nm,  $c = 0.2978$  nm) agrees with ED characterizations [Ma et al., 2003].

### 1.3.3 Aerogels and xerogels

#### 1.3.3.1 General presentation

Aerogels are materials coming from sol-gel synthesis of a gel followed by a drying process that permits to maintain the tenuous structure of the gels, particularly their high porous volume. Generally, such materials are obtained via a supercritical drying, the only processing way that permits to avoid capillary stresses. The pioneer researches on elaboration of aerogels have been conducted by Kistler in 1932 [Kistler, 1932]. Xerogels are namely gels that have been dried by an evaporative process, during which the capillary tensions have deeply modified their initial structure and have particularly contributed to reduce their initial level of porous volume [Brinker and Scherer, 1990].

Schematically, literature distinguishes two families of gels: mineral and organic gels [Phalippou and Kocon, 2004].

- **Mineral gels.**

Two different types of precursors are used: ionic and molecular precursors.

**Ionic precursors.** They are constituted of a metal cation and a counter-ion (generally, carbonate, nitrate and halide-like). Ionic precursors are soluble in water (reaction media in which this type of sol-gel synthesis is performed) and react according to chemical mechanisms involving their different acido-basic forms [Phalippou and Kocon, 2004]. Recently, ionic precursors-based sol-gel synthesis has been studied in presence of epoxides, a way which permits to synthesize a wide variety of metal oxides gels ( $\text{SnO}_2$ ,  $\text{ZrO}_2$ , ...) [Gash et al., 2001].

**Molecular precursors.** This group of precursors includes carboxylates  $\text{M}(\text{O}_2\text{CR})_n$ ,  $\beta$ -diketonates  $\text{M}(\text{b-dik})_n$ , [b-dik =  $\text{-(O)CRCHCRC(O)}$ ], alcoxide  $\text{M}(\text{OR})_n$  or oxoalcoxide  $\text{MO}(\text{OR})_n$ . M is a metal element and R an alkyl group. Alcoxides are by far the more widely used precursors. The corresponding sol-gel synthesis is performed in an organic reaction media. Various mineral aerogels can be elaborated this way ( $\text{Al}_2\text{O}_3$  [Pierre et al., 1999],  $\text{ZrO}_2$ ,  $\text{TiO}_2$ , ...) but the most studied ones are silica aerogels ( $\text{SiO}_2$ ). They can be synthesized with sodium silicate [Kistler, 1932] as well as with silicon alcoxides [Pajonk et al., 1995].

- **Organic gels.**

Organic gels are classified according to the reactions involved in their sol-gel synthesis: polycondensation and addition.

**Organic gels issued from polycondensation.** Many gels can be synthesized by polycondensation (polyamide, polyester,...), only few permit to obtain aerogels (polyurethane [Rigacci et al., 2004], melamine-formaldehyde [Alviso and Pekala, 1991], ...). Among these organic aerogels, the most famous are the

ones based on polycondensation of resorcinol in presence of formaldehyde [Pekala, 1989] (Figure 1.24, right).

**Organic gels issued from addition.** In most cases, corresponding precursors present double carbon-carbon bonds like vinylic monomers. Such aerogels can also be obtained with subsequent polymeric precursors like PVC (i.e. polyvinyl chloride) [Yamashita et al., 2003].

Nowadays, many works are dedicated to organic-inorganic hybridization studies to elaborate hybrid aerogels/xerogels through combination of mineral and organic sol-gel routes [Husing et al., 1999].



**Figure 1.24. Examples of mineral aerogels and organic gels. Left : monolithic silica aerogels issued from supercritical drying [Masmoudi, 20062006]; right : resorcinol-formaldehyde based-gels (private collection of Dr. Sandrine Berthon-Fabry, MINES ParisTech, CEP, Sophia Antipolis, France)**

Generally, the global elaboration scheme can be divided into four principal steps which are: sol-gel synthesis, aging of the gel, subsequent drying and final post-drying treatments of the aerogels [Brinker and Scherer, 1990].

- **Sol-gel synthesis:** Sol-gel synthesis can be divided into two complementary steps: sol preparation/evolution and sol-gel transition.

Sol preparation. A sol is defined as a colloidal stable dispersion of solid particles within a liquid. It is composed of the precursors, the solvent and the catalyst necessary to the gelation. It continuously evolves with the advancement of the sol-gel reactions but its viscosity remains nearly constant until the sol-gel transition is reached.

Sol-gel transition. At the gelation point, the solid particles (elementary particles and/or clusters and/or aggregates) composing the sol percolate and form suddenly a tridimensional solid system. The viscosity tends to the infinity. At this stage, the system has become a gel which is a solid porous network in equilibrium with a liquid phase retained in the pores. With mineral gels based on alkoxydes precursors, gelation reactions leading to the gel formation are hydrolysis and condensation.

- **Aging:** After the sol-gel transition, the structure of the gel continues its evolution because of remaining reactive groups and thanks to the flexibility of the solid skeleton. Most of the aging studies have been performed on silica gels and led by Prof. M.A. Einarsrud from Trondheim University [Einarsrud et al., 2001].
- **Drying:** Three processes can be used to remove the liquid from the porosity of the gels: evaporation, extraction in supercritical conditions and freeze drying (corresponding materials are called cryogels) [Pajonk, 1989]. At the end of this step, an amorphous dry material is generated.
- **Post-treatment:** After drying, many treatments can be performed on aerogel materials. For example, their surface chemistry can be modified by different grafting techniques. But above all, the most practiced treatments are thermal ones. Among others, mineral aerogels can be calcinated and organic aerogels can be pyrolyzed. Calcination of mineral aerogels is used to generate crystal phases and/or to increase mechanical properties by densification via sintering, even partial. One of the most famous examples is the calcination of silica aerogels leading to elaboration of glasses at relatively moderate temperatures [Phalippou and Kocon, 2004]. Pyrolysis of organic aerogels is intensively studied to create new forms of nanostructured carbons [Pekala, 1989].

### 1.3.3.2 Sol-gel synthesis [Phalippou and Kocon, 2004]

In this thesis I have elaborated mineral aerogels (i.e. TiO<sub>2</sub> aerogels) and used alcoxides as precursors (M(OR)<sub>4</sub>). Thus, in this section I have decided to focus the discussion on this specific family of metal oxide gels.

These gels are synthesized through reactions of hydrolysis of the metal alcoxide (Figure 1.25) and polycondensation between the subsequent hydrolyzed species (Figure 1.26).

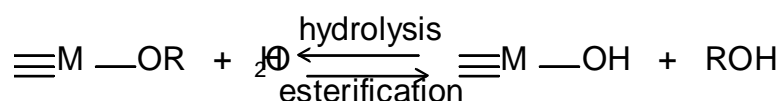
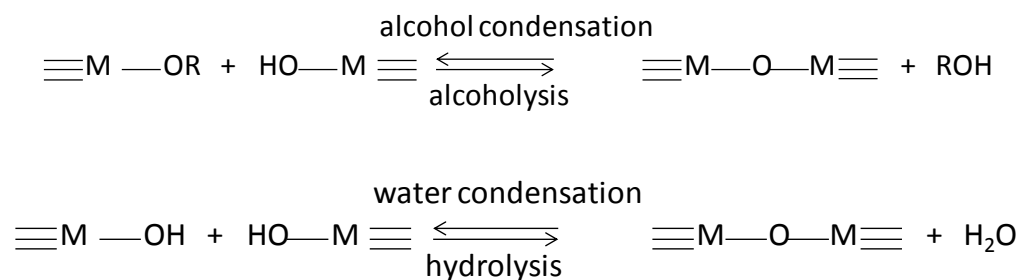


Figure 1.25. Representation of hydrolysis/esterification reactions of a metal alcoxide M(OR)<sub>4</sub> [Brinker and Scherer, 1990]



**Figure 1.26. Representation of polycondensation reactions between metal alkoxides  $\text{M}(\text{OR})_4$  and their hydrolyzed counterparts  $\text{M}(\text{OR})_{4-y}(\text{OH})_y$  [Brinker and Scherer, 1990]**

These simultaneous reactions lead to the oxide gel formation through the global balance expressed as follows (equation 1.30).



The reactions take place in the sol whose basic components are: precursors, reagent (i.e. water), solvent and catalyst.

- **Precursor.** Metal alkoxides determine the chemical composition of the final metal oxides. Within the frame of this work the metal atom M is Ti thus the precursor is Ti(IV)-type (i.e.  $\text{Ti}(\text{OR})_4$ ).
- **Water.** Water is necessary to hydrolyze the metal alkoxide in order to form intermediates for further polycondensation reactions ( $\text{M}(\text{OR})_{4-y}(\text{OH})_y$ ). It is sometimes considered as the reagent.
- **Solvent.** First of all, the solvent permit to generate miscibility zones between metal alkoxide and water. Then, it also permits to control the solid concentration of the sol. As we have already seen, this kind of sol-gel synthesis is conducted in an organic media which is generally the *parent* alcohol (ROH) of the alkoxide used  $\text{M}(\text{OR})_n$ .
- **Catalyst.** Catalyst plays a fundamental role on the gelation kinetics as well as on the reactions mechanisms.

Many parameters have a significant influence on the internal structure of the gel (polarity of the solvent, solid concentration of the sol, nature of the alkyl chains of the precursors, ...). Amongst them, one can for example set off i) hydrolysis ratio and ii) nature of the catalyst: they have both strong influences on aggregation mechanism and can very simply illustrate the sol-gel influence on the structure of the gel, hence the final dry product.

For the one hand, the hydrolysis ratio is defined as the molar ratio of water on precursor  $R_w$  (Equation 1.31).

$$R_w = \frac{|H_2O|}{|M(OR)_n|} \quad (\text{eq.1.31})$$

Schematically it can be said that if,

- $R_w < 1$ , probability for forming an infinite solid network is almost zero,
- $1 < R_w < n$ , polymeric chains are favored,
- $R_w > n$ , formation of cross-linked polymers, gels or precipitated is promoted.

For the other hand, roughly speaking, the acid catalysis is known to promote hydrolysis rather than polycondensation (in other terms, hydrolysis kinetics turns faster than the condensation one). Thus formation of species with low hydrolysis level ( $M(OR)_3OH$ ) and dimers is promoted. Consequently, branched linear gels (so-called polymeric gels) are generally obtained (Figure 1.27). On the contrary, the basic catalysis is known to promote condensation rather than hydrolysis because it favors highly hydrolyzed species (i.e.  $M(OH)_4$ ). Thus the aggregation can be, in this case, governed by a cluster-cluster aggregation process. The final gel is generally considered to be colloidal-like (Figure 1.27).

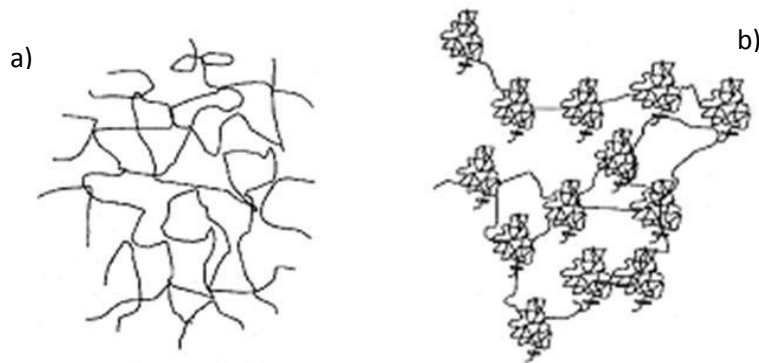


**Figure 1.27 Schematic illustration of global gels structure depending on their catalysis mode : a) acid catalysis, b) basic catalysis. [Wright and Sommerdijk, 2001]**

Since the pioneer works of Kistler in the thirties, the large majority of the efforts on aerogel materials have been dedicated to silica gels, with a huge part focused on hydrolysis and condensation of silica alkoxides. Nevertheless, many others works have deeply studied elaboration of aerogels with metal transition alkoxides (for example,  $TiO_2$  [Teichner et al., 1976],  $V_2O_5$  [Chaput et al., 1995] and  $ZrO_2$  [Mrowiec-Bialon et al., 1998]). From a very general point of view, it can be said that the main difference between these related systems and silicates lies in the fact that they are much more reactive. This matter of fact is directly coming from their lower electronegativity and their ability to present several coordination states. Consequently, two main factors govern the kinetics of hydrolysis and condensations of transition metal alkoxides : the electrophilicity of the metal atom (Ti, Zr, Hf, Th, ...) and their

ability to expand their coordination state (in other words, the extension of their oligomerization degree, generally referred as their molecular complexity). Here-after some of these specificities are stressed through comparison with silicon alkoxides.

- **The electrophilicity of the metal.** Since transition metals are very electropositive, the hydrolysis and condensation kinetics of transition metal alkoxides are significantly much faster than for their silica-based homologues  $\text{Si}(\text{OR})_4$ . At pH 7 the hydrolysis rate for  $\text{Si}(\text{OEt})_4$  is  $5 \cdot 10^{-9} \text{ M}^{-1} \text{ s}^{-1}$ , while for  $\text{Ti}(\text{OR})_4$  it is estimated to be around  $10^{-3} \text{ M}^{-1} \text{ s}^{-1}$ .

- **The extent of oligomerization of the metal alkoxides.** The molecular complexity depends on the nature of the metal atom as well as the nature of the ligand. For some metal alkoxides of the same group, it increases with the atomic size of the metal atom. As an illustration, molecular complexity of  $\text{Ti}(\text{OEt})_4$  is 2.9 instead of 6.0 for  $\text{Th}(\text{OEt})_4$  which can be correlated to covalent radii of the respective metals : 1.32 Å for Ti and 1.55 Å for Th.

Focusing on  $\text{Ti}(\text{OR})_4$  precursors, it can be stressed, as an illustration of the impact of the ligand, that  $\text{Ti}(\text{OEt})_4$  generally leads to oligomeric species (Figure 1.28) on the contrary of  $\text{Ti}(\text{OPr}^i)_4$  which remains monomeric. Obviously, the choice of the precursor can be crucial for the structure of the gel and thus the final aerogel. Still focusing on  $\text{Ti}(\text{OR})_4$  precursors, it can be underlined, as an example, that for a series of titanium n-alkoxides ( $\text{Ti}(\text{OR}^n)_4$ ), the hydrolysis rate decreases with the alkyl chain length which is consistent with the steric effect expected for an associative nucleophilic substitution reaction mechanism. The influence of the alkyl chain length on condensation has been illustrated qualitatively by observations that i) precipitation occurs when R is Et,  $\text{Pr}^n$  or  $\text{Pr}^i$ , and ii) stable sols are formed when R is  $\text{Bu}^n$ .

Evidently, hydrolysis and condensation reactions of transition metal alkoxides are also strongly influenced by catalysis. For example, acid catalysts enhance drastically reaction kinetics. Monolithic gels can be obtained through acid catalysis even if low  $R_w$  values are used. On the other hand, when high acid concentrations are processed, condensation kinetic turns dramatically low. A different situation is observed in basic conditions. Contrary to  $\text{Si}(\text{OR})_4$ , basic conditions slow down the hydrolysis rate of  $\text{Ti}(\text{OBu})_4$ . Condensation, instead, is enhanced under basic conditions.

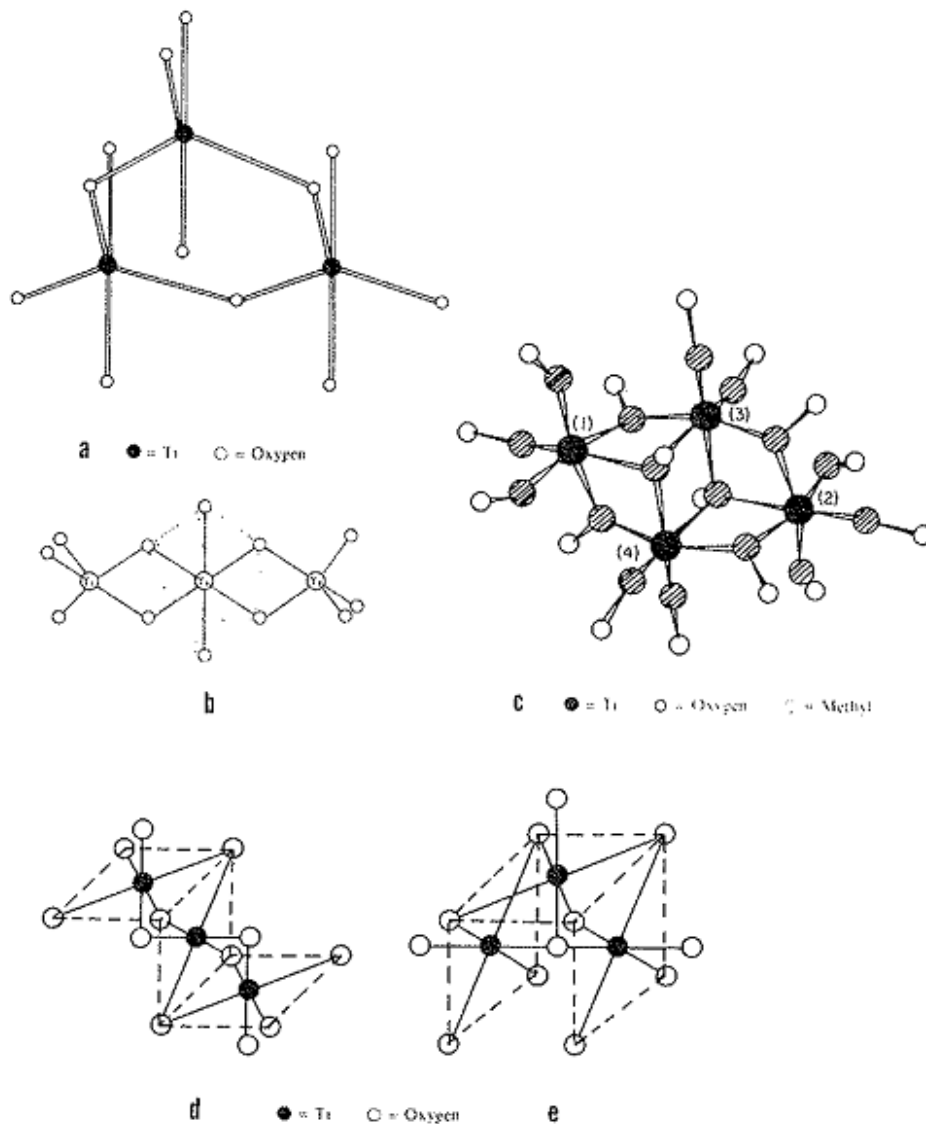
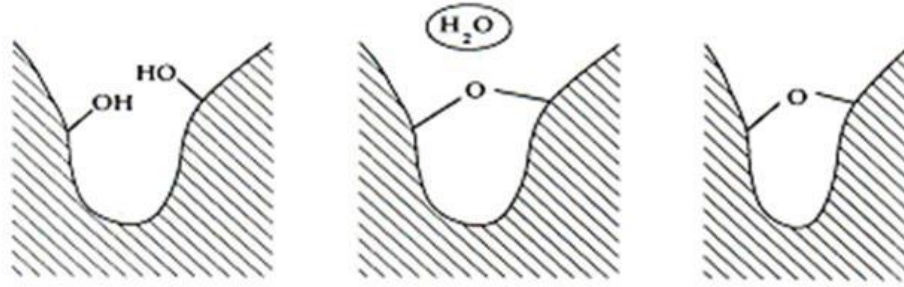


Figure 1.28 Possible structures of  $\text{Ti}(\text{OR})_4$  oligomers. From [Bradley et al., 1978]: (a)  $[\text{Ti}(\text{OEt})_4]_3$ ; (b)  $\text{Ti}_3(\text{OEt})_{12}$ ; (c)  $[\text{Ti}(\text{OMe})_4]_4$ ; (d)  $[\text{Ti}(\text{OEt})_4]_3$ ; (e)  $[\text{Ti}(\text{OEt})_4]_3$

### 1.3.3.3 Aging

After the sol-gel transition, the structure of the gel continues its evolution. If the chains are flexible enough, the remaining reactive groups at the surface of the pores ( $\equiv\text{M}-\text{OH}$  and  $\equiv\text{M}-\text{OR}$ ) can react together (*i.e.* through polycondensation of water and/or alcohol). This reaction induces shrinkage of the gel accompanied by expulsion of liquid from the pores (equivalent to the global volume reduction of the gel). This phenomenon is called syneresis.



**Figure 1.29. Schematic illustration of irreversible shrinkage resulting from condensation between neighboring groups on the gel surface as the strain in the new bond relaxes [Brinker and Scherer, 1990]**

During the aging step, Ostwald ripening can occur too. It is fairly described by Kelvin equation (equation 1.33). Two mechanisms can be involved in this second phenomenon as schematically represented at Figure 1.30: i) dissolution of solid from the convex surfaces of the particles ( $r^{22} > 0$ ) and its precipitation at the interparticles junctions ( $r < 0$ ) and ii) dissolution of the solid phase from the smallest particles which precipitates in the larger particles [LionelVayssieres, 2008].

$$S_l = S_{l0} \exp\left(\frac{2\gamma_{sl}V_m}{r_p RT}\right) \quad (\text{eq. 1.32})$$

with,  $S_l$ , the solubility of the spherical particle ( $\text{mol.l}^{-1}$ ),  $S_{l0}$ : the solubility of the planar surface ( $\text{mol.l}^{-1}$ ),  $\gamma_{sl}$ : the solid-liquid surface tension ( $\text{N.m}^{-1}$ ),  $V_m$ : the molar volume of the solid ( $\text{cm}^3.\text{mol}^{-1}$ ) and  $r_p$  the particle radius (m).

<sup>22</sup>  $r$  is the curvature radius of the particles constituting the solid network of the gel.

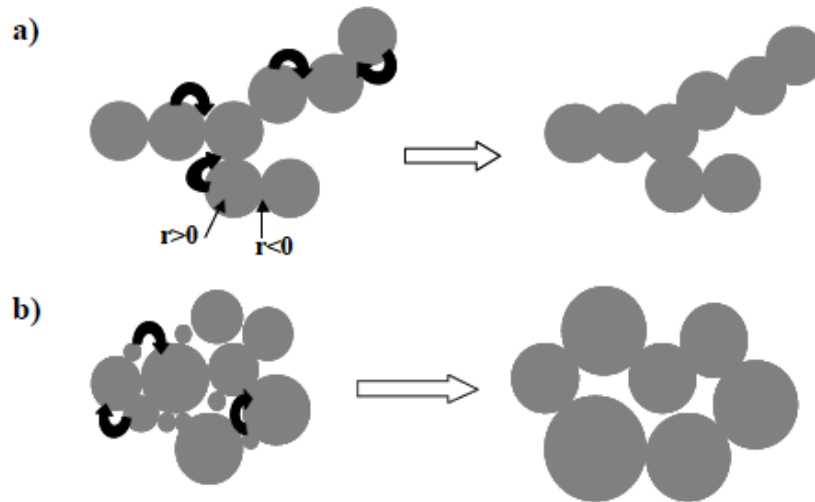


**Figure 1.30. Schematic illustration of Ostwald ripening mechanism occurring during aging of a mineral gel : a) dissolution of solid from convex particles and precipitation in the concave interparticle region, b) dissolution of solid from the smallest particles and precipitation in the larger ones [Masmoudi, 2006].**

Aging is generally performed to strengthen the gels before drying as well as for further utilizations of the dry material. After aging, the solid network : i) is more reticulated (thanks to syneresis) and ii) present larger (*i.e.* stronger) particles necks. Mechanical properties like shear modulus are significantly increased. Aging phenomena depend on several reaction parameters like pH, temperature, water and alcohol concentrations, ... Syneresis is controlled by hydrolysis and condensation reactions, so it depends directly on parameters regulating the sol-gel synthesis. For its part, Ostwald ripening is governed by dissolution of the solid thus it depends directly from the solubility of the solid phase and thus, it depends strongly on pH.

#### 1.3.3.4 Drying

After aging, the gel must be dried. As already written before, three different ways can be followed to perform the drying step depending on i) the triple point is bypassed, ii) the gas-liquid equilibrium is crossed and iii) the critical point is bypassed (Figure 1.31). The related processes are called respectively i) freeze-drying, ii) evaporative drying and iii) supercritical drying.

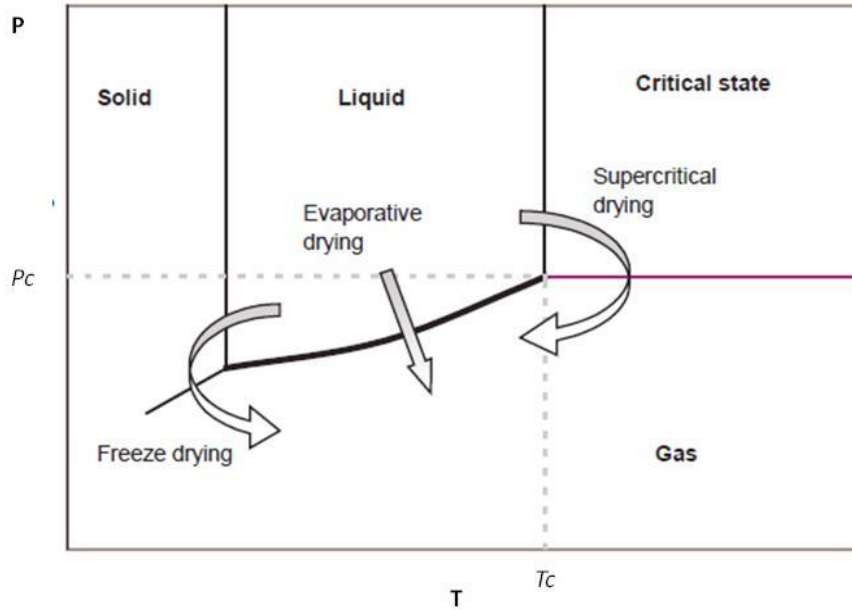


Figure 1.31. Phase diagram illustrating the different possible drying routes [Bisson et al., 2003]

- **Freeze-drying:** Freeze-drying is very marginally used except for the cellulosic-based gels [Hoepfner et al., 2008]. It generally leads to powdered samples when employed with mineral gels ( $\text{SiO}_2$ ,  $\text{TiO}_2$ , ...). Evaporative and supercritical dryings are generally preferred by far.

- **Evaporative drying:** Evaporative drying is the easiest route to be followed from a process point of view. Indeed, it can be performed in room conditions and thus does not require extreme conditions (respectively low and high P-T couples for freeze-drying and supercritical drying). Nevertheless, from a material point of view, it is a really delicate process if the internal structure of the gel generated during the sol-gel step is to be preserved as much as possible. Indeed, significant densification is very often associated to this type of drying. The densification of the solid network is the result of the capillary tensions occurring in the (small) pores of the gel. These tensions are located at the menisci appearing at the energetic interface between the liquid and the gaseous phases.

Evaporative drying is composed, of three stages [Hench and West, 1990]. They are respectively named: i) the constant rate period, ii) the first falling rate period and iii) the second falling rate period [Scherer, 1990]. Before the beginning of the first period, gas-liquid menisci are flat. Then liquid begins to evaporate at the surface of the gel and it experiments tensile stresses governed by the Laplace law (equation 1.33).

$$\Delta P = \gamma_{LV} \left[ \frac{1}{R_1} + \frac{1}{R_2} \right] \quad (\text{eq. 1.33})$$

where  $\gamma_{LV}$  is the gas-liquid surface tension,  $R_1$  and  $R_2$ , the characteristic radii of the curvature (e.g. the major and minor radii of an elliptic meniscus).

If we do the hypothesis that pore is a cylinder, the meniscus is hemispherical, thus  $R_1$  and  $R_2$  are equal. The equation becomes:

$$\Delta P = \gamma_{LV} \frac{2}{R_c} \quad (\text{eq. 1.34})$$

where  $R_c$  is the radius of the cylindrical meniscus.

The meniscus radius is depending on the contact angle  $\theta$ , representative of the degree of wetting of the pore surface (equation 1.35).

$$R_c = -\frac{r_p}{\cos \theta} \quad (\text{eq. 1.35})$$

where  $r_p$  is the mean radius of the pores.

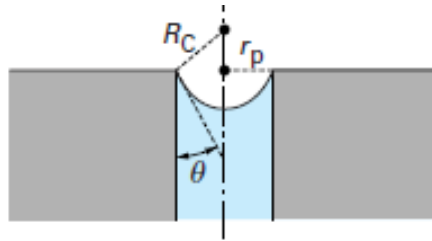


**Figure 1.32. Radius of curvature of liquid-vapor interface [Phalippou and Kocon, 2004]**

As the first period advances, the gel retracts (in proportions directly related to the evaporated volume of solvent) and the solid is under compression to balance the tensions in the liquid. This contraction is accompanied by a decrease of the curvature radius  $R_c$ . This densification induces a mechanical strengthening of the solid network. After a while, the solid becomes so resistant that its contraction is not possible anymore. At this stage, the curvature radius  $R_c$  is minimal equal to the mean pore  $r_p$  and the tension stress is maximal. At this moment (designed as the critical point), the constant rate period is over and the first falling rate period starts. No more shrinkage occurs and the menisci are entering the porous network. The liquid is leaving the gel via i) a funicular transport process and ii) diffusion of vapor directly from the bulk. Finally, the second falling rate period is beginning when funicular process is no longer feasible and only evaporation from the heart of the gel is possible. These drying phenomena explain why during the evaporative drying process, gels shrink significantly.

In addition, it must be underlined that this type of drying can also induce some fissures. Cracks are likely to occur around the critical point when mechanical stress is exceeding the strength of the solid network. Schematically, before the critical point, the evaporation kinetics is responsible for the cracking. Indeed, during this period, a flow of liquid equal to the evaporated solvent must move from the heart of the gel to the surface through the tortuous porous structure. Since these gels have a very low permeability (in some cases as low as some  $\text{nm}^2$ ), a gradient of pressure generally occurs between surface and bulk and the gels experiment there intense mechanical stresses (generally illustrated with Darcy law) leading to

some irreversible fissures. At the critical point, a second fracture mechanism can also occur. It is mainly related to the sudden relaxation of the mechanical stresses when the evaporation front migrates from the surface towards the interior of the gel.

In conclusion, during evaporative drying, the global structure of the gels is dramatically damaged. Density increases, the specific porous volume and surface area decrease, monolithicity is lost, ... Since having a high surface area is one of the important features for a photocatalyst, lowering down the mechanical stresses is a crucial point. In order to reduce the capillary forces, many solutions have been studied for years for example, i) lowering down the interfacial tension  $\gamma_{LV}$ , ii) increasing the contact angle  $\theta$  (*i.e.* using non-wetting solvents or modifying the surface chemistry of the pore walls) and iii), for silica gels, generating a so-called *spring-back* effect through syllilation of the pores together with a rapid evaporation. Actually, for the majority of the gels, the most efficient process is the first one. If the solvent trapped in the pores is led to its supercritical conditions, the liquid and the gas phases do not exist anymore and only one phase is present, the critical state. In these monophasic conditions the interfacial tensions disappear.

- **Supercritical drying:** The supercritical drying of such gels was first introduced by Kistler [Kistler, 1932]. In the original supercritical drying processes, the gels were dried in the supercritical conditions of the solvent contained in the pores (Figure 1.33). To reach these supercritical conditions, the heating must be low to avoid strains on the solid network susceptible to lead to cracks. These strains are mainly due to the differential thermal dilatation between the solid network and the liquid phase of the pores together with the weak permeability of the gel. After a step of thermal stabilization, the pressure is lowered down to drain off the interstitial fluid. This step must be performed isothermally (to avoid condensation of the fluid in the porosity) and slowly (still because of the very low permeability of the gel). When the atmospheric pressure is reached, the temperature is lowered down to room conditions.

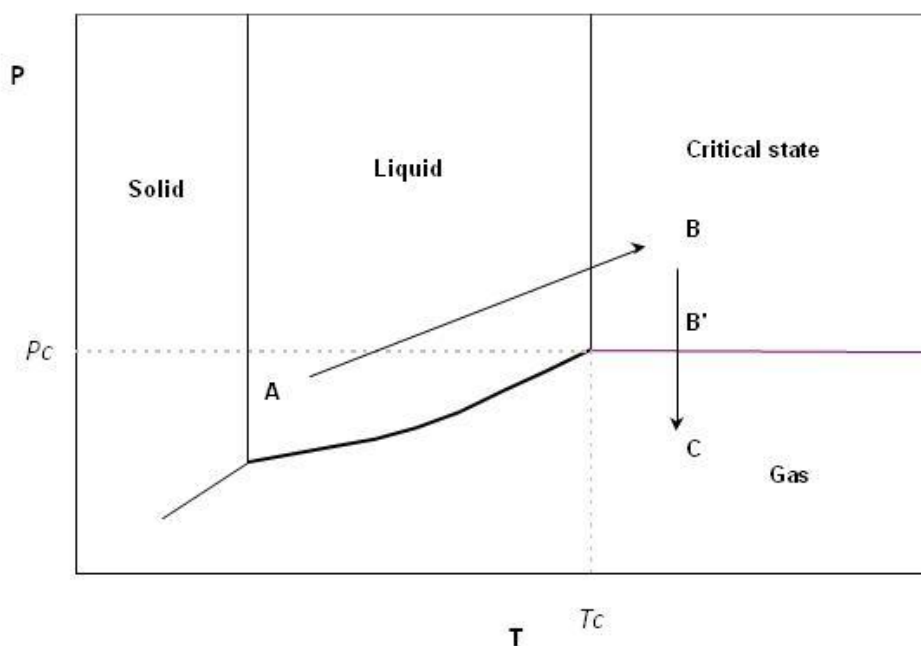


**Figure 1.33. Schematic view of the supercritical drying operating conditions [Bisson et al., 2003]**

Table 1.2 sums up the supercritical conditions of some usual organic solvents generally used for supercritical drying of gels.

<b>Solvent</b>	<b>T<sub>c</sub> (°C)</b>	<b>P<sub>c</sub> (bar)</b>
Isopropanol	264	52
Ethanol	241	61
Acetone	235	46

**Table 1.2 Supercritical conditions of some usual solvents**

In these elevated temperature conditions, some reactions may occur. Particularly the reesterification of the surface of the gels in presence of supercritical alcohol. It could consequently induce some subsequent condensation between neighbor groups. Besides, this drying process could be dangerous especially when inflammable solvents as alcohols are used in their supercritical stage. Consequently, researchers have developed a new supercritical drying mode at moderate temperature (very close to the room conditions). A fluid with lower critical temperature is used to substitute the initial organic solvent before the supercritical extraction. Several fluids have low supercritical conditions, as table 1.3 reports, and are potentially interesting for such a process. Among these fluids, carbon dioxide (CO<sub>2</sub>) has been selected because of several advantages: among others, it is not flammable, not toxic, and not expensive. Moreover it has a high chemical inertness and it is miscible with several common organic solvents like the ones employed for the sol-gel synthesis (acetone, ethanol, isopropanol. ...).

<b>Fluid</b>	<b>T<sub>c</sub> (°C)</b>	<b>P<sub>c</sub> (bar)</b>
Carbon dioxide (CO <sub>2</sub> )	31.1	73.8
Nitrogen protoxide (N <sub>2</sub> O)	36.5	72.4
Freon 13 (CClF <sub>3</sub> )	28.9	38.6
Freon 23 (CHF <sub>3</sub> )	25.9	48.2

**Table 1.3. Supercritical conditions of some specific fluids**

The initial experimental procedure consists of four main steps [Tewari et al., 1985].

- First, the gels are placed in the autoclave and recovered with the synthesis (or washing) solvent.
- Then, the autoclave is flushed with liquid CO<sub>2</sub>. The liquid CO<sub>2</sub> substitutes the solvent in the pores, mainly thanks to diffusion phenomena.
- When the huge majority of the initial organic solvent is recovered, pressure and temperature of the system are brought above the supercritical CO<sub>2</sub> conditions.
- Finally, the autoclave is slowly and isothermally depressurized.

This procedure has been refined by van Bommel and de Haan [Van Bommel1994] by using directly CO<sub>2</sub> in supercritical conditions instead of liquid CO<sub>2</sub> to flush the autoclave. Even if supercritical phases are less dense than their liquid homologues (and thus are not able to solubilize species as efficiently), their diffusion coefficient are higher, partly because of lower viscosity, which is very efficient regarding the very small pores size where the solvent to be extracted is trapped. Generally, the different supercritical drying processes permit to maintain the integrity of the initial gels: monoliticity and high specific porous volume. This is particularly true for silica gels.

### 1.3.3.5 Post-treatments

Once dried, aerogels/xerogels can undergo many different post-treatments. In the specific case of TiO<sub>2</sub> aerogels for photocatalytic applications, aerogels/xerogels are calcined. Schematically, this heat treatment presents two main aims:

- to remove surface chemical species (chemically combined water of hydration and carbon dioxide, decomposition of carbonates issued from synthesis procedure, ...),
- to crystallize the initial amorphous product.

Removal and degradation of so-to-say pollutants is crucial because they can act as recombination centers during the photocatalytic activity of TiO<sub>2</sub>. Crystallization is also fundamental because a crystallized photocatalyst is obviously much more active than an amorphous one. It must be noted too that calcination also involves the sintering phenomenon. Crystallization and sintering by diffusion are generally considered to be in competition which makes very difficult the analysis of their specific impacts.

From a crystallographic point of view, TiO<sub>2</sub> aerogels pass from amorphous to anatase, without appearance of TiO<sub>2</sub>-B phase as observed for nanotubular morphologies. The temperature of this transition is around 400 °C. Anatase is stable until the rutile appears, at about 600 °C. The complete transformation of anatase in rutile is obtained at 700 °C [Dagan and Tomkiewicz, 1993], [Tursiloadi et al., 2006].

Because of their very high specific area, sintering of aerogels occurs at exceptionally low temperatures. Sintering is a densification process driven by interfacial energy when some thermal energy is brought to the system. The direct consequences of this densification are the loss of porosity (and associated surface area) and the particle growth. Sintering mechanisms of amorphous and crystallized materials are different: amorphous materials sinter by viscous flow whereas crystalline materials sinter by diffusion. Viscous sintering is governed by the energy gained by reduction in surface area. This energy is the product of the specific surface energy and the difference in surface area. Theory of viscous sintering has been developed by Frenkel. The models he developed have permitted to state that sintering rate is faster for bodies with small particles or pores. In the case of TiO<sub>2</sub> aerogels, primary solid particles have a diameter of about 10 nm so their densification by sintering is very fast.

As we have already said,  $\text{TiO}_2$  aerogel is amorphous until anatase phase appears, generally around  $400\text{ }^\circ\text{C}$ . From this point, sintering is here governed by diffusion and the driving force is then the surface energy (case of sintering of a crystalline material). During sintering matter move from region of convex curvature to region of concave curvature, so necks between particles constituting the solid skeleton of the aerogel are filled which contributes to strengthen the solid skeleton.

### 1.3.3.6 Applications

Aerogels are potentially interesting for various applications [Pierre and Pajonk, 2002]. They are known to be very interesting for catalysis, acoustic insulation, optical applications (Cherenkov counters, luminescence, ...), energy applications (fuel cell/batteries/capacitors electrodes, dielectric materials, ...), encapsulation, life science [Buisson et al., 2001], ... Today, the most promising massive application field remains the thermal insulation domain. Because of their extremely low thermal conductivity, silica aerogels and xerogels are now developed at industrial level to be incorporated in superinsulating components and devices, for transparent as well as translucent [Ackerman et al., 2001] and opaque [Venkateswara et al., 2005] applications.

### 1.3.3.7 Short overview of the recent literature on $\text{TiO}_2$ -based aerogels

At present, to conclude this general section on aerogels materials, some specific information on  $\text{TiO}_2$  aerogels are briefly presented here-after.

Synthesis of  $\text{TiO}_2$  gels for aerogels preparation is generally performed with alkoxydes precursors like titanium isopropoxyde ( $\text{Ti}(\text{O}-i\text{C}_3\text{H}_7)_4$ ) ([Kolen'ko et al., 2005], [Zacharaki et al., 2008]) and titanium n-butoxyde  $\text{Ti}(\text{O}-n\text{C}_4\text{H}_9)_4$  ([Yoda et al., 2001], [Tursiloadi et al., 2006]) (Figure 1.34). Sol-gel synthesis are classically conducted in alcohols (essentially ethanol and propanol or isopropanol and sometimes methanol) but some works in other reaction media can be found: for example, ethyl acetoacetate-based solutions [Hirashima et al., 1998] and cyclohexane [Matejova et al., 2010]. Reactions are classically acid-catalyzed using mainly nitric acid  $\text{HNO}_3$  [Baia et al., 2006] as well as hydrochloric acid  $\text{HCl}$  [Boujday et al., 2004] and even acetic acid  $\text{CH}_3\text{COOH}$  [Shimoyama et al., 2010].



Figure 1.34. Schematic view of titanium isopropoxyde  $\text{Ti}(\text{O}-i\text{C}_3\text{H}_7)_4$  (left) and titanium n-butoxyde  $\text{Ti}(\text{O}-n\text{C}_4\text{H}_9)_4$  (right)

In most of the works performed within the TiO<sub>2</sub> aerogels area, gels are dried with supercritical CO<sub>2</sub>. Even in such very smooth drying conditions compared to evaporation, such gels experiment many cracks during this step and can turn powdered at the end. This feature has been explained in literature by the high ionic degree of the polar covalent bonds between Ti and O atoms [Pierre and Pajonk, 2002].

If one wants to use the dry product as a monolithic material, coupling with silica aerogels is generally used. Indeed, silica gels appear as a clever tool to give cohesion to the TiO<sub>2</sub> aerogels fragments or powders. Silica aerogels is there often named *nanoglue* ([Morris et al., 1999], [Luo et al., 2009]). This rather simple sol-gel based shaping process can be of high interest when TiO<sub>2</sub> is to be used in photocatalytic films, for example deposited on some glass substrates.

TiO<sub>2</sub> materials obtained after supercritical drying are nanostructured (Figure 1.35), present very high specific surface areas (larger than 500 m<sup>2</sup>/g in some cases [Baia et al., 2006]) which dramatically decrease after calcinations. Even if some rather large values can be found in literature (a value of 228 m<sup>2</sup>/g after calcination at 773 K has been reported in the works of Yoda et al. ([Yoda et al., 2001]), rare are the studies that show such high levels after calcination. Indeed, BET specific surface of calcinated materials are commonly around some tens of m<sup>2</sup>/g (for example, between 80 and 100 m<sup>2</sup>/g after calcinations at 500 °C [Boujday et al., 2004]).

Few attempts of evaporative drying have been tested but corresponding xerogels appear much more dense and less nanostructured (Figure 1.36). Compared to their aerogels counterparts, they present specific areas significantly lower: from 46 m<sup>2</sup>/g (*versus* 82 m<sup>2</sup>/g) to 3 m<sup>2</sup>/g (*versus* 81 m<sup>2</sup>/g) depending on the sol-gel parameters<sup>23</sup> [Boujday et al., 2004].

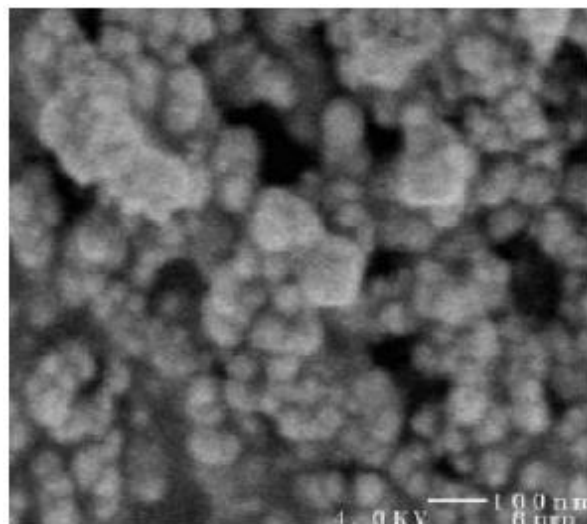


**Figure 1.35. Representative SEM image of a TiO<sub>2</sub> aerogel [Baia et al., 2006]**

---

<sup>23</sup> In this example, calcinations were performed at 550°C and two catalysts were studied and compared (HNO<sub>3</sub> and HCl).

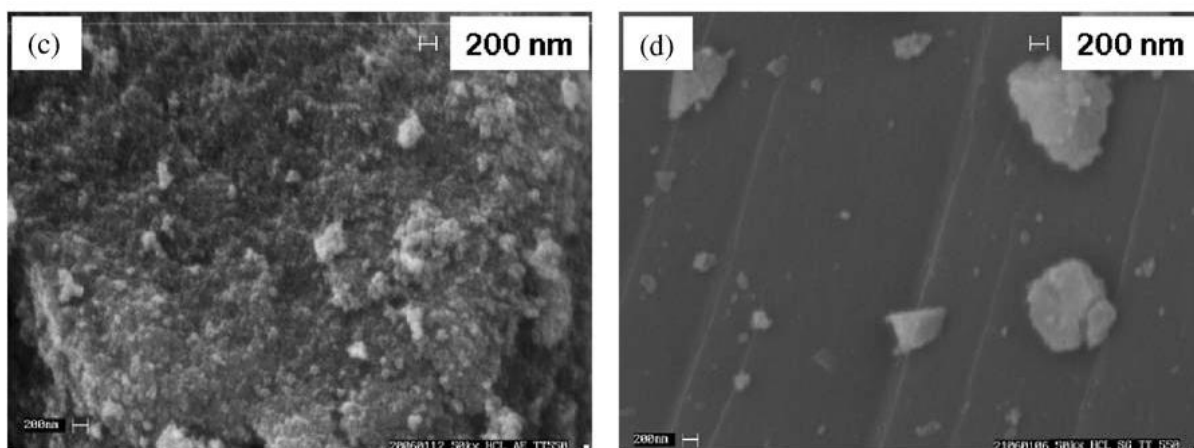


Figure 1.36. SEM pictures of a TiO<sub>2</sub>-aerogel (left) and its xerogel counterpart (right) after calcinations at 550 °C.

TiO<sub>2</sub> aerogels coming from *soft* supercritical CO<sub>2</sub> drying (*i.e.* dried in rather low pressure and temperature conditions) are amorphous and need to be calcinated to present satisfactory photocatalytic efficiency but some recent works have shown that in more drastic conditions, crystallization can occur directly in the autoclave. Indeed, Tursiloadi *et al.* have detected significant presence of anatase after supercritical CO<sub>2</sub> drying at 60 °C and 22 MPa [Tursiloadi et al., 2006]. Other authors have shown some even more spectacular crystallization effects, drying their TiO<sub>2</sub> gels in supercritical alcohol instead of CO<sub>2</sub>. Indeed, Kolen'ko and co-workers have obtained pure anatase operating supercritical drying with isopropanol at 235 °C and 4.7 MPa (Figure 1.37) [Kolen'ko et al., 2005].

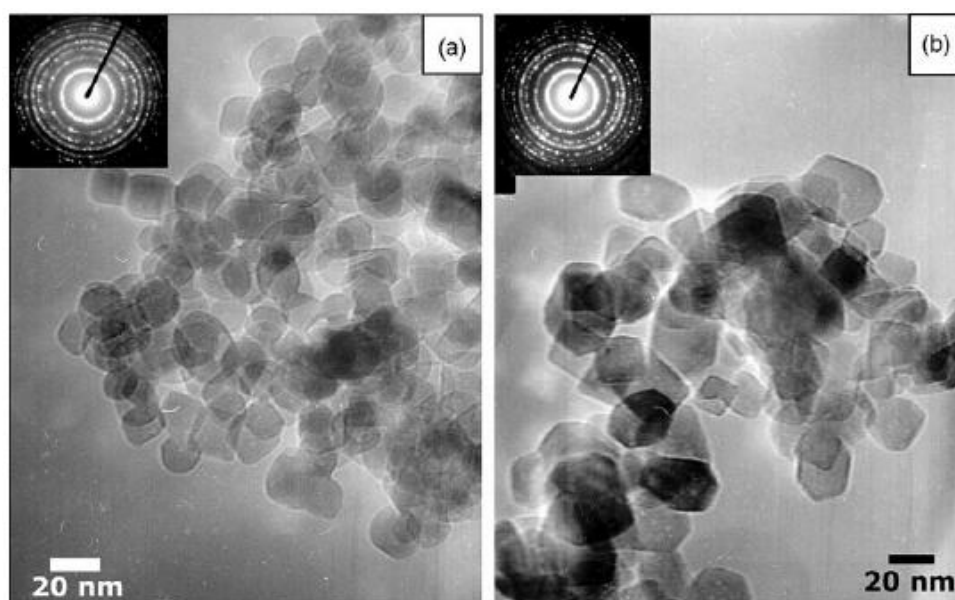
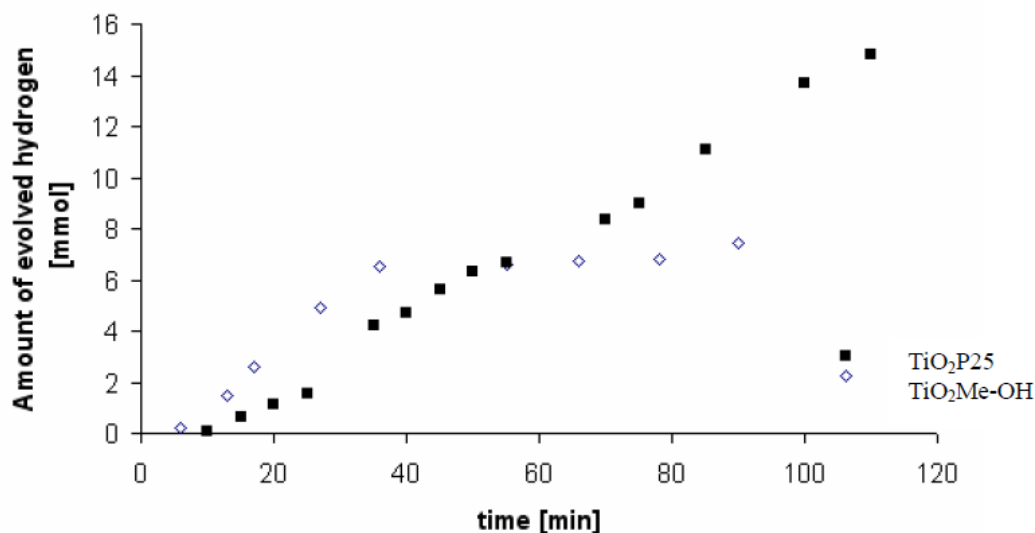


Figure 1.37. TEM micrographs of TiO<sub>2</sub> anatase particles synthesized by sol-gel method followed by supercritical drying in isopropanol before calcinations (left) and after calcinations (right) at 550 °C [Kolen'ko et al., 2005]

Like SiO<sub>2</sub> aerogels, TiO<sub>2</sub> aerogels have attracted much attention from the scientific community for their great potential in several applications fields. One of the first works on elaboration and test of titania aerogels was the study of Dagan et al. [Dagan1993] on the photocatalytic degradation of salicylic acid. In more recent years, titania aerogels are mainly studied, as an illustration, for degradation of pollutants like decomposition of phenol ([Znaidi et al., 2001] and [Boujday et al., 2004]) and p-chlorophenol [Malinowska et al., 2003], for CO oxidation [Pietron et al., 2002], for methanol treatment [Kim et al., 2007] but also within the medical sphere for example for antimicrobial applications [Yeung et al., 2008].

Recently, the energy domain has been investigated more intensively. Researches performed by the group of Debra Rolison from US Naval Research Laboratory (Washington DC) are very representative of what is actually arising within this new applicative area. D. Rolison and co-workers studied deeply the electrochemical properties of titania aerogels for their use as potential semiconductor for photovoltaic and solar cells. Their works have given important contributions [Rolison et al., 1997], [Pietron and Rolison, 2001], [Pietron et al., 2007]. Amongst other they have deeply studied the surface chemistry on charge separation. Such studies opened up the possibility of improving the electronic properties of TiO<sub>2</sub> by simply modifying the surface chemistry (for example, through functionalization reactions) while keeping a high level of specific surface area. Indeed Pietron and Rolison have evidenced that replacing surface hydroxyls (*i.e.* titanols which act as charge traps) by electrogenerated isopropoxyl moieties permits to significantly enhance the photoresponse of TiO<sub>2</sub> aerogels [Pietron and Rolison, 2004].

Within this area, even if many works deal with sol-gel based TiO<sub>2</sub> materials for H<sub>2</sub> photogeneration by watersplitting ([Sreethawong et al., 2005], [Sreethawong and Yoshikawa 2006], [Sreethawong et al., 2007]), very few of them are directly focused on TiO<sub>2</sub> aerogels for this application. Amongst these rare examples, A. Piotrowska and J. Walendziewski have shown that TiO<sub>2</sub> aerogels could have rather close efficiency than P25 in their specific experimental conditions (Figure 1.38) [Piotrowska and Walendziewski, 2005].



**Figure 1.38** H<sub>2</sub> evolution of Pt-TiO<sub>2</sub> aerogel suspension in CH<sub>3</sub>OH/H<sub>2</sub>O solution (10 ml and 400 ml, respectively) under UV irradiation. Platinum load is 0.3 %wt, catalyst concentration is 0.73 g/l and operating temperature is 40 °C) [Piotrowska and Walendziewski, 2005]

To end-up with this very short bibliographic overview, it can be underlined here that : *i*) TiO<sub>2</sub> aerogels are also evaluated for photoelectrochemical cell (PEC) for solar-hydrogen production, as-prepared [Silipas et al., 2009] or as ZnO-TiO<sub>2</sub> co-aerogels [Indrea et al., 2009] and *ii*) their doping is studied with increasing attention, particularly concerning nitrogen doping ([Cheng et al., 2004], [Horikawa et al., 2008] and [Popa et al., 2010]). The latter will be discussed in details in the next section dedicated to doping.

## 1.4. Doping

### 1.4.1 Generalities

As already underlined, improvement of visible light absorption and charge separation are two of the crucial points for photo-catalytic efficiency increase. Charge recombination can be limited adding electron donors or noble metal loading. Insertion of elements in the photocatalyst is one of the most used techniques for improving the visible light absorption. The foreseen impact of doping is to reduce the bandgap either by lowering the bottom of the conduction band or by increasing the top of the valence band. This may be realized provided that the energy levels introduced in the bandgap by the doping elements are close enough to the corresponding energy band to allow some overlap. However, it must be underlined that, as a consequence, in the case of TiO<sub>2</sub>, creating mid-gap energy levels or broadening conduction band has negative impacts on photo-activity because in any case energy level is under 0 eV and must be avoided and moreover mid-gap energy levels can act as charge carriers traps

In his paper Nagaveni [Nagaveni et al., 2004] studied the impact of several doping metals (W, V, Ce, Zr, Fe and Cu) for degradation of 4-nitrophenol. Corresponding doped TiO<sub>2</sub> materials

are less active than the pristine undoped materials. XPS and photoluminescence measurements allow to position the energy defects, induced by this kind of doping, near the conduction band for most of them (Figure 1.39), and permit to explain the degradation of the TiO<sub>2</sub> activity.

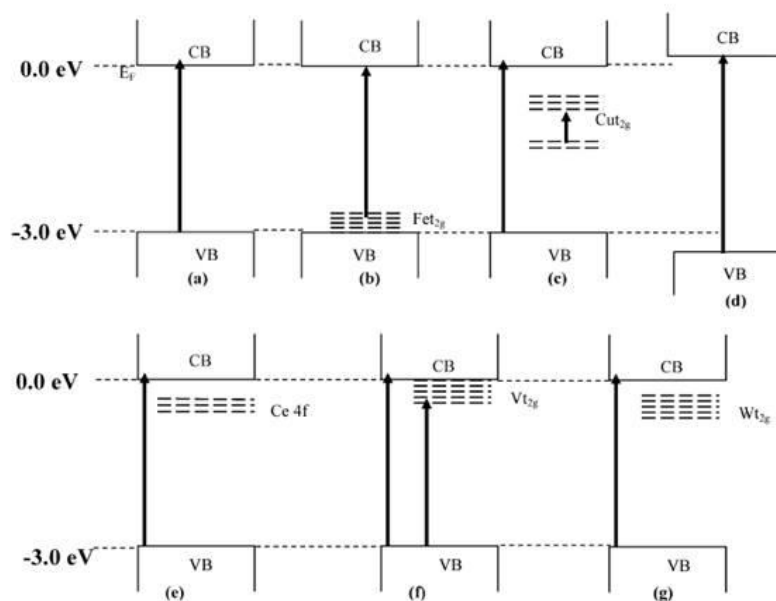


**Figure 1.39. Energy levels induced by cation doping: a)pristine TiO<sub>2</sub> b) Fe-doped TiO<sub>2</sub> c) Cu-doped TiO<sub>2</sub> d) Zr-doped TiO<sub>2</sub>, e) Ce-doped TiO<sub>2</sub>, f) V-doped TiO<sub>2</sub> and g) W-doped TiO<sub>2</sub> [Nagaveni et al., 2004]**

In the scientific research of TiO<sub>2</sub> (summed up in the Table 1.4), two keystones for the improvement of the visible light harvesting are the works of Choi in 1994 [Choi et al., 1994] and of Asahi in 2001 [Asahi et al., 2001]. For the first time Choi et al. carried out a systematic study on the effect of a cationic doping on TiO<sub>2</sub> materials. Asahi's article [Asahi et al., 2001], instead, is considered as the first reporting on nitrogen-doped TiO<sub>2</sub>, although Sato in 1986 [Sato, 1986] already reported the elaboration of N-doped TiO<sub>2</sub>. These two studies are breakthrough for the development of TiO<sub>2</sub> science through doping strategies.

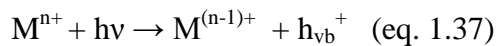
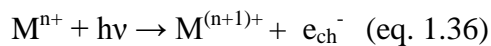
Year	Topics	Research
1972	Photosensitization effect of the TiO <sub>2</sub>	Honda and Fujishima
1977	A short-circuited photoelectrochemical cell	Bard
1980	Decomposition of H <sub>2</sub> O on Pt-loaded TiO <sub>2</sub> powder	Sato and White
1980	Photoelectrochemical and photocatalytic reaction for the decomposition of H <sub>2</sub> O	Samorjai
1984	Development of highly active Ti-oxide single site photocatalysts on SiO <sub>2</sub> porous glass	Anpo and Kubokawa
1986	Size quantization effect of TiO <sub>2</sub> nanoparticles	Anpo and Kubokawa
1991	Wet system solar cell using TiO <sub>2</sub> nanoparticles and Ru-dye molecules	Grätzel
1994	Metal ion-doped TiO <sub>2</sub> photocatalysts	Choi and Hoffmann
1995	Application to environmental issues	Hashimoto and Fujishima
1997	Photocatalytic reduction of CO <sub>2</sub> with H <sub>2</sub> O on Ti-oxide single site photocatalysts prepared within the framework of silica thin film photocatalysts	Anpo and Ikeue
1997	Super-hydrophilic property of TiO <sub>2</sub> thin films	Hashimoto and Fujishima
1998	Second-generation TiO <sub>2</sub> enabling absorption and operation under visible light irradiation (by applying a metal ion-implantation synthesis method)	Anpo and Yamashita
2001	Anion doping of TiO <sub>2</sub> with N, C and S	Asahi

Table 1.4. Mapping of the crucial dates of TiO<sub>2</sub> research [Kitano et al., 2007]

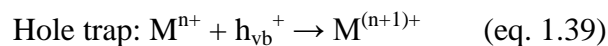
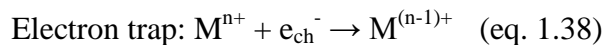
### 1.4.2 Cationic doping (metal doping)

Ion doping is the most immediate technique to expand the photo-response of TiO<sub>2</sub> into visible spectrum. From the first systematic study of ion doping effect [Choi et al., 1994], several articles have been published to investigate effects of metals such as Fe, Mo, Ru, Os, V, Rh, Ni, Co, Cu, Zn on photo-catalytic waste water and air treatment [Dvoranova et al., 2002], [Paola et al., 2002], [Wilke and Breuer, 1999].

During excitation of metal impurities, energy levels in the bandgap of TiO<sub>2</sub> are modified [Ni et al., 2007]:



Furthermore, electron (hole) transfer between metal ions and TiO<sub>2</sub> can alter the electron-hole recombination as [Ni et al., 2007]:



These modifications and alterations can increase the response of the semiconductor in the visible range and improve the separation of the carriers.

Very few studies have been carried out to analyze impact of metals doping on photo-catalytic water splitting [Ni et al., 2007].

Among the cations Choi individuates, as positive doping elements for photocatalytic application, vanadium strongly shifts the photo-response of the material into the visible light [Zhao et al., 1999], [Zhao et al., 2002]. Effect of vanadium is positive if doping is near the surface. No effect is shown when vanadium is in the bulk [Bettinelli et al., 2007].

Table 1.5 sums up some works reporting elaboration and characterizations of vanadium doped TiO<sub>2</sub>.

Reference	Elaboration route	Percentage of V (Oxidation state)	Characterizations/ Photoactivity tests
Sene et al. [Sene et al., 2002]	Sol-gel: titanium ethoxide, vanadium triisopropoxide, ethanol, HNO <sub>3</sub> .	0.5, 1, 2.5, 5 at. % (V <sup>4+</sup> /V <sup>5+</sup> )	Degradation of oxalic acid: 1% V better sample
Bhattacharyya et al. [Bhattacharyya et al., 2009]	Sol-gel: titanium isopropoxide, NH <sub>4</sub> VO <sub>3</sub> , isopropanol.	5 at. % (V <sup>5+</sup> )	Degradation of ethylene: vanadium doped sample better than undoped
Liu et al. [Liu et al., 2009]	Sol-gel: tetrabutyl titanate, NH <sub>4</sub> VO <sub>3</sub> , ethanol.	0.1, 0.5, 1 at.% (V <sup>5+</sup> )	Degradation of methyl orange: 0.5 at.% better sample
Zhou et al. [Zhou et al., 2009]	Sol-gel: tert-butoxide, NH <sub>4</sub> VO <sub>3</sub> , HNO <sub>3</sub> to adjust the pH.	Ti:V=20,30,40,50:1 (V <sup>5+</sup> /V <sup>3+</sup> )	Degradation of methyl orange: Ti:V=40:1 better sample

**Table 1.5. Some representative vanadium-doped titania xerogels extracted from the literature. \*not specified the vanadium precursor and the doping method; \*\* not specified of atomic or weight ratio**

Table 1.5 shows that vanadium doping increases the photodegradation of several compounds. All these authors have used sol-gel elaboration method and chose low doping ratio. Oxidation degree of vanadium is reported to be 4 or 5, in one case is 3.

The improvement of vanadium doped TiO<sub>2</sub> photoactivity can be ascribed i) to a better charge separation [Zhou et al., 2009] or ii) to the adsorption of the pollutant to be treated on the photocatalyst surface [Sene at al., 2002].

In Zhou's study the photocatalytic tests were carried out under fluorescent lamp, whose wavelength range was from 400 to 750 nm. These researchers explained that up to Ti:V = 40:1, the higher photoactivity of vanadium is due to the increase of the surface energy barrier and the consequent reduction of the space charge region. This situation induces a large electric field that avoids the recombination of the electron-holes couples. However, if the vanadium amount is too high, the space charge region becomes too narrow, the light penetration depth exceeds the space charge layer and the recombination of the carriers becomes easier. Therefore the optimum concentration of doping ions creates a thickness of the space charge layer equal to the light penetration depth.

In Sene's article, instead, the photocatalytic tests were performed under Xe-Hg arc lamp. They found that photoactivity increases for samples doped up to 1 at.% for the degradation of oxalic acid. Contrary to Zhou, Sene et al. ascribed the higher performance of these samples to the shift of the isoelectric point. Adding vanadium makes the surface of the photocatalysts more positive, so the adsorption of negatively charged anions on the material surface is improved. When the doping percentage exceeds 1 at.%, the isoelectric point decreases and the photoactivity as well. In conclusion, Sene et al. correlated the photocatalytic behavior to the adsorption power of the pollutants on the doped samples.

Sene theory is supported by Bhattacharyya et al. who deeply investigated the state of the vanadium by EPR and stated that in their samples vanadium is in the  $V^{4+}$  form. FT-IR was performed in situ to investigate the evolution of the species during the photocatalytic degradation of ethylene under 400 W mercury vapor lamp. In this paper, as in Sene's one, the better photocatalytic behavior of doped samples is ascribed to the better adsorption of the species on the surface.

If all these works are focused on the investigation of vanadium doped  $TiO_2$ , the precipitation of vanadium oxides, especially  $V_2O_5$  is easy during their synthesis.

Vanadium can be directly bound to elements of the host matrix (for example vanadium replaces titanium), but if synthesis conditions are favorable (amount of doping precursor, temperature, synthesis method), vanadium forms compounds in the matrix, creating interfaces between the host phase and the new phase. Literature is abundant on the interfaces between  $TiO_2$  and vanadium oxides. In this case the technique for improving the properties of  $TiO_2$  is not the doping anymore but the creation of composite semiconductor.

In Klosek's work [Klosek and Raftery, 2001], doping percentages were 0.5 V wt% and 1.7 V wt%<sup>24</sup>. Zhao [Zhao et al., 1999], instead, has chosen lower doping quantities and demonstrated that larger vanadium quantity accelerate  $V_2O_5$  precipitation.

The synergetic effect of vanadia/titania mixed systems has largely been studied:  $TiO_2$  and  $V_2O_5$  coupling improves the absorption of light because  $V_2O_5$  has a bandgap of 2.05 eV [Liu

---

<sup>24</sup> As Ti and V standard atomic weights are respectively 47.867 and 50.9415 g.mol<sup>-1</sup>, weight ratio and atomic ratio are almost equal.

et al., 2006] that is narrower than TiO<sub>2</sub> anatase, and the charge separation because V<sub>2</sub>O<sub>5</sub> has conduction band potential higher than TiO<sub>2</sub> [Liu et al., 2006].

Historical application of V<sub>2</sub>O<sub>5</sub>/ TiO<sub>2</sub> composite material is the selective catalytic reduction (SCR) [Bosch and F.Janssen, 1988]. Ciambelli studied physico-chemical properties of vanadia-titania catalyst. UV-vis Spectroscopy shows this sample absorbs visible light [Ciambelli et al., 1995]. Significant result of this paper is that NO conversions increase with the loading of vanadium.

Optical properties of vanadium oxides (VO<sub>2</sub> and V<sub>2</sub>O<sub>5</sub>) have been largely investigated, because of the wide range of industrial application, as for example as metal insulator transitions (MIT). Parker [Parker et al., 1990] reported that VO<sub>2</sub> has metallic nature due to the V d orbitals overlapping with the O p orbitals. Their investigations also pointed out that band transition has an indirect behaviour. On the other hand, V<sub>2</sub>O<sub>5</sub> has a high anisotropic nature due to the features of its electronic band structure. This anisotropic nature induces a stronger absorption light along the a-b directions than in c direction.

In his paper Silvesmit [Silversmit et al., 2005] elaborates vanadium oxide layer on TiO<sub>2</sub> by reactive DC magnetron sputtering. Valence band of the composite material has been analyzed by Ultra-violet Photoelectron Spectroscopy. This investigation has pointed out that increasing vanadium oxide deposition time on anatase, the valence band spectra gradually change from the TiO<sub>2</sub> shape to the V<sub>2</sub>O<sub>5</sub> spectrum. This article also confirms that vanadium shifts photo-response of the sample into visible region. In this article samples are tested for hydrocarbons oxidation, because vanadium oxide enhances reactivity and selectivity of the TiO<sub>2</sub>.

Liu et al. [Liu et al., 2006] discussed the effect of TiO<sub>2</sub>-V<sub>2</sub>O<sub>5</sub> coupling on photo-degradation of methylene blue. After 3 h the sample TiO<sub>2</sub>:V<sub>2</sub>O<sub>5</sub>=10:1 completely degrades the colorant, while TiO<sub>2</sub> pure sample takes much longer time.

Work of Bulushev in 2000 [Bulushev et al., 2000] was devoted to examine reasons of the better photo-activity on a TiO<sub>2</sub>/V<sub>2</sub>O<sub>5</sub> for the oxidation of toluene. TiO<sub>2</sub>/ V<sub>2</sub>O<sub>5</sub> sample is more active than TiO<sub>2</sub> due to the bridging oxygen in the V–O–Ti bond that acts as active sites.

This paper also correlates preparation method and photo-activity properties: photo-activity properties are increased by the solid-state interaction of monomeric vanadia species with TiO<sub>2</sub> and formation of monomeric vanadia is controlled by the calcination step.

### **1.4.3 Anionic doping (non-metal doping)**

For several authors, cationic doping is detrimental for TiO<sub>2</sub> activity because it either lowers the bottom of the conduction band, which makes H<sup>+</sup> photoreduction less favourable, or creates charge traps in the bandgap ([Herrmann, 1999] and [Serpone, 2006]). Thus, anionic doping has now received much attention for its ability to reduce TiO<sub>2</sub> band gap increasing valence band top energy level.

Although other elements (as C, S, B, P and F), have been considered ([Khan et al., 2002], [Umebayashi et al., 2003], [Zhao et al., 2004], [Lin2005] and), N-doped TiO<sub>2</sub> materials are

the most synthesized and studied because nitrogen doping seems to narrow the band gap with a very slight lowering of the conduction band [Sakthivel et al., 2004].

Within this frame, researchers have increasingly focused their attention on both physical and chemical methods for incorporating nitrogen in TiO<sub>2</sub> matrix.

Asahi article [Asahi et al., 2001] is recognized being the pioneer work of anionic doping. In this crucial paper, photocatalysts active in the VIS region have been synthesized sputtering TiO<sub>2</sub> in N<sub>2</sub>/Ar gas mixture or calcining TiO<sub>2</sub> in NH<sub>3</sub>/Ar atmosphere.

Among the physical processes, the most useful are indeed i) heat (or plasma) treatment in a NH<sub>3</sub>/Ar gas mixture or ii) sputtering the TiO<sub>2</sub> target in a N<sub>2</sub> (40 vol. %)/Ar gas mixture ([Asahi et al., 2001], [Kang et al., 2007], and [Suzuki2008]).

Chemical processes usually involve sol-gel techniques, with urea or thiourea as the nitrogen source ([Sato, 1986], [Horikawa et al., 2008] and [Sano2004]). The nitrogen source can be dispersed in the solution containing the metal precursor [Wei et al., 2008] or mixed with the sol [Cong et al., 2007, Cheng2007], or with the gel [Ananpattarachai et al., 2009]. On the other hand several articles report the doping procedure by mixing powders issued from the gel drying and powders of the nitrogen source [Nosaka et al., 2005], [Beranek and Kisch, 2007], [Horikawa et al., 2008].

Although the most widely used nitrogen source is urea, other materials are employed, like ammonium chloride (NH<sub>4</sub>Cl), ammonium hydroxide solution (NH<sub>4</sub>OH), 4-aminoantipyrine (C<sub>11</sub>H<sub>13</sub>N<sub>3</sub>O), potassium ferricyanide (K<sub>3</sub>Fe(CN)<sub>6</sub>), diethanolamine (DEA) and triethylamine (TEN) [Ananpattarachai et al., 2009].

In 1986 Sato [Sato, 1986] reported that NH<sub>4</sub>Cl impurities are responsible for the TiO<sub>2</sub> photoreponse in visible light region. The coloration centers were identified as NO<sub>x</sub>.

Methods of elaboration reported in the literature generally allow the formation of NO<sub>x</sub>-TiO<sub>2</sub> rather than N-doped TiO<sub>2</sub>.

About the N-doped materials, at present the scientific topic concerns the two following fundamental points [Fujishima2008]:

- the origin of the absorption in the visible light region;
- the states of nitrogen atoms in the TiO<sub>2</sub> lattice.

For the first point it seems that low percentages of dopant (N/O at.% ) induce mid-gap levels just above valence band. As for cationic doping, these centers can allow trapping of charges and be detrimental for photo-activity. High percentages of nitrogen can fulfill energetic levels near the valence band and contribute to reduce the band gap [Serpone, 2006]. Burda et al. [Burda et al., 2003] have fixed at 8 at.% the limit percentage of nitrogen above which TiN<sub>x</sub> is very probably formed [Chen et al., 2007].

Doping states of nitrogen atoms have been largely investigated by X-rays Photoelectron Spectroscopy (XPS). This analysis allows to identify two main nitrogen peaks: at 396 and 400

eV. Although debates still animate scientific discussions, researchers seem to agree that the peak at 396 eV corresponds to substitutional nitrogen doping and the peak at 400 eV to interstitial nitrogen doping.

## 1.5 Summary and comments

Among the eleven known TiO<sub>2</sub> allotropic forms, anatase, rutile and TiO<sub>2</sub>-B have attracted much attention for their strong photoactivity. Industrial application range of TiO<sub>2</sub> is wide, because it is cheap, abundant, environmentally friendly and chemically stable.

Recently the increasing demand of energy has led scientific community to reconsider TiO<sub>2</sub> as a clever potential photocatalyst for clean hydrogen production. For hydrogen production from water splitting, anatase is the most active phase, because although the bandgap of anatase is 3.2 eV, the energy value of its conduction band is - 0.2 eV. Since a semiconductor must have a conduction band lower than 0 eV and a valence band higher than 1.23 eV to be considered for water splitting, anatase, appears to be, among the diverse TiO<sub>2</sub> structures, the best candidate for this application. However, composites can also present a high photoactivity, as Degussa P25 product proves in several applications.

Although TiO<sub>2</sub> is the most frequently studied semiconductor for hydrogen water splitting application, its photoactivity is significantly limited by:

- low absorption in the visible light,
- fast recombination of photogenerated couples,
- fast backward reaction that forms water from oxygen and hydrogen.

Literature reports several techniques to improve the charges separation: the addition of electron donors, such as methanol, and noble metal loading, such as platinum.

One of the parameters that could sensibly avoid the recombination of the charges is suspected to be the morphology of the TiO<sub>2</sub> nano-objects. In the literature a systematic study on the effect of the shape of the semiconductor on its photoactivity was absent at the beginning of this PhD work. For this reason, one of the main parts of this thesis is devoted to the elaboration and evaluation of different morphologies using three methods:

- precipitation of TiCl<sub>4</sub> with NaOH to produce nanoparticles;
- alkaline hydrothermal treatment to have nanotubes;
- sol-gel route to have aerogels and xerogels.

An improvement of the harvesting of the visible light can be achieved by the doping technique. After the bibliographic study, vanadium and nitrogen seem to deeply modify the bandgap of TiO<sub>2</sub> and shift its response in the visible light. They have been chosen to evaluate the doping of the TiO<sub>2</sub> morphologies I have selected.



## 2. Samples elaboration and characterization: particles, 1D-structures and aerogels/xerogels

As previously summarized in the bibliographic section, anatase is the relevant phase for watersplitting because of position of its conduction band and of easy obtention of small grain size, higher surface area comparing to other forms of TiO<sub>2</sub> [Yeredla and Xu, 2008], [Nada et al., 2005]. Furthermore, as also mentioned in the bibliographic part, the morphology factor is also known to have a significant influence on the photocatalytic behaviour of semiconductor materials because it can improve the charge separation [Mor et al., 2005], [Sreethawong et al., 2007], [Park et al., 2006]. Based on this statement, the present chapter is devoted to the elaboration and characterizations of significantly different morphologies of anatase TiO<sub>2</sub>.

Among various possibilities, three anatase families presenting radically different morphologies coming from soft chemistry were selected:

- nanoparticles;
- one-dimension (so-called 1D) nanostructures;
- aerogels and xerogels.

The first two families are elaborated in aqueous media by precipitation and/or hydrothermal crystallization, the last one by sol-gel in alcoholic reaction media. Such TiO<sub>2</sub> species present very different geometrical form factors: we assume that nanoparticles are spherical, 1D are tubular (with length  $\gg$  diameter) and sol-gel derived materials are more or less equivalent to 3D-interconnected network of covalently bonded TiO<sub>2</sub> particles, clusters and aggregates.

The aim of this chapter is to study the different selected anatase TiO<sub>2</sub> morphologies.

The present chapter is divided into three parts respectively focused on nanoparticles, 1D nanostructures and aerogels/xerogels. Each part presents first the elaboration process, then it sums up the most important characterization results and finally draws the main conclusions on a family-by-family basis. Bandgap estimation and watersplitting results are gathered in a specific chapter dedicated to the foreseen application.

It is underlined within the frame of this introduction that structural, morphological features, size and surface area of photocatalysts have been characterized by:

- (High Resolution) Transmission Electron Microscopy (HR-TEM) for determining particles (or clusters in the case of aerogels) size and phase;
- X-Rays Diffraction (XRD) for identifying phase and calculating crystallites size (L) by Scherrer formula, considering A(101) and R(110). A and R are respectively anatase and rutile:

$$L_{hkl} = K\lambda / \text{FWHM}_{(hkl)} \cos\theta \quad (\text{eq. 2.1})$$

where:

- K is a constant, depending on the shape factor. Close to 1, this precise knowledge of K value is not necessary for comparisons, as some authors established for other kind of nanoparticles we may consider  $K=0.9$ ;
  - $\lambda$  is the incident wavelength;
  - FWHM is the full width of the peak at half maximum intensity
  - $\theta$  is the Bragg angle.
- nitrogen physical sorption using BET model for measuring surface area  $S_{\text{BET}}$ , analyzing shape of isotherms and calculating average particle diameter (D):

$$D = f / S_{\text{BET}} \cdot \rho_s \quad (\text{eq.2.2})$$

Where:

- f is the shape factor (6 for nanoparticles and aerogel, 4 for wires);
- $S_{\text{BET}}$  is the surface area;
- $\rho_s$  is the density of the phase ( $\text{g}\cdot\text{cm}^{-3}$ ) [Rouquerol et al, 2003].

In parallel, nitrogen physisorption using BJH model gave informations on pore size distribution and average pore size diameter.

## 2.1 Nanoparticles

### 2.1.1 Elaboration and samples

#### 2.1.1.1 Synthesis

Nanoparticles of  $\text{TiO}_2$  were obtained by precipitation of  $\text{TiCl}_4$  and  $\text{NaOH}$  followed by hydrothermal crystallization.

Figure 2.1 shows the experimental equipment. Precipitation was carried out in a 1 l double jacketed batch reactor, equipped of a TTP45 turbine for assuring the mechanic stirring. Water circulating in the jacket keeps the temperature at the set value. Acidic and basic solutions are in two different open tanks. After filling the reactor with 0.5 l of distilled water, basic and acidic solutions are simultaneously injected in diametrically opposite points near the blades. Flow rates of the two solutions are roughly the same and controlled by the peristaltic pumps. During the reaction pH is adjusted at set value by an automatic burette (radiometer PHM290) containing  $\text{NaOH}$  1.6 M solution.

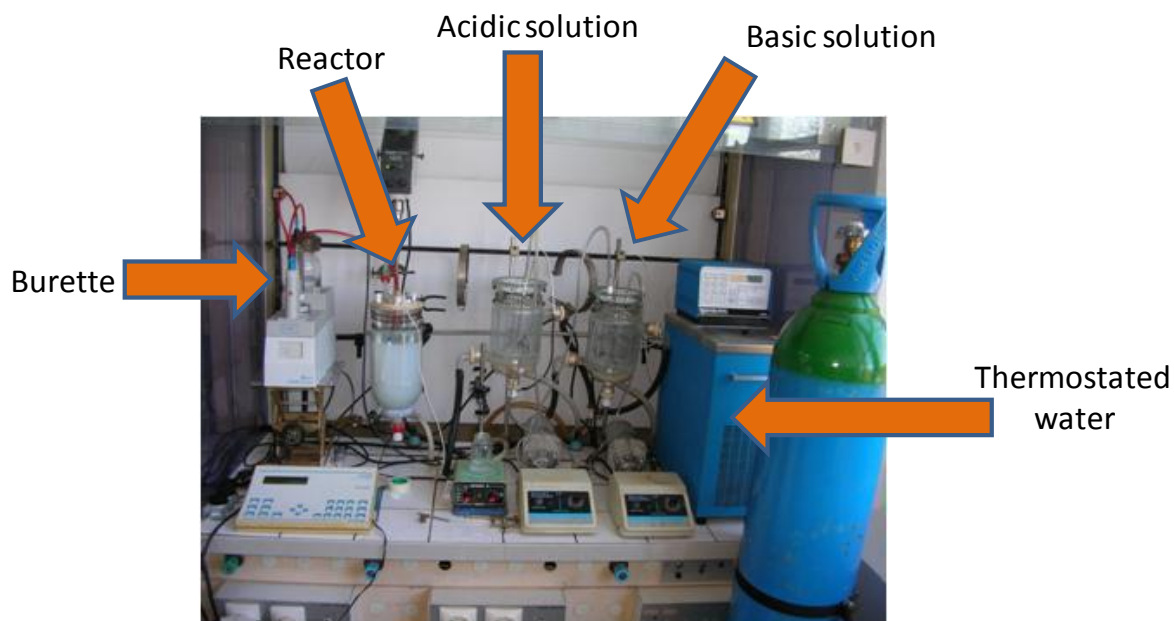


**Figure 2.1** Batch reactor equipment

The reactants solutions were 250 ml of water solution of  $\text{TiCl}_4$  (Fluka 89545) 0.4 M plus 10 ml of HCl (Fluka 84415, assay > 37% (T)) and 250 ml of aqueous solution of NaOH (Sigma-Aldrich S8045) 2 M. The pH was kept at a value close to 2 in the reactor during injection thanks to the automatic burette, residence time was 1 h, temperature 25 °C, pressure 1 atm. Quantity of  $\text{TiCl}_4$  was calculated in order to have 0.1 mol of  $\text{TiO}_2$  (8 g) as final product.

During the hydrolysis, one main reaction occurs (Equation 2.3)<sup>25</sup>:



After precipitating, the white suspension was washed with distilled water in order to remove salts and impurities. This washing treatment has been repeated three times. Once washed, the volume of the product was adjusted to 1 liter by distilled water. At the end of this step, an amorphous product is issued. Starting from this suspension many different nanoparticles have been synthesized. As shown in the Figure 2.2, a part of the amorphous product has been directly crystallized in an autoclave. Two temperatures and two pH have been chosen: 2 and 10. Another part has been aged in batch conditions at pH 10, 80 °C for 30 h. After aging, the product has been crystallized at two different temperatures.

<sup>25</sup> Since the tetravalent elements are too polarizing to form stable  $\text{Ti}(\text{OH})_4$ , they form  $\text{TiO}(\text{OH})_2$ . During crystallization oxolation leads to dehydration that leads to  $\text{TiO}_2$

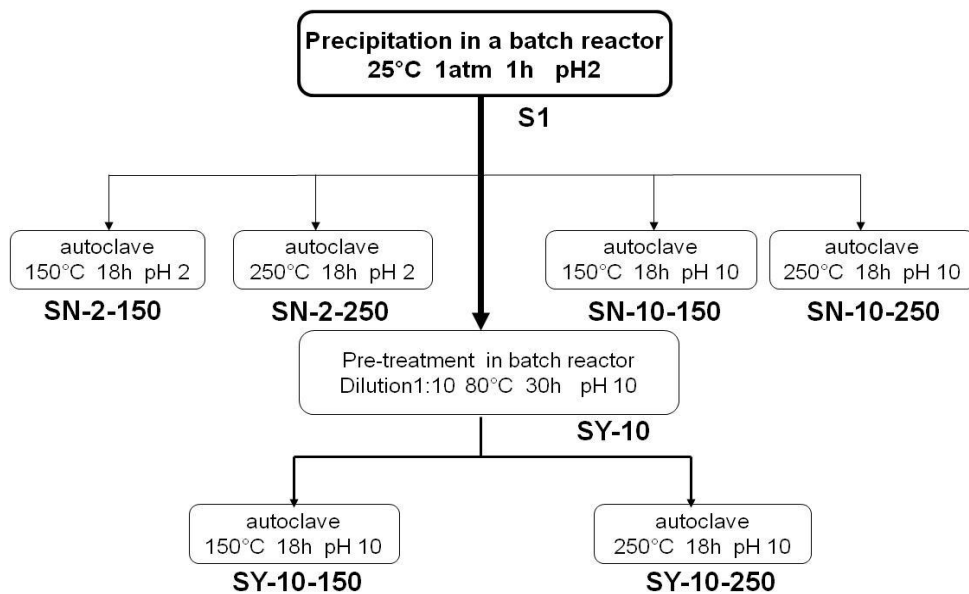


**Figure 2.2 Pattern of TiO<sub>2</sub> nanoparticles synthesis**

In any case, crystallization has been carried out in a Teflon lined Hastelloy autoclave shown in Figure 2.3. Temperature and pH change, time has been kept constant at 18 h.



**Figure 2.3 Autoclave for hydrothermal crystallization**

### 2.1.1.2 Samples

Table 2.1 sums up the eight samples elaborated following the procedure described above.

Sample	Pre-treatment	pH crystallization	T crystallization(°C)
SN-2	No	-	-
SN-2-150	No	2	150
SN-2-250	No	2	250
SN-10-150	No	10	150
SN-10-250	No	10	250
SY-10	Yes	-	-
SY-10-150	Yes	10	150
SY-10-150	Yes	10	250

Table 2.1 Elaborated samples

### 2.1.2 Characterizations

#### 2.1.2.1 X-rays Diffraction<sup>26</sup>

X-rays diffractograms in Figure 2.4-2.7 show all samples are anatase, except SN-2-250, which is mixture of anatase and rutile. Observing the peaks of the XRD data, the less crystallized sample is SY-10, the most crystallized is SN-10-250.

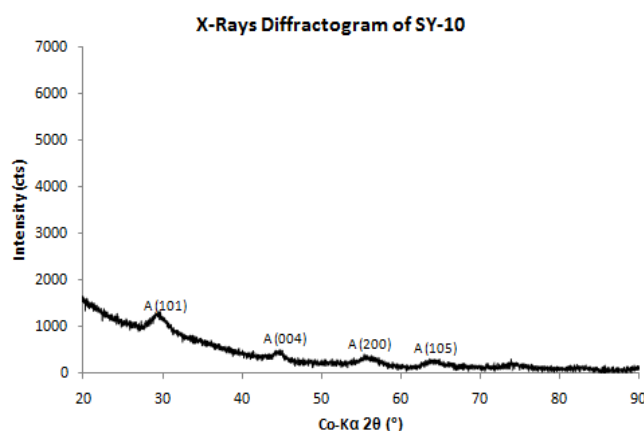
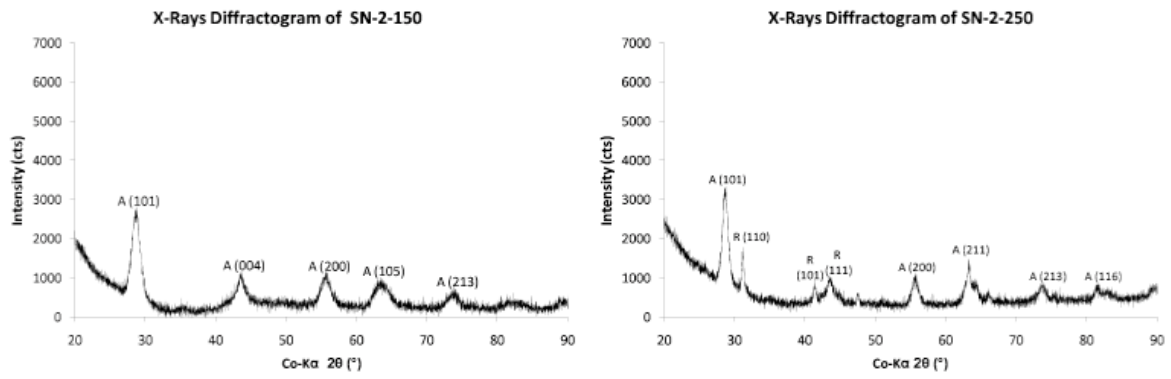
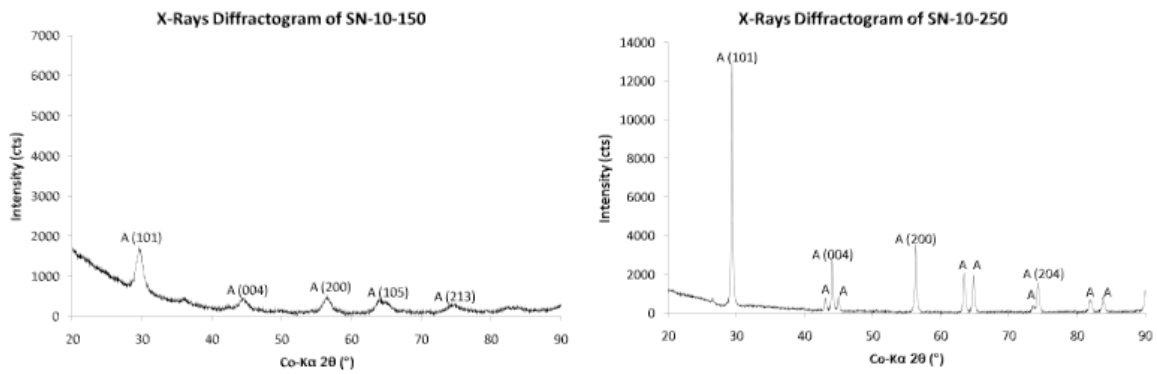


Figure 2.4 X-Rays Diffractograms of SY-10

<sup>26</sup> XRDs have been performed using Bruker D8, with Cobalt as X-rays source, at the CEP/SCPI laboratory of MINES ParisTech.



**Figure 2.5 X-Rays Diffractograms of SN-2-150 and SN-2-250**



**Figure 2.6 X-Rays Diffractograms of SN-10-150 and SN-10-250**

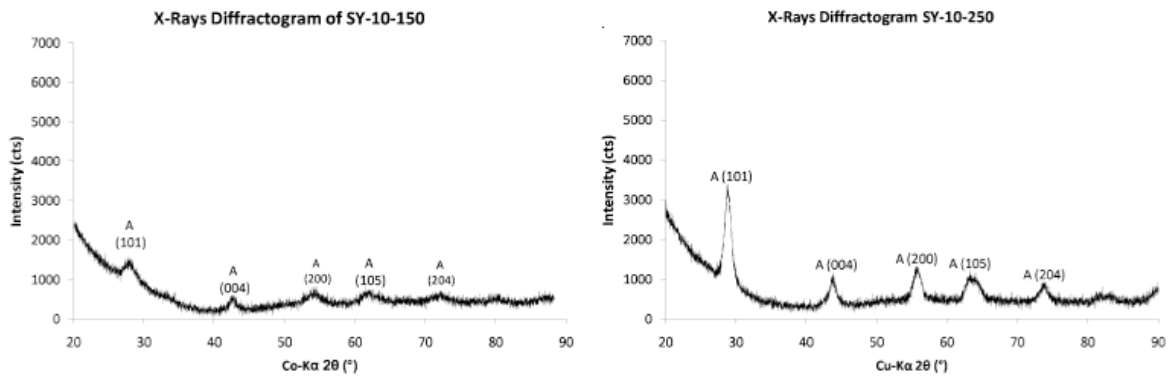


**Figure 2.7 X-Rays Diffractograms of SY-10-150 and SY-10-250**

The Table 2.2 sums up crystallites size determined by Scherrer formula. All samples except SN-10-250 have similar anatase crystallites size, because at high temperature and high pH crystal growth is improved. Rutile crystallite size of SN-2-250 is 28 nm.

Sample	XRD $\pm$ 0.3 (Phase and L (nm))
SN-2-150	7
SN-2-250	11, 28*
SN-10-150	9
SN-10-250	42
SY-10	6
SY-10-150	14
SY-10-250	9

**Table 2.2 Summarize of XRD characterizations. \* is crystallite size of rutile (110)**

We have used the Equation 1.2 [Zhang et al., 2000] to calculate the amount of rutile and anatase in SN-2-250: anatase is 53%, rutile 47%.

$$X_R = (1 + (0.8I_a/I_r))^{-1} \quad (\text{eq. 2.4})$$

where:

- $X_R$  is the weight rutile fraction in the powder;
- $I_a$  is the intensity of XRD peak of anatase (101);
- $I_r$  is the intensity of XRD peak of rutile (110).

### 2.1.2.2 Transmission Electron Microscopy

Figure 2.8-2.11 show Transmission Electron Microscopy analyses<sup>27</sup>. Aggregates are evident in the samples SN-2 and SN-10-150. SN-2-150, SN-2-250, SN-10-250, SY-10, SY-10-150 and SY-10-250 are well dispersed particles. SY-10-250 and SN-10-150 seem to have plate particles, in agreement with nitrogen physisorption results. Our results are similar to what reported in the literature, since Cho et al. have obtained plate-like particles from crystallization of a precipitate in autoclave at high pH [Cho et al., 2005].

Table 2.3 sums up particles diameter from TEM analysis. Except SN-2-250 and SN-10-250, samples have similar particles size. We observe a good correlation between particle diameter obtained according to TEM and crystallite size obtained according to XRD analysis by Scherrer formula. This suggests that particles are monocrystalline. Size of anatase and rutile

<sup>27</sup> Analyses have been performed by Dr. Marie-Hélène Berger, from Material Center of Mines ParisTech, Evry. The microscope used is a TEM Tecnai 20F ST.

nanoparticles of SN-2-250 agrees with its size of anatase and rutile crystallite. SN-10-250 has the highest particles size, confirming XRD results.

Name	TEM: Phase and l (nm) $\pm 0.4$
SN-2	Germes of anatase
SN-2-150	8
SN-2-250	8, 27*
SN-10-150	10
SN-10-250	37
SY-10	4
SY-10-150	7
SY-10-250	9

Table 2.3. Size of nanoparticles estimated by TEM analysis. \*is the rutile

HR-TEM of Figure 2.12 proves that the sample pre-treated in batch conditions at 80 °C, pH 10 and 30 h and crystallized in autoclave at 150 °C are anatase. Sample not pre-treated and crystallized at 250 °C pH 2 contains rutile (Figure 2.13), in agreement with XRD results.

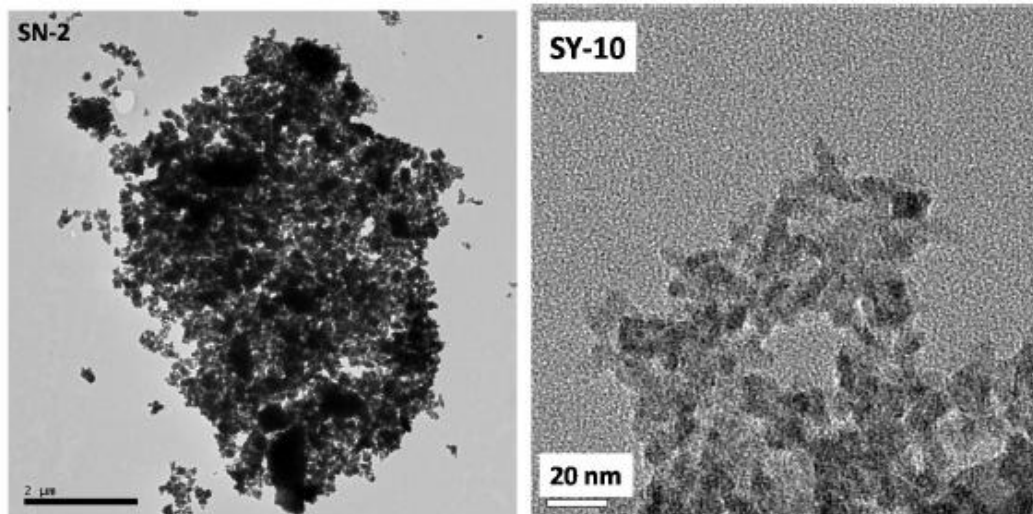


Figure 2.8 Transmission Electron Microscopy of SN-2 and SY-10 samples

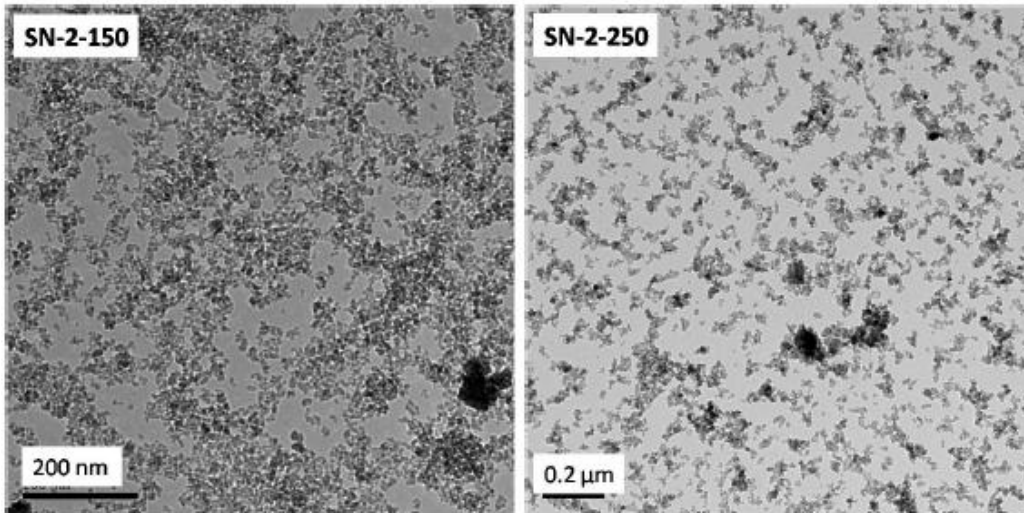


Figure 2.9 Transmission Electron Microscopy of SN-2-150 and SN-2-250 samples

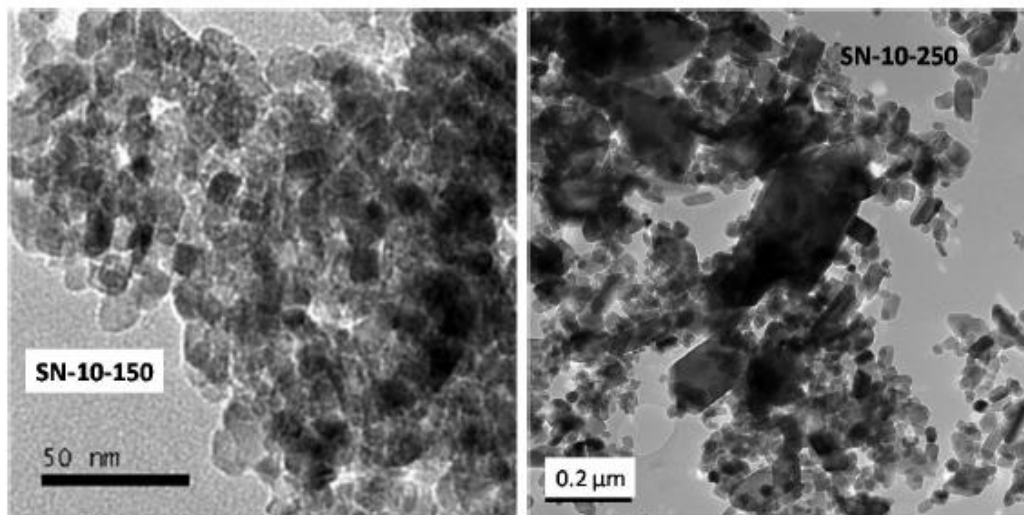


Figure 2.10 Transmission Electron Microscopy of SN-10-150 and SN-10-250 samples

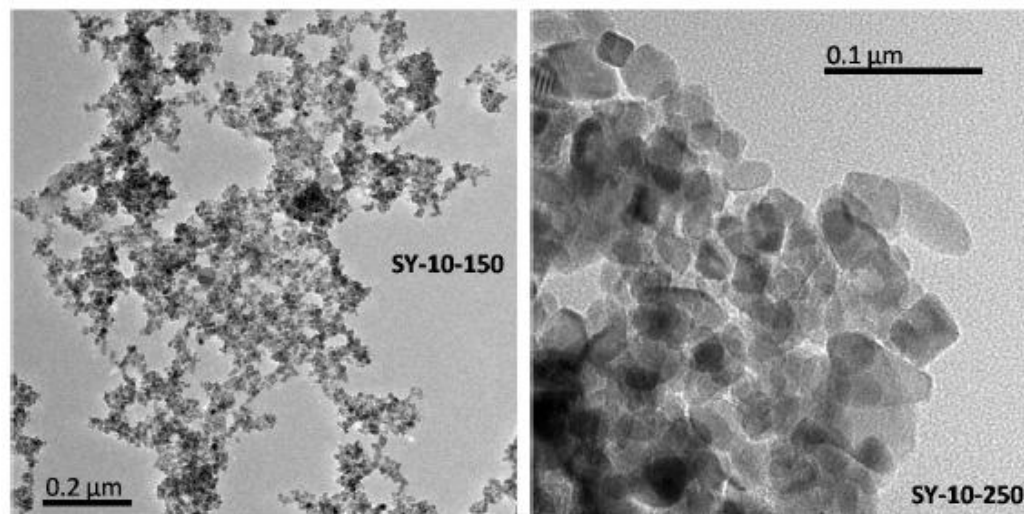


Figure 2.11 Transmission Electron Microscopy of SY-10-150 and SY-10-250 samples

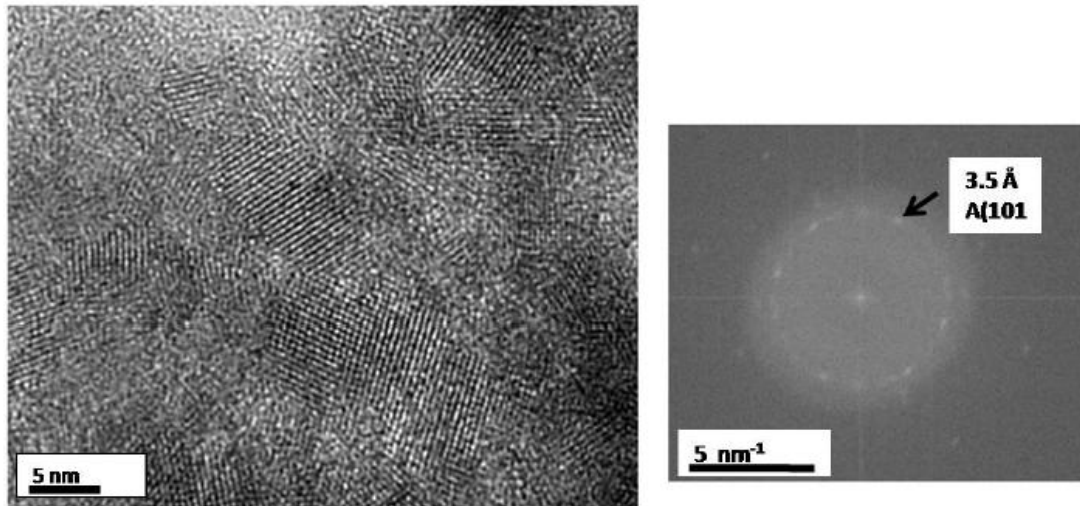


Figure 2.12 Reverse Fourier Function Transform on SY-10-150

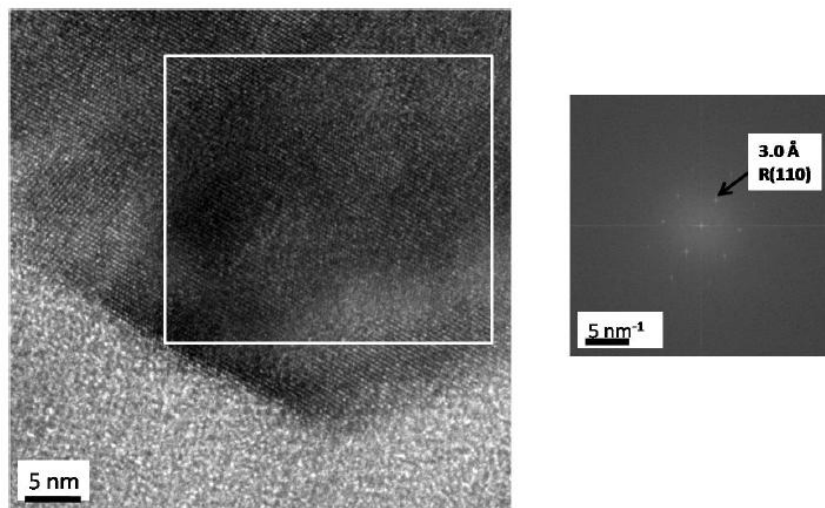


Figure 2.13 Reverse Fourier Function Transform on SN-2-250

### 2.1.2.3 Nitrogen adsorption/desorption

Table 2.4 sums up nitrogen adsorption/desorption isotherms results.<sup>28</sup>

Name	$S_{BET}$ ( $m^2g^{-1}$ )	$V_P$ ( $cm^3g^{-1}$ )	$\delta_1$ (2-3 nm)	$\delta_2$ (10-11 nm)	$\delta_3$ (> 50 nm)	d (nm)	D (nm)
SN-2-150	148	0.19	x	-	-	5	10
SN-2-250	88	0.19	-	-	-	9	17
SN-10-150	143	0.32	-	-	x	9	10
SN-10-250	17	0.10	x	x	-	24	90
SY-10	8	0.03	x	x	-	14	192
SY-10-150	164	0.52	x	-	-	4	9
SY-10-250	40	0.22	x	x	x	22	38

**Table 2.4 Data from BET and BJH treatments. D is the particles diameter from geometric formula ( $D=6/(S_{BET}\cdot\rho_s)$ ), d is the average pore diameter considering pore as cylinder ( $d=4/(V_p\cdot S_{BET})$ ),  $\delta_1$ ,  $\delta_2$  and  $\delta_3$  correspond to peaks of the volumic pore size distribution**

Figure 2.14 and Figure 2.15 are the nitrogen physisorption isotherms of the eight samples. Sample with higher surface area is SY-10-150 ( $164\ m^2g^{-1}$ ), while lower one is for SY-10 ( $8\ m^2g^{-1}$ ).

All the eight isotherms have a hysteresis loop correlated with capillary condensation taking place in mesopores [Sing, 1982]. These eight loops can be divided into three groups: SN-2-250 and SN-10-150 in the first group, SY-10-150 and SN-2-150 in the second group, SN-10-250, SY-10 and SY-10-250 in the third group.

According to IUPAC, initial part of isotherms of first group (SN-2-250 and SN-10-150) is associated to monolayer-multilayer adsorption<sup>29</sup>. The shape of the hysteresis is due to agglomerates or compacts of approximately uniform spheres in fairly regular array, and hence to have narrow distributions of pore size.

The loops of the second group (SY-10-150 and SN-2-150) looks like the loops associated to corpuscular systems (e.g. silica gels). In these cases the distribution of pore size and shape is not well-defined [Sing, 1982].

For the third group (SN-10-250, SY-10 and SY-10-250), the loop does not exhibit any plateau at high  $P/P_0$ , which is observed with aggregates of plate-like particles giving rise to slit-shaped pores [Sing, 1982].

<sup>28</sup> Nitrogen adsorption/desorption isotherms were measured at 77 K using a Micromeritics ASAP2010 model, at CEP Mines ParisTech.

<sup>29</sup> “The beginning of the almost linear middle section of the isotherm, is often taken to indicate the stage at which monolayer coverage is complete and multilayer adsorption about to begin.”

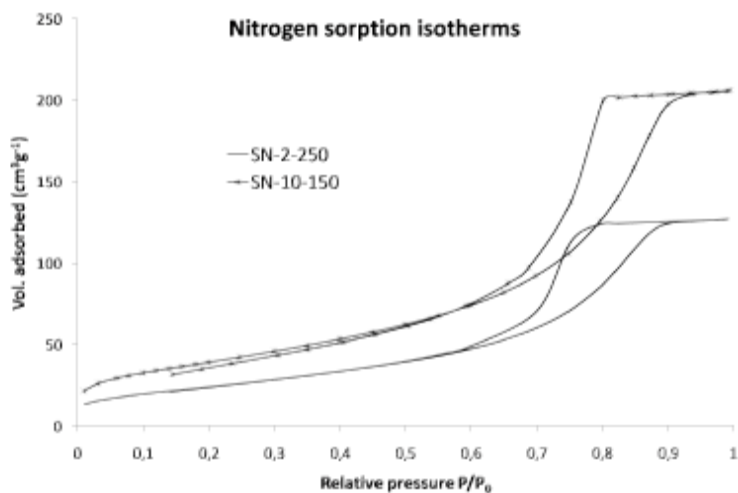


Figure 2.14 N<sub>2</sub> adsorption/desorption isotherm of, SN-2-250 and SN-10-150

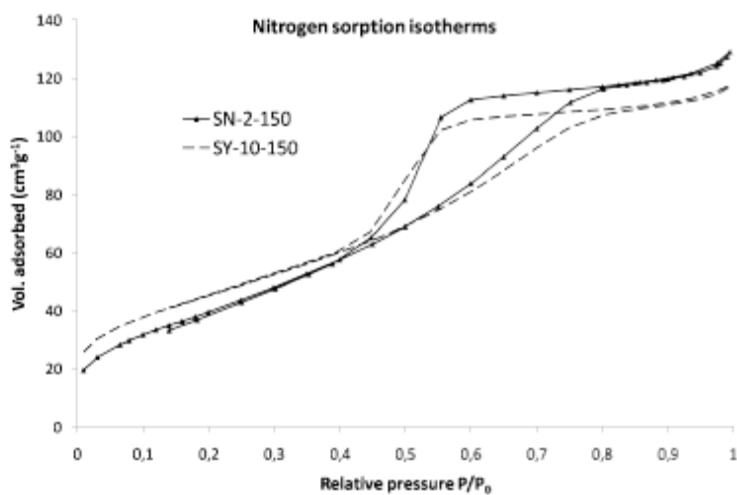


Figure 2.15 N<sub>2</sub> adsorption/desorption isotherm of SN-2-150, and SY-10-150

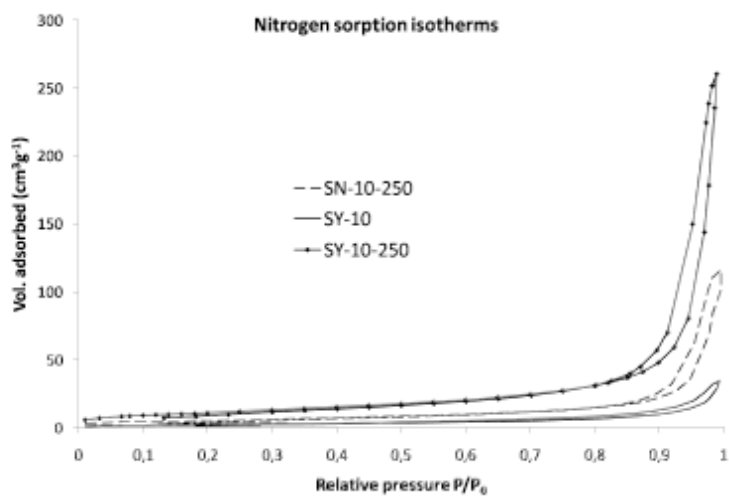


Figure 2.16 N<sub>2</sub> adsorption/desorption isotherm of SN-10-250, SY-10 and SY-10-250

BJH curves of the samples can be divided in three families: SN-2-250 and SN-10-150; SN-2-150 and SY-10-150; SN-10-250, SY-10 and SY-10-250.

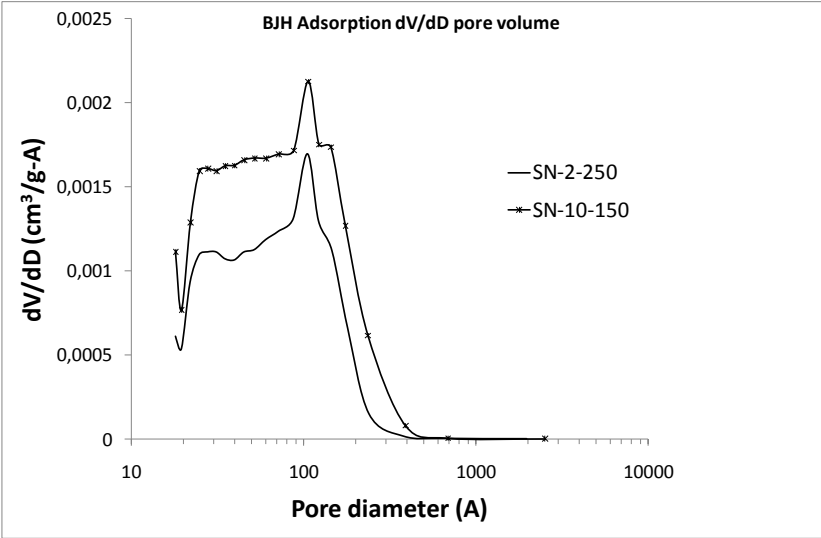


Figure 2.17 Pore size distribution of SN-2-250 and SN-10-150 samples

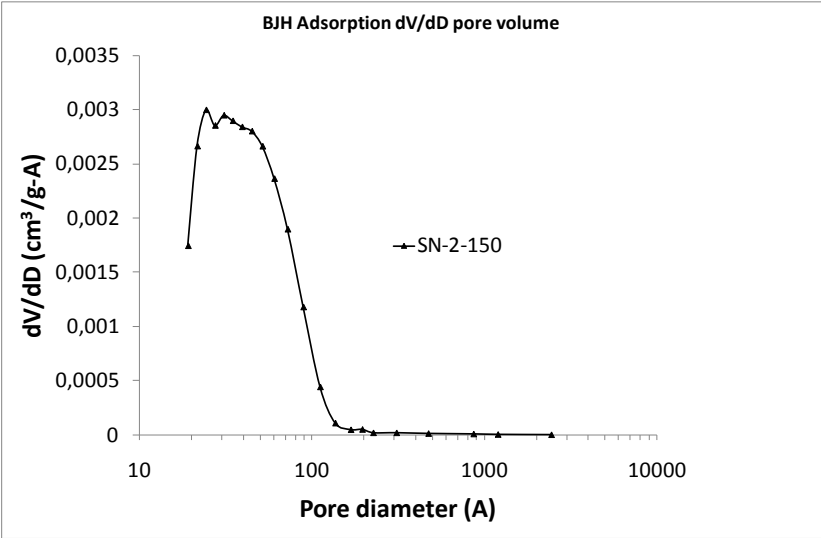


Figure 2.18 Pore size distribution of SN-2-150 sample

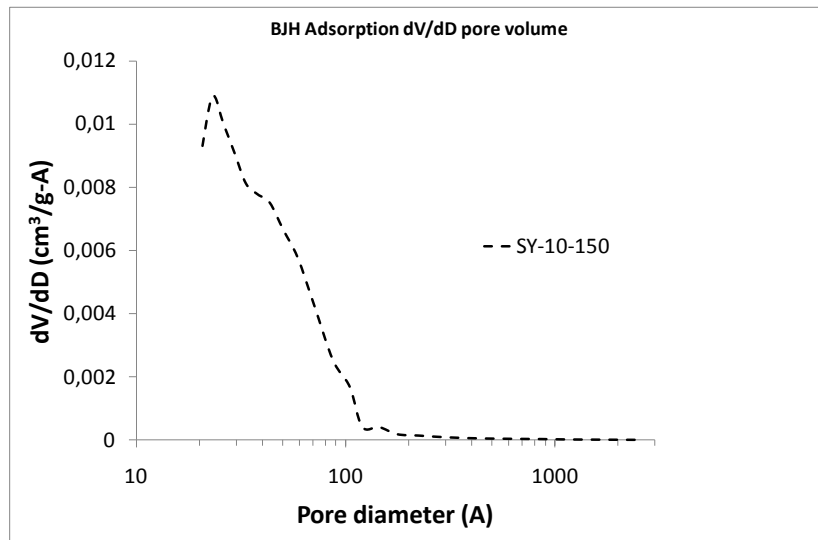


Figure 2.19 Pore size distribution of SY-10-150 sample

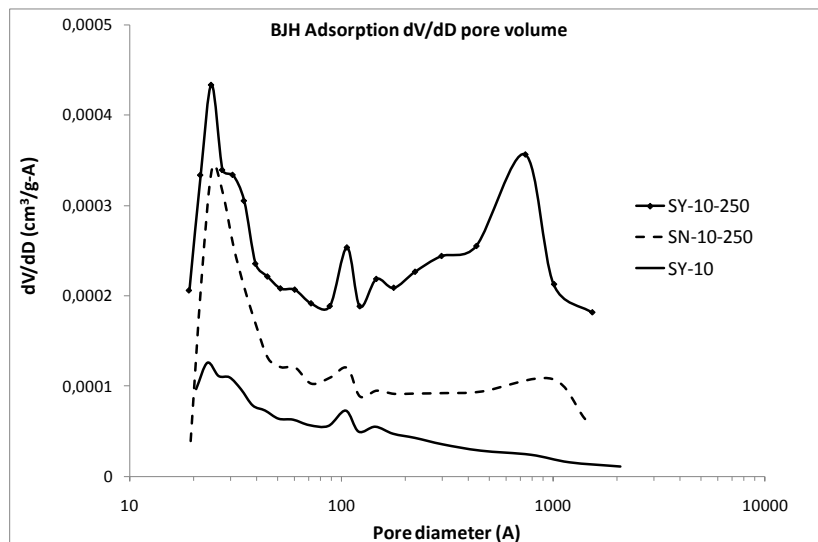


Figure 2.20 Pore size distribution of SY-10-250, SN-10-250 and SY-10 samples

Pores size distributions of Figure 1.17 shows that first family (SY-10-150 and SN-2-250) has two pores distributions size at 2 and 11 nm. SN-2-150 (Figure 2.18) and SY-10-150 (Figure 2.19) have one pores size distribution at 2 nm.

The samples of the third family (Figure 2.20) have similar BJH curves and have several pores size distributions. SY-10-250 has three pore size distributions: 2, 11 and 74 nm. SN-10-250 has three pore size distributions: 2, 11 and 99 nm. SY-10 has only pore size distributions at 2 and 11 nm.

### 2.1.3 Discussion

Table 2.5 sums up characterizations results of the samples and clearly underlines that an increase of the crystallization temperature leads to bigger particles and smaller specific surface areas.

Name	$S_{\text{BET}}$ ( $\text{m}^2\text{g}^{-1}$ )	D (nm)
SN-2-150	148	10
SN-2-250	88	17
SN-10-150	143	10
SN-10-250	17	90
SY-10	8	192
SY-10-150	164	9
SY-10-250	40	38

Table 2.5 Summarize of nitrogen physisorption characterizations

This study is focused on the effects of crystallization conditions (pH and temperature) and of an aging treatment on the features of the final products.

At 250 °C particles size increases and, consequently, surface area decreases. SY-10, thanks to the pre-treatment, is partially crystallized, with low surface area. SN-2-150 and SN-10-150 are similar, in nanoparticles size and surface area. Samples crystallized at 250 °C and pH 10 is just anatase, at 250 °C and pH 2 is a mixture of rutile and anatase.

At 150 °C, anatase is formed at pH 2 or 10, with or without an aging treatment. At this crystallization temperature we notice germination of anatase with restricted growth of particles. At 150 °C and pH 2 we did not obtain rutile because, as Finnegan reports [Finnegan et al., 2007], at this temperature low transformation kinetic does not allow growth of particles and rutile formation. Only the crystallization of amorphous in anatase occurs.

At 250 °C and pH 2 we obtained a mixture of anatase and rutile (SN-2-250), while at the same temperature and pH 10 (SN-10-250) we obtained anatase. At the nanoscale, it may be tricky to discuss the respective roles of kinetics and thermodynamics to explain the competition between polymorphs. We cite here a recent study about pH dependent selectivity to produce anatase or rutile. As Finnegan reports, we hypothesize that at this temperature crystallization process occurs in two steps:

1. dissolution of the particles of anatase of the presursor (SN-2 for SN-2-250 and SN-10-250, SY-10 for SY-10-250);
2. recrystallization in a more stable phase.

Dissolution of particles of anatase occurs in both acidic or basic medium. Later the formation of particles occurs. The phase that crystallizes is the phase with the lower Gibbs free energy.

The free enthalpy energy is the sum of the bulk free enthalpy ( $G_b$ ) and the surface free enthalpy ( $G_s$ ):

$$G = G_b + G_s \text{ (eq. 2.5)}$$

The surface free enthalpy ( $G_s$ ) is the sum of the surface electrostatic energy ( $\sigma\psi A$ ) and the interfacial energy ( $\gamma A$ ):

$$G_s = \sigma\psi A + \gamma A \text{ (eq. 2.6)}$$

Where  $\sigma$  is the surface charge per unit area ( $C.m^{-2}$ ),  $\psi$  the surface potential (V),  $A$  the total surface area ( $m^2$ ), and  $\gamma$  the interfacial tension ( $J.m^{-2}$ ). When pH solution is close to the point of zero charge (PZC), the main contribution is given by the interfacial tension term,  $\gamma A$ ; when pH is far from the PZC by the surface charge term,  $\sigma\psi A$ . Both these terms are functions of pH. The surface charge term ( $\sigma\psi A$ ) is 0 at PZC, since  $\sigma$  is 0; is always greater than 0 at pH far from the PZC (Figure 2.21). The interfacial tension term ( $\gamma A$ ) has its maximum at the PZC, and decreases at pH far from PZC, because the concentration of adsorbed potential determining ions increases (Figure 2.21). In both anatase and rutile, the values of the interfacial tension term are lower than those of surface charge term. The sum of these two contributions gives the total free enthalpy  $G_s$  (or  $G$ ) as function of the pH.

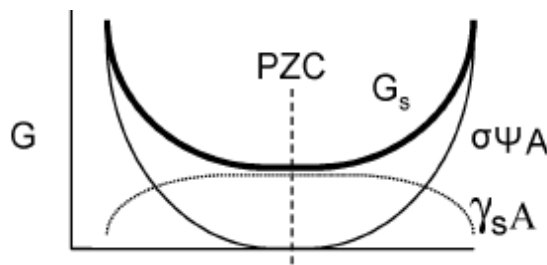


**Figure 2.21. Plot of free energy versus pH for both the electrostatic energy component and the surface tension component [Finnegan et al., 2007]**

Shapes of the  $G_s$  vs pH curves of anatase and rutile are similar. Since the PZC of anatase is 6.3 and that of rutile 5.9, the  $G$  curve of anatase shifts of 0.4. Moreover, since the  $G_b$  of rutile is lower than  $G_b$  of anatase, the  $G$  of rutile at its PZC is lower than that of anatase at its PZC by an amount of  $\sim 6 \text{ kJ.mol}^{-1}$ . Figure 2.2.2 displays the  $G$  curves of anatase and rutile as function of pH:

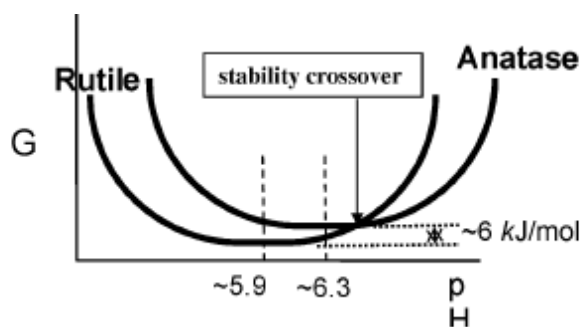


**Figure 2.22.  $G$  curves of anatase and rutile as function of pH [Finnegan et al., 2007]**

So at low pH free enthalpy of rutile is lower than that of anatase, so rutile precipitates and vice-versa. So, thermodynamically speaking, at the nanoscale we rather expect rutile particles in acidic conditions and anatase particles in basic conditions.

Not only thermodynamic but also kinetic plays a role in the crystallization of rutile or anatase. If the temperature is low, even at low pH, formation of rutile does not occur. Temperature of 250 °C is high enough for a significant dissolution-recrystallization of the amorphous precipitate in anatase or rutile, depending on pH.

In Finnegan experience pH is 1 and hydrothermal transformation 53 hours long, so samples issued from this experience are completely rutile. Since pH of our crystallization was 2 and crystallization time just 18 hours, we have obtained for the sample SN-2-250 a mixture of 47% of rutile and 53% of anatase, using the equation of Zhang [Zhang et al., 2000].

At high pH free enthalpy of anatase is lower than that of rutile, so only anatase phase is formed (sample SN-10-250).

Shape of particles also depends on crystallization pH. As Cho reports, alkaline conditions lead to elongated and almost flat nanocrystals [Cho et al., 2005]. Not only TEM but also nitrogen isotherm of SN-10-250 sample agrees with these data in the literature. Starting from Lazzeri and Banfield kinetic growth models [Lazzeri et al., 2001], [Penn and Banfield, 1999], Cho hypothesizes four growth steps:

1. precipitation of equidimensional anatase nuclei;
2. orientation attachment between (0 0 1) surfaces;
3. {1 0 1} surface flattening by dissolution-precipitation;
4. a bipyramidal nanocrystals with faceted {1 0 1} surfaces.

Since we did not investigate kinetics of nanocrystals growth, we cannot state our materials follow the same evolution of Cho's work. However both our and Cho's final morphologies are very similar. So we can suppose that maybe the same phenomenon could occur. Figure 1.22 shows HRTEM of Cho's material (at the left) and our sample. Shape of final anatase nanocrystals are very similar and supports our hypothesis that both our and Cho's material follow the same crystallization mechanism.

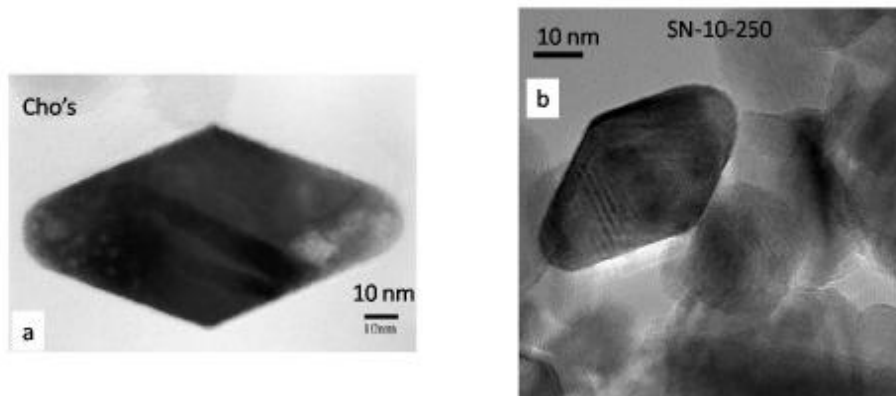


**Figure 2.23 HRTEM of a) Cho's material and b) SN-10-250**

In conclusion, pH and temperature play a crucial role in the evolution of particles, defining the size and the shape of the final products. As in previous works [Penn and Banfield, 1999], [Cho et al., 2005], not only Ostwald ripening, but also a second coarsening mechanism occurs and influence shape of nanoparticles.

We have also checked the effect of an intermediate aging treatment after precipitation and before crystallization. This aging treatment has been carried out at alkaline pH (10) and 80 °C for 30 h. Features of SY-10-150 are similar to those of SN-2-150 and SN-10-150, so we can affirm that aging treatment has no influence on the crystalline nature of the final product. Regardless to SN-2-250, SY-10-250 is anatase, and rutile does not appear, due to crystallization pH. SN-10-250 and SY-10-250, instead, are different in particles size and surface area. Although our characterizations do not lead to definitive conclusions, we hypothesize that aging treatment increases number of anatase germs and decreases the reactivity of the solid for the further steps. So SY-10 is more crystallized and less soluble than SN-2. This difference in the precursors induces differences of the final products: growth of anatase is slower in the SY-10-250 than in SN-2-250.

Literature reports several works on the effects of the aging treatment. Table 2.6 sums up main results of six works on synthesis of titania nanoparticles. Pottier et al. [Pottier et al., 2003] report that size slightly increases with aging time when pH of the precipitate is higher than 5; samples are never fully anatase, but brookite is always synthesized, even in small amounts. pH and aging time, instead, are strongly linked in Cassaignon's work [Cassaignon et al., 2007]. Low pH and short aging time lead to anatase synthesis with small percentage of brookite; low pH and long aging time lead to rutile. Stronger acidity medium allows formation of brookite and limits the influence of the aging time on the phase. Cassaignon et al. study points out that brookite is more stable than anatase: the process of dissolution-crystallization on long aging time occurs for anatase but not for brookite. Nevertheless any synthesis condition leads to a mixture of anatase with other titania forms, like brookite or rutile. Except for not yet crystallized samples (SN2 and SY-10), instead, characterizations

show our materials are almost pure anatase <sup>30</sup>. We have obtained a mixture just in one case (SN-2-250).

Addamo et al. [Addamo et al., 2005] synthesized titania nanoparticles by adding  $\text{TiCl}_4$  to distilled water. After boiling, authors purified products by dialysis process; pH of the final product was 5. This elaboration method gives pure anatase material, although size of crystallite is slightly higher than that of Pottier and Cassaignon: 12 nm for Addamo, 5-9 for Pottier and Cassaignon. Addamo et al. obtained only anatase made samples, particles of which have a size similar to our smallest samples.

Except for Cho's work, in all these study materials are crystallized by the aging treatment.

In our work first we use precipitation of  $\text{TiCl}_4$  and NaOH to have a precursor, after we crystallize under hydrothermal conditions. Crystallizing a precursor in hydrothermal conditions is a less time consuming method regarding to aging regarding to aging under  $100^\circ\text{C}$  at atmospheric pressure treatment of a product issued from hydrolysis process. Moreover it allows to separate precipitation and crystallization processes.

---

<sup>30</sup> Since XRDs are noisy maybe a not-visible secondary phase is present.

Article	Elaboration method	Composition	Crystallite size (nm)
Matthews1976 [Matthews, 1976]	Precipitation of TiCl <sub>4</sub> and NaOH at different pH followed by hydrothermal crystallization	0 < pH < 2.8 rutile 2.8 < pH < 8.8 anatase	-
Cheng1995 [Chang et al., 1995]	Hydrolysis of TiCl <sub>4</sub> followed by hydrothermal crystallization	Anatase at pH >7 200 °C, 2h	10
Pottier2003 [Pottier et al., 2003]	Hydrolysis TiCl <sub>4</sub> in HCl 2 ≤ pH ≤ 6 Aging at 60 °C	80% A, 20% R	5-9
Addamo2005 [Addamo et al., 2005]	Hydrolysis TiCl <sub>4</sub> in water (1:50 vol.) boiling 2h dialysis Final pH 5	100 % A	12
Cho2005 [Cho et al., 2005]	Mixing TiCl <sub>4</sub> with NaOH Hydrothermal crystallization in pH 9.5, 250 °C for 4h	100% A	9
Cassaignon2007 [Cassaignon et al., 2007]	Hydrolysis TiCl <sub>4</sub> in HNO <sub>3</sub> 0.5 ≤ [HNO <sub>3</sub> ] ≤ 2 mol.h <sup>-1</sup> aging at 95 °C for 24h	72 % A, 22 % R, 6 % B	5

**Table 2.6 Studies on synthesis of anatase nanoparticles.\*calculated by Scherrer formula on (101) plain**

## 2.2 1 D structures

### 2.2.1 Elaboration and samples

#### 2.2.1.1 Synthesis

Figure 2.24 summarizes the synthesis process of TiO<sub>2</sub> 1 D structures. A commercial, fine TiO<sub>2</sub> powder (anatase, AlfaAesar 036199, 99.9% purity) was used as a starting material. A total of 8 g of TiO<sub>2</sub> powder and 100 mL of 10M NaOH aqueous solution are put in the autoclave shown in Figure 1.3. The autoclave is stirred and heated at 150 °C for 72 h. After cooling down to room temperature, precipitate is washed three times by distilled water. The pH of the suspension is lowered to 2 using a solution 2 M of HCl. After 4 h stirring, the solution is centrifuged and washed three times with distilled water. The HCl treatment followed by distilled water treatment is repeated three times. At the end of this stage hydrogen titanate is obtained [Yoshida et al., 2005].

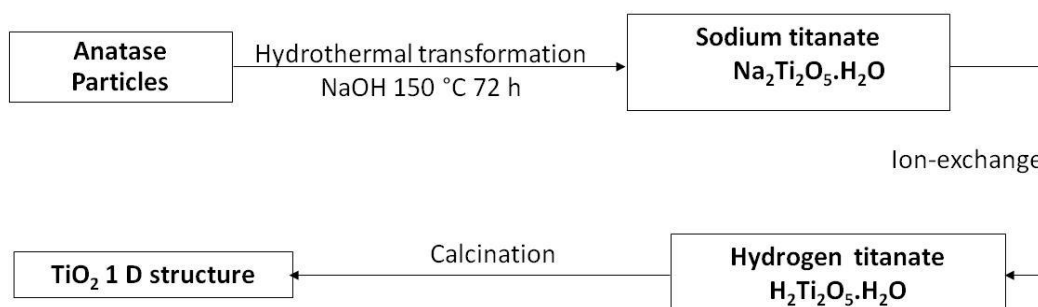


Figure 2.24 Pattern of 1 D structures synthesis process

#### 2.2.1.2 Samples

Once dried in air or by freeze-drying, hydrogen titanate has been calcined at three temperatures: 400, 500 and 600 °C. For all samples plateau time was 2 h and heating ramp was 2 °C/min. Final morphology of product strongly depends on speed of the heating ramp: a slow treatment preserves the shape, while a fast one changes it. Since nanotubes easily break into nanoparticles and testing tubular structure is the objective of this work, we have preferred a slow treatment to a fast one.

Three samples have been elaborated (Table 2.7):

Name	Calcination temperature (°C)
UNT	-
UNT300	300
UNT400	400
UNT500	500

Table 2.7 Undoped nanotubes

## 2.2.2 Characterizations

### 2.2.2.1 X-Rays Diffraction

XRD shows that the structure of not calcined nanotubes is similar to that expected for a layered titanate of nominal  $H_2Ti_xO_{2x+1}$ . Most probably an analogue  $H_2Ti_2O_5 \cdot H_2O$  (ICSD 00-044-0131) is the phase of the sample.

XRD of UNT300, UNT400 and UNT500 show a peak at  $29,033^\circ$ . This peak can be attributed both to  $TiO_2$ -B (110) and anatase (101), because of the same reticular distance of  $3.5 \text{ \AA}$ .

In the case of UNT300 we can attribute this peak to  $TiO_2$ -B (110), since its XRD spectrum agrees with what reported in the literature [Jitputti et al., 2008]. Moreover,  $300^\circ\text{C}$  is too low temperature to have anatase.

In the case of UNT400 and UNT500 we hypothesize we have a mixture of anatase and  $TiO_2$ -B, but XRD is not the suitable technique to estimate the ratio of these two phases. As we will see in the next chapter, Raman Spectroscopy can be used to calculate it. However XRD can indicate if sample is a composite anatase  $TiO_2$ -B (UNT400, Figure 2.26) or anatase is the major phase (UNT500, Figure 2.27).

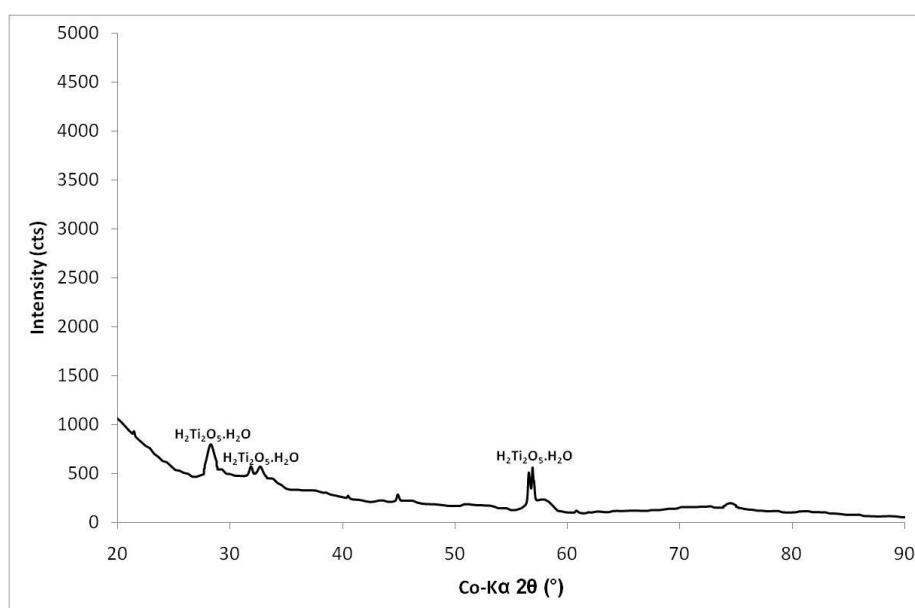
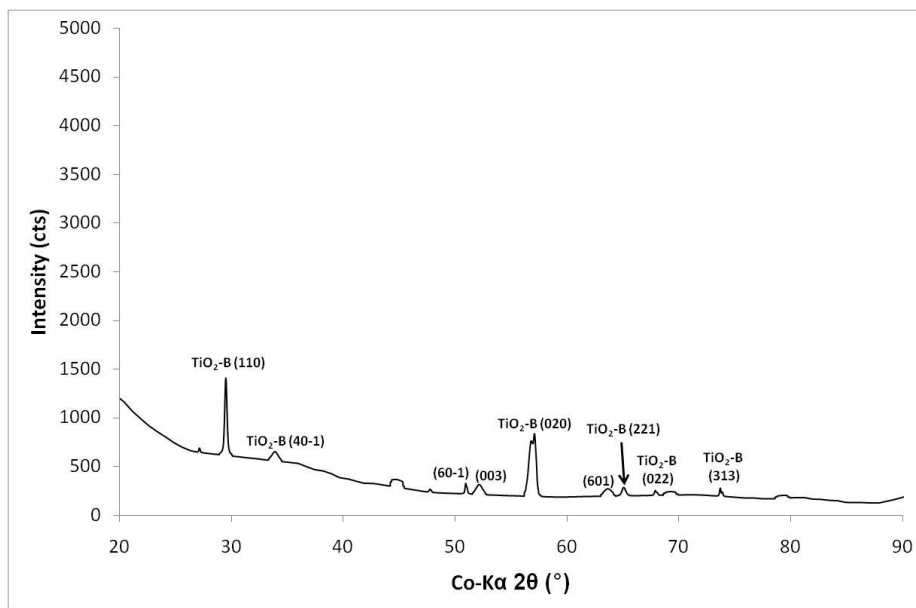
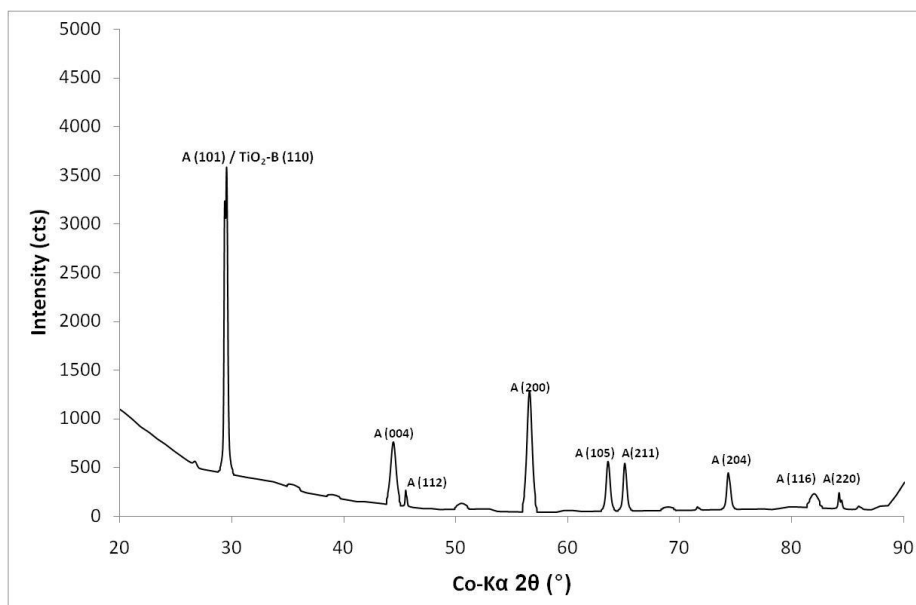


Figure 2.25 X-ray diffraction of undoped not calcined nanotubes



**Figure 2.26 X-ray diffraction of undoped nanotubes calcined at 300 °C**



**Figure 2.27 X-ray diffraction of undoped nanotubes calcined at 400 °C**

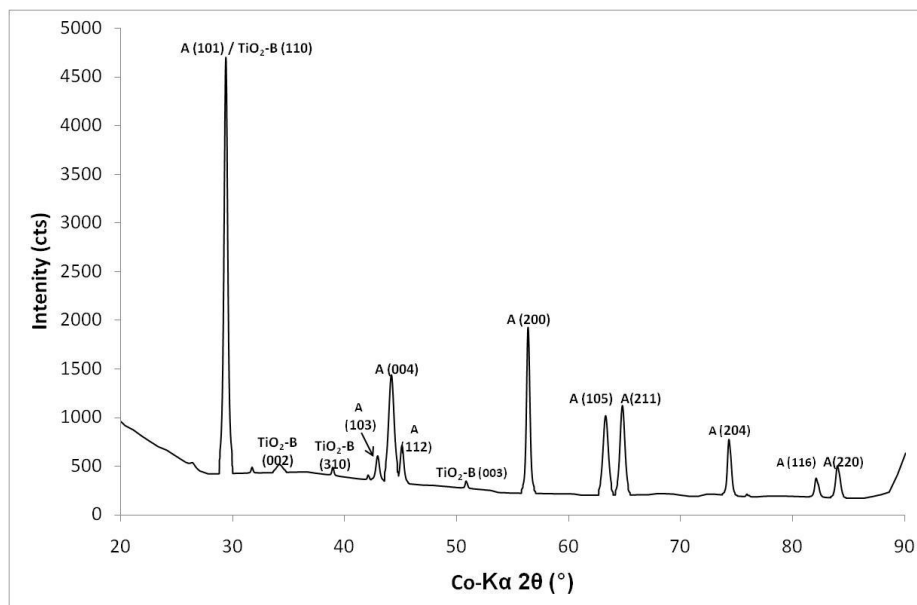


**Figure 2.28 X-ray diffraction of undoped nanotubes calcined at 500 °C**

### 2.2.2.2 Transmission Electron Microscopy

Figure 2.29-2.36 show the results of the Transmission Electron Microscopy.

1D morphology is completely kept for UNT300, since TEM does not identify any particles. Fractures of the tube start to appear when calcinations temperature is 400 °C. At this temperature little degradation of nanotubes in nanoparticles occurs (Figure 2.29). Much more nanotubes break into particles for the UNT500 sample. These particles form agglomerates, as Figure 1.33-1.34 show. These figures also show that nanoparticles stay on the surface.

TEM provides informations not only on morphology but also on porosity. Figure 2.29-a shows our materials are hollow while Figure 2.30 that they also are porous, in perfect agreement with nitrogen physical sorption results.

In addition TEM allows to deeply study the texture evolution of samples. For UNT300 we observe material is formed by TiO<sub>2</sub>-B and no anatase appears. The interreticular distances 2.3 Å corresponds to TiO<sub>2</sub>-B (202), 3.5 Å to TiO<sub>2</sub>-B (110), 1.9 Å to TiO<sub>2</sub>-B (40-3), 2.9 Å to TiO<sub>2</sub>-B (400) (Figure 1.28).

UNT400 is more crystallized in anatase than UNT300, as shown in Figure 2.31. However traces of TiO<sub>2</sub>-B still remain. Zone axis investigations on anatase (111) and TiO<sub>2</sub>-B (001) prove that anatase is associated to slightly elongated nanoparticles morphology, while TiO<sub>2</sub>-B to nanotubular. TEM investigation reveals that UNT400 has more anatase than TiO<sub>2</sub>-B. This analysis agree with XRD data: XRD peaks of anatase of UNT400 are much stronger than peaks of TiO<sub>2</sub>-B.

Not only is UNT500 the most destroyed sample, but it is also the best crystallized in anatase, as both TEM and XRD results prove (Figure 2.27 and Figure 2.35). Nevertheless, traces of  $\text{TiO}_2\text{-B}$  still are on the UNT500 sample (Figure 2.36).

The most significant conclusions of this TEM analysis is that the phase  $\text{TiO}_2\text{-B}$  is associated to a tubular structure and anatase to particles. So we can affirm that UNT400 and UNT500 are mixtures of  $\text{TiO}_2\text{-B}$  nanotubes and anatase nanoparticles.

TEM proves that at high calcination temperature (500 °C), we have almost totally destroyed the 1 D structure and we have obtained agglomerates of anatase nanoparticles. Size of particles of this sample is 13x22 nm (Figure 1.35).

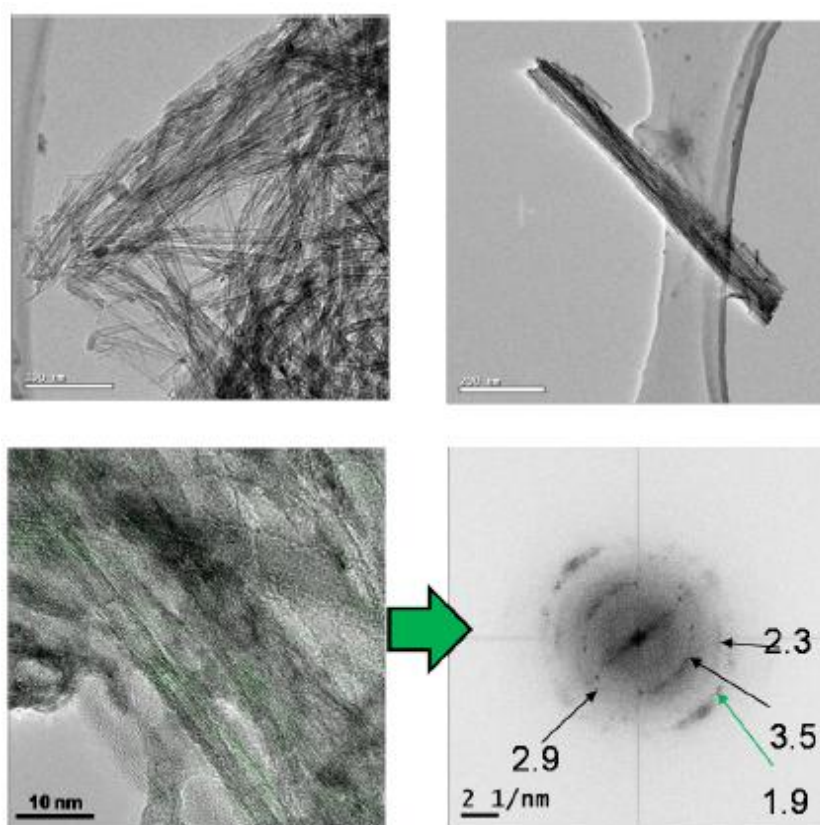


**Figure 2.29 TEM of UNT300. The contrast reveals nanotubes are hollow. Interreticular distances of green zones have been processed by Fourier Function Transformed**

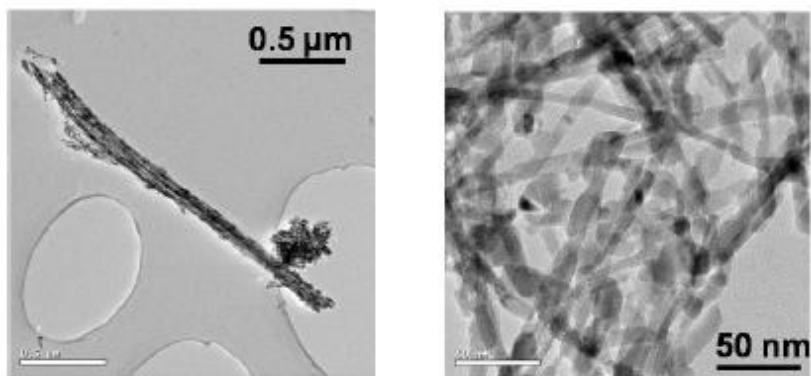


**Figure 2.30 TEM of UNT400. Micro-fractures are visible on the right figure**

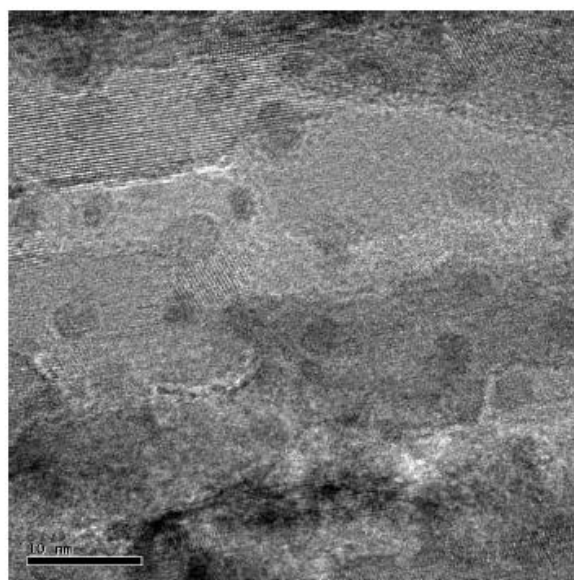


**Figure 2.31 TEM of UNT400. Pores are visible**

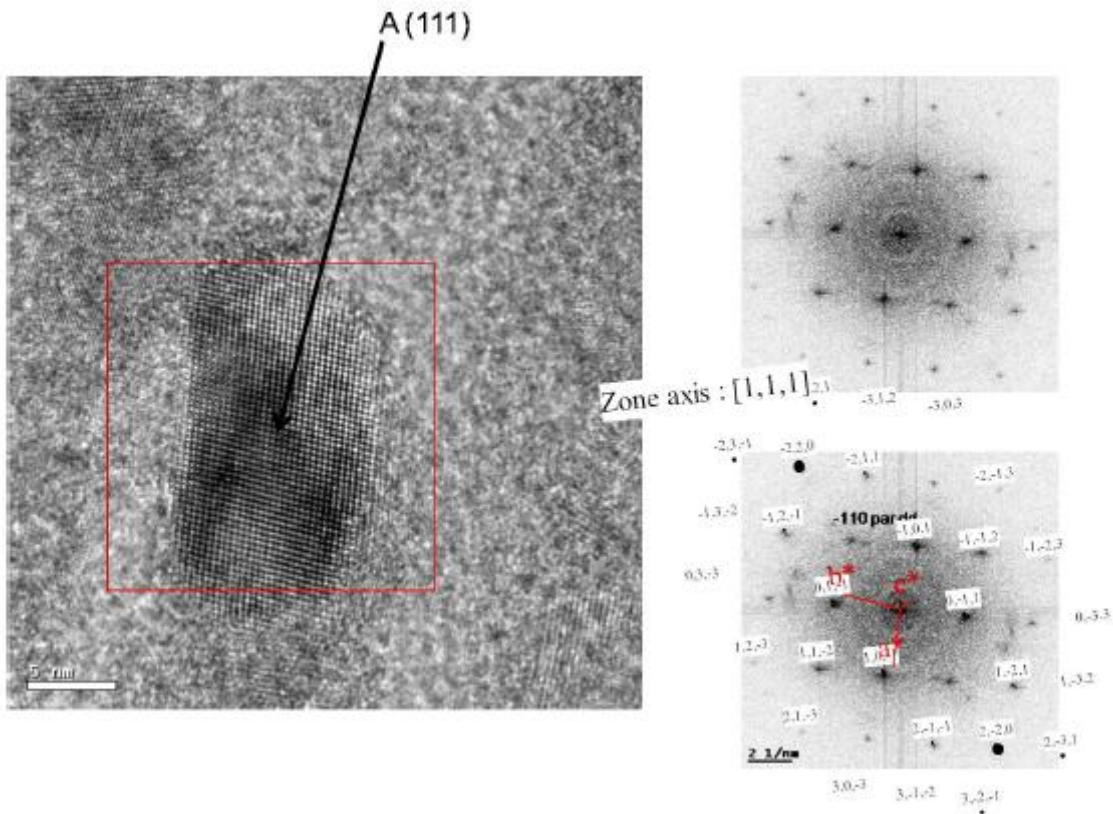


Figure 2.32 TEM of UNT400. Analysis of axis zone of Anatase (111)

Fig

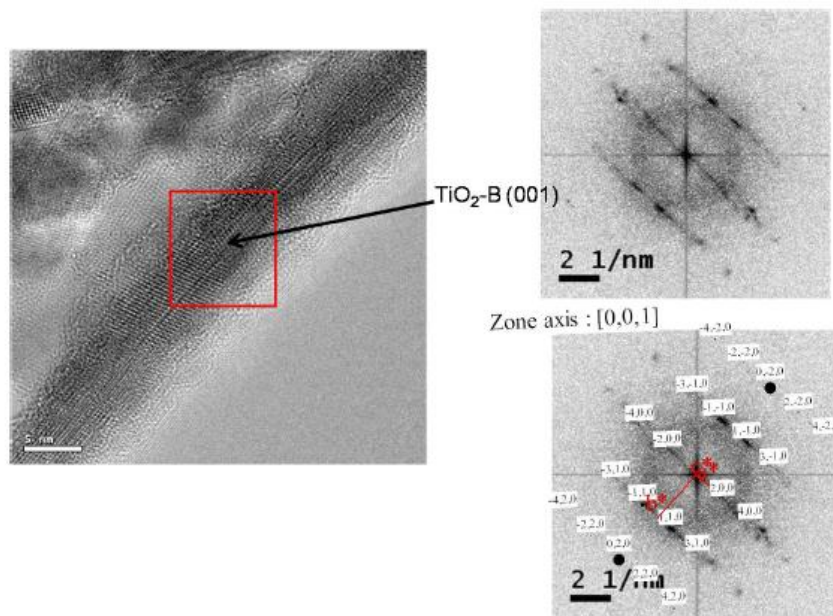
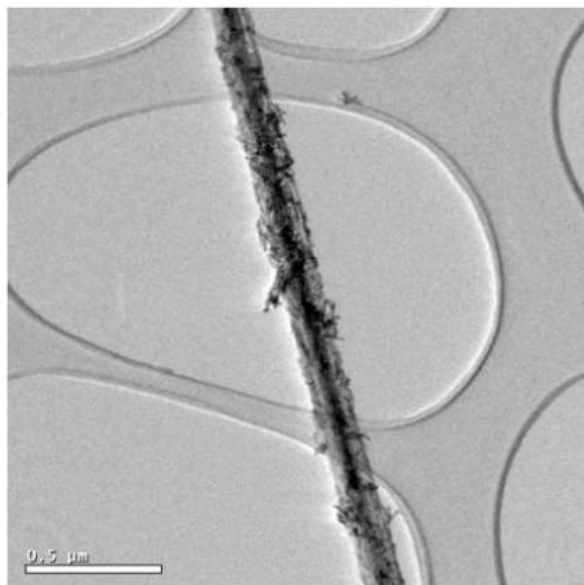
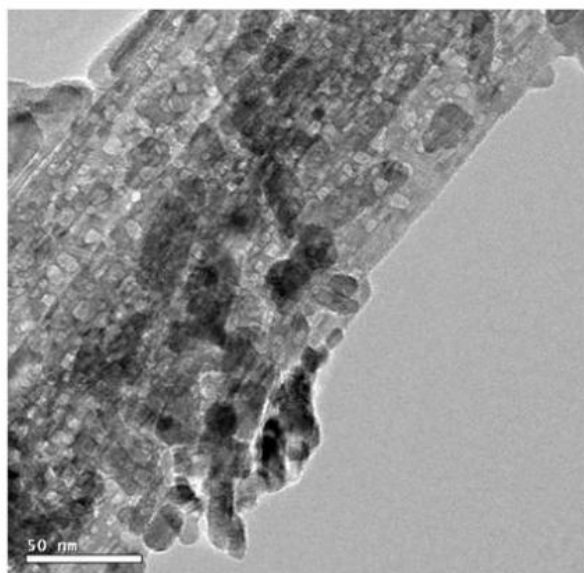


Figure 2.33 TEM of UNT400. Analysis of axis zone of  $\text{TiO}_2\text{-B}$  (001)



**Figure 2.34 TEM of UNT500**



**Figure 2.35 TEM of UNT500. Breaking of nanotubes in nanoparticles**

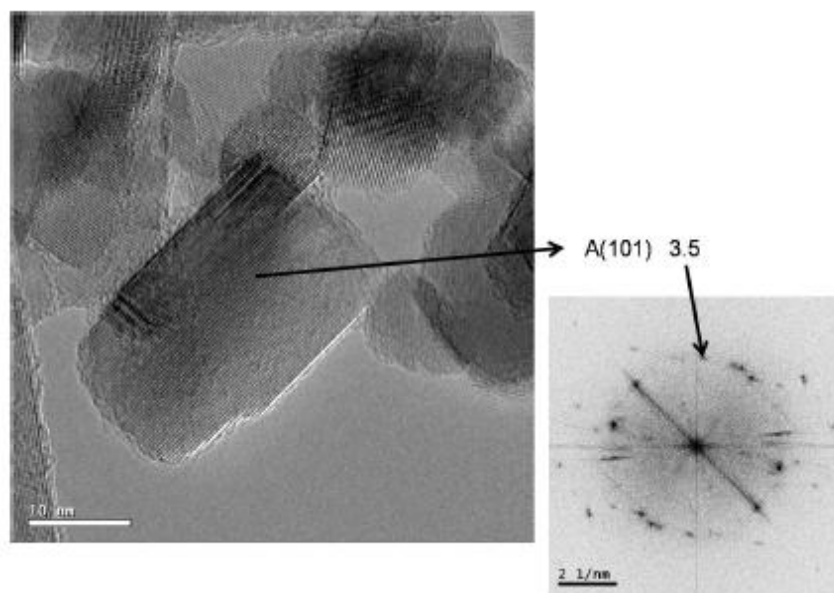


**Figure 2.36 TEM of UNT500. Analysis of axis zone of Anatase (101)**

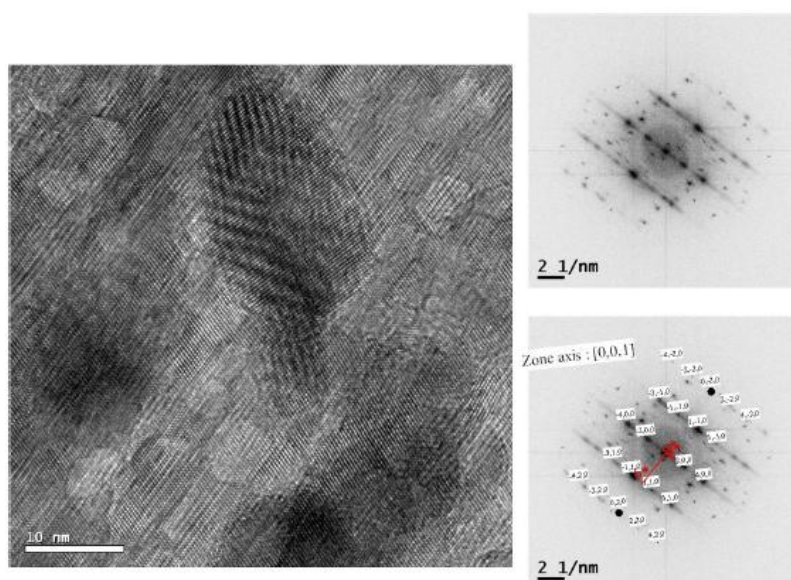


**Figure 2.37 TEM of UNT500. Analysis of axis zone of TiO<sub>2</sub>-B (001)**

### 2.2.2.3 Nitrogen adsorption/desorption

Table 2.8 sums up results (surface area, porous volume and average pore diameter) of nitrogen adsorption/desorption isotherms treated by BET model. Figure 2.38 shows the isotherms of samples. Surface area of UNT is  $292 \text{ m}^2.\text{g}^{-1}$ . It slightly decreases for UNT300:  $246 \text{ m}^2.\text{g}^{-1}$ . Surface area drops of half for UNT400 sample to ( $117 \text{ m}^2.\text{g}^{-1}$ ), while slight decreases for 400 and 500 °C. Our data agree with literature: in Kuo et al. [Kuo et al., 2007] experience nanotubes calcined at 300 °C have a surface area of  $240 \text{ m}^2.\text{g}^{-1}$  and those calcined at 400 °C have a surface area of  $132 \text{ m}^2.\text{g}^{-1}$ .

Name	$S_{\text{BET}}$ ( $\text{m}^2\text{g}^{-1}$ )	$V_{\text{P}}$ ( $\text{cm}^3\text{g}^{-1}$ )	$\delta_1$ (nm)	$\delta_2$ (nm)
UNT	292	0.65	3	-
UNT300	246	0.71	3	-
UNT400	117	0.52	3	22
UNT500	90	0.42	3	46

Table 2.8 Summarize of  $\text{N}_2$  physisorption characterizations

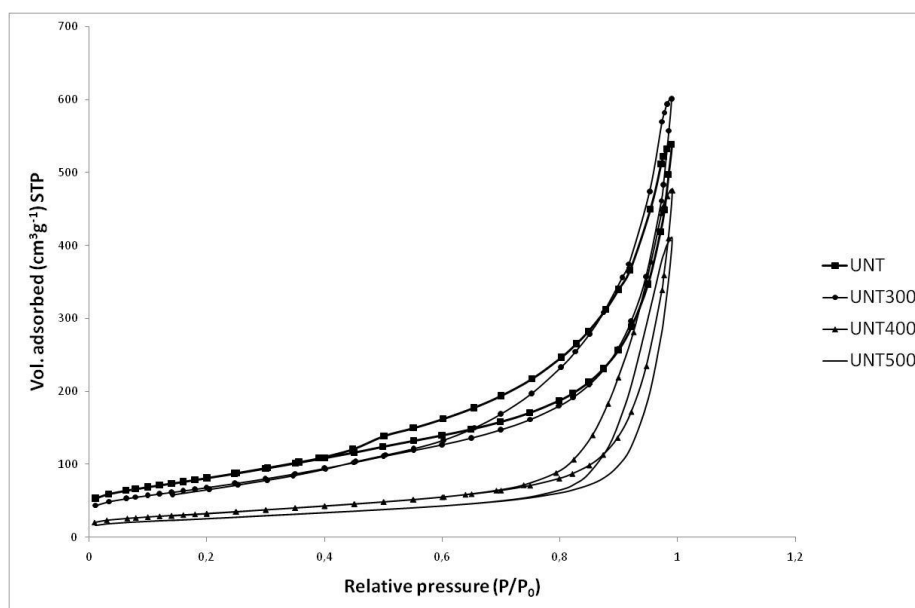
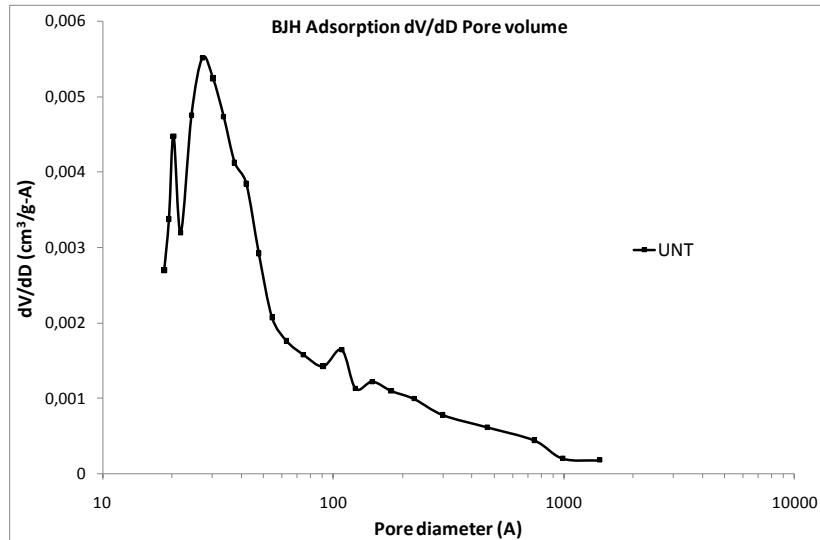


Figure 2.38  $\text{N}_2$  physisorption isotherms of nanotubes

Nitrogen physisorption also gives the distribution of pores size using BJH model (cf. Chapter 2). Figure 2.39 and Figure 2.40 show that the pore volume distribution of UNT and UNT300 exhibits one peak centered at 3 nm. UNT and UNT300 have high surface area and pore volume and, as TEM shows, a tubular morphology. These observations can allow to state that the peak centered at 3 nm corresponds to inner tube porosity.

Profiles of UNT400 and UNT500 (Figure 2.41 and Figure 2.42), instead, are different from profiles of pore distributions of UNT and UNT300 (Figure 2.39 and Figure 2.40).



**Figure 2.39 Pore size distribution of UNT**

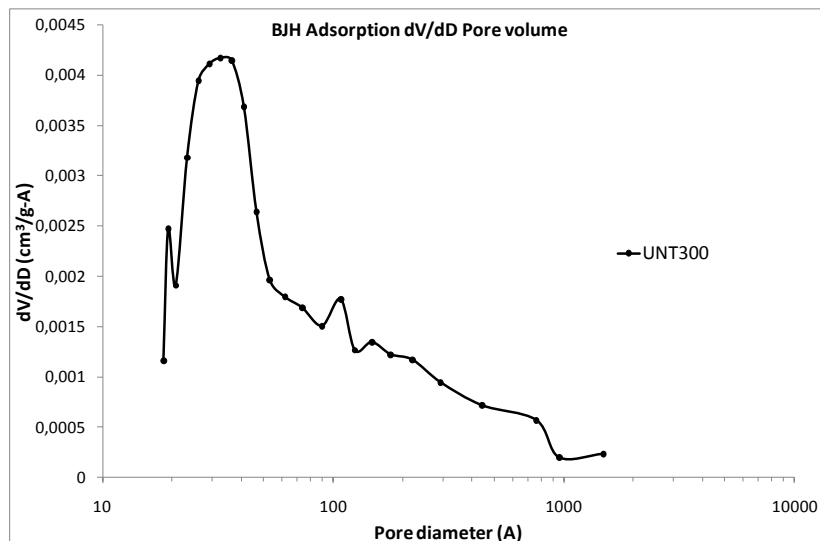


**Figure 2.40 Pore size distribution of UNT300**

BJH curve of UNT400 presents two peaks, one at 3 nm and the other one at 22 nm. BJH curve of UNT500 has one peak at 3 nm and another at 46 nm. The first peak at 3 nm still corresponds to the inner porosity of tubes; the second one is linked to an outer porosity. Since the second pore size population appears when tubes break into particles, this outer porosity is the porosity of the anatase nanoparticles packing [Beuvier, 2009].

BJH results show that tubular morphology has been kept for UNT and UNT300, while UNT400 and UNT500 are a mixture of 1D and 3D structures.

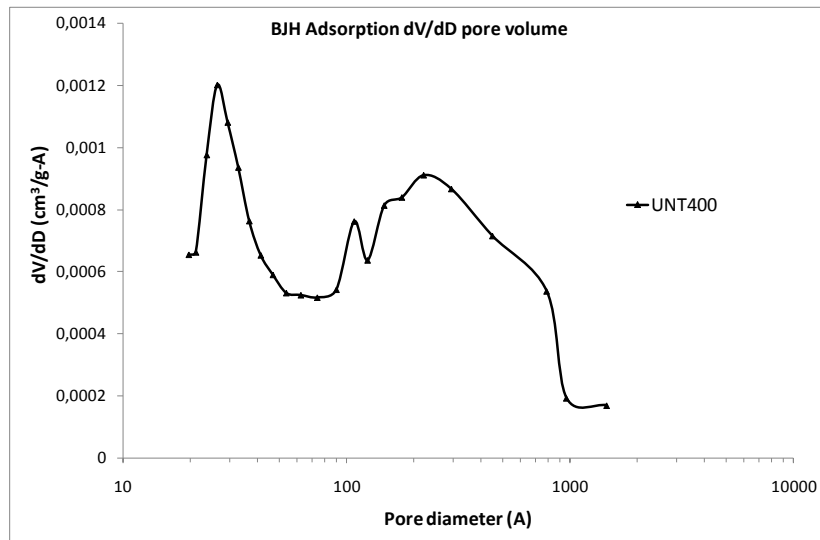


**Figure 2.41 Pore size distribution of UNT400**

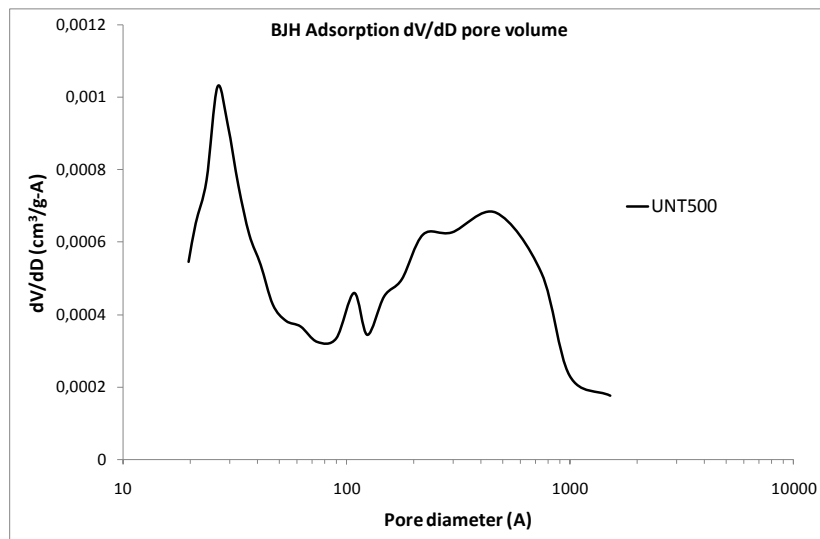


**Figure 2.42 Pore size distribution of UNT500**

We could use geometric formula (eq.2.7) to calculate diameter of the nanocylinder [Rouquerol et al.]:

$$D = 4/S_{BET} \cdot \rho_S \quad (\text{eq.2.7})$$

However, only UNT and UNT300 are nanotubes, UNT400 and UNT500 are mixture of tubes and particles, so we cannot use the formula. Diameter of UNT and UNT300 is 4 nm, in good agreement with the TEM results.

### 2.2.3 Discussion

- **Structural characterizations**

Table 2.9 sums up characterizations results of the four samples.

Name	XRD (Phase)	TEM [l(nm) x $\varphi$ (nm)] $\pm$ 0.5 *	S <sub>BET</sub> (m <sup>2</sup> .g <sup>-1</sup> )	D (nm)
UNT	H <sub>2</sub> Ti <sub>2</sub> O <sub>5</sub> .H <sub>2</sub> O		292	4
UNT300	TiO <sub>2</sub> -B	40 x 9	246	4
UNT400	Anatase and TiO <sub>2</sub> -B	115 x 9	117	9
UNT500	Anatase		90	11

**Table 2.9 Undoped nanotubes. \*l is the length measured with the photo-evaluation of TEM images,  $\varphi$  is the diameter**

We have obtained titanate for UNT, TiO<sub>2</sub>-B for UNT300, mixture of TiO<sub>2</sub>-B and anatase for UNT400, anatase for UNT500. Increasing the calcination temperature decreases the specific surface area, with a sharp variation at TiO<sub>2</sub>(B)-anatase transition.

Nanotubes form aggregates and measuring diameter and length from TEM observations is not always possible. This is the reason why we were able to estimate the size of the nanotubes only for UNT300 and UNT400.

- **Hydrothermal growth**

Literature [Ma et al., 2003], [Ma et al., 2004], [Li et al., 2007] reports that structure of titanium 1D materials is lepidocrocite type. Mechanism leading to nanotubular morphology from spherical nanoparticles is still under discussion [Bavykin et al., 2006], [Beuvier, 2009]. However all scientists agree that titania 1D structures are always multi walls, and no author reports synthesis of single wall by hydrothermal transformation [Bavykin et al., 2006].

The aim of our work was not the investigation of the formation mechanism of nanotubes. Nevertheless, if we compare our product UNT300 with Li [Li et al., 2007] one using TEM analysis, we see that both materials have boundaries darker than the body, sign that both materials are multi-walls products:

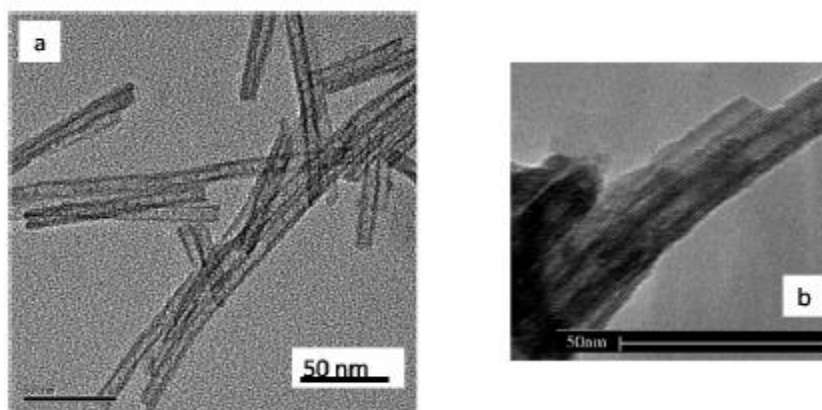


Figure 2.43 TEM of nanotubular morphologies: a) UNT300 b) Li's product

- Morphology and phase evolution with calcination temperature

Both TEM and BJH characterizations prove that UNT and UNT300 have a tubular structure, while UNT400 and UNT500 are mixtures of tubular and particles morphologies. Higher calcination temperatures allow both formation of anatase and destruction of tubular structure. An increase of the calcinations temperature also leads to a decrease of the surface area.

XRD nor TEM cannot be used to estimate the ratio  $\text{TiO}_2\text{-B}$  on anatase. XRD peaks of  $\text{TiO}_2\text{-B}(110)$  and anatase(101) are at the same angle and since the peak of anatase is the main peak it is hard to calculate the ratio  $\text{TiO}_2\text{-B}/\text{anatase}$ . Raman spectroscopy is the most suitable technique to calculate the amount of  $\text{TiO}_2\text{-B}$  and anatase in a sample [Beuvier, 2009].

Our TEM observations show that no anatase nanotubes have been synthesized and that anatase phase is in the shape of nanoparticles. Phase of nanotubes is always  $\text{TiO}_2\text{-B}$ .

Shape and phase of 1 D structure at different calcinations temperatures depends on several synthesis parameters, like, for example, time, temperature and stirring of hydrothermal transformation, concentration of NaOH solution, ratio of the solution volume by the total volume of the autoclave, type and concentration of the starting material [Beuvier, 1999] [Bavykin et al., 2006].

Our experimental protocol is very similar to that of Sreethawong et al. published in 2008 [Sreethawong et al., 2007]. Two are the differences: the concentration and type of starting material. We have used a concentration of 8 g of anatase nanoparticles by 100 ml of NaOH. Yoshikazu Suzuki, instead, has used and 0.5 g of Degussa P25 by 50 ml of NaOH solution. These apparently little differences have great impact on the photocatalysts after calcinations. After calcinations at 600 °C Sreethawong obtained anatase nanotubes: 1 D morphology in the anatase phase. Maybe in his experiment the rutile of Degussa P25 stabilizes the elongated shape and allows the transformation of  $\text{TiO}_2\text{-B}$  in anatase without destroying the morphology.

Our experimental protocol is similar to Kuo's work too [Kuo et al., 2007]. In this study the concentration of precursor is lower than in our study and the temperature of hydrothermal transformation as well. Interestingly, we have obtained similar results.

## 2.3 Aerogels and xerogels

### 2.3.1 Elaboration and samples

According to literature (as summarized in the previous bibliography chapter), the elaboration process of crystallized TiO<sub>2</sub> aerogels and xerogels we have followed is classically composed of the four standard steps:

- sol-gel synthesis,
- aging and washing of the gel,
- drying,
- calcination.

Here-below, each elaboration step is briefly described.

#### 2.3.1.1 Sol-gel synthesis

Gels have been synthesized at room temperature in isopropanol (CH<sub>3</sub>CH(OH)CH<sub>3</sub> noted iPrOH) by acid-catalysed sol-gel method. The sols were prepared, slowly<sup>31</sup> adding an aqueous solution of nitric acid (HNO<sub>3</sub>), partially diluted in iPrOH, to an alcoholic solution of titanium tert-butoxyde (Ti(OtBu)<sub>4</sub> (purity ≥ 97.0wt%), under continuous mechanical stirring<sup>32</sup>. The catalyst HNO<sub>3</sub> (2M) and the Ti(IV) precursor have been respectively purchased from Riedel-de Haën (product reference 35278) and Fluka (product reference 86910). For *clean* hydrolysis purpose, deionized water was used in the recipe. The molar ratio we used was selected from Boujday *et al.* [Boujday et al., 2004] and is detailed here-after. Except the specific nature of the Ti(IV) precursor, the sol-gel system we worked with is similar to the one of Boujday *et al.* [Boujday, 2004].



(which corresponds, for a sol of 100 ml, to respective volumes of  
19.15, 77.60, 2.31 and 0.94 ml)

Two solutions have been prepared: one with 75% of the total iPrOH volume plus water and catalyst (solution A), one with the complementary iPrOH volume (*i.e.* 25% vol.) and the precursor (solution B). The two solutions are previously stirred with a magnetic bar for 15 minutes. Later solution A is added to solution B, always under gentle stirring. Stirring is stopped when the adding step is finished.

After 30 minutes the solution is gelled<sup>34</sup>. The gels are monolithic and transparent as shown in Figure 2.44.

---

<sup>31</sup> Typically some minutes (< 5 min) for some 100 cm<sup>3</sup>-sols.

<sup>32</sup> Stirring is mechanically performed with a magnetic bar at 210 rpm.

<sup>33</sup> Which is slightly above the stoichiometric ratio.

<sup>34</sup> Gelation time is not precisely characterized (for example, with rheology methods) but is simply evaluated when gels are considered to no longer flow during handling.



**Figure 2.44** Example of a TiO<sub>2</sub> gel synthesized according to our sol-gel route

As already described in the chapter dedicated to the state-of-the-art, the sol-gel process is composed of two sets of *simultaneous* reactions: hydrolysis and polycondensation.

### ***Hydrolysis***

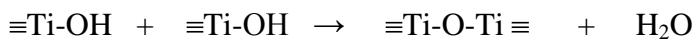


Theoretically, various states of hydrolysis are possible towards orthotitanic acid Ti(OH)<sub>4</sub>.

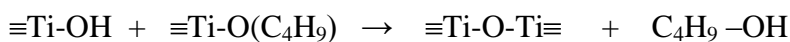


### ***Polycondensation***

Condensation of water :



Condensation of propanol :



#### **2.3.1.2 Aging and washing**

After the sol-gel transition, TiO<sub>2</sub> gels are covered with iPrOH to avoid drying by evaporation. Immersed in iPrOH, they are aged at room temperature for 4 days to complete the syneresis. At this stage, the initial volume of the gel (~ 50 cm<sup>3</sup>) decreases towards an asymptotic value

of  $\sim 46 \text{ cm}^3$ . This shrinkage ( $\sim 8 \text{ vol. } \%$ ) permits to gently cast the gels from their moulds for further elaboration steps.

Then, the gels are washed with iPrOH, still at room temperature. This washing step is governed by molecular diffusion<sup>35</sup>. It is performed to obtain a rather *pure* iPrOH phase in the porosity of the gels before drying. Indeed, it is important to avoid water being entrapped in the porosity, because it is not readily soluble in  $\text{CO}_2$ , the fluid subsequently used for supercritical drying step. Nevertheless, since water is a product of polycondensation reactions and gels are hydrophilic (because they can contain some remaining  $\equiv\text{Ti-OH}$  groups even after syneresis), some adsorbed water can still remain in the gel, even after washing.

### 2.3.1.3 Drying

Once aged and washed, the gels are dried according to two different routes. A first set of gels has been dried with supercritical  $\text{CO}_2$ , leading to aerogels, the second set via an evaporative process in room conditions (*i.e.* ambient T and P), leading to xerogels.

Supercritical drying is typically carried out in three steps, according to a previous protocol developed at the laboratory [Masmoudi, 2006]. The first step consists in replacing the iPrOH contained in the porosity of the gels by supercritical  $\text{CO}_2$  at 80 bar and  $37 \text{ }^\circ\text{C}$ . The second step is the extraction of the  $\text{CO}_2$  from the porosity through isothermal depressurization of the dryer until atmospheric pressure is reached. During the third and final step, the autoclave is finally cooled at room temperature by natural convection. Figure 2.45 shows the autoclave used for the supercritical drying process.



Figure 2.45. Photography of the autoclave used for supercritical  $\text{CO}_2$  drying

As already mentioned, during this work, some subcritical evaporative drying of  $\text{TiO}_2$  gels has been also performed at atmospheric pressure. The evaporation is simply realized leaving the

---

<sup>35</sup> Washing baths are regularly exchanged during a period of 48 hours without any external forced convection.

gel (only paying attention to free its evaporation surfaces) in the laboratory fume hood until as complete as possible evaporation of the iPrOH.

Both aerogel (Figure 2.46) and xerogel materials are cracked after drying. They finally lose the initial macroscopic monolithic character they present at the wet stage. Some authors have proposed to explain this cracking phenomenon regarding the ionic degree of the polar covalent bonds between Ti and O [Pierre and Pajonk, 2002]. Compared to the well-known  $\text{SiO}_2$  aerogels which conserve their monolithicity during supercritical drying, it can be assumed that the higher ionic character of Ti-O bond (ionic fraction of 0.7 compared to 0.54 for Si-O) is responsible for lowering the associated bonding angle flexibility ( $\equiv\text{Ti-O-Ti}\equiv$ ) and thus for the cracking of the wet  $\text{TiO}_2$  network even during supercritical drying.

Anyway, regarding the targeted photocatalytic application, this is not prejudicial. Nevertheless, it must be underlined here that each piece of dry material (aerogel and xerogel) can be considered as a macroscopic object (so-called a bulk material) compared to finely divided nanomaterials like nanoparticles and nanotubes I have elaborated (and presented in the previous sections of this chapter).



**Figure. 2.46. Example of  $\text{TiO}_2$  aerogels obtained according to our elaboration process (diameter of the grid is around 9 cm)**

#### **2.3.1.4 Calcination**

After drying and before any further treatment, all the materials are finely crushed in an agate mortar. Since after drying the samples are amorphous, a step of calcination is necessary to crystallize them. For all calcination, heating rate is  $2\text{ }^\circ\text{C}/\text{min}$  and calcination duration at the calcination temperature is 2 hours. The furnace as well as the thermal profile is shown here after (Figures 2.47 and 2.48).

To study the impact of such a thermal treatment on the materials, I have calcined aerogels in air at four different temperatures (400, 500, 600 and 700 °C). After studying cristallinity, texture and porosity of calcined aerogels, I have chosen 500 °C for the reference calcination temperature, also applied for the xerogels.

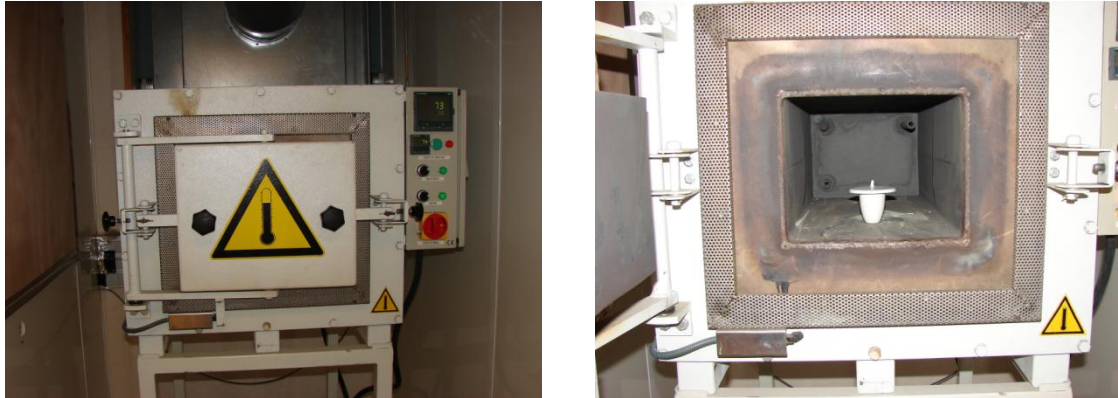


Figure 2.47. Laboratory furnace used for calcinations (left) and view of a refractory crucible (right)

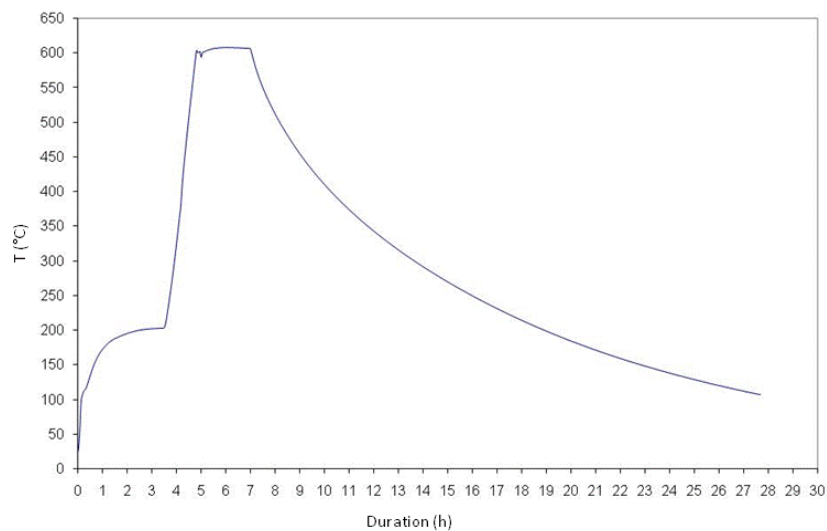
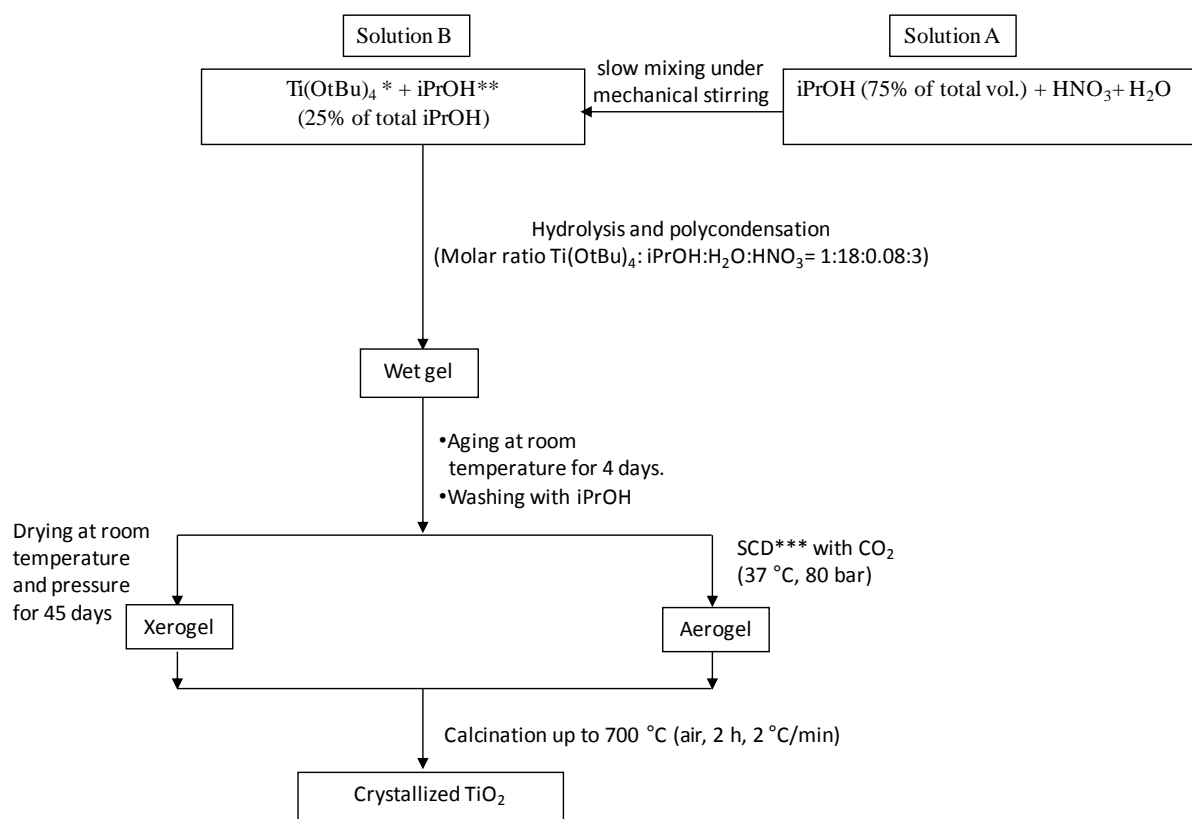


Figure 2.48 Experimental temperature profile corresponding to a calcination at 600 °C

### 2.3.1.5 Synoptic view of the elaboration process

The Figure 2.49 schematically summarizes the whole elaboration procedure described here above.



**Figure 2.49** Scheme of the elaboration process of  $\text{TiO}_2$  aerogels and xerogels  
 (\* $\text{Ti}(\text{OtBu})_4$  is titanium tert-butoxyde, \*\*iPrOH is isopropanol and \*\*\*SCD is supercritical  $\text{CO}_2$  drying)

### 2.3.1.6 Samples

Five sets of aerogels and two sets of xerogels have been characterized in details. All the gels have been synthesized according to the same sol-gel protocol presented in the previous section. The dried samples only differ in their drying route and their calcination temperature.

Reference	Drying method	Calcination temperature (°C)
AA	Supercritical $\text{CO}_2$ drying	As-prepared
A400		400
A500		500
A600		600
A700		700
AX	Evaporation in room conditions	As-prepared
X500		500

**Table 2.10** Aerogels and xerogels prepared for further characterizations and evaluation

## 2.3.2 Characterizations

### 2.3.2.1 X-Rays Diffraction

First of all, the crystallographic nature of as-prepared aerogels has been studied by High Temperature X-Rays Diffraction<sup>36</sup> (HT-XRD), in order to: i) identify the temperature of anatase-rutile transition and ii) then select the temperature of further calcinations to obtain anatase-based materials.

Figure 2.50 shows that the as-prepared TiO<sub>2</sub> aerogels (i.e. not calcined) are amorphous until 300 °C. In the specific HT-XRD conditions (defined in the corresponding annex), the anatase phase appears between 300 and 400 °C and grows up to 700 °C. Between 700 and 800 °C rutile appears. Between 800 and 900 °C anatase disappears.

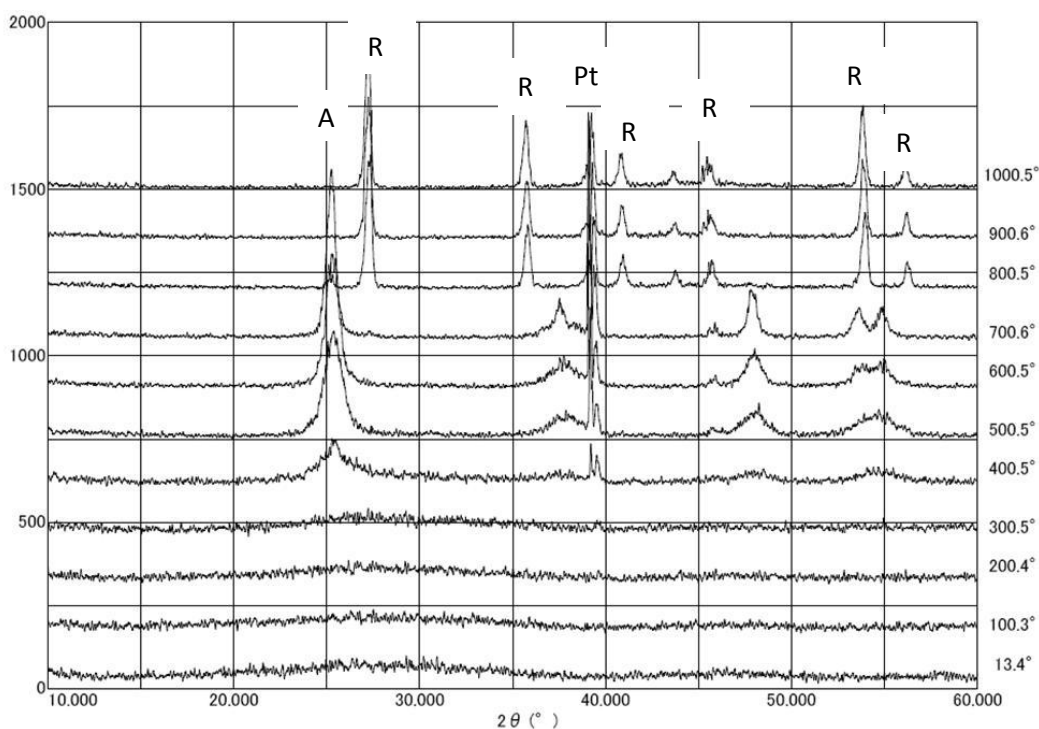


**Figure 2.50** HT-XRD patterns of as-prepared TiO<sub>2</sub> aerogels (A is anatase, R is rutile)

Based on these HT-XRD results, as-prepared aerogels have thus been calcined at 400, 500, 600 and 700 °C in our laboratory furnace and studied by room temperature X-Rays Diffraction (XRD). XRD results are illustrated in Figure 2.51. They clearly show that as-prepared materials are amorphous and that at 400 and 500 °C samples A400 and A500 are

<sup>36</sup> HT-XRD analyses of this thesis were performed by under the guidance of Assistant-Professor Yoshikazu Suzuki, at Kyoto University, on a Rigaku RINT-2500 multiuex diffractometer.

formed of anatase. They also underline that in standard calcinations conditions (defined in the corresponding annex), the phase transformation of anatase in rutile starts between 500 and 600 °C<sup>37</sup>, which is in good agreement with literature ([Malinowska et al., 2003], [Boujday et al., 2004], [Tursiloadi et al., 2006] and [Kim et al., 2007]). Finally, they show that at 700 °C, sample A700 consists only of rutile.

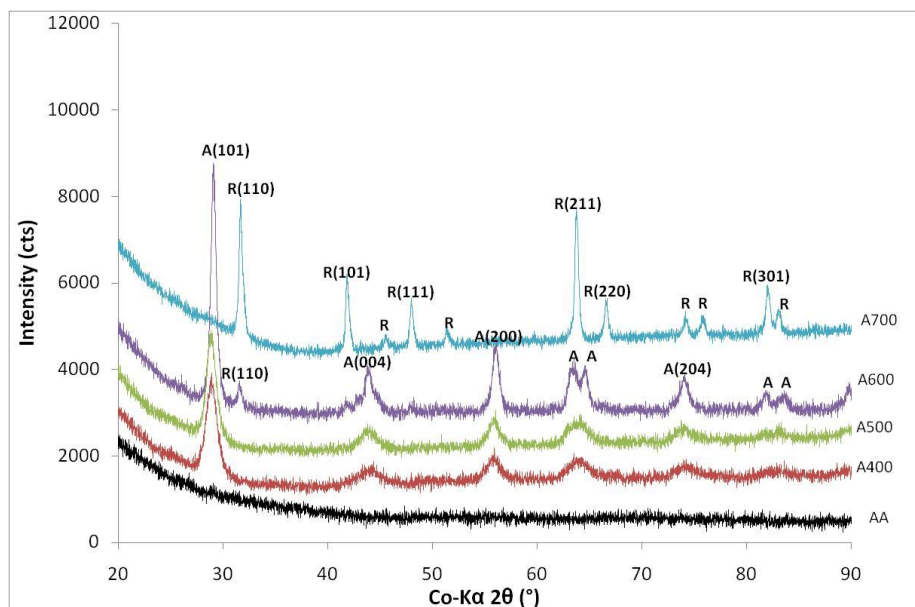
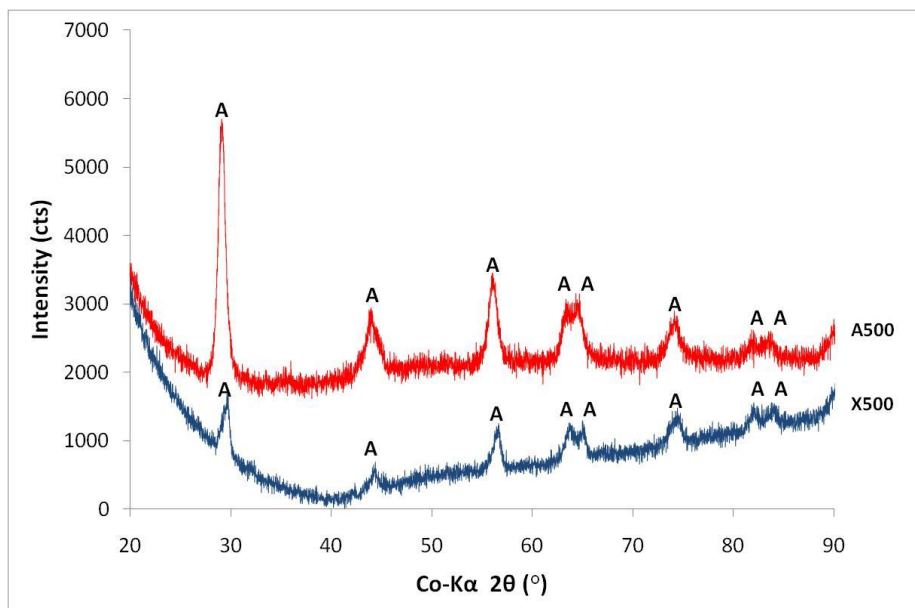


Figure 2.51 XRD patterns of AA, A400, A500, A600 and A700 aerogels. (A is anatase, R is rutile)

Since 500 °C appears to be the temperature that leads to peaks of well-crystallized anatase without presence of rutile, I have decided to calcinate xerogels at this temperature for posterior comparison with aerogels. As for aerogel calcined at 500 °C is anatase. However, in identical calcinations conditions (heating rate and calcinations temperature), XRD peaks of xerogels appear significantly less intense than the ones observed for the aerogels.

<sup>37</sup> Percentage of anatase in the sample A600 is 90 wt. % calculated by the formula  $(1 - X_R) = \left(1 + 0.8 \frac{I_a}{I_r}\right)^{-1}$  [Zhang et al., 2000] where  $X_A$  is the anatase mass fraction,  $I_a$  the intensity of the XRD peak of A(101) and  $I_r$  the intensity of the XRD peak R(110).



**Figure 2.52 XRD patterns of aerogel A500 (red spectrum) and xerogel X500 (blue spectrum) (A is anatase)**

Finally, the crystallites size of the calcined aerogel and xerogel materials has been calculated by the Scherrer formula. The results are summed up in the Table 2.11. This table shows that size of crystallite does not significantly increase with the calcinations temperature. From 400 to 500 °C size of crystallite of anatase increases slightly. At 600 °C rutile appears. The crystallite size of rutile does not increase significantly at 700 °C. We could thus hypothesize that, at this temperature, we still have germination and not yet growing of rutile cristallites.

In parallel, crystallites size of X500 and A500 are identical. We can thus conclude that drying procedure did not seem to influence the size of crystallite.

Sample	L (nm) <sup>38</sup> ± 0.4
AA	-*
A400	11 <sup>A</sup>
A500	14 <sup>A</sup>
A600	11 <sup>A</sup> ; 15 <sup>R</sup>
A700	15 <sup>R</sup>
AX	-*
X500	14 <sup>A</sup>

**Table 2.11 Crystallite size (L) estimated from Scherrer analysis of XRD pattern. (\* no crystallite because amorphous samples, A and R are respectively anatase and rutile)**

<sup>38</sup> Calculated on the A(101) and R(110) directions.

### 2.3.2.2 Transmission Electron Microscopy

TEM observations have been performed on both TiO<sub>2</sub> aerogels and xerogels. Concerning aerogels, it has first been confirmed visually that the size of the particles constituting the solid skeleton increases with temperature (Figures 2.53, 2.54, 2.55, 2.56, and 2.57). In parallel, comparing aerogels and xerogels states that xerogel particles seem to be larger than aerogels ones (Figures 2.53 and 2.58 as well as figures 2.55 and 2.59). The characteristic size of the particles has been estimated from the micrographs by “statistic” study on distinctive particles *i.e.* without considering agglomerates.

Finally, HR-TEM coupled to electronic diffraction has been performed on A500 and X500 samples. HR-TEM and electronic diffraction confirm that A500 and X500 are composed of anatase. Inset of the Figures 2.55 and 2.59 shows that inter-reticular distance is 3.5 Å, which can theoretically correspond to anatase (101) or other phase of TiO<sub>2</sub>, like TiO<sub>2</sub>-B (110). Since HR-TEM only detects anatase, we can affirm that inter-reticular distance of 3.5 Å corresponds to anatase (101).

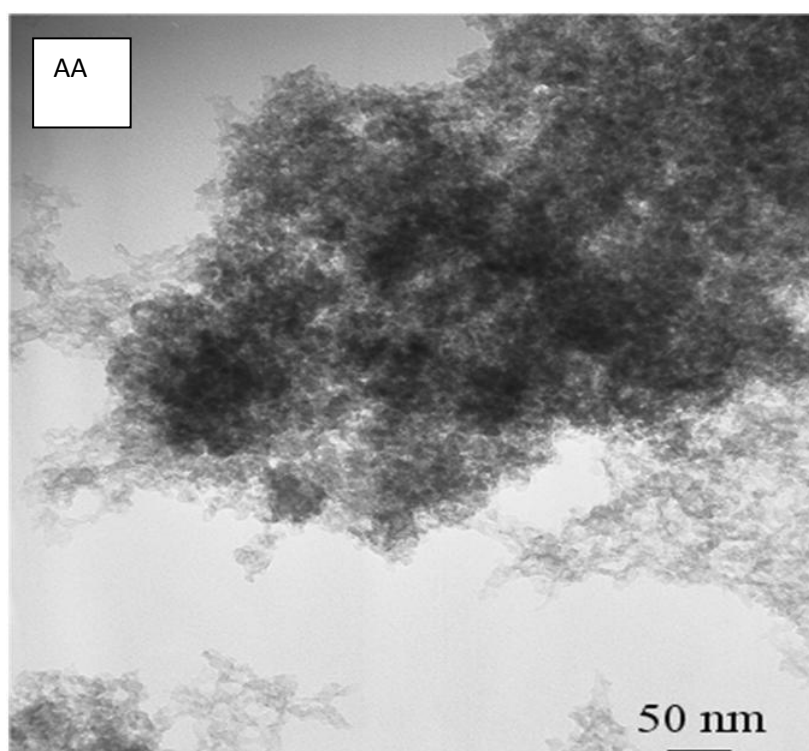


Figure 2.53 TEM micrograph of as-prepared TiO<sub>2</sub> aerogel (*i.e.* not calcined)

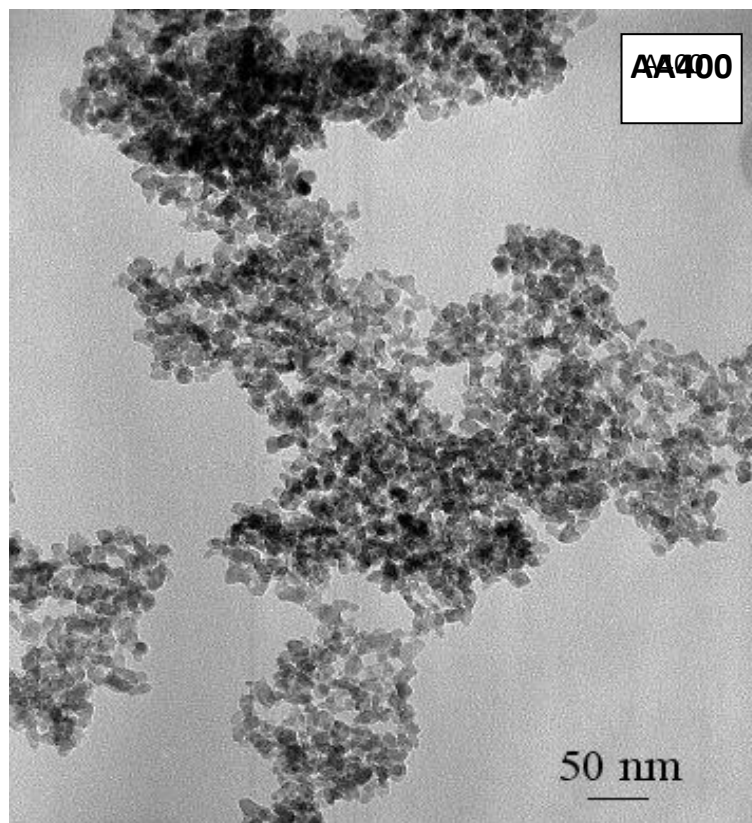


Figure 2.54 TEM micrograph of A400 TiO<sub>2</sub> aerogel

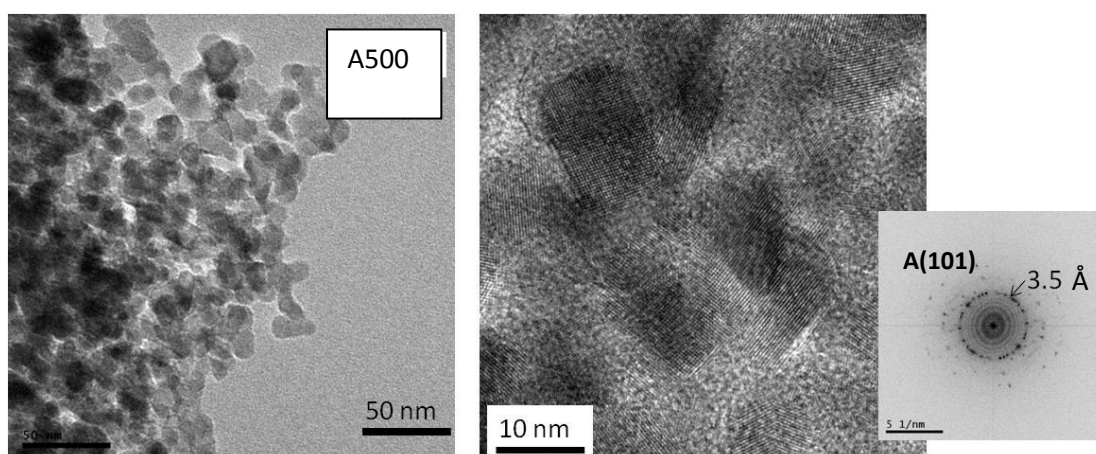


Figure 2.55 TEM (left) and HR-TEM (right) micrographs of A500 TiO<sub>2</sub> aerogel.  
(Inset: Fourier transform of the HR-TEM)

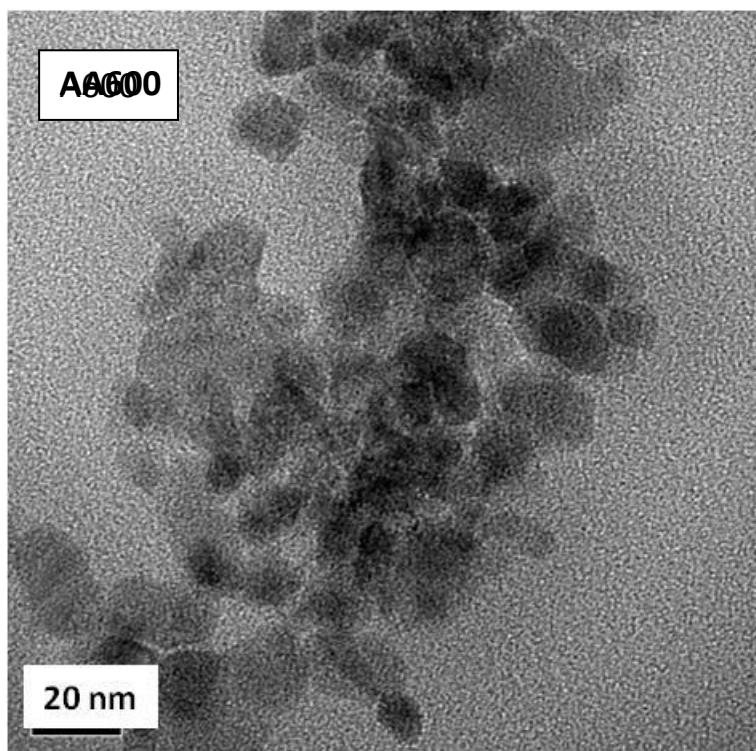


Figure 2.56 TEM micrograph of A600 TiO<sub>2</sub> aerogel.

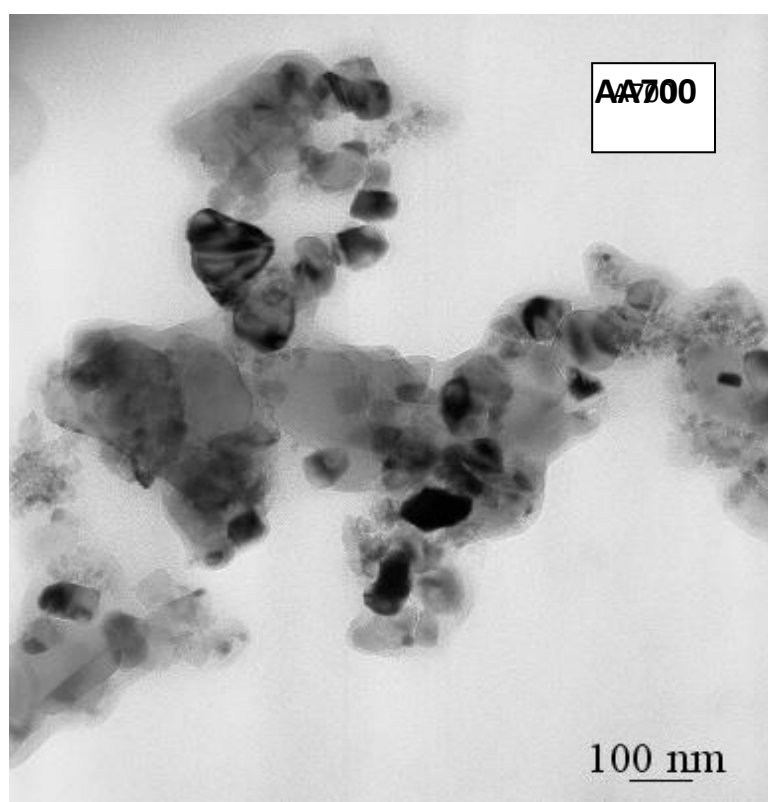
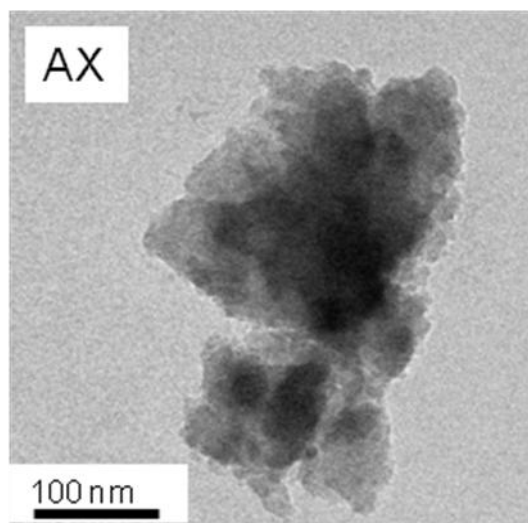
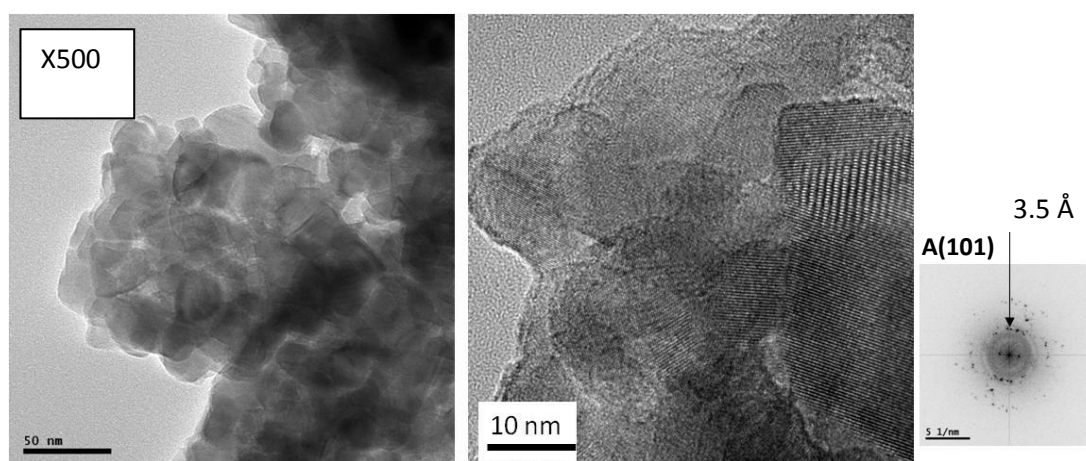


Figure 2.57 TEM micrograph of A700 TiO<sub>2</sub> aerogel



**Figure 2.58** TEM micrograph of as-prepared TiO<sub>2</sub> xerogel (*i.e.* not calcined)



**Figure 2.59** TEM (left) and HR-TEM (right) micrographs of X500 TiO<sub>2</sub> xerogel.  
(Inset: Fourier Transform of the HR-TEM)

Table 2.12 sums up the particles size analysis from TEM “photo-interpretation”. Amorphous particles of sample AA are around 3 nm. After calcinations, size of particles increases significantly but anatase particles sizes of A400, A500 and A600 samples are rather similar ( $\sim 10 \text{ nm} \pm 2$ ). (This result agrees with XRD’s one: crystallite sizes of these three samples are very close too.) Rutile particles size of samples A600 and A700, instead, are significantly different, although crystallite size is the same (as previously shown by XRD). Finally, figures 2.58 and 2.59 show that xerogel samples AX and X500 are strongly agglomerated, so individuating single particles can mislead final results regarding photo-interpretation of the corresponding TEM micrographs. For this reason the particles size of samples AX and X500 has not been determined by TEM.

Name	l (nm) ± 0.5
AA	3*
A400	8 <sup>A</sup>
A500	12 <sup>A</sup>
A600	10 <sup>A</sup> ; 22 <sup>R</sup>
A700	76 <sup>R</sup>
AX	-**
X500	-**

**Table 2.12 Particles size (l) estimated from TEM micrographs (\*, AA is amorphous, A and R are respectively anatase and rutile; \*\*, AX and X500 samples are too agglomerated to individuate single particles to perform photo-evaluation)**

### 2.3.2.3 Nitrogen physisorption

For practical reasons, N<sub>2</sub> physisorption characterizations have only been performed on aerogels.

First of all, the results show that, according to the international IUPAC classification, the shape of N<sub>2</sub> isotherms of aerogels is typical of mesoporous materials (e.g. type IV) [Sing, 1982]. Then, the influence of the calcination temperature on the porous and solid networks of these aerogels appears also very clear (Figure 2.60). When the calcination temperature increases, the hysteresis is progressively passing from H1 to H2 type<sup>39</sup>, adsorbed volume (thus specific porous volume, V<sub>p</sub>) significantly decreases as well as the specific surface area (S<sub>BET</sub>) as illustrated in Table 2.13.

<sup>39</sup> IUPAC [Sing, 1982] states that agglomerates or compact uniform spheres often give a H1 hysteresis loop while corpuscular systems, as silica gels, give H2 loops.

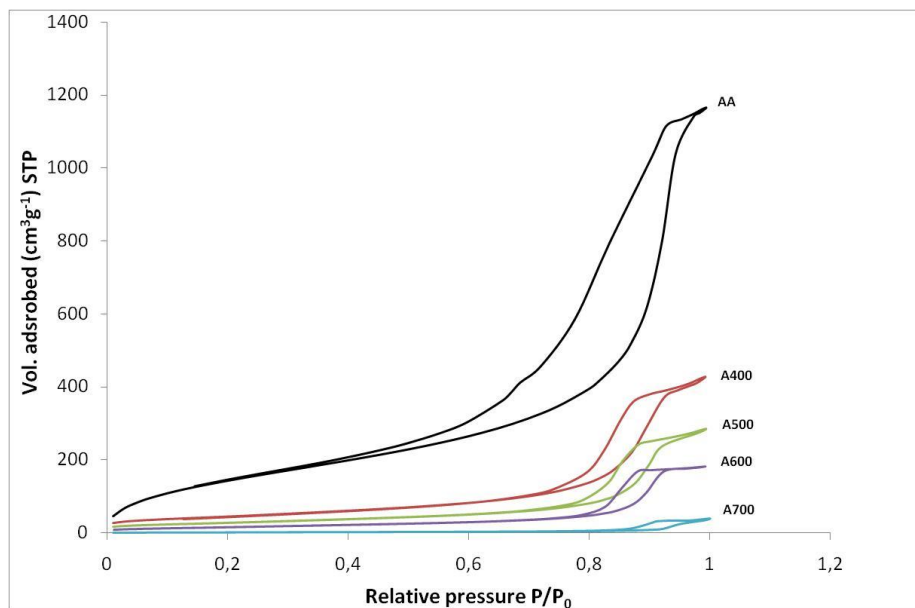


**Figure 2.60** N<sub>2</sub> sorption isotherms of TiO<sub>2</sub> aerogels A400 (red curve), A500 (green curve), A600 (purple curve) and A700 (blue curve)

In parallel, Figure 2.61 and Figure 2.62 show results of BJH treatment of the adsorption branch. All the PSDs clearly show two main peaks probably corresponding to two populations of pores. Samples A400, A500 and A600 seem to be constituted of mesopores located around 3 nm and mesopores centered around 20 nm. They are respectively noted  $\delta_1$  and  $\delta_2$ . For these calcined samples,  $\delta_2$  slightly increases with calcination temperature.

Finally, from these results complementary morphological parameters have been evaluated: i) characteristic pore size ( $d^{40}$ ) and ii) characteristic particle size ( $D^{41}$ ). To calculate  $D$  I have used skeletal densities ( $\rho_s$ ) tabulated in literature. I assumed  $3.9 \text{ g.cm}^{-3}$  for aerogels A400 and A500 (because constituted of anatase) and  $4.3 \text{ g.cm}^{-3}$  for aerogel A700 (because constituted of rutile). Skeletal density of aerogel A600 (constituted of anatase and rutile) was calculated equal to  $3.94 \text{ g.cm}^{-3}$  using the equation of Zhang [Zhang et al., 2000] with the respective anatase and rutile fraction extracted from the XRD pattern.

These geometrical factors ( $d$  and  $D$ ) evolve similarly: they increase with calcination temperature. Since the size of first pores population (characterized by  $\delta_1$ ) does not increase with the calcinations temperature, the largest contribution to the increase of the average pore size  $d$  is driven by the second pore population (characterized by  $\delta_2$ ).  $D$  is an average value, so we cannot distinguish the contribution of the anatase and rutile phases but we can underline some general observations. For samples A400 and A500, particles size slightly increases on the contrary of particles constituting samples A600 and A700 whose size increases drastically.

<sup>40</sup>  $d$  can be considered as the average pores size diameter calculated with the geometric formula  $4V_p/S_{\text{BET}}$  from treatment of the sorption isotherms.  $S_{\text{BET}}$  ( $\text{m}^2.\text{g}^{-1}$ ) is the surface area and,  $V_p$  is the specific pore volume ( $\text{cm}^3.\text{g}^{-1}$ ) calculated from the N<sub>2</sub> sorption isotherms.

<sup>41</sup>  $D = f/(S_{\text{BET}}*\rho_s)$  with the form factor  $f$  equal to 6 and  $\rho_s$  being the density of the TiO<sub>2</sub> skeleton.

From a qualitative point of view, these results are in very good agreement with the evolution shown by TEM results. Table 2.13 sums up results issued from N<sub>2</sub> sorption isotherms.

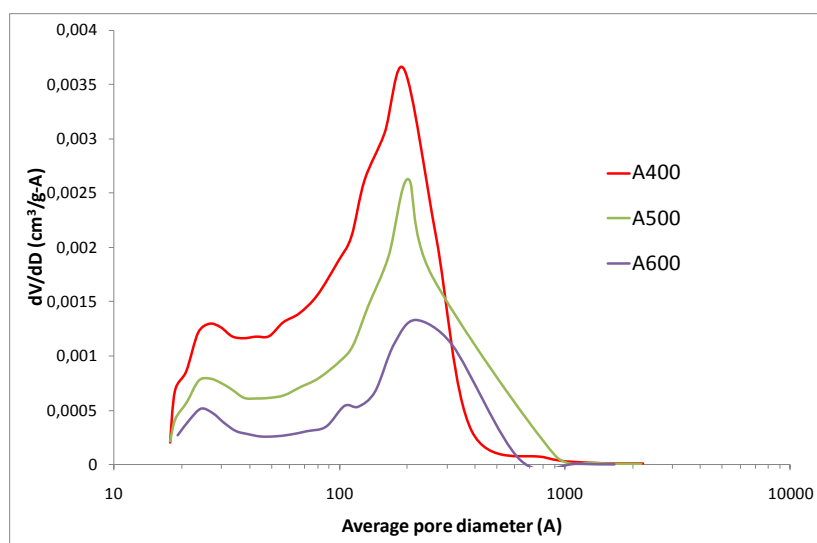


**Figure 2.61 BJH pore size distribution of TiO<sub>2</sub> aerogels A400, A500 and A600**

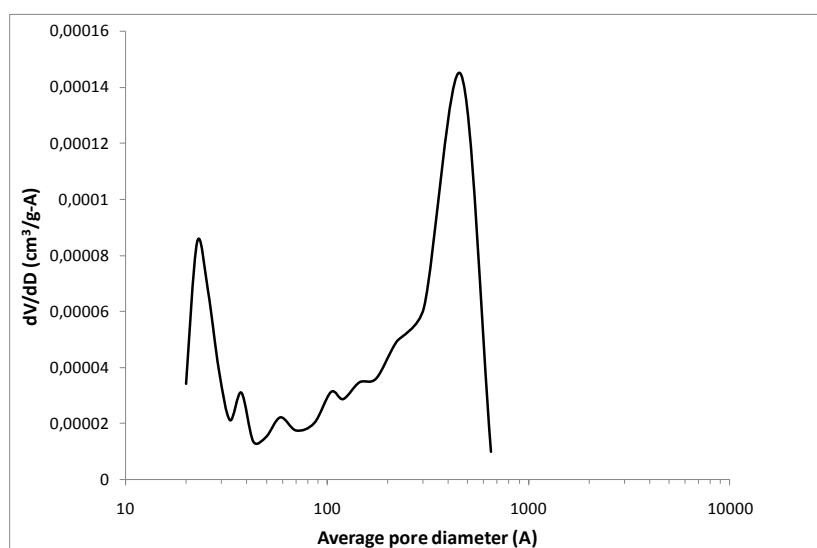


**Figure 2.62 BJH pore size distribution of TiO<sub>2</sub> aerogels A700**

Samples	$S_{\text{BET}} \pm 0.92^*$ ( $\text{m}^2 \text{g}^{-1}$ )	$V_p$ ( $\text{cm}^3 \text{g}^{-1}$ )	$\delta_1$ (nm)	$\delta_2$ (nm)	$d$ (nm)	$D \pm 0.3^*$ (nm)
AA	568	- <sup>42</sup>	-	-	-	3 <sup>43</sup>
A400	158	0.63	3	20	16	10
A500	97	0.43	3	20	17	16
A600	59	0.27	3	22	19	26
A700	6	0.05	3	46	33	232

**Table 2.13 Results from BET and BJH treatments of  $N_2$  sorption isotherms.  $V_p$ <sup>44</sup> is the specific pore volume,  $\delta_1$  and  $\delta_2$  correspond to pore size population directly issued from BJH PSD,  $d$  is the average pore diameter considering pore as cylinder ( $d = 4/(V_p * S_{\text{BET}})$ ) and  $D$  is the particles diameter calculated from the following geometric formula  $D = 6/(S_{\text{BET}} * \rho_s)$ . (\*The errors quoted here are the average of the errors of each sample.)**

#### 2.3.2.4 Elementary Analysis

The chemical compositions of samples A500 and X500 have been characterized by elementary analysis. Four elements (Ti, O, C and H) have been analysed. Results are presented in Table 2.14.<sup>45</sup>

These results clearly state that the final material is mostly made up of Ti and O. Indeed, experimental mass fractions of Ti and O are very close to the expected theoretical ones for *pure*  $\text{TiO}_2$  (respectively equal to 0.6 and 0.4 *i.e.* 60 and 40 wt%). Table 2.14 also underlines that hydrogen is present as traces. H coming from both residual isopropanol and remaining  $(\text{Ti}(\text{OtBu})_4)$  oligomers, can probably be neglected because these species have been eliminated during the thorough washing process. Moreover, the unavoidable adsorbed layer of *i*PrOH which is present after drying has also surely been desorbed during the heat-treatment at 500 °C. Consequently, H traces probably derive from the presence of titanols ( $\equiv\text{Ti-OH}$ ) issued

<sup>42</sup>Because of an experimental *artefact*, results on porosity (specific porous volume, PSD and associated characteristics) cannot be presented for aerogel AA.

<sup>43</sup> I have assumed here that density of amorphous aerogel is  $3.44 \text{ g.cm}^{-3}$  [Dagan and Tomkiewicz, 1993].

<sup>44</sup> The value of  $V_p$  is underestimated, because of the contraction of the material under  $N_2$  capillary condensation [Dagan1993].

<sup>45</sup> Measurements have been carried out at CNRS in Solaize, France. For major contents (upper than 10 at%) the accuracy of the analyser used for C, H, O and N detection is  $\pm 0.3\%$ . The detection limit depends on the sample matrix (generally 0.3 at.%).

from incomplete condensation reactions occurring during the sol-gel synthesis and subsequent syneresis. Indeed, C cannot be detected which militates in favor of the presence of  $\equiv\text{Ti-OH}$  instead of remaining alcoxy groups (*i.e.*  $\equiv\text{Ti-OC}_4\text{H}_9$ ). Of course, specific characterizations like FTIR spectroscopy<sup>46</sup> should be performed to verify this hypothesis.

Finally, it can be noted that the sum of experimental data is lower than 100 % for both calcined aerogels and xerogels. Measurement error is probably partly responsible for this result (which is 1-2% for Ti and O, 0.10% for C and H) but it can be observed that this tendency is much more pronounced for xerogels.

	<b>Ti</b> (wt. %)	<b>O</b> (wt. %)	<b>C</b> (wt. %)	<b>H</b> (wt. %)	<b>Tot.±2*</b> (wt. %)
<b>A500</b>	57.33	40.64	< 0.30	0.53	< 98.80
<b>X500</b>	57.50	36.33	< 0.30	< 0.30	< 94.43

Table 2.14 Elementary analysis of TiO<sub>2</sub> aerogel A500 and xerogel X500. \*As total error we have considered the maximum error of Ti and O.

### 2.3.3 Discussion

Based on a bibliographic sol-gel path, I have elaborated some nanostructured and mesoporous amorphous TiO<sub>2</sub> species so-called aerogels and xerogels. By calcination, I have crystallized the initial amorphous matrixes to generate anatase. The so-obtained materials have been characterized with standard techniques (XRD, TEM, N<sub>2</sub> sorption and elementary analysis) to study their structure.

This part mainly highlights that calcinations temperature and drying mode have a significant influence on the final aerogels. These points are briefly discussed here-after.

#### • Influence of calcination temperature

When temperature of calcination increases, several phenomena occur. Among them we can underline i) physical (water, COV, ...) and chemical (-OH and -OR) desorption, ii) crystallization and iii) phase transition plus sintering.

Based on TEM and N<sub>2</sub> sorption results obtained on aerogels, it seems clear that the average particles size increases with the calcination temperature. XRD, instead, suggests that anatase and rutile crystallite sizes do not significantly increase with this temperature. The evolution of the particle size may thus partly be explained by sintering process (which is known to occur on aerogels at such low temperatures (amongst others, because of their relatively high specific area)).

As a direct consequence of particles growth, sintering would also have a dramatic impact on the porous network and particularly on the specific surface area. Indeed S<sub>BET</sub> tends to decrease significantly with the elevation of the calcinations temperature. This evolution is probably

<sup>46</sup> Fourier Transformed Infrared spectroscopy.

also enhanced by the decrease of microporosity (closing of the micropores, disappearance of particles roughness, ...).

The influence of these thermally induced phenomena on the average pore size as-estimated is not so pronounced on the contrary of the impact on the pore size distribution (as obtained by BJH method). PSDs point out that the macropores fraction is significantly reduced which is probably inducing an overall densification of the final material.

#### • Influence of the drying mode

Although aerogels and xerogels samples have been elaborated following the same sol-gel preparation and have been calcined at the same temperature, they present very different final morphologies. They are very different in particle size and, as TEM pictures clearly show, in structure. Xerogels seems much more compact than aerogels. So drying method appears as a processing parameter that deeply affects the morphology of the final material.

As described in chapter 1, during evaporation of the solvent from the gels, an energetic liquid-gas interface is created in the porosity and induces intense capillary tensions on the solid phase. These tensions produce an irreversible densification of the gel. This densification is due to the occurrence of reactions between remaining  $\equiv\text{Ti-OH}$  and  $\equiv\text{Ti-OC}_4\text{H}_9$  groups localized at the surface of the pores (i.e. which have not reacted nor during sol-gel, neither after syneresis). Because the solid chains constituting the gels present some flexibility, these groups, initially too far to condense, can become close enough to react. This covalent bonding can contribute i) to close the microporosity, ii) to increase the cross-linking ratio and, as a consequence, iii) to increase the particle size. On the contrary of evaporation, supercritical drying does not induce any capillary tensions, so the gel does not retract and can keep its initial particles size (i.e. as generated during the sol-gel step). Figure 2.63 clearly shows that AX sample is much more compact than its aerogel counterpart AA and appears made up of significantly bigger particles.

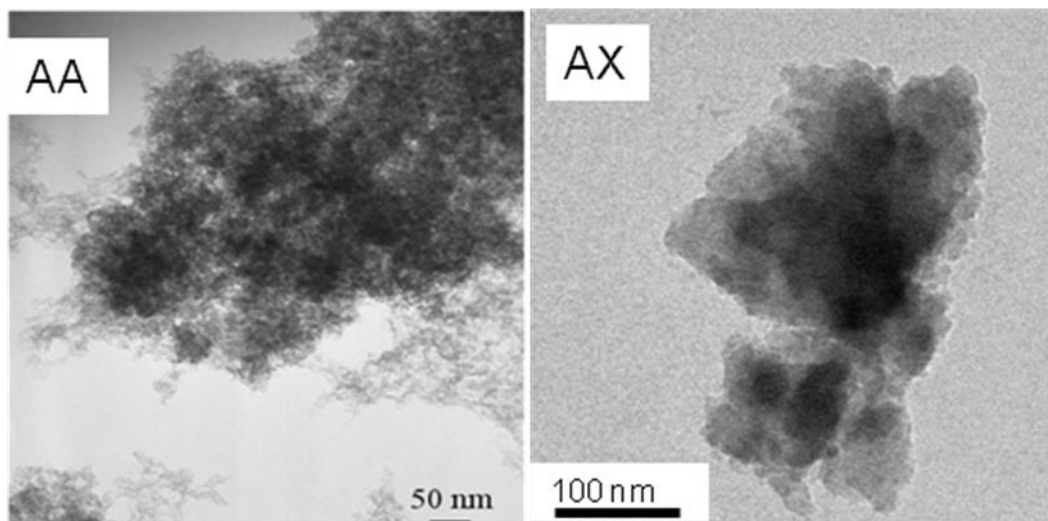


Figure 2.63 TEM micrograph of AA (left) and of AX (right) samples

More interesting, this initial difference between aerogels and xerogels is maintained after calcination. As sets off by comparison between Figures 2.55 and 2.59, aerogel A500 still presents smaller particles than xerogel X500. The starting-point (*i.e.* the morphology of the materials before calcinations) clearly influences the evolution of the particles growth during calcination.

Furthermore, it can be added that this initial difference can also affect the degree of crystallization of the calcined materials. Despite the same calcination conditions (2 °C/min, 500 °C, 2 hours), XRD results have shown that xerogel X500 is less crystallized than its aerogel counterpart A500 (Figure 2.49). Indeed, through very rough kinetics considerations, it can be stated that the larger particles constituting the as-prepared xerogel skeleton will need more time to be homogeneously crystallized than the smaller ones building the aerogel solid network. In order to verify this hypothesis we have calcined a xerogel at 550 °C for 168 hours instead of 2 hours. Then we have performed complementary XRD to check the crystallization degree of the resulting material (Figure 2.64)<sup>47</sup>. This analysis has clearly proven that longer calcinations duration can improve anatase xerogel crystallization.

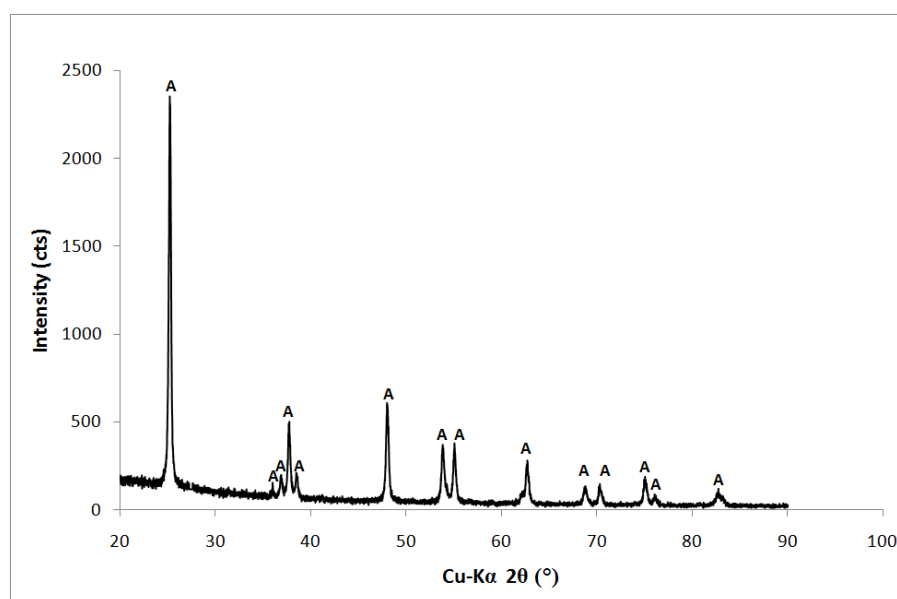


Figure 2.64 XRD pattern of a xerogel calcined in specific conditions : 2 °C/min, 550 °C, 168 h

Finally, another interesting result from Tursiloadi's works is the observation of an initial crystallization of anatase during the supercritical CO<sub>2</sub> drying. Supercritical drying conditions in this article are 22 MPa and 60 °C. At this high pressure conditions, the authors stated that the residual water in the gel (probably mainly adsorbed on remaining titanols) allows the hydrothermal crystallization of a part of the amorphous skeleton in anatase, as they detected it by HR-TEM. In our specific work we have also identified by HR-TEM some TiO<sub>2</sub>

---

<sup>47</sup> This XRD characterization has been performed by Gabriel Monge at CEMEF (MINES ParisTech / Sophia Antipolis) using X'Pert PRO MPD by Panalytical, with Copper as X-rays source.

nanocrystals (Figure 2.65) in the as-prepared aerogel (sample AA), i.e. before any calcinations treatment. In our case we could also hypothesize that a crystallization phenomenon occurs during the supercritical CO<sub>2</sub> drying. On the contrary, the as-prepared xerogel (sample AX), in fact, is completely amorphous, as HR-TEM of the Figure 2.66 tends to prove. However, our as-prepared aerogel material is far less crystallized than that of Tursiloadi' study. We could assume that this difference might be due to the far lower supercritical drying conditions. Indeed, in our experimental conditions pressure is 85 bar and temperature is 39 °C. The lower pressure probably lowers down the crystallization degree of the TiO<sub>2</sub> gel by eventual hydrothermal phenomena. On the basis of these results, we could stress that this differential crystallization before calcinations might also contribute to the different degree of crystallization observed after calcinations (in identical processing conditions).

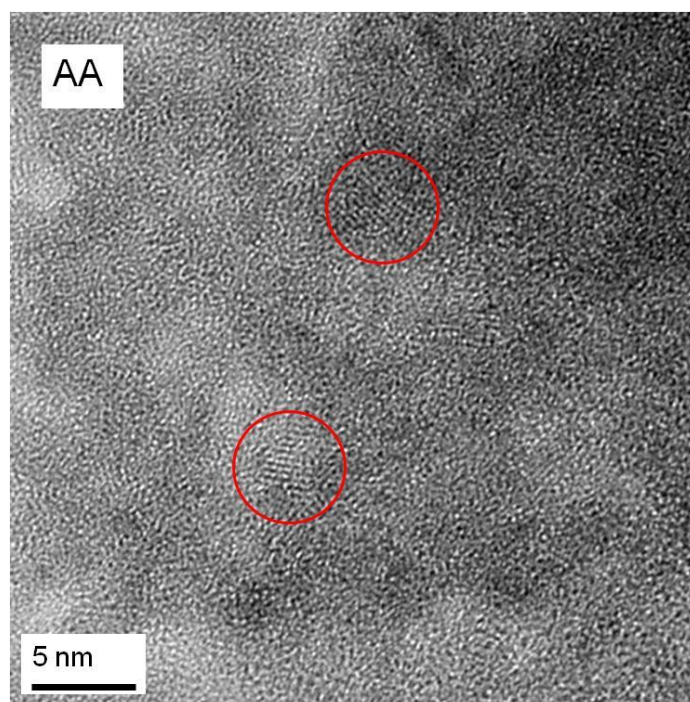


**Figure 2.65 TEM micrograph of AA aerogel sample. Red circles highlight the TiO<sub>2</sub> nanocrystals<sup>48</sup>**

---

<sup>48</sup> Since we did not perform the electronic diffraction, we cannot affirm that nanocrystals are anatase.

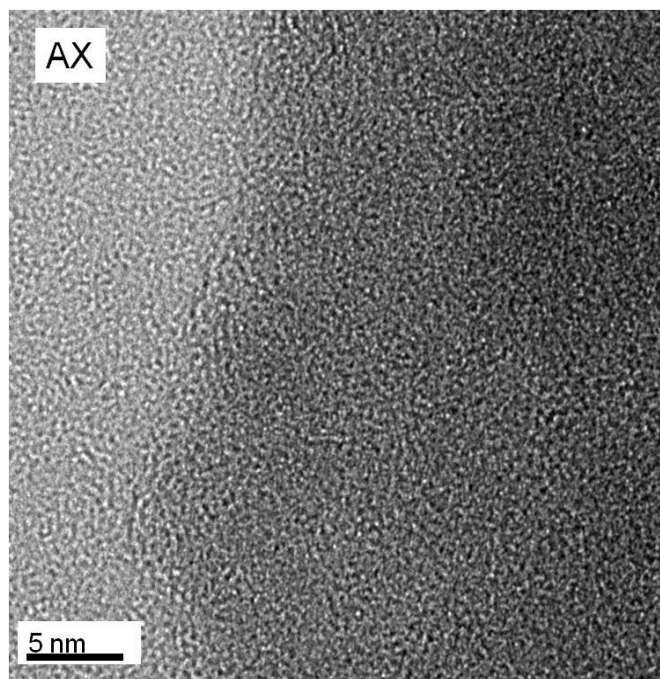


**Figure 2.66 TEM micrograph of AX xerogel sample.**

## **2.4 Conclusion**

In this chapter, I have described the elaboration of three radically different  $\text{TiO}_2$  nanostructured species : nanoparticles, nanotubes and aerogels/xerogels. I have also presented the main characterization results.

This part has permitted to prepare the reference materials for the study on hydrogen evolution as well as the substrates for doping, as presented in the following chapter.



### 3. Doping: vanadium-doped nanotubes and nitrogen-doped aerogels and xerogels

In the previous chapter, I have reported elaboration and characterisations of the three TiO<sub>2</sub> morphologies I have selected within this PhD studies:

- nanoparticles,
- nanotubes,
- aerogels/xerogels.

Among these morphologies, 1D structures (*i.e.* nanotubes) as well as aerogels and xerogels have received much attention regarding doping for their ease of elaboration and their very good performance in some photocatalytic reactions [Rolison et al., 1997], [Jitputti et al., 2007].

This chapter is divided in two main sections devoted to elaboration and characterizations of:

- vanadium-doped nanotubes,
- nitrogen-doped aerogels and xerogels.

Materials have been characterized by XRD, TEM, elementary analysis and N<sub>2</sub> physisorption (using BET and BJH treatments). Moreover, for these doped samples some additional investigations have been performed, in collaboration with external laboratories as listed here-below.

- Raman Spectroscopy performed by Professor Jean-Christophe Valmalette from Université du Sud Toulon Var. This technique theoretically allows the determination of anatase/TiO<sub>2</sub>-B ratio in vanadium-doped samples. It is thus useful to check deformation of anatase lattice after inserting nitrogen.
- High Temperature X-Rays Diffraction (HT-XRD) performed on vanadium-doped samples by Assistant-Professor Yoshikazu Suzuki from Institute of Sustainability Science (ISS) at Kyoto University. HT-XRD is able to identify the phases of the samples in a range from 30 to 900 °C. Incorporation of vanadium is susceptible to shift the anatase-rutile transition temperature which can theoretically be observed with this technique.
- X-Rays Photoemission Spectroscopy (XPS) carried out on nitrogen-doped samples by Dr. Yannick Fagot-Revurat from IJL of Nancy University, in order i) to check if our chemical procedure succeeded in doping our TiO<sub>2</sub> substrates and ii) to investigate the energetic states of the incorporated nitrogen atoms.

Similarly to the previous chapter, bandgap estimations and photoactivity analyses are gathered in the final chapter dedicated to H<sub>2</sub> evolution (*i.e.* chapter 4).

## 3.1 Vanadium doped nanotubes

### 3.1.1 Elaboration

Vanadium doped anatase nanotubes synthesis is divided into three parts:

- 1 synthesis of titanate nanotubes ( $\text{H}_2\text{Ti}_2\text{O}_5 \cdot \text{H}_2\text{O}$ ) following the procedure described in the previous chapter;
- 2 wet impregnation of titanate by acetyl acetonate ( $\text{VO}(\text{C}_5\text{H}_7\text{O}_2)_2$ ) to have vanadium doped titanate nanotubes;
- 3 calcination of titanate to have vanadium doped anatase nanotubes.

We have chosen Vanadyl acetylacetonate ( $\text{VO}(\text{C}_5\text{H}_7\text{O}_2)_2$  Sigma Aldrich 99.99% purity) as doping precursor. Four samples were prepared: V0 (0% V/Ti at.), V0.5 (0.5%), V1 (1%), V2 (2%). Initially the suspensions were stirred until doping precursor complete dissolution. Later, still under stirring conditions, these products were heated up  $100^\circ\text{C}$  until water evaporation. At the end of this stage, titanate doped nanotubes were obtained. Figure 3.1 is a scheme of synthesis procedure.

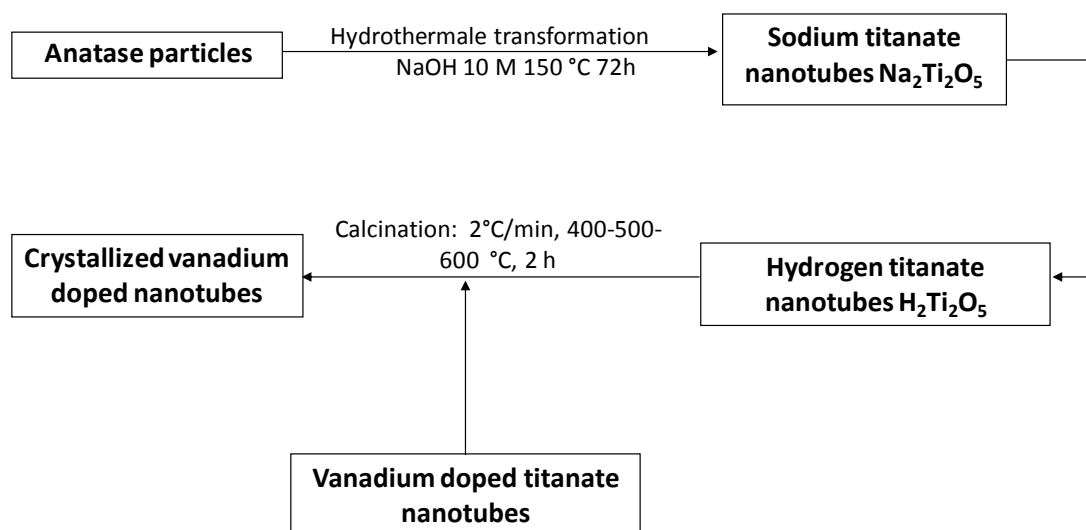


Figure 3.1: Synthesis of anatase doped nanotubes

Calcination of all samples has been carried out in an oven similar to that described in the annexe. For all samples atmosphere is air. Table 3.1 sums up calcination conditions:

Sample	% V/Ti at.	Calcination temperature ( $^\circ\text{C}$ )	Theoretical % V/Ti at.	Experimental % V/Ti at.
V0	0%	400	0	0
V0.5	0.5%	400	0.5	0.38
V1	1%	500	1	0.84
V2	2%	600	2	1.54

Table 3.1 Calcination and synthesis conditions. Calcination time is 2 h, heating ramp is  $2^\circ\text{C}/\text{min}$

Calcination time and heating ramp are the same for all samples but calcination temperature changes (because an increase of the doping ratio leads to a shift of the anatase formation at higher temperature (*cf.* Appendix 1)). Samples features as theoretical and experimental V/Ti atomic doping ratios and calcination temperatures are summed up in Table 3.1. Theoretical ratio V/Ti has been calculated hypothesizing that all vanadium of the vanadyl acetyl acetate enters in the structure. Experimental V/Ti has been calculated on the base of the results of elementary Chemical Analysis.

Color of samples depends on quantity of vanadium. Undoped nanotubes are white, doped samples are more yellowish. Figure 3.2 shows color change of the samples.



Figure 3.2: Color change of vanadium doped nanotubes

### 3.1.2 Characterizations

#### 3.1.2.1 X-Rays Diffraction

XRD (Figure 3.3 - Figure 3.6) reveals that vanadium doped samples are made up of two phases: anatase (PDF file n°21-1272) and TiO<sub>2</sub>-B (PDF file n°35-0088). Distinguishing and calculating the ratio of this two phases is difficult because intense (101)(d=3.520Å) or (200)(d=1.892Å) reflections of anatase are close to reflections of similar relative intensity (110) (d=3.560Å) and (020) (d=1.873Å) of TiO<sub>2</sub>-B.

However, we can notice that peaks of TiO<sub>2</sub>-B do not disappear while increasing the calcination temperature. The calcination conditions were chosen to maintain 1D morphology, at the price of a fraction of TiO<sub>2</sub>-B.

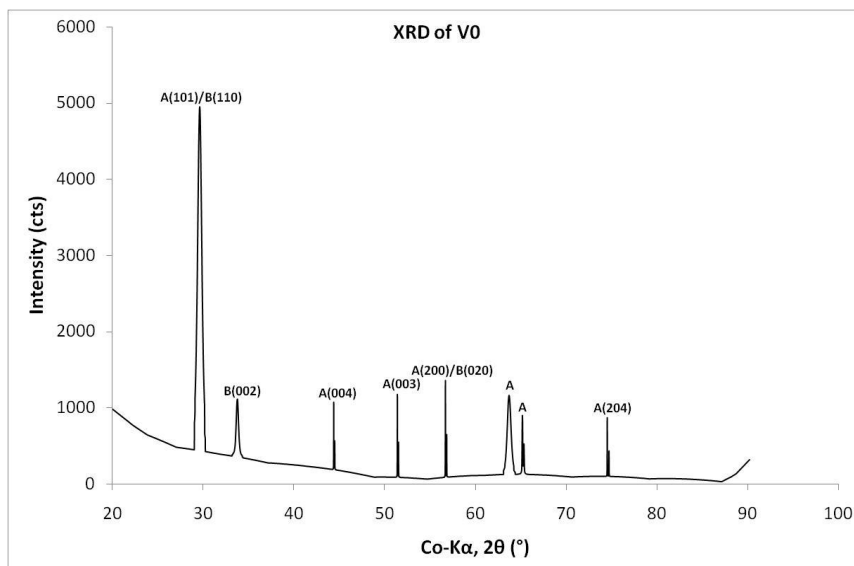


Figure 3.3: X-Rays Diffractograms of V0 ( $T_{\text{calcination}} = 400\text{ }^{\circ}\text{C}$ )

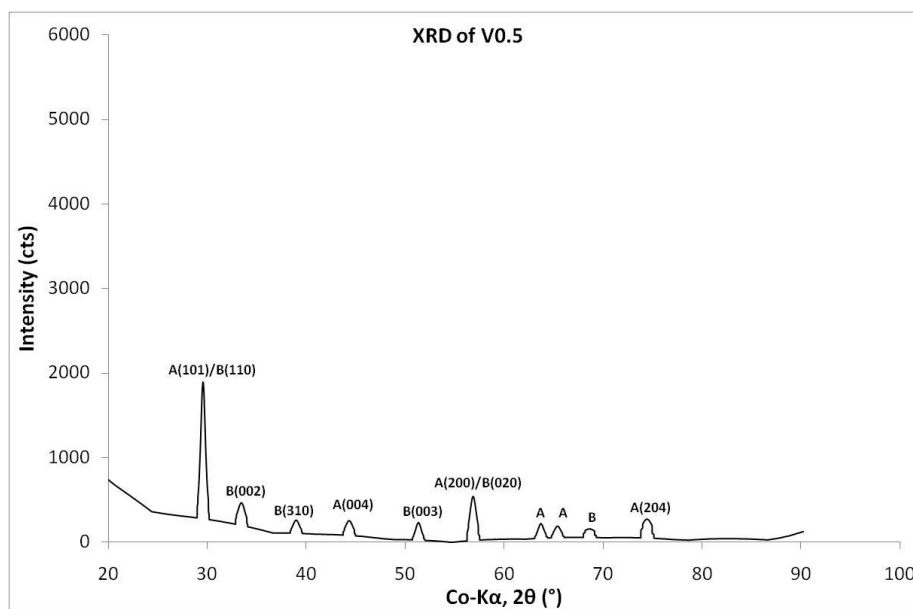


Figure 3.4: X-Rays Diffractograms of V0.5 ( $T_{\text{calcination}} = 400\text{ }^{\circ}\text{C}$ )

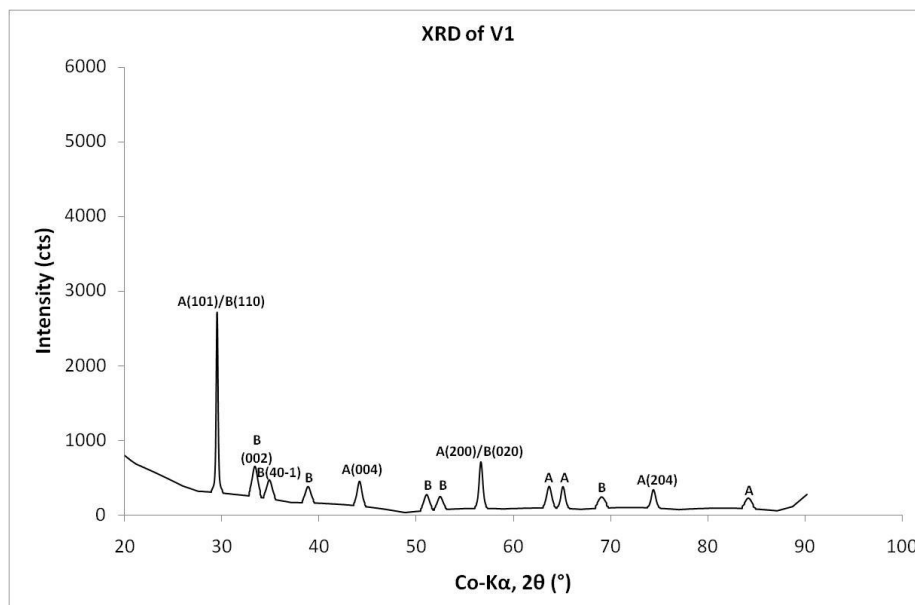


Figure 3.5: X-Rays Diffractograms of V1 ( $T_{\text{calcination}} = 500\text{ }^{\circ}\text{C}$ )

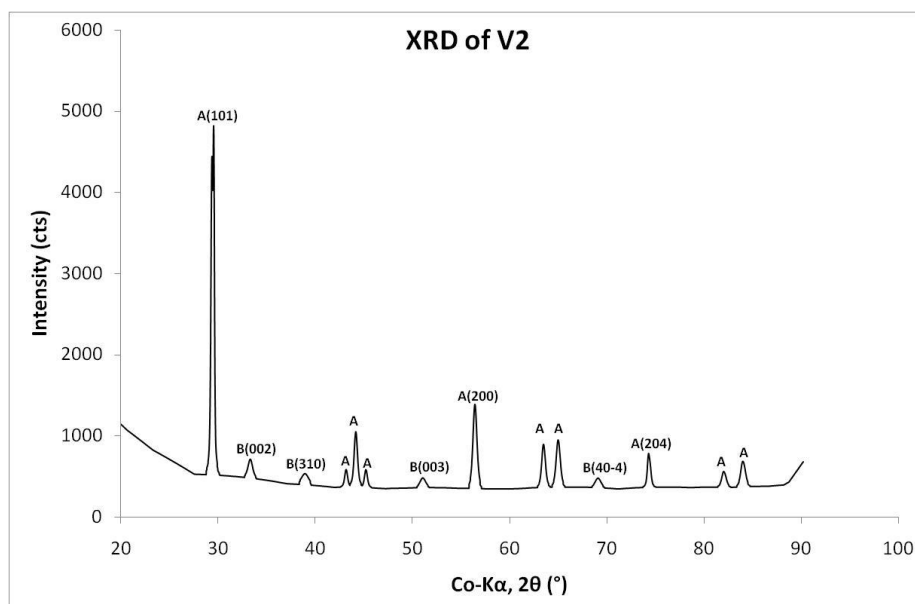


Figure 3.6: X-Rays Diffractograms of V2 ( $T_{\text{calcination}} = 600\text{ }^{\circ}\text{C}$ )

### 3.1.2.2 Raman Spectroscopy<sup>49</sup>

Raman spectroscopy is a powerful tool to investigate the modification of the vibrational structure of materials. Results for undoped nanotubes are in agreement with literature [Lei et al., 2001]. Raman spectrum of undoped nanotubes (Figure 3.7) corresponds to the anatase

<sup>49</sup> Measurements have been carried out at the University of Toulon and of Var, Laboratory of materials and microelectronic by Professor Jean-Christophe Valmalette. The equipment is a LabRAM HR, main components of which are a high resolution microscope, a spectrograph of 800 nm focal and a Charge-Coupled Device (CCD) detector.

phase with a characteristic strong vibrational mode at  $144\text{ cm}^{-1}$ , three medium at  $397$ ,  $516$  and  $640\text{ cm}^{-1}$ , and a weak mode at  $197\text{ cm}^{-1}$ . Nevertheless a peak at  $123\text{ cm}^{-1}$  appears.

Raman spectroscopy is the most appropriate tool to quantify the weight ratio anatase/ $\text{TiO}_2\text{-B}$ . The method we propose is issued from Beuvier's PhD thesis [Beuvier, 2009]. Anatase has 6 vibrational modes active in Raman ( $144$ ,  $197$ ,  $399$ ,  $513$ ,  $519$  and  $639\text{ cm}^{-1}$ ), the most intense is  $144\text{ cm}^{-1}$ .  $\text{TiO}_2\text{-B}$  has 18 vibrational modes, the most intense being at  $123\text{ cm}^{-1}$ .

The ratio  $I_A/(I_A + I_B)$ , where  $I_A$  is the intensity diffused by the peak of the anatase at  $144\text{ cm}^{-1}$  and  $I_B$  is the intensity diffused by the peak of  $\text{TiO}_2\text{-B}$  at  $123\text{ cm}^{-1}$ , is function of the weight ratio  $m_A/(m_A + m_B)$  [Beuvier, 2009].

$I_A$  and  $I_B$  are proportional to  $m_A$  and  $m_B$  ( $I_A = m_A \cdot \sigma_A$ ,  $I_B = m_B \cdot \sigma_B$ ).  $K_r$ , the ratio of the two proportional coefficients ( $\sigma_A / \sigma_B$ ), equals 6.2, according to the calibration procedure carried out by Beuvier.

Determination of  $K_r$  leads to the definition of the weight fraction of anatase:

$$X_A = y/(K_r - 5.2y)$$

where:

$$y = I_A/(I_A + I_B)$$

For estimating percentage of anatase in our samples, we have used data displayed in Figure 1.7. Shifts of peaks of doped materials are due to doping insertion.

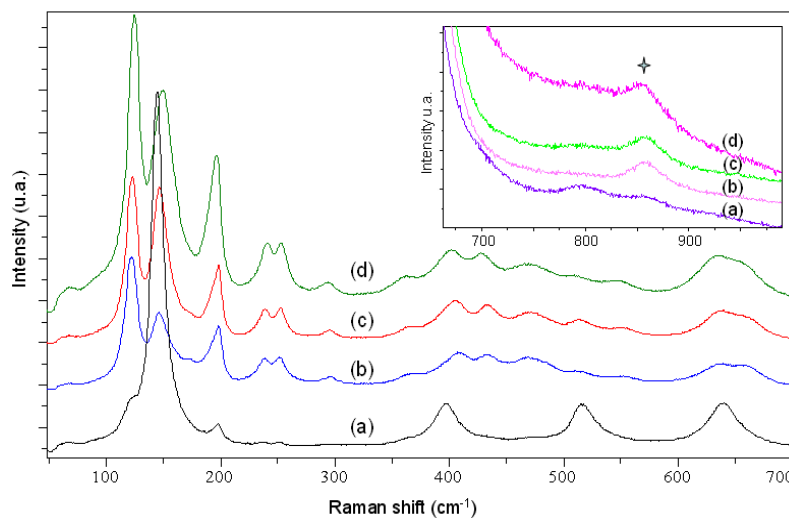


**Figure 3.7** Raman spectra of doped nanotubes. a) is spectrum of V0, b) of V0.5, c) of V1 and d) of V2

After subtracting background from spectra and decomposition of the two  $\text{TiO}_2$  contributions, we have estimated that anatase in V0 is 80%, in V0.5 2%, in V1 9%, in V2 4%. These results clearly show that only V0 is mostly made up of anatase. The other materials are  $\text{TiO}_2\text{-B}$ . These results clearly demonstrate that vanadium stabilizes the  $\text{TiO}_2\text{-B}$  phase even at high

calcination temperature, and that we could not establish a preparation protocol for having vanadium doped anatase tubular morphology at high temperature.

### 3.1.2.3 Transmission Electron Microscopy

Transmission Electron Microscopy has been performed on all materials to investigate the morphology of the samples.

We observed (Figure 3.8-3.13) that although samples are mainly nanoribbons and bundles of nanotubes, nucleation of anatase nanoparticles in the  $\text{TiO}_2\text{-B}$  occurs (Figure 3.11). According to TEM, ribbons/bundles length ranged from 0.4 to 1.45  $\mu\text{m}$  and the average width was around 70 nm; particles length (Figure 3.11) ranges from 18 to 36 nm, diameter from 9 to 18 nm.

As we state in the chapter 2, morphology is strictly correlated with the phase:  $\text{TiO}_2\text{-B}$  for nanotubes, anatase for nanoparticles. Moreover, Raman Spectroscopy on vanadium doped samples reveals that we kept the  $\text{TiO}_2\text{-B}$  at high calcination temperatures. So we have mainly kept the nanotubes morphology because we have kept the  $\text{TiO}_2\text{-B}$  phase. The nucleation of anatase we observe by TEM is correlated with the loose of morphology of vanadium doped samples.

HRTEM observations (Figure 3.9) of the tubes/ribbons reveal some dislocations. Since this may be due to overlap of structures, we cannot affirm nanotubes are monocrystalline.

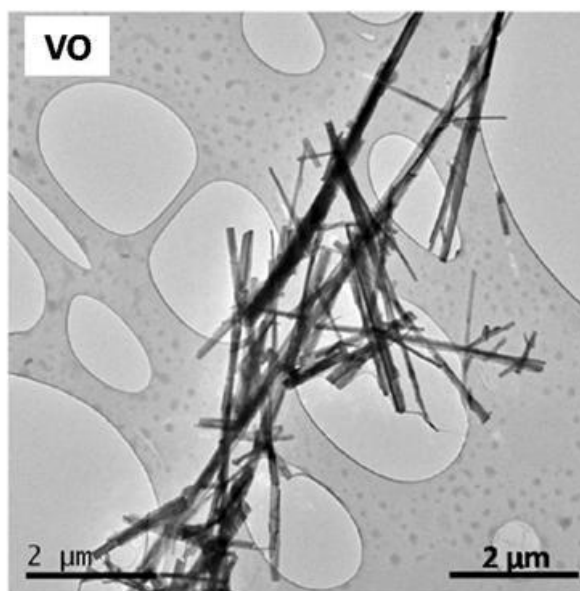


Figure 3.8 TEM picture of VO

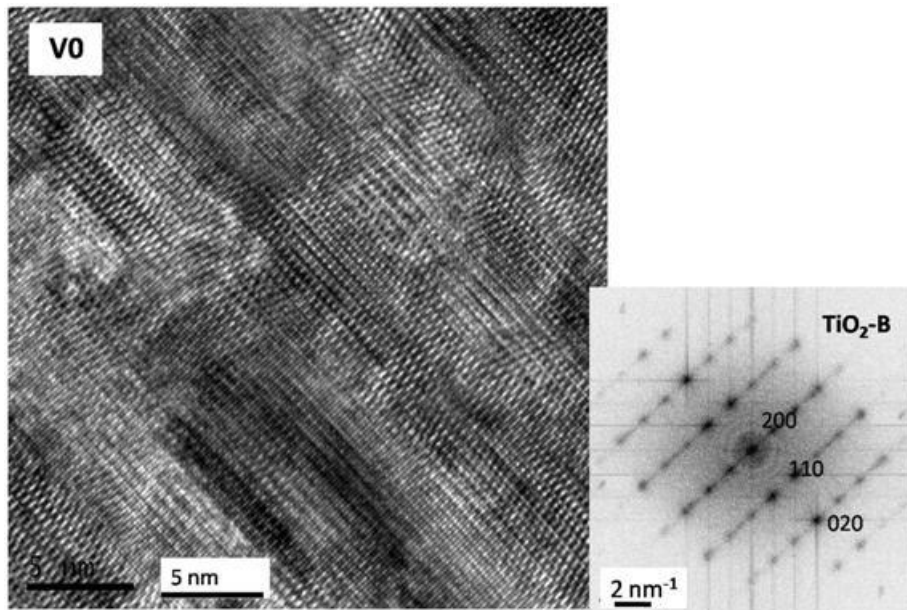


Figure 3.9 TEM picture of V0. Fourier Transform Function indicates that on this zone phase is TiO<sub>2</sub>-B

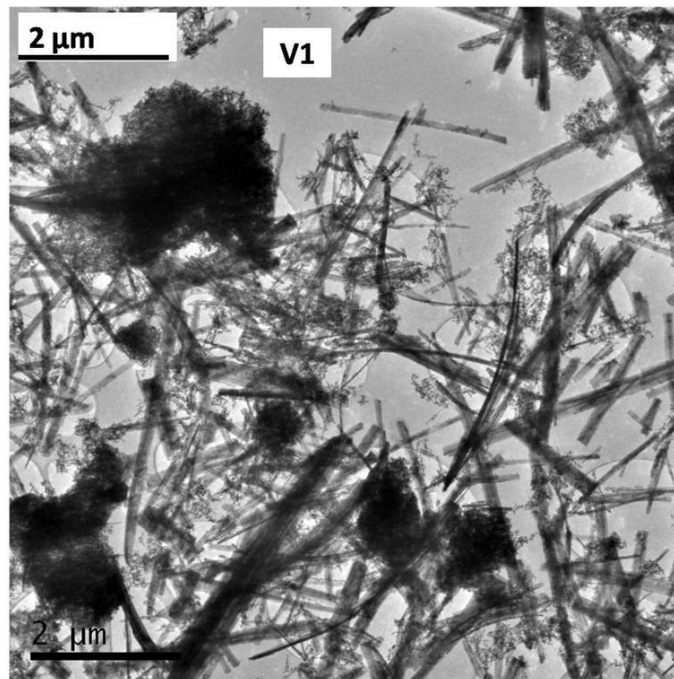


Figure 3.10 TEM picture of V1

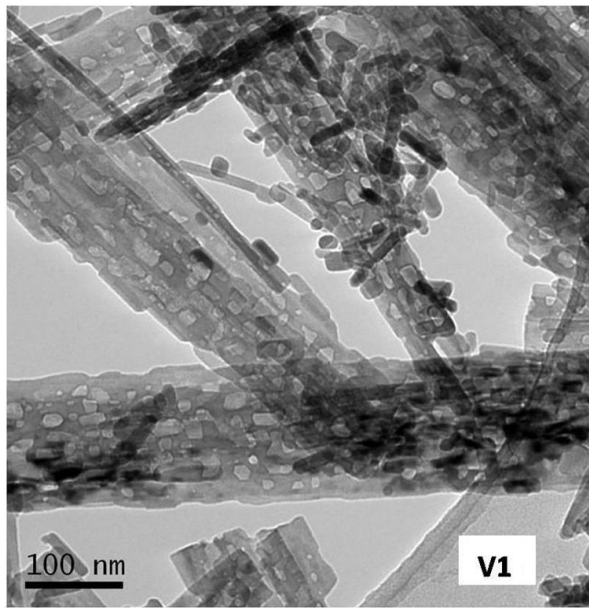


Figure 3.11 TEM picture of V1. Some particles appear

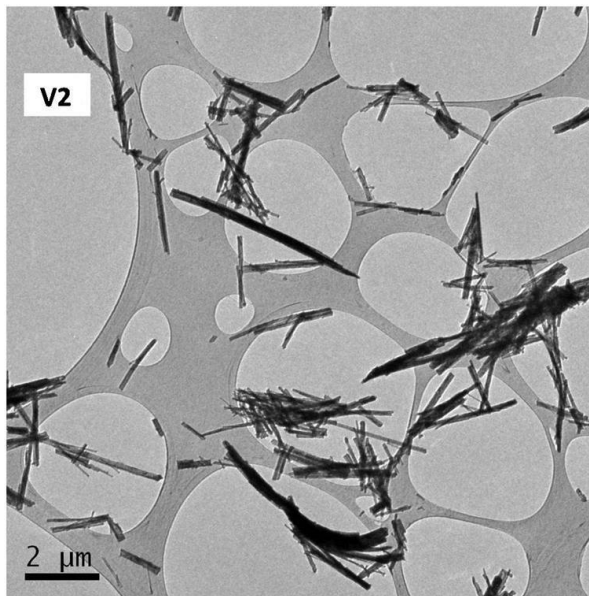
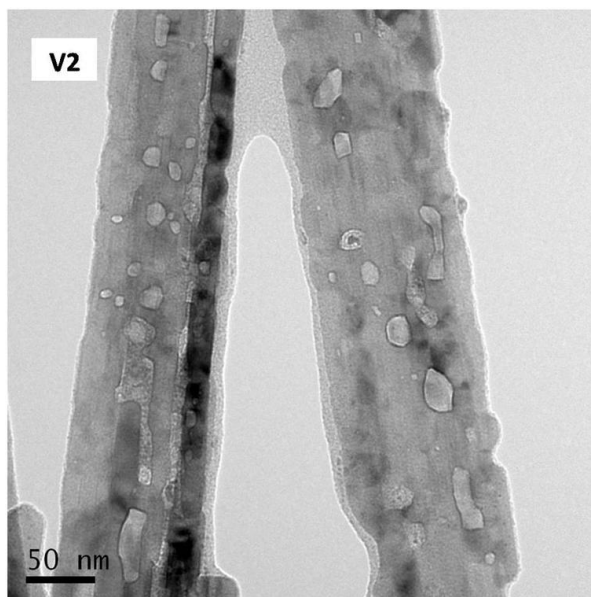
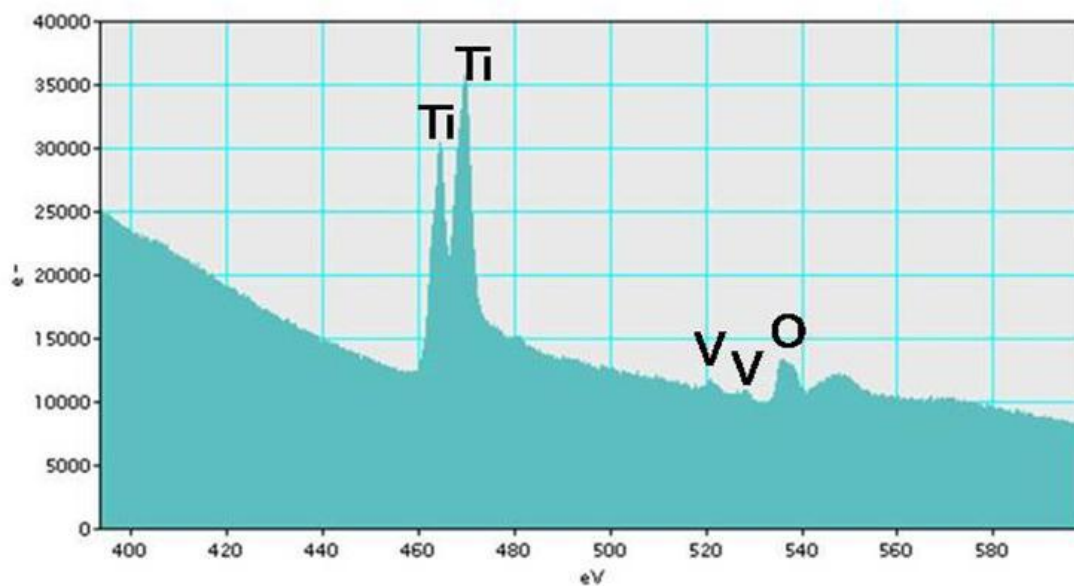


Figure 3.12 TEM picture of V2



**Figure 3.13 TEM picture of V2. Pores are visible**

For all the samples, the electron energy loss spectroscopy has been carried out on the nanotubes. As shown in the Figure 3.14, the peaks of Ti, V and O are present on the same spectrum, proving the presence of vanadium on the TiO<sub>2</sub>-B.



**Figure 3.14 EELS spectrum on doped nanotubes**

### 3.1.3 Discussion

Table 3.2 sums up XRD, Raman and TEM results of vanadium doped anatase nanotubes:

Name	Calcination temperature (° C)	XRD (Phase)	Raman (%anatase)	TEM [l (μm)*φ (μm)]±0.5
V0	400	TiO <sub>2</sub> -B, anatase	80	0.5-1.29 * 0.065-0.13
V0.5	400	TiO <sub>2</sub> -B, anatase	2	
V1	500	TiO <sub>2</sub> -B, anatase	9	0.4-0.8 * 0.1
V2	600	TiO <sub>2</sub> -B, anatase	4	0.72-1.45 * 0.18

Table 3.2 Vanadium doped nanotubes. \*l is the length, ζ is the diameter

As a conclusion, we can summarize here that we can see that in V0 the major phase is anatase, while the doped samples are TiO<sub>2</sub>-B with a little (lower than 10%) amount of anatase. Length of nanotubes is in the range 0.4-1.45 μm, diameter in the range of 0.065-0.18 μm.

## 3.2 Nitrogen-doped aerogels and xerogels

### 3.2.1 Elaboration

#### 3.2.1.1 Synthesis, drying and calcination

Aerogels and xerogels materials were elaborated following the general procedure described in the second chapter of this manuscript. The present sol-gel process only differs from the one presented in chapter 2 by the use of a nitrogen-based specie. Urea (H<sub>2</sub>NCONH<sub>2</sub>) has been selected as the nitrogen source. As we have described in the bibliography part, urea has already been used as a rather *simple* nitrogen source in some chemical routes involving sol-gel techniques. Urea, in fact, is easy to manipulate and is not toxic which is in quite good accordance with *soft* chemistry spirit. Within the frame of this work, urea has been solubilized in solution A (composed of the HNO<sub>3</sub> catalyst, water and 75% of the total volume of isopropanol) still at room temperature under mechanical stirring. Compared to the standard recipe (*i.e.* without addition of urea), solution B remains unchanged.

After four days aging at room temperature in mother liquor and washing with isopropanol, the gels have been dried either by (slow<sup>50</sup>) evaporation in room conditions for xerogels (corresponding samples are noted XN) or by supercritical CO<sub>2</sub> drying for aerogels (corresponding samples are noted AN). Once dried, all the materials have been calcined in air at 500 °C for 2 hours (keeping the same ramp of 2 °C/min as previously used). Figure 3.15 summarizes the general scheme of the elaboration process.

Note that:

---

<sup>50</sup> To be sure to remove the huge majority of the entrapped solvent in *simple* room conditions, duration of the evaporation step has been significantly overestimated. In my specific conditions, evaporative drying stands for 45 days.

- Unless specified, the results presented here concern the calcined materials.
- Within this chapter, AN0 and XN0<sup>51</sup> correspond to the same formulation as A500 and X500 respectively (*confer* chapter 2) but are different samples (*i.e.* are coming from different elaboration batches).

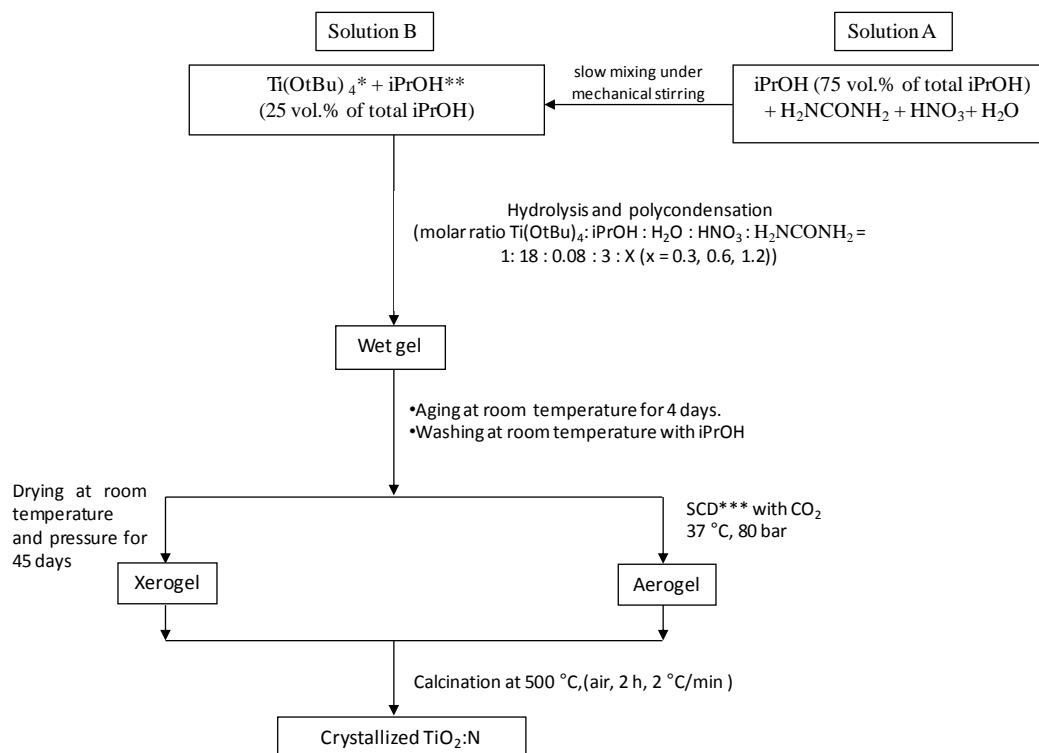


**Figure 3.15. Scheme of the elaboration process of N-modified xerogels and aerogels**

(\*Ti(OtBu)<sub>4</sub> is the titanium tert-butoxide, \*\* iPrOH is isopropanol, \*\*\*SCD is supercritical CO<sub>2</sub> drying)

### 3.2.1.2 Samples

The amounts of urea have been calculated based on the urea/TiO<sub>2</sub> ratio following the articles of Yuan *et al.* [Yuan et al., 2006], Horikawa *et al.* [Horikawa et al., 2008] and Zacharaki *et al.* [Zacharaki et al., 2008]. They are reported in Table 3.5. These amounts correspond actually to theoretical 0.3, 0.7 and 1.3 N/O at% in the TiO<sub>2</sub> matrix, assuming a complete reaction of urea.

The amounts of alkoxyde (Ti(OtBu)<sub>4</sub>) have been calculated hypothesizing that the precursor is completely reacting to give TiO<sub>2</sub>.

<sup>51</sup> These notations are only used for N<sub>2</sub> physisorption analysis and XPS characterizations.

Sample	Expected Urea/TiO <sub>2</sub> wt%	Experimental Urea/ Ti(OC <sub>4</sub> H <sub>9</sub> ) <sub>4</sub> wt%	Theoretical N/O at%
AN0.25 and XN0.25	0.25	0.06	0.3
AN0.5 and XN0.5	0.5	0.12	0.7
AN1 and XN1	1	0.24	1.3

**Table 3.3** Expected and experimental urea ratios for N-modified TiO<sub>2</sub> aerogels and xerogels and corresponding theoretical N/O ratio

The color of the calcined chemically modified materials varied with the urea ratio and the drying method (Figures 3.16 and 3.17). After calcination, the as-prepared photocatalyst is white, contrary to colored N-modified samples. Increasing the urea concentration in the sol tends to color the samples in yellow. The yellowish color is all the more pronounced that urea concentration is high. Furthermore, it can be underlined here that the color of aerogels only slightly changes with the urea concentration while the variation of that of xerogels is significantly stronger.

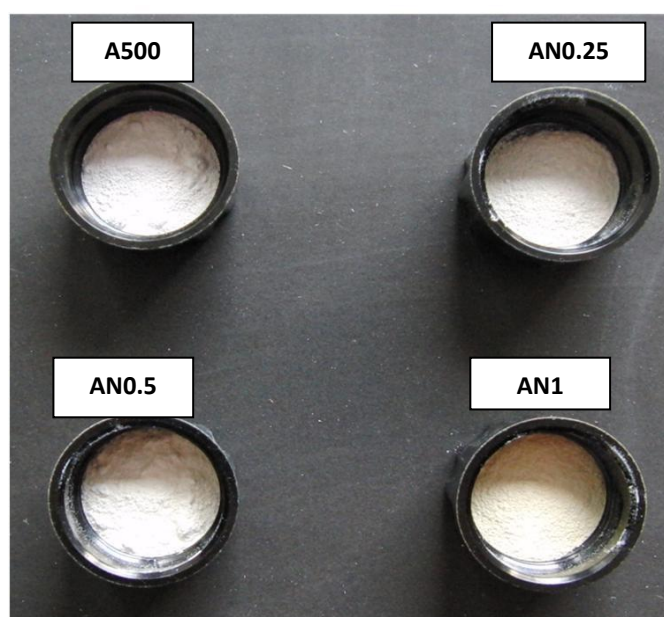


**Figure 3.16** Colors of A500 and N-modified TiO<sub>2</sub> aerogels after calcination (air, 500 °C, 2 °C/min, 2h)

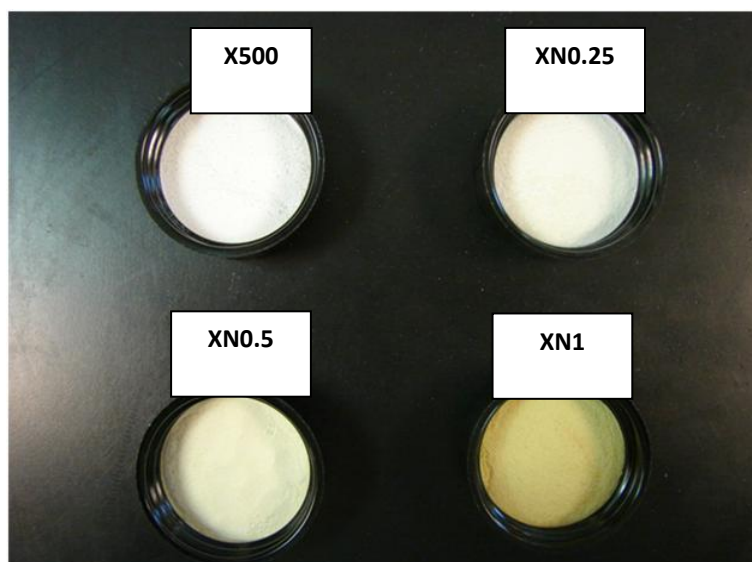


Figure 3.17 Colors of X500 and N-modified TiO<sub>2</sub> xerogels after calcination (air, 500 °C, 2 °C/min, 2h)

### 3.2.2 Characterizations

#### 3.2.2.1 X-Rays Diffraction

X-Rays diffractograms of aerogels and xerogels (Figures 3.18 and 3.19) show that:

- all calcined samples are anatase,
- calcined xerogels are less crystallized than their aerogels counterparts, as already observed in the second chapter (Figure 3.20).

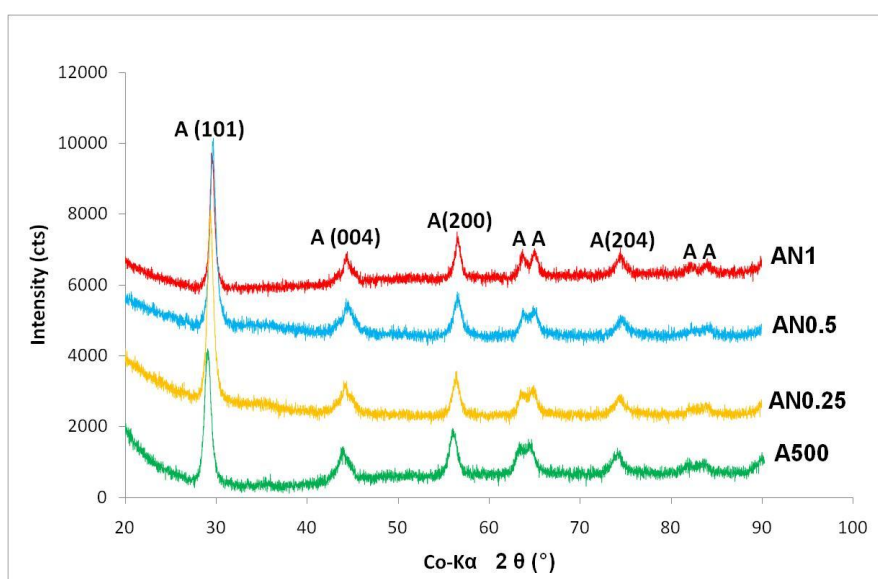
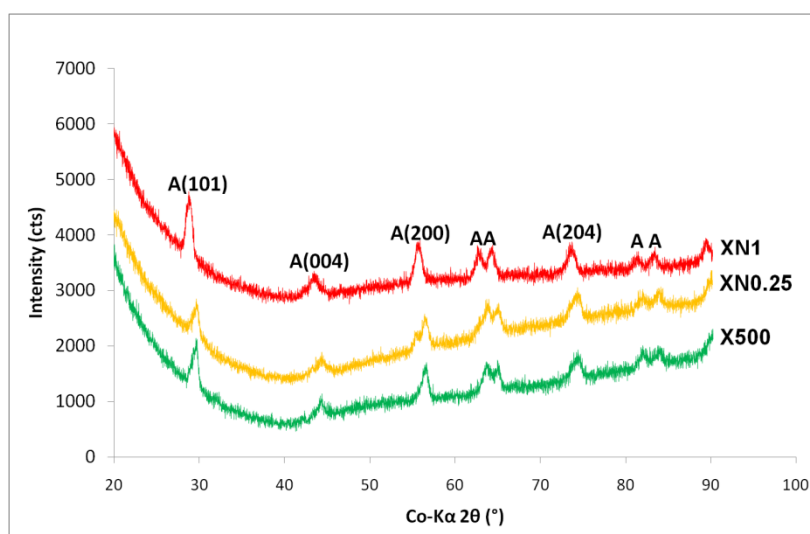
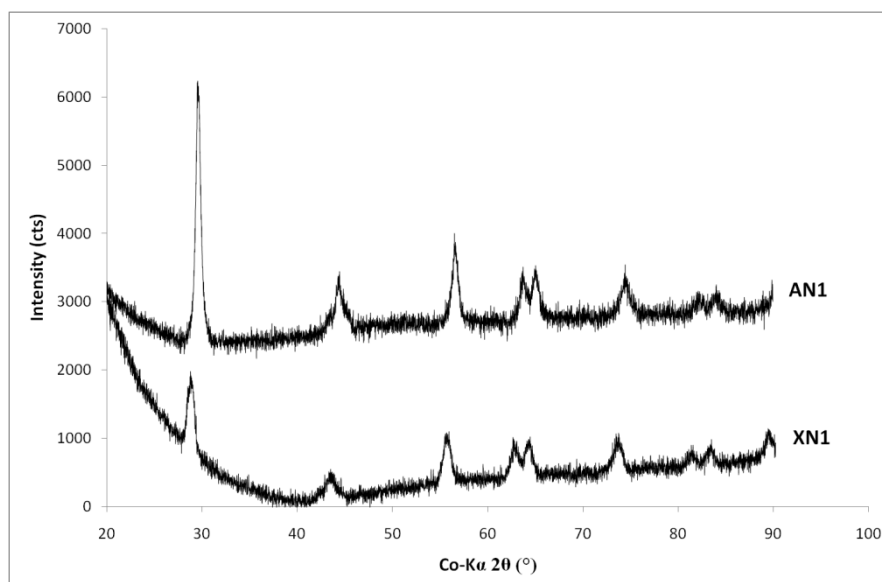


Figure 3.18 X-rays Diffractograms of A500 and N-modified TiO<sub>2</sub> aerogels



**Figure 3.19 X-Rays Diffractograms of X500 and N-modified TiO<sub>2</sub> xerogels**



**Figure 3.20 X-Rays Diffractograms of XN1 and AN1 samples**

Tables 3.4 and 3.5 present the crystallites size of calcined aerogels and xerogels using the Scherrer formula for the different following planes [101], [004], [004], [200] and [204].

First of all, we can observe that the crystallites size of aerogels is similar to that of xerogels, showing that the drying process does not modify it. In addition, the nitrogen modification does not seem to affect clearly this crystallite size both for aerogels and xerogels.

Sample	A500 L (nm) ± 0.4	AN0.25 L (nm) ± 0.4	AN0.5 L (nm) ± 0.4	AN1 L (nm) ± 0.4
A(101)	17	14	17	14
A(004)	18	11	15	18
A(200)	16	16	14	19
A(204)	12	13	17	17

**Table 3.4. Crystallites size of N-modified TiO<sub>2</sub> aerogels (calculated using the Scherrer formula)**

	X500 L (nm) ± 0.4	XN0.25 L (nm) ± 0.4	XN1 L (nm) ± 0.4
A(101)	14	14	14
A(004)	15	15	13
A(200)	16	16	13
A(204)	17	13	13

**Table 3.5. Crystallites size of N-modified TiO<sub>2</sub> xerogels (calculated using the Scherrer formula)**

### 3.2.2.2 Raman spectroscopy

Figures 3.21 and 3.22 display Raman spectra of calcined aerogels and xerogels. For both families of materials, peaks of anatase at 144, 397, 518 and 640 cm<sup>-1</sup> can clearly be identified. It appears also clear that the characterized materials are only made of anatase (because no other phase are noticed) which confirms previous XRD results. Theoretically, Raman could detect other TiO<sub>2</sub> phases (like TiO<sub>2</sub>-B or rutile) and any peaks shift could permit to underline structural modifications due to incorporation of nitrogen in the samples. In the specific case of these samples, anatase is the only detected phase and position of the peaks of the samples suspected to contain N do not change regarding to as-prepared sample (*i.e.* prepared without urea in the sol). So we can conclude that the urea treatment has no observable effect on the crystalline structure of calcined aerogels.

Although, for practical reasons, we could not perform Raman spectroscopy of sample XN0 (nor X500), we can conclude it is also the case for xerogels. Indeed, the position of peaks of N-modified xerogels (XN0.25, XN0.5 and XN1) corresponds to that of anatase and XRD has already proven that XN0 is anatase.

Of course, deeper treatments of Raman spectra could permit to obtain more results (particularly from a fundamental point of view) but, within the frame of this work, we did not decide to do so.

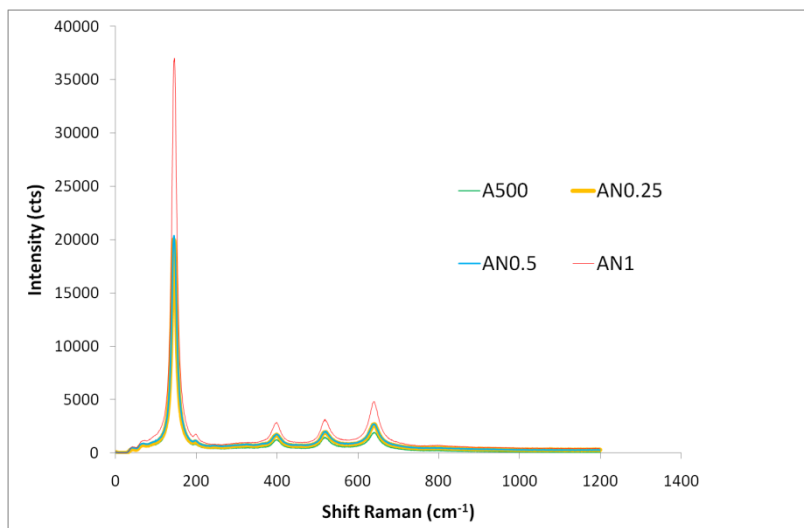


**Figure 3.21 Raman spectra of A500 and N-modified TiO<sub>2</sub> aerogels**

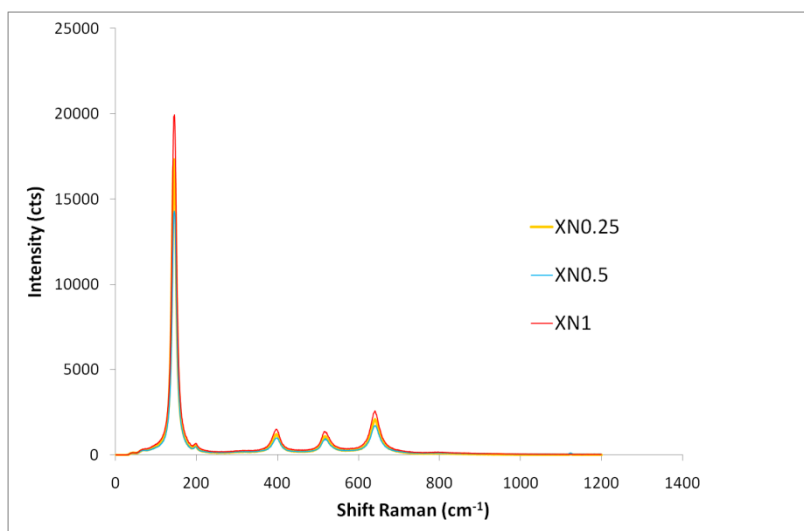


**Figure 3.22 Raman spectra of N-modified TiO<sub>2</sub> xerogels**

### 3.2.2.3 Transmission Electron Microscopy

TEM investigations (Figures 3.23 to 3.27) show that the solid skeleton of all the samples appears made up of aggregated particles. The characteristic size of these particles depends clearly on the drying process. In xerogels they are significantly bigger than in aerogels probably because of the densification coming from capillary stresses occurring during the drying step which is responsible of the collapse of the initial tenuous structure of the gel (as already explained in the bibliographic chapter).

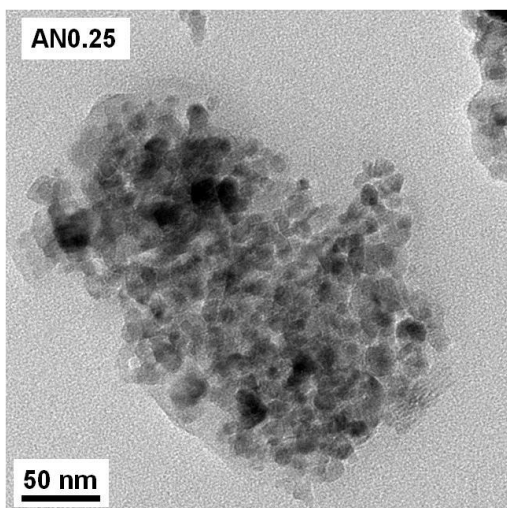


Figure 3.23 TEM of N-modified TiO<sub>2</sub> aerogel AN0.25

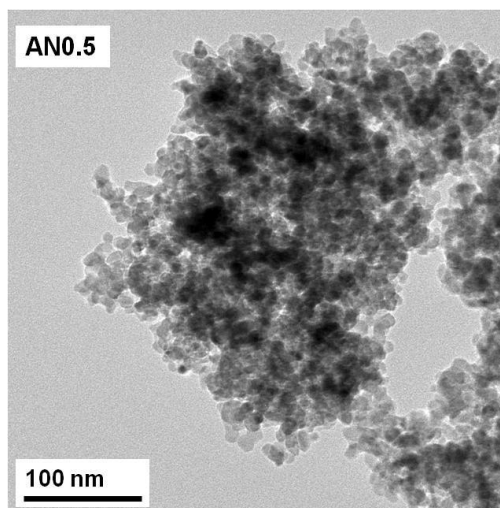


Figure 3.24 TEM of N-modified TiO<sub>2</sub> aerogel AN0.5

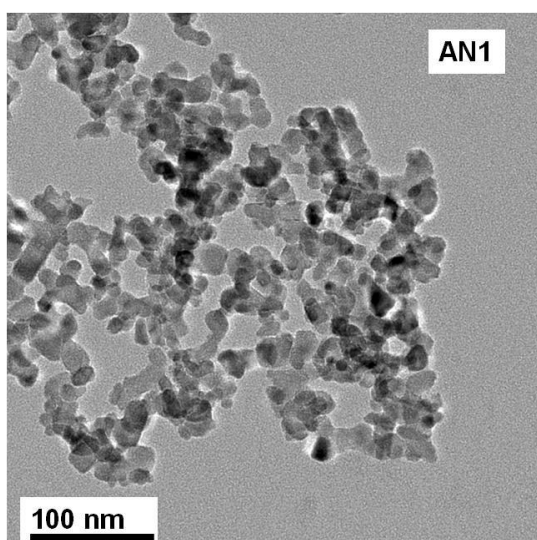


Figure 3.25 TEM of N-modified TiO<sub>2</sub> aerogel AN1

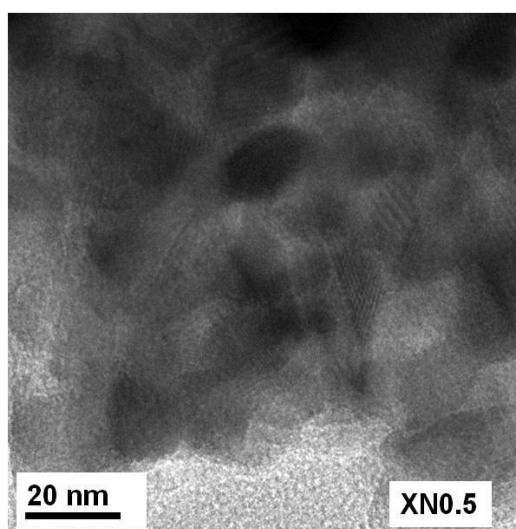
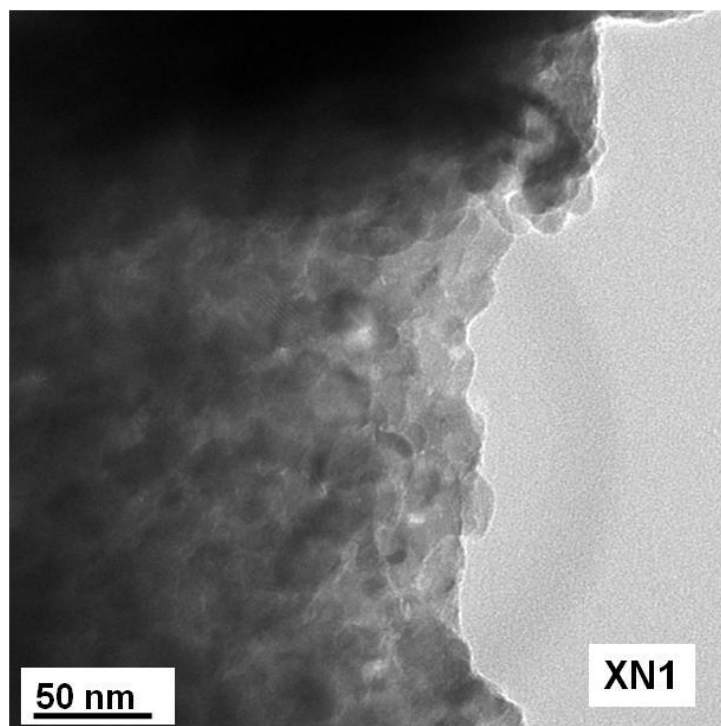


Figure 3.26 TEM of N-modified TiO<sub>2</sub> aerogel XN0.5



**Figure 3.27 TEM of N-modified TiO<sub>2</sub> aerogel XN1**

Table 3.6 sums up the estimation of the particles size of aerogels<sup>52</sup> from TEM micrographs. The particles size does not significantly evolve with the concentration of urea in the sol, showing that the eventual presence of nitrogen does not seem to deeply modify the morphology of the solid network. Moreover, it can be underlined that these results are rather close to the crystallite sizes  $L$  obtained previously from XRD data using the Scherrer formula.

<b>Sample</b>	<b>TEM <math>l</math> (nm) <math>\pm</math> 0.5</b>
A500	12
AN0.25	12
AN0.5	10
AN1	13

**Table 3.6 Particle average size ( $l$ ) from TEM images**

#### **3.2.2.4 Nitrogen adsorption/desorption**

For practical reasons, N<sub>2</sub> physisorption isotherms have only been obtained for aerogels. These isotherms have been treated by BET model in order to evaluate the specific surface area and by BJH model in order to characterize the pore size distribution (PSD).

<sup>52</sup> As already stated in chapter 2, evaluation of the particles size by simple observation of the TEM micrographs is not possible to be performed precisely. For example, some image analysis techniques are necessary to do so.

The figures 3.28-3.31 show N<sub>2</sub> physisorption isotherms of samples AN0, AN0.25, AN0.5 and AN1 respectively. The hysteresis of these isotherms is associated with capillary condensation taking place in mesopores [Sing, 1982]. The hysteresis shape of these isotherms is rather close to H1-type.

Specific surface areas ( $S_{\text{BET}}$ ) are in the range of 60 – 100 m<sup>2</sup>.g<sup>-1</sup>. Specific porous volumes derived from N<sub>2</sub> adsorption ( $V_p$ ) are in the range of 0.45 – 0.65 cm<sup>3</sup>.g<sup>-1</sup>. For both  $S_{\text{BET}}$  and  $V_p$ , results show no clear correlation with the concentration of urea in the sol (Table 3.9). For example, the sample AN0.5 has the largest specific surface area and specific pore volume, AN0.25, the smallest ones.

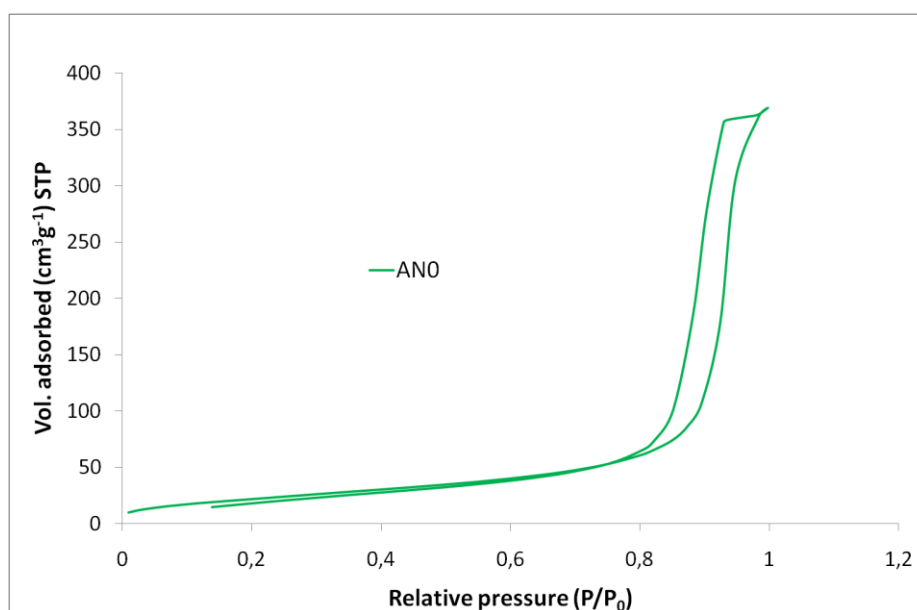


Figure 3.28 Sorption isotherm of AN0 TiO<sub>2</sub> aerogel

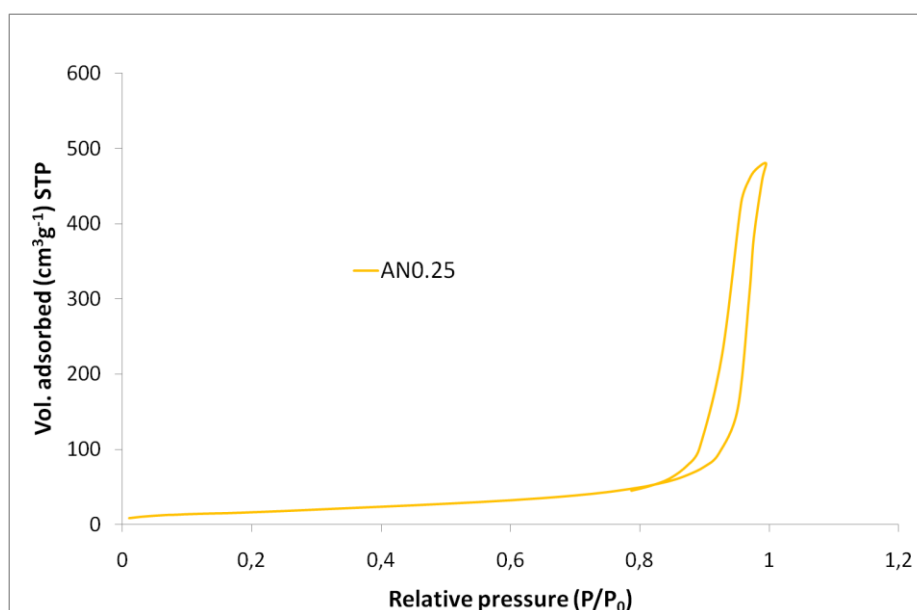


Figure 3.29 Sorption isotherm of AN0.25 TiO<sub>2</sub> aerogel

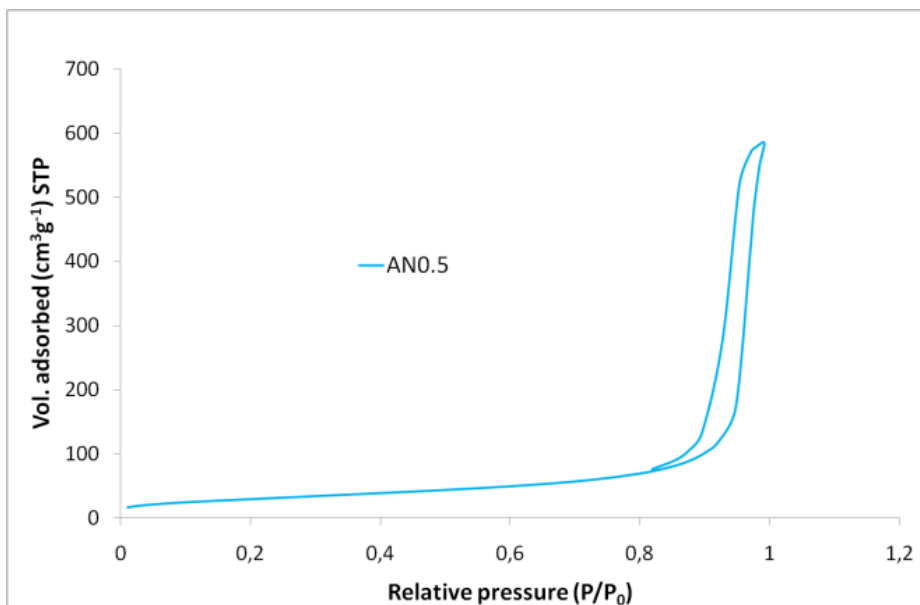


Figure 3.30 Sorption isotherm of AN0.5 TiO<sub>2</sub> aerogel

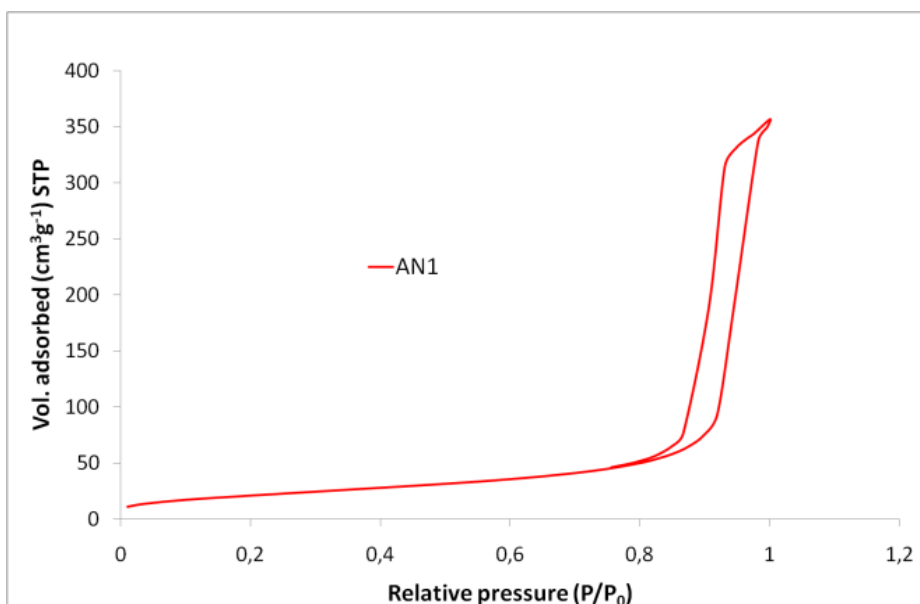


Figure 3.31 Sorption isotherm of AN1TiO<sub>2</sub> aerogel

The Figure 3.32 illustrates results of the BJH treatment of the adsorption branch. The PSD of all samples shows two main peaks which may correspond to two distinct major populations of pores. The first population (pore diameter noticed  $\delta_1$  in table 3.7) is centered on about 2.5 nm for all the aerogel samples. The characteristic size of the second one (pore diameter noticed  $\delta_2$  in Table 3.9) is rather larger: about 40 nm for AN0 and AN1, about 70 nm for AN0.25 and AN0.5 samples. This second family of pores appears predominant. Indeed, for AN0 aerogel, integrating the PSD shows that the volume fraction corresponding to the larger pores ( $\delta_2$ ) is around 91%, for AN0.25 it is 94% and 93% for AN0.5 and AN1 respectively.

From these results, the characteristic particle size ( $D$ ) has been estimated. As XRD has shown that all aerogel samples are anatase, we have assumed a skeletal  $\text{TiO}_2$  density of  $3.9 \text{ g.cm}^{-3}$  [Dagan and Tomkiewicz, 1993] to calculate  $D$ . This geometrical analysis gives results rather far from the ones obtained by TEM:  $D$  appears significantly larger than  $l$  (i.e. an average value of 19 nm instead of 12 nm). This is probably resulting from the simplicity of the techniques used to estimate these values (compared to more accurate methods like SAXS<sup>53</sup>).

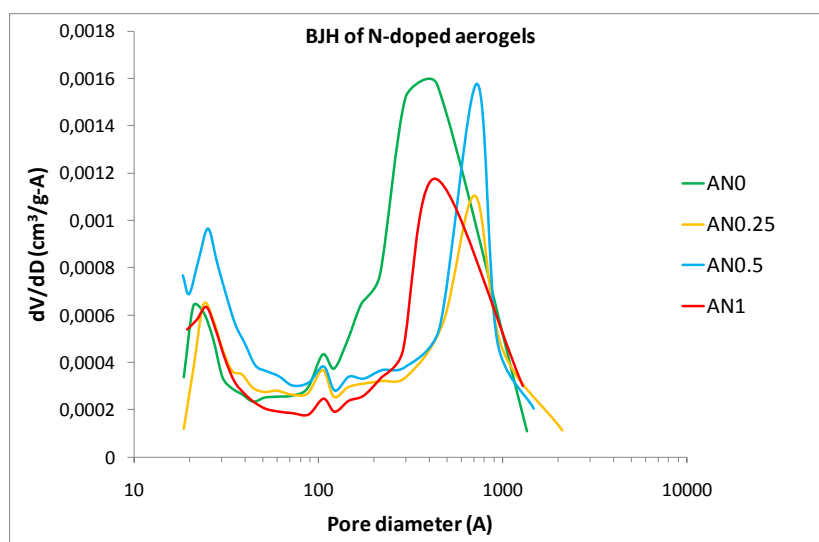


Figure 3.32 BJH of AN0, AN0.25, AN0.5 and AN1 aerogels

Sample	$S_{\text{BET}} \pm 0.32^*$ ( $\text{m}^2 \text{g}^{-1}$ )	$V_p$ ( $\text{cm}^3 \text{g}^{-1}$ )	$\delta_1$ (nm)	$\delta_2$ (nm)	$D \pm 0.3$ (nm)
AN0 <sup>54</sup>	83	0.56	2.1	44	18
AN0.25	60	0.47	2.4	71	25
AN0.5	107	0.65	2.5	73	14
AN1	78	0.52	2.5	43	19

Table 3.7 Data from BET and BJH treatments:  $V_p$  is the specific pore volume,  $\delta_1$  and  $\delta_2$  correspond to pore size population directly issued from BJH curves, and  $D$  is the characteristic particles diameter calculated from the following geometric formula  $D = 6/(S_{\text{BET}} \times \rho_s)$ . \*The errors quoted here are the average of the errors of each sample.

<sup>53</sup> Small Angle X-ray Scattering.

<sup>54</sup> From this table, it can be seen that surface areas from  $\text{N}_2$  physisorption results on AN0 and A500 materials are quite close: 97  $\text{m}^2/\text{g}$  for A500 (cf chapter 2) and 83  $\text{m}^2/\text{g}$  for AN0. These two values may underline the rather correct reproducibility of the experimental procedure.

### 3.2.2.5 Elementary analysis

The chemical compositions of one set of N-modified aerogels and xerogels have been characterized by elementary analysis in order to check the amount of nitrogen effectively present in the final materials. Five elements (Ti, O, C, H and N) have been analyzed. Table 3.8 sums up the results.

First of all, as for not-chemically modified materials (*cf* chapter 2), Ti and O are the main elements of the final materials and their experimental mass percentage are very close to the expected theoretical ones for pure TiO<sub>2</sub> (60 % for Ti, 40 % for O, which correspond to atomic fraction of 1/3 for Ti and 2/3 for O).

Traces of C and H can also be detected (slightly above the detection threshold of 0.3 wt%), respectively for some xerogels (XN0.25 and XN0.5) and some aerogels (A500 and AN0.5). As for not-modified materials, we could hypothesize that the traces of C and H could be due to the presence of both titanols ( $\equiv\text{Ti-OH}$ ) and alcoxy groups ( $\equiv\text{Ti-OC}_4\text{H}_9$ ) issued from uncomplete hydrolysis-condensation reactions occurring during the sol-gel synthesis. Of course, part of residual C and H could also come from remaining urea and/or eventual reaction products.

Finally, traces of N have also been detected (slightly above the detection threshold of 0.1 wt%), proving that some N atoms coming from urea, the only possible nitrogen source in the process, are present in the final materials. However we have obtained a significant value only for the samples coming from the most concentrated sols: AN1 and XN1. Based on this value, we can roughly estimate that only 30% of the expected nitrogen amount has been retained in the final TiO<sub>2</sub> network.

Sample	Ti (wt.%)	O (wt.%)	C (wt. %)	H (wt. %)	N (wt. %)	Tot. % ± 2*
A500	57.33	40.64	< threshold (= 0.30)	0.53	< threshold (= 0.10)	98.8
AN0.25	57.38	39.14	< threshold (= 0.30)	< threshold (= 0.30)	<threshold (=0.10) Expected value : 0.12	97.28
AN0.5	57.50	40.44	< threshold (= 0.30)	0.46	< threshold (= 0.10) Expected value : 0.23	98.80
AN1	56.02	39.86	< threshold (= 0.30)	< threshold (= 0.30)	0.17 Expected value : 0.47	96.65
X500	57.50	36.33	< threshold (= 0.30)	< threshold (= 0.30)	< threshold (= 0.10)	94.43
XN0.25	56.90	37.74	0.59	< threshold (= 0.30)	< threshold (= 0.10) Expected value : 0.12	95.63
XN0.5	57.40	40.43	0.35	< threshold (= 0.30)	< threshold (= 0.10) Expected value : 0.23	98.58
XN1	59.30	35.56	< threshold (= 0.30)	< threshold (= 0.30)	0.13 Expected value : 0.47	95.64

**Table 3.8 Elementary analysis of N-modified TiO<sub>2</sub> aerogels and xerogels<sup>55\*\*</sup>As total error we have considered the maximum error of Ti and O.**

### 3.2.2.6 X-Rays Photoemission Spectroscopy characterization

X-Rays Photoemission Spectroscopy (XPS) has been performed at Nancy University (by Dr. Yannick Fagot-Revurat, *Institut Jean Lamour*) in order to *i*) check the presence of nitrogen, *ii*) investigate the doping states of nitrogen atoms and *iii*) check their influence on the top of the valence band.

To this end, both core electrons of Ti2p, O1s and N1s orbital and peripheral electrons of O2p, N2p or Ti3d orbital have been sounded, the former to characterize the doping and the latter to characterize the valence band.

<sup>55</sup> Finally, to be as precise as possible, it must be underlined here again that for all samples the sum of the experimental data is classically lower than 100%, for the same experimental reasons stated in chapter 2.

### • Doping characterization

First of all, Ti 2p and O 1s XPS spectra of aerogel and xerogel samples are presented respectively on Figures 3.33 and 3.34. The results are in good agreement with what has been previously reported in literature ([Asahi et al., 2001], [Horikawa et al., 2008], [Fujishima et al., 2008]), showing two peaks at 459.4 and 465.2 eV for Ti 2p, corresponding to  $\text{Ti}^{4+}$ , and one peak at 530.7 eV for O 1s.

At least for aerogels (Figure 3.33), we can notice an almost perfect superposition of the spectra of Ti 2p and O 1s of undoped sample (A500) with chemically modified ones (AN0.5 and AN1). This observation is in agreement with results from Beranek *et al.* [Beranek and Kisch, 2007] who also pointed out no significant shift of the Ti 2p binding energy for  $\text{TiO}_2:\text{N}$  compared to pristine  $\text{TiO}_2$ . Concerning xerogels, only XN1 sample has been characterized. The Ti 2p related peaks are again located at 459.4 and 465.2 eV. For O 1s, besides the peak at 530.7 eV, already observed on aerogel samples, the spectrum shows an additional peak at 533 eV (Figure 3.35). This peak is typical of the binding energy of titanols (i.e.  $\equiv\text{Ti-OH}$ ), probably issued from the synthesis method and/or posterior hydroxylation of the surface [Jun et al., 2006].

It is noteworthy that no shoulder at 455 eV on the first Ti 2p related peak (459.4 eV), ascribed in the literature to the presence of  $\text{Ti}^{3+}$  [Batzill et al., 2006] has been observed, neither for aerogels nor for xerogels. Hence, the chemical modification of these samples does not seem to induce any  $\text{Ti}^{3+}$ .

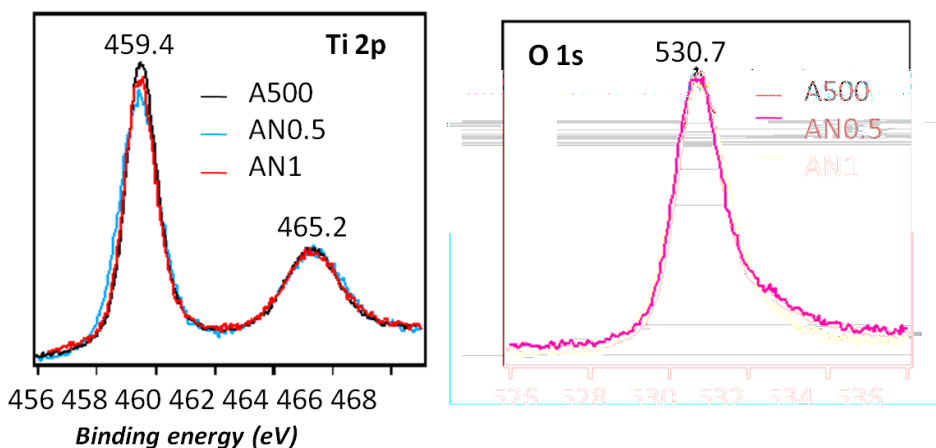


Figure 3.33 Ti 2p and O 1s XPS spectrum of A500, AN0.5 and AN1 aerogels (Mg-K $\alpha$ ;  $h\nu = 1254,6$  eV)

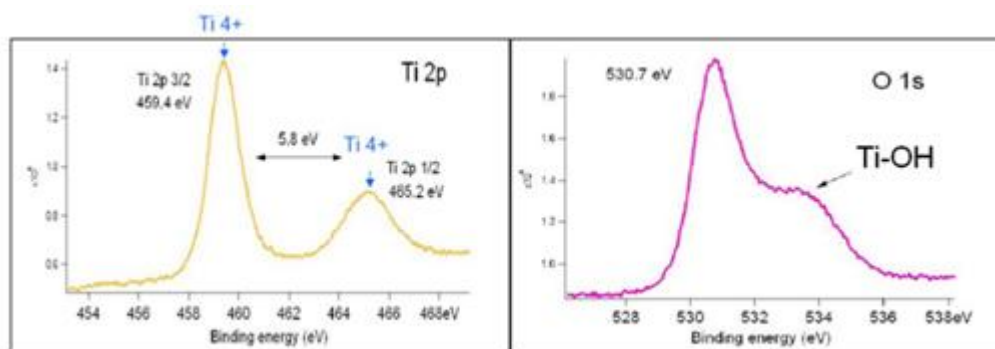


Figure 3.34 Ti 2p and O 1s XPS spectrum of XN1 xerogel (Mg-K $\alpha$ ;  $h\nu = 1254,6$  eV).

The N1s XPS spectra of chemically modified aerogel and xerogel samples are presented on the figure 3.35, both showing a peak at 400.3 eV.

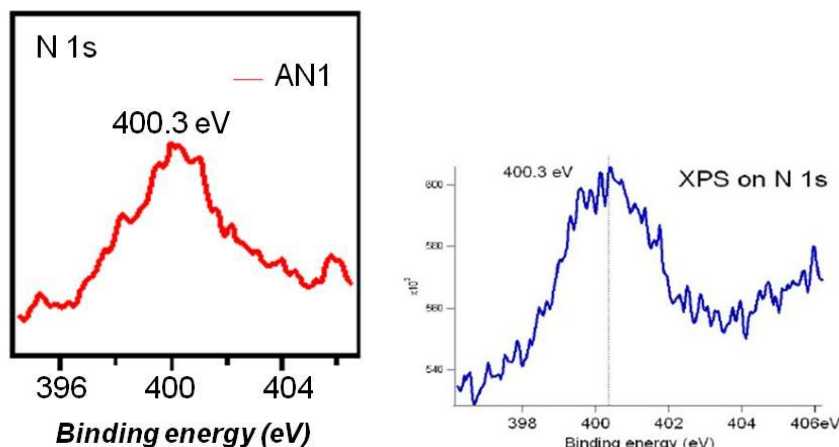


Figure 3.35 N 1s XPS spectrum of AN1 aerogel (left) and XN1 xerogel (right) (Mg-K $\alpha$  ;  $h\nu = 1254,6$  eV).

Since the pioneer work of Asahi [Asahi et al., 2001] on TiO<sub>2</sub>, several scientists (among others, [Sato, 1986] and [Livraghi et al., 2006]) have tried to associate the binding energy of a given XPS peak to specific chemical bounds of nitrogen atom.

These XPS studies of N-modified TiO<sub>2</sub> materials generally report two kinds of N 1s peaks : one at around 396 eV, the other one at around 400 eV which is often observable for materials issued from chemical elaboration in liquid phase ([Sakthivel et al., 2004] and [Diwald et al., 2004]).

Fujishima [Fujishima et al., 2008] assigned the N 1s peak at around 396 eV to a substitutional N doping and to Ti-N bounds [Nosaka et al., 2005], and the N 1s peak at 400 eV to an interstitial N doping, due to nitrogen compounds (as mentioned in Table 3.11). This has been confirmed by Beranek et al. [Beranek and Kisch, 2007] who studied TiO<sub>2</sub>:N films using urea as nitrogen source. In the related article the N 1s signal at 400.4 eV is attributed to nitrogen

species in a higher oxidation state, perhaps hyponitrite<sup>56</sup> or an NO site within the TiO<sub>2</sub> matrix. So these authors stated that nitrogen is in the form of nitrogen compounds and not as an element in the lattice.

Table 3.9 sums up some of the main representative examples found in the literature about XPS analysis of nitrogen-doped TiO<sub>2</sub> materials in relation with the elaboration process (not only by sol-gel). This table clearly underlines that the nitrogen state depends on the elaboration process. Treatment of single crystals of rutile with ammonia seems to give substitutional doping [Diwald et al., 2004], while sol-gel route seems to induce interstitial doping.

Consequently, following the considerations of the literature together with our XPS characterizations showing a peak at 400.3 eV, we could hypothesize that we have obtained, for both aerogel and xerogel samples, an interstitial N-doping due to the insertion of some nitrogen compounds, still to be determined, probably coming from the urea degradation during the samples elaboration.

Unfortunately, we did not have the possibility to perform N 1s XPS analysis of AN0.25 and AN0.5 aerogels for one hand and XN0.25 and XN0.5 xerogels for the other hand. Consequently, regarding elementary analysis results, presence of nitrogen in these samples remains *questionable* (cf. Table 3.8).

---

<sup>56</sup> Hyponitrite : N<sub>2</sub>O<sub>2</sub><sup>2-</sup>, ([ON=NO]<sup>2-</sup>).

Authors	Elaboration route	XPS position of N 1s peaks (eV)	Associated N-based chemical bounds
Ananpattarachai et al. [Ananpattarachai et al., 2009]	Sol-gel : TTIP* : EtOH : HNO <sub>3</sub> : H <sub>2</sub> O : urea = 1 : 20 : 1 : 1 : 1 molar ratio Calcination at 800 °C	402.5 406.1 409.7	-
Beranek et al. [Beranek and Kisch, 2007]	Sol-gel : Film of TiO <sub>2</sub> in a Schlenk tube with urea heated in a muffle oven at 400 °C	400.4	Hyponitrite or NO
Cong et al. [Cong et al., 2007]	Sol-gel: Cyclohexane, Ti(OtBu) <sub>4</sub> ** and HNO <sub>3</sub> , triethylamine, urea, thiourea, and hydrazine hydrate. Crystallization under hydrothermal conditions at 120 °C for 13 h	401.2	-
Diwald et al. [Diwald et al., 2004]	Rutile (111) single crystal treated at 597 °C with NH <sub>3</sub>	396.7 399.6	N <sup>2-</sup> N-H
Nosaka et al. [Nosaka et al., 2005]	Mixing of commercial TiO <sub>2</sub> powders with aqueous solution of urea	396 400 400 400	Ti-N N-N N-C N-O
Horikawa et al. [Horikawa et al. 2008]	Sol-gel : TTIP* : Cyclohexane = 1 : 2.5 molar ratio. + N-doping via mechanical mixing of dried samples and urea, followed by treatment under NH <sub>3</sub> or N <sub>2</sub> +NH <sub>3</sub> at 500 °C.	ca. 400	-
Prokes et al. [Prokes et al., 2005]	Direct nitridation at room temperature of porous TiO <sub>2</sub> nanocolloids using alkyl ammonium compounds	401.3	Ti-O-N
Sakthivel et al. [Sakthivel et al., 2004]	Sol-gel: TTIP* or TiCl <sub>4</sub> + urea (no detail on the reagents ratio) Calcinations at 400-600 °C	400.1 405.3 and 412.2 406.8 and 409.2	hyponitrite nitrite nitrite nitrate nitrate
Wei et al. [Wei et al., 2008]	Sol-gel : Ti(OtBu) <sub>4</sub> ** : EtOH : H <sub>2</sub> O : urea with H <sub>2</sub> O : C <sub>2</sub> H <sub>5</sub> OH = 1 : 9 volume ratio	400.1	γ-N <sub>2</sub> molecular chemisorbed to titanium

**Table 3.9 Literature overview of XPS study of N-doped TiO<sub>2</sub> materials with urea**  
(\*TTIP is the titanium isopropoxide and \*\* Ti(OtBu)<sub>4</sub> is the titanium tert-butoxide)

• *Investigation of the valence band*

Since anionic doping may affect the valence band of TiO<sub>2</sub>, Dr. Yannick Fagot-Revurat studied by XPS the electronic state of the valence band of AN0, AN0.5 and AN1 within the frame of a collaborative action.

The Figure 3.36 displays main results of this investigation. The red line corresponds to experimental data and the black one to a fit of these data. The dotted line indicates the deconvolution of the two peaks, the dashed line the background. Three peaks have been observed, at 5.5 and 8 eV for the undoped aerogel (A500) plus one additional peak shifting from 4 to 3 eV respectively for AN0.5 and AN1.

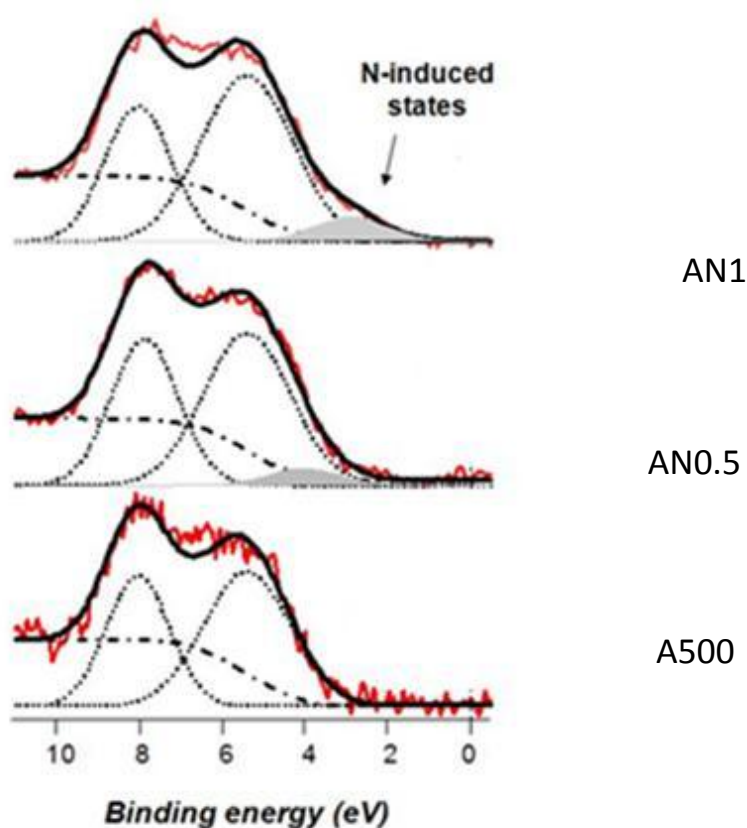


**Figure 3.36 Investigation on the influence of nitrogen on the valence band of A500, AN0.5 and AN1 samples by XPS (Mg-K $\alpha$ ; hv=1254.6 eV)**

First of all, these XPS measurements show that the doping did not entail the formation of any oxygen vacancies, that would have induced a new peak at 1 eV [Batzill et al., 2006], thus confirming that no Ti<sup>3+</sup> is formed. It must be noticed here that Batzill et al., performed UPS<sup>57</sup>,

<sup>57</sup> Ultra-violet Photoemission Spectroscopy

spectroscopy more surface sensitive than XPS. However, energy used for our XPS study is small enough to detect eventually oxygen vacancies and, consequently,  $Ti^{3+}$ .

The peaks at 5.5 eV is assigned to nonbonding O 2p states [Gopel et al. 1984], while the peak at 8 eV to hybridisation of O 2p with Ti 3d states [Takahashi et al., 2008].

From these results we can see that for AN0 the only contribution to the valence band is given by O 2p orbital and that value of the top of the valence band is 3 eV, corresponding to the starting of the red and black curves, as we have reported in chapter 1. So the contribution in the valence band is still given by O 2p and not by O 2 p plus Ti 3d orbitals [Batzill et al., 2006].

Comparing our data with literature [Batzill et al., 2006], we can suppose that doping induces new states above the valence band, and shifts the starting point of the curves of AN0.5 and AN1 between 3 and 1 eV. Takahashi et al. [Takahashi et al., 2008] attributes this shift to the presence of low bandgap states, which are an extension of the valence band and are assigned to N 2p derived states.

As in Batzill study, the O 2 p-derived maximum of the peak at 5.5 eV of AN0, AN0.5 and AN1 did not shift. Comparing our results with Batzill's ones suggests that the N-induced states are due to localized N 2 p states whose maximum peak intensity can be seen between 4 and 3 eV depending on the doping ratio. This result supports most recent Density Functional Theory (DFT) calculations [Valentin et al., 2007] Di Valentin et al. report that interstitial nitrogen states lie higher in the gap, at around 450 nm. So visible light irradiation induces an electronic transition not from band to band but from localized states to the conduction bands.

Complementary Infra Red and Electron Paramagnetic Resonance (EPR) analysis [Valentin et al., 2007] should be performed to investigate the chemical state of nitrogen.

### 3.2.3 Discussion

Table 3.10 sums up main results of characterizations on our calcinated N-doped  $TiO_2$  aerogels and xerogels. I have obtained anatase samples for all chemically modified samples. The presence of nitrogen compounds in the  $TiO_2$  matrix does not significantly modify the texture and the structural properties of both calcined aerogels and xerogels materials. Besides, elementary analysis have stressed that very little N amount remains in the  $TiO_2$  matrix. Experimental data show only approximately one third of the intended amount has finally been retained in the matrix, at least for both AN1 and XN1 samples. A loss of nitrogen (in molecular and/or intermediate compounds form) during the different steps of elaboration, as drying and calcination, could be invoked. Further investigations are obviously necessary to explain this preliminary result.

In parallel, XPS investigations have shown that both aerogels and xerogels are N-doped and the presence of a N 1s peak at 400.3 eV argues for an interstitial doping.

Sample	L (nm) <i>A(101)</i>	l (nm)	S <sub>BET</sub> ± 0.32 (m <sup>2</sup> g <sup>-1</sup> )	D (nm)	N wt%
A500	17 <sup>A</sup>	12 <sup>A</sup>	83	18	< threshold (= 0.10)
AN0.25	18 <sup>A</sup>	12 <sup>A</sup>	60	25	< threshold (= 0.10)
AN0.5	16 <sup>A</sup>	11 <sup>A</sup>	107	14	< threshold (= 0.10)
AN1	12 <sup>A</sup>	13 <sup>A</sup>	77	19	0.17
XN0	14 <sup>A</sup>	-	-	-	< threshold (= 0.10)
XN0.25	15 <sup>A</sup>	-	-	-	< threshold (= 0.10)
XN0.5	16 <sup>A</sup>	-	-	-	< threshold (= 0.10)
XN1	17 <sup>A</sup>	-	-	-	0.13

**Table 3.10 Summary of the results from XRD, TEM and N<sub>2</sub> sorption isotherms analysis plus elementary analysis (N wt%). For XRD and TEM results, phase is anatase (A). *L* is the crystallite size from Scherrer treatment of XRD curves, *l* is the average particle size estimated from observation of TEM micrographs, S<sub>BET</sub> is the specific surface area from BET treatment of N<sub>2</sub> sorption isotherms, D is the average particles size from geometrical treatments of BET data from N<sub>2</sub> sorption isotherms**

A noticeable point of the sol-gel synthesis procedure followed in this study is the use of HNO<sub>3</sub> as a catalyst. Literature is very poor on the interaction of HNO<sub>3</sub> with the metal precursor (titanium-tert-butoxyde) [Cheng et al., 2004], [Chen et al., 2005]. However it seems to be probable that HNO<sub>3</sub> not only catalyzes the sol-gel reaction but also the degradation of urea [Tokmakov et al. [http://www.chem.missouri.edu/Thompson/research/Tokmakov-Alavi-Thompson\\_JPCA\\_revised.pdf](http://www.chem.missouri.edu/Thompson/research/Tokmakov-Alavi-Thompson_JPCA_revised.pdf)]. Consequently, the influence of the degradation of urea on N-doping of the final product could be an interesting point to be studied in further works on this topic. In order to contribute to answer to this question, I have summarized in the Table 3.10 some examples found in the literature about N-doped TiO<sub>2</sub> materials elaborated via sol-gel synthesis using urea as the nitrogen source as well as through mechanical mixing of TiO<sub>2</sub> and urea powders. Comparing these different elaboration routes might contribute to analyse if decomposing urea during the sol-gel synthesis is crucial for the final energetic states of the doping N-elements. This table clearly highlights that in all urea-based sol-gel systems, whatever the catalyst utilized, final materials are interstitially doped. So the catalyst seems to have no specific significant role on the resulting doping type. Even if differences in the elaboration processes lead to different nitrogen-based chemical species, analyzing data from the literature, we may conclude that HNO<sub>3</sub> does not seem to have a fundamental role in the doping mode of our final TiO<sub>2</sub> materials.

### 3.3 Conclusions

In this chapter I have described elaboration of vanadium-doped nanotubes and nitrogen-doped aerogels and xerogels and presented the associated characterization results.

Nanotubes have been elaborated by hydrothermal transformation followed by an ion exchange treatment, a wet impregnation with  $\text{VO}(\text{acac})_2$  and a calcination. Vanadium stabilizes  $\text{TiO}_2\text{-B}$  and hinders the evolution of this phase to anatase, the small amount of which is present in the form of nanoparticles.

Nitrogen-doped aerogels and xerogels have been synthesized via sol-gel synthesis using urea as the nitrogen source diluted in the sol. Some nitrogen has been retained in the final  $\text{TiO}_2$  matrix without modifying the porous and solid networks nor altering the comparison between aerogels and xerogels. Furthermore, XPS characterizations let us think that some interstitial N-doping has been realized through this simple way. Finally, XPS has also given information on the valence band: N 2 p states induce localized N-states and not a broadening of the valence band.



## 4. Evaluation of hydrogen evolution

In the previous two chapters I have described elaboration procedures of the TiO<sub>2</sub>-based nanomaterials I study and presented the associated characterization results. In the present chapter, I will first of all present results of diffuse reflectance UV-VIS spectroscopy characterization performed on these materials in order to estimate their bandgap. Then, I will report results of H<sub>2</sub> photogeneration obtained with the three different TiO<sub>2</sub> nanostructures (nanoparticles, nanotubes and aerogels/xerogels) and nitrogen-doped sol-gel photocatalysts. Our vanadium doping procedure, in fact, has been detrimental for the photocatalysis and V-doped samples showed an almost zero activity regarding watersplitting. Consequently, the related results have been reported in appendix 1.

Diffuse reflectance UV-VIS spectroscopy measurements have been carried out at Nice - Sophia Antipolis University (UNSA), in close collaboration with Professor M. Benabdesselam from LPMC H<sub>2</sub> tests have been performed in two institutes: Institute of Sustainability Science (ISS) at Kyoto University (with the close collaboration of Ass.-Prof. Yoshikazu Suzuki and Dr. Jaturong Jitputti who directly performed photolysis experiments) and Laboratory of Materials, Surfaces and Processes for the Catalysis (LMSPC) at University Louis Pasteur de Strasbourg – CNRS (in close collaboration with Dr. Nicolas Keller and Dr. Valérie Keller-Spitzer who supervised the tests I have realized). For both experimental sessions, two commercial products have been used: Degussa P25 and Anatase AlfaAesar 036199 as reference materials for comparison, of our samples with these very well-known commercial TiO<sub>2</sub> products.

Consequently, this fourth chapter is divided in four main interconnected parts as follows.

- Description of the experimental setup used in Kyoto and Strasbourg universities and samples preparation,
- Presentation of the structural and optical characterizations of the commercial materials used as references,
- Presentation of diffuse reflectance UV-VIS spectroscopy on the different TiO<sub>2</sub> nanomorphologies I have elaborated,
- Presentation of H<sub>2</sub> evolution results

## 4.1. Experimental set-up

### 4.1.1 Testing device and procedure

#### 4.1.1.1 General description

As already underlined, photoactivity testing has been carried out with two different reactors in two different laboratories:

- a reactor in which a continuous N<sub>2</sub> gas removes the gaseous products for sampling, in the Laboratory of Materials, Surfaces and Processes for the Catalysis (LMSPC),
- a reactor without any gas circulation, the sampling being realized directly in the reactor, in Institute of Sustainability Science at Kyoto University (ISS).

As described in the first chapter, photocatalytic reactors can be cell or slurry systems. Both used reactors in this thesis are slurry systems and for the two geometries the lamp is placed in the inner central part of the reactor. Complete assembly of the two reactors consists of:

- tank for suspension (distilled water, photocatalyst powders plus sacrificial reagent),
- magnetic stirrer,
- inner chamber for the lamp,
- jacket around the lamp chamber for controlling temperature of the lamp.

First of all, TiO<sub>2</sub> photocatalyst is suspended in distilled water solution and continuously stirred by magnetic stirrer to avoid sedimentation of the powder. To maintain constant the reaction temperature during the course of reaction and, above all, to cool the lamp, circulating water temperature is set at 30 °C for reactor in ISS and 15 °C in LMSPC. Tests are performed at atmospheric pressure. As explained in the chapter one, a TiO<sub>2</sub> water suspension for H<sub>2</sub> production needs a sacrificial reagent. For the carried out experiments, methanol (10 % vol. of total water solution) has been used. Before irradiation starts, air is purged with nitrogen (N<sub>2</sub>). N<sub>2</sub> purging is a crucial step because O<sub>2</sub> is a reaction product. If significant O<sub>2</sub> quantities from air still remain in the reactor before testing, analyses of data recorded during H<sub>2</sub> evolution experiments can lead to biased results and O<sub>2</sub> can react with the produced H<sub>2</sub> as well. After N<sub>2</sub> purging, operator can switch on the lamp and H<sub>2</sub> evolution experiments can start. During the water splitting test, an on-line gas phase chromatograph (GPC) analyzes the products of the reaction. Typically, such a test lasts five hours.

#### 4.1.1.2 Description of the ISS testing facility

For testing some of our materials, Ass-Prof. Suzuki and Dr. Jitputti performed experiments at Kyoto University, using the reactor illustrated in the Figure 4.1.

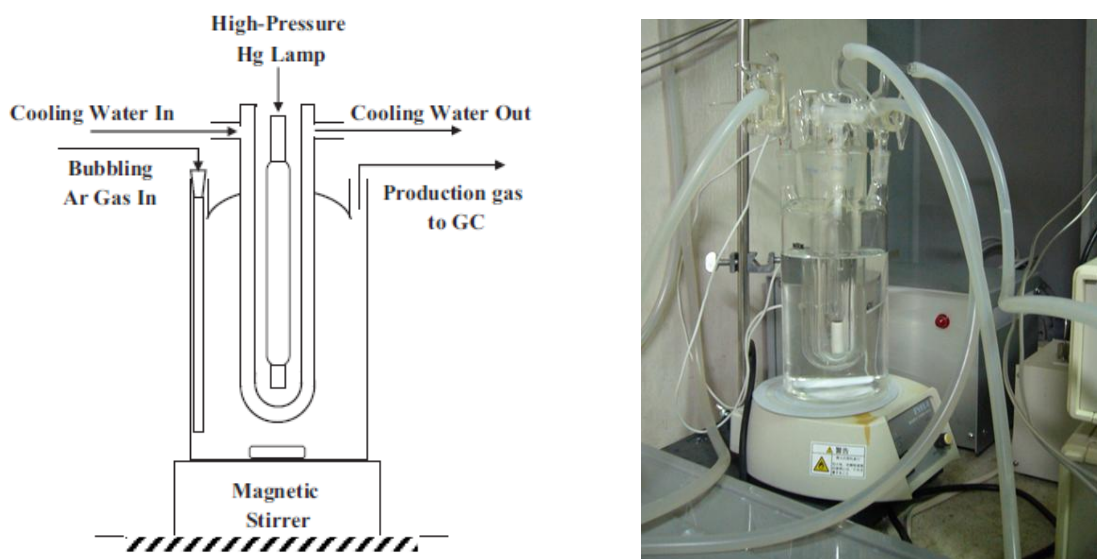
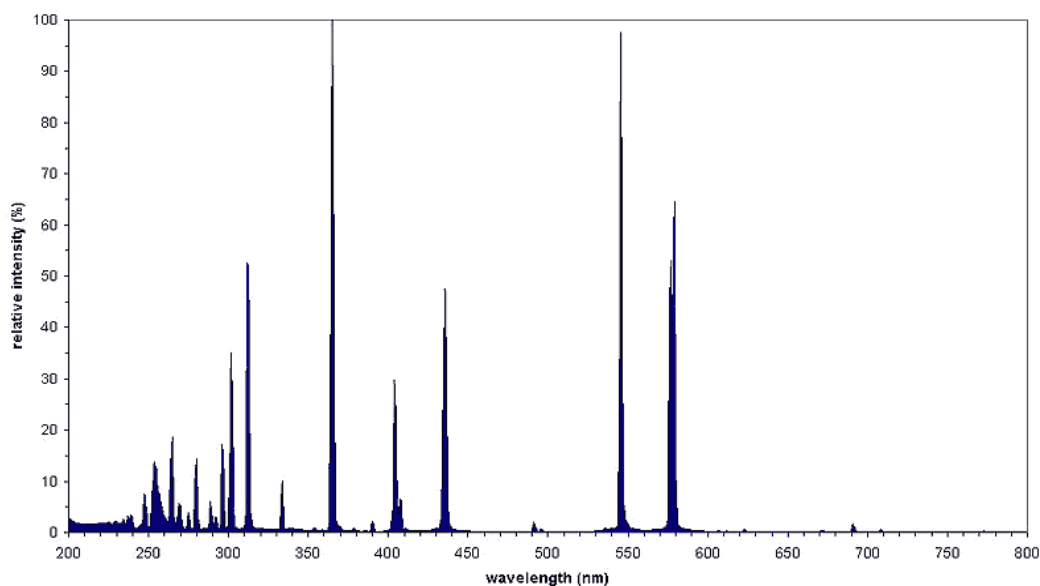


Figure 4.1. Testing reactor used at ISS (Kyoto University)

Reactor is a 7874.38 Pyrex Immersion Well, provided by Ace Glass Incorporated ACE, it has 14/20 angled joint for sparger tube, one 24/40 vertical joint for condenser and one 7 Ace Thred for thermometer. Actual working volume is 1100 ml which is approximately 40-50% of total free volume.

For this equipment, light source is a high-pressure Hg lamp (Ushio, UM-452 450 W). Figure 4.2 displays the spectrum of this lamp. Strongest intensity of this lamp is in the UV-A and UV-B regions. However it has a quite high intensity in the visible region too.



**Figure 4.2 Spectrum of Hg lamp (Ushio, UM-452 450 W) used at ISS (Kyoto University)**

N<sub>2</sub> purging lasts 30 minutes and H<sub>2</sub> test lasts five hours. Gaseous H<sub>2</sub> produced is analyzed every 30 minutes by an on-line GPC (Shimadzu GC-8A, Molecular sieve 5A, TCD, Ar carrier).

#### **4.1.1.3 Description of the LMSPC testing facility**

Figure 4.3 is a scheme of the complete testing assembly used at LMSPC: reactor, magnetic stirrer and GPC-based analysis system. Figure 4.4 is focused on the assembly of the photoreactor.

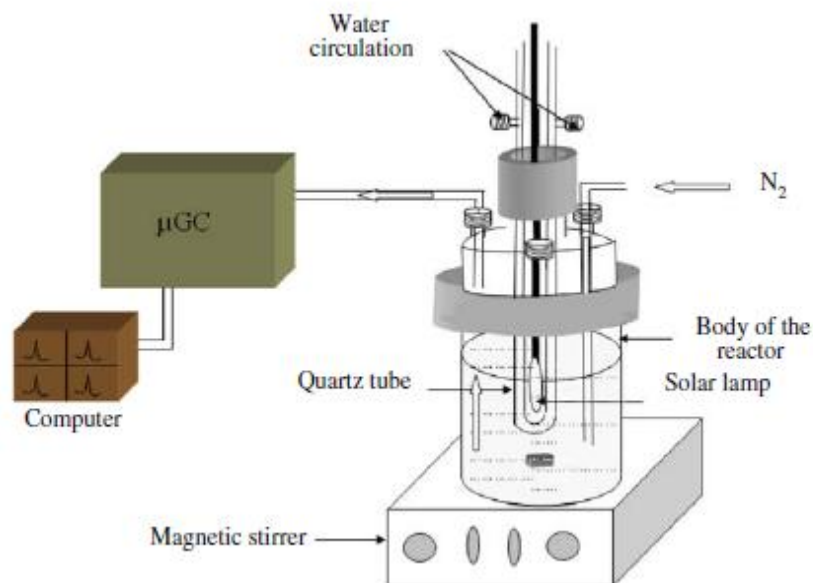


**Figure 4.3** Scheme of the testing reactor used in LMSPC (Strasbourg University) [Rosseler et al., 2010]

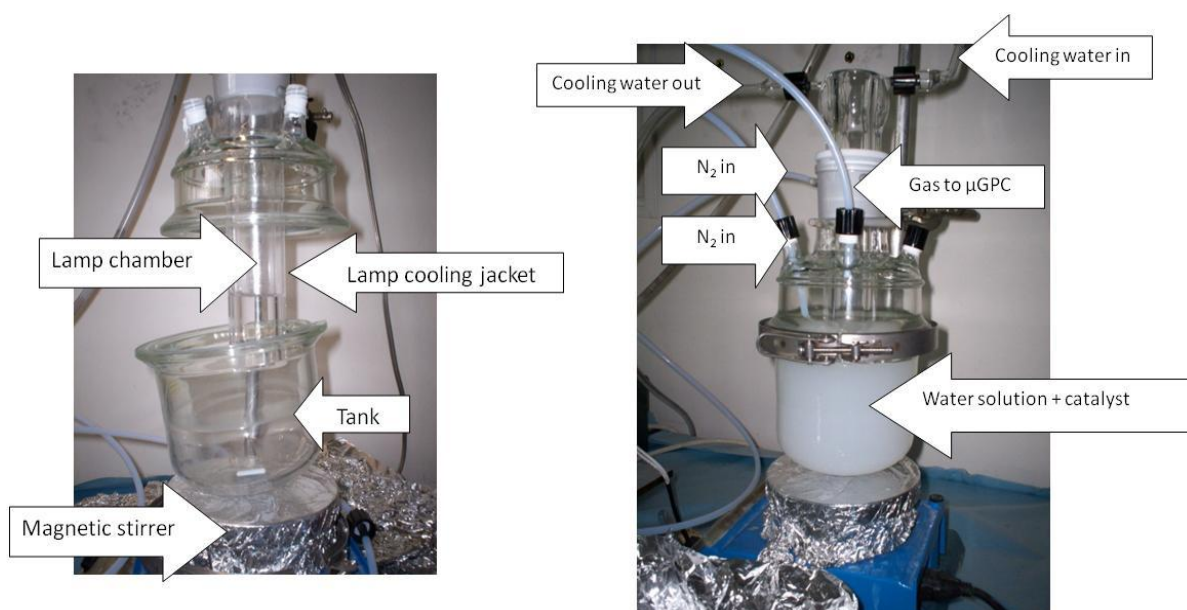


**Figure 4.4** View of the testing reactor used in LMSPC (Strasbourg University).

For this equipment, the light source is a halide lamp (BLV-Licht, C-HIT 150 W). The Figure 4.5 reports the associated spectrum. Wavelengths are mainly in the visible light range.

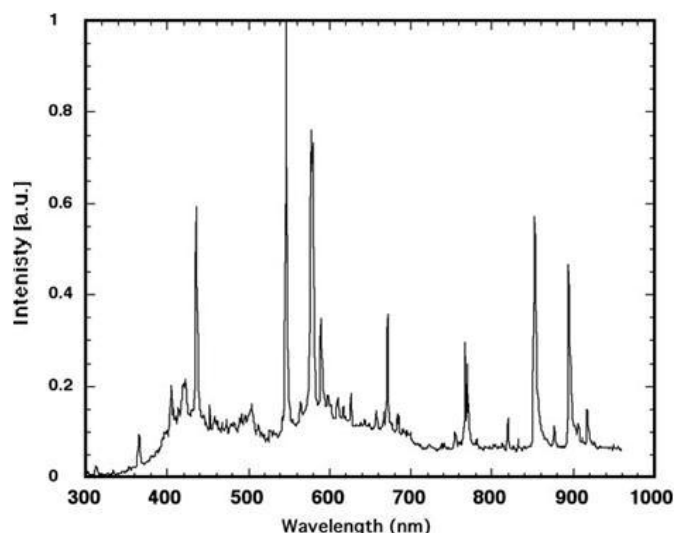


**Figure 4.5.** Spectrum of the halide lamp (BLV-Licht, C-HIT 150 W model) used at LMSPC (Strasbourg University).

N<sub>2</sub> purges lasts 90 minutes and H<sub>2</sub> evolution test 100 minutes. In this reactor a flow of N<sub>2</sub> (500 cm<sup>3</sup>.min<sup>-1</sup>) continuously removes reaction products. The products are analyzed every 2 minutes by an on-line GPC (SRA Instruments μGC 200). Two columns analyze products: one, with Ar carrier, for H<sub>2</sub>, O<sub>2</sub> and N<sub>2</sub>; the other one, with He carrier, for CO<sub>2</sub>. However, during the tests, we couldn't detect any CO<sub>2</sub>. It is assumed that produced CO<sub>2</sub>, if any, remains dissolved in the testing solution (confer chapter 1).

GPC records data are in ppm<sub>v</sub>. A mixture of H<sub>2</sub>/N<sub>2</sub> with a concentration of H<sub>2</sub> equals to 1000 ppm<sub>v</sub> has been previously used for calibration. Relationship between peak surface and H<sub>2</sub> concentration has been found to be linear. In this case, the instantaneous amount (dn/dt in mol/min) of H<sub>2</sub> is calculated as follows:

$$\dot{n} = \frac{\mu\text{mol}}{\text{min}} = \text{ppm}_v \times \frac{500}{22400} \quad (\text{eq. 4.1})$$

where N<sub>2</sub> flow is 500 cm<sup>3</sup>.min<sup>-1</sup> and 22 400 is the volume occupied by 1 mol of gas at 0 °C (in cm<sup>3</sup>.mol<sup>-1</sup>) and ppm<sub>v</sub> the concentration of H<sub>2</sub> (in ppm<sub>v</sub>) calculated from the analysis result.

Integrating these rates give total molar amount produced during the whole experiment.

### 4.1.2 Samples preparation procedure

Tests have been carried out on i) materials without any further treatment<sup>58</sup> and ii) materials loaded with platinum (Pt), in order to enhance the H<sub>2</sub> evolution, as explained in the chapter one.

The platinized samples have been loaded with Pt directly at LMSPC by wet deposition and have only been tested on LMSPC facilities. Procedure of Pt loading consists of 4 steps and is summarized here-after.

- Step 1: adding hexachloroplatinic acidic aqueous solution (H<sub>2</sub>PtCl<sub>6</sub>, x H<sub>2</sub>O ) (5 ml water/g<sub>TiO<sub>2</sub></sub>) in order to obtain Pt/TiO<sub>2</sub> equal to 0.3 wt.% (5 ml water/g<sub>TiO<sub>2</sub></sub>),
- Step 2: evaporation of solvents under magnetic stirring at 60 °C and drying at 110°C for 1 hour directly in air (at the end of this step a yellowish powder is obtained),
- Step 3: calcination of samples at 350 °C for 1 hour in flowing air (this step allows a good dispersion of Pt on the photocatalyst surface),
- Step 4: reduction of samples under H<sub>2</sub> flow (flow rate) at 350 °C for 1 hour, in order to reduce the Pt<sup>59</sup>.

Final powders obtained through this recipe are grey.

## 4.2 Properties of the commercial TiO<sub>2</sub> products used as references

We have chosen Anatase AlfaAesar (product reference 036199), Anatase ST-01 and Degussa P25 as commercial reference materials, in order to compare our products with reference ones. Here I have summarized the structural and optical behaviors of these two photocatalysts according the following characteristics:

- XRD and diffuse reflectance UV-VIS spectroscopy (for both product),
- N<sub>2</sub> physisorption (only for Degussa P25),
- TEM observation (only for Anatase AlfaAesar since Degussa P25 has already been deeply analyzed in the current literature).

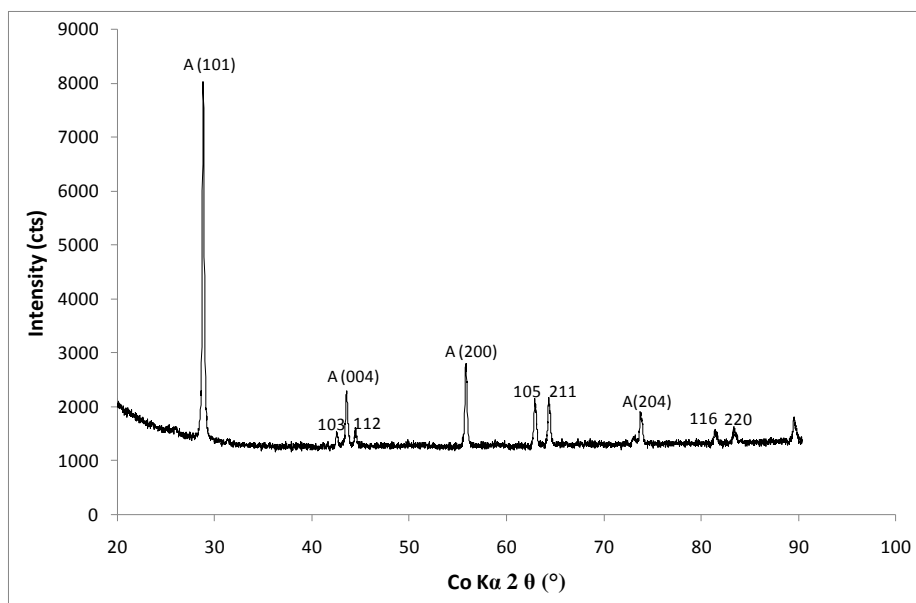
### 4.2.1 X-Ray diffraction

Figure 4.6 shows that AlfaAesar 036199 is only constituted of anatase. Figure 4.7 shows XRD pattern of Degussa P25. This diffractogram underlines that Degussa P25 is a mixture of anatase and rutile. Ratio of anatase on rutile is there 4:1, calculated following the equation of Zhang [Zhang et al., 2000].

---

<sup>58</sup> Since I have crushed the samples before calcinations, powders are ready for testing, even if not-Pt-loaded.

<sup>59</sup> Temperature of 350 °C removes the chloride ions.



**Figure 4.6. XRD pattern of commercial anatase AlfaAesar (036199)**

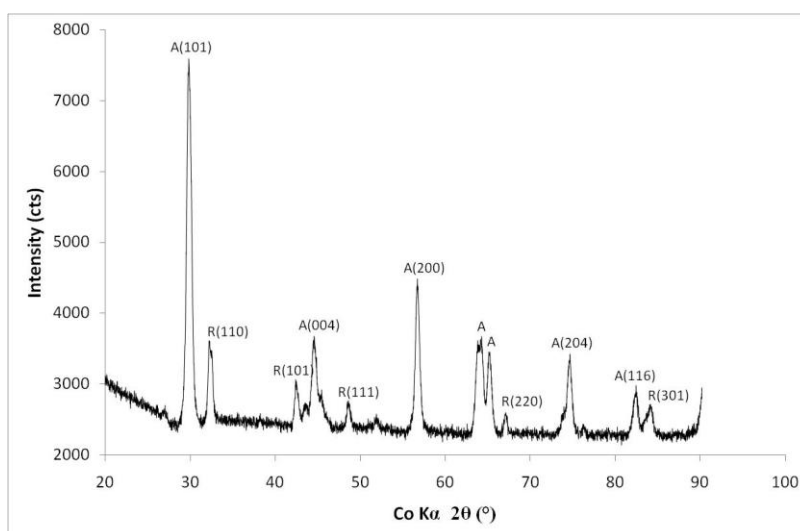


**Figure 4.7 XRD pattern of Degussa P25**

#### 4.2.2 Nitrogen adsorption/desorption

Figure 4.8 shows the  $N_2$  physisorption isotherms of Degussa P25. Using the BET treatment we can evaluate a surface area of  $46 \text{ m}^2 \cdot \text{g}^{-1}$ . Figure 4.9 presents the BJH treatment on the adsorption branch of  $N_2$  isotherm. We can mainly individuate one pores population with a characteristic size about 2 nm.

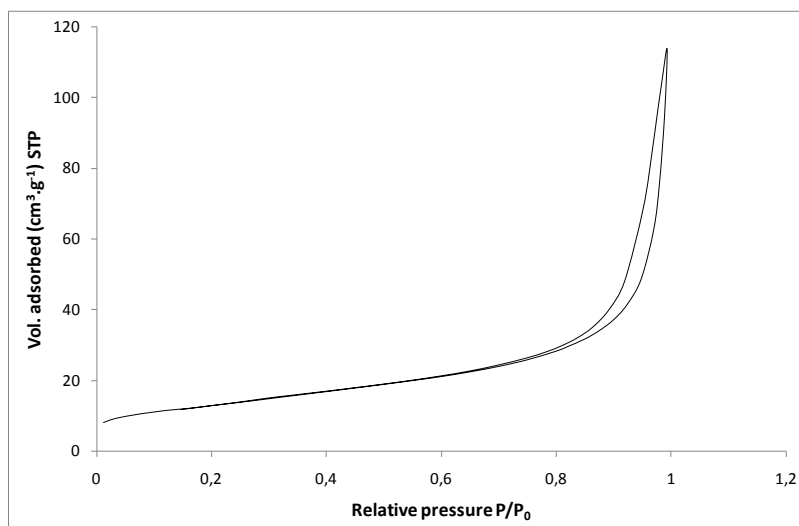


**Figure 4.8 N<sub>2</sub> physisorption isotherms of Degussa P25**

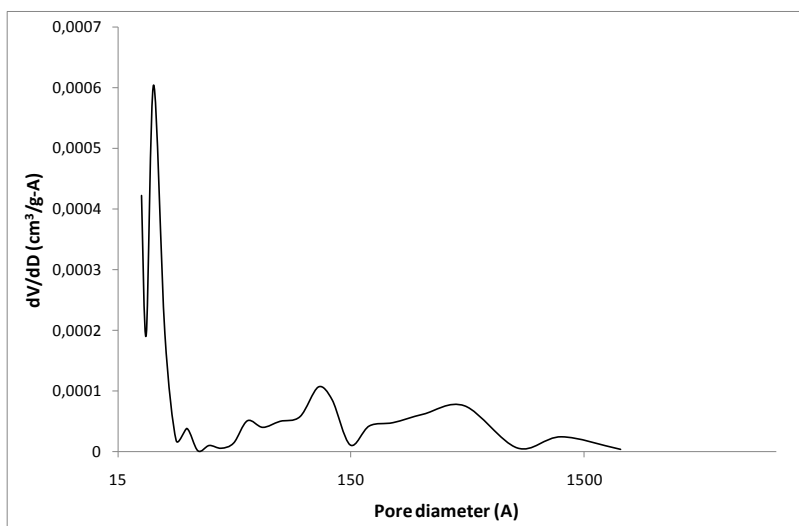


**Figure 4.9 Pore size distribution of Degussa P25 from BJH treatment of N<sub>2</sub> adsorption isotherm**

Figure 4.10 shows the N<sub>2</sub> physisorption isotherms of AlfaAesar 036199. Using the BET treatment we can evaluate a surface area of 7.4 m<sup>2</sup>.g<sup>-1</sup>. Figure 4.11 presents the BJH treatment on the adsorption branch of N<sub>2</sub> isotherm. We can mainly individuate two pores population with a characteristic size about 40 and 121 nm.

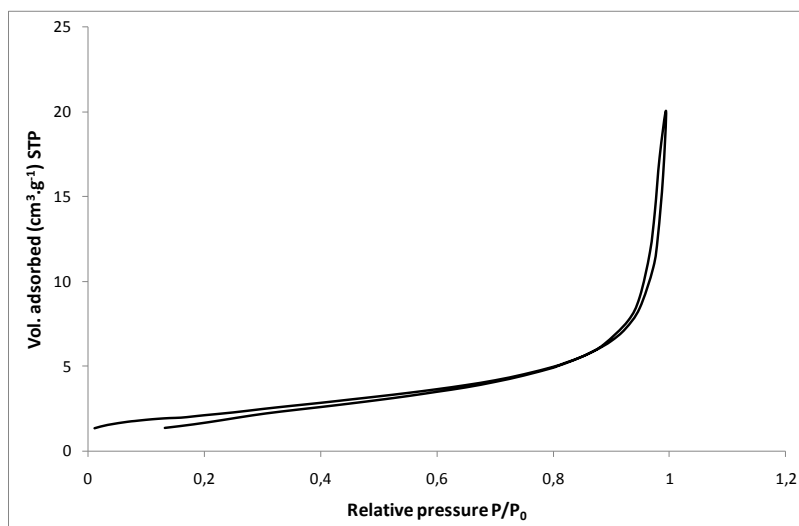


Figure 4.10 N<sub>2</sub> physisorption isotherms of AlfaAesar 036199

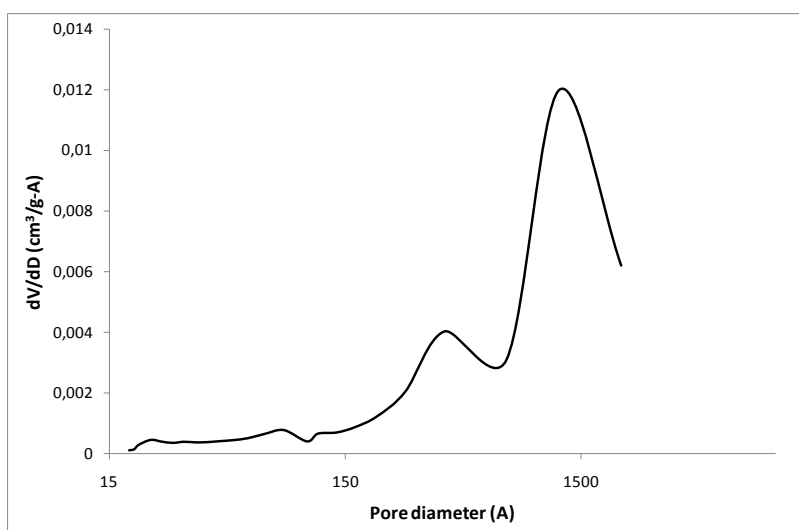


Figure 4.11 Pore size distribution of AlfaAesar 036199 from BJH treatment of N<sub>2</sub> adsorption isotherm

Table 4.1 sums up results of BET and BJH treatments obtained for P25 and AlfaAesar 036199. Density of Degussa P25 has been calculated as a weighted average assuming that Degussa P25 is a mixture of 80 wt% of anatase and 20 wt% of rutile.

$S_{BET}$ ( $m^2 \cdot g^{-1}$ )	$D \pm 0.3$ (nm)	$d$ (nm)	$\delta_1$ (nm)	$\delta_2$ (nm)	$V_p$ ( $cm^3 g^{-1}$ )
46	30	8.4	2	–	0.09
7.4	206	8.9	40	121	0.01

Table 4.1. Data issued from BET and BJH treatments of N<sub>2</sub> physisorption isotherms of Degussa P25 and AlfaAesar 036199: D is the characteristic particles diameter from geometric formula ( $D = 6/(S_{BET} \cdot \rho_s)$ ), d is the average pore diameter considering pore as cylinder ( $d = 4/(V_p \cdot S_{BET})$ ),  $\delta_1$  and  $\delta_2$  correspond to the main pore size population directly issued from BJH curve and  $V_p$  is the specific pore volume

### 4.2.3 Transmission Electron Microscopy

TEM have been performed on anatase AlfaAesar 036199. After a visual study on 30 nanoparticles we can say that the characteristic nanoparticles size is approximately around 180 nm.

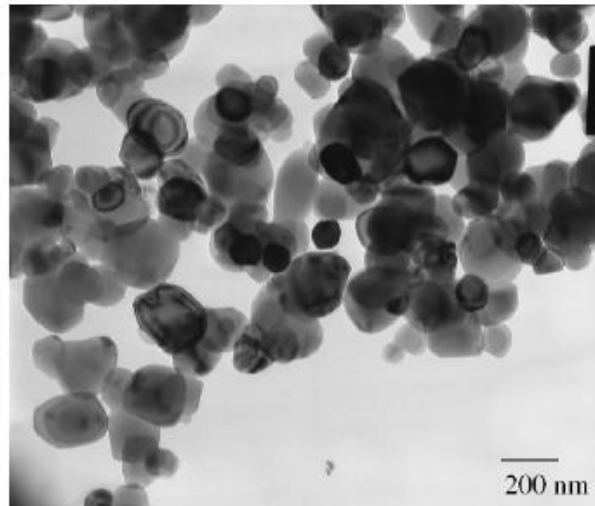


Figure 4.12 TEM micrograph of commercial anatase AlfaAesar (036199)

TEM study of Degussa P25 is issued from literature (Figure 4.13) and confirms that characteristic nanoparticles size is around 30 nm.

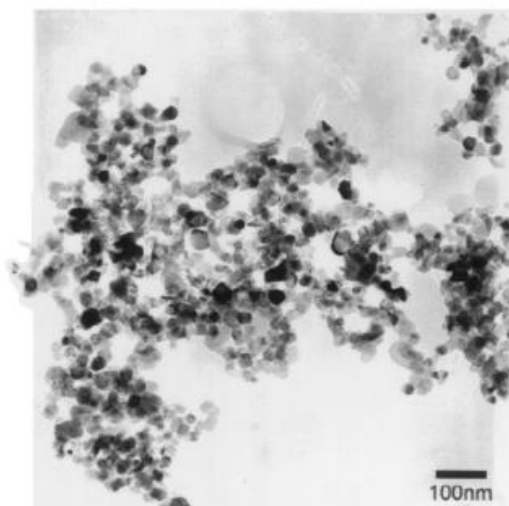
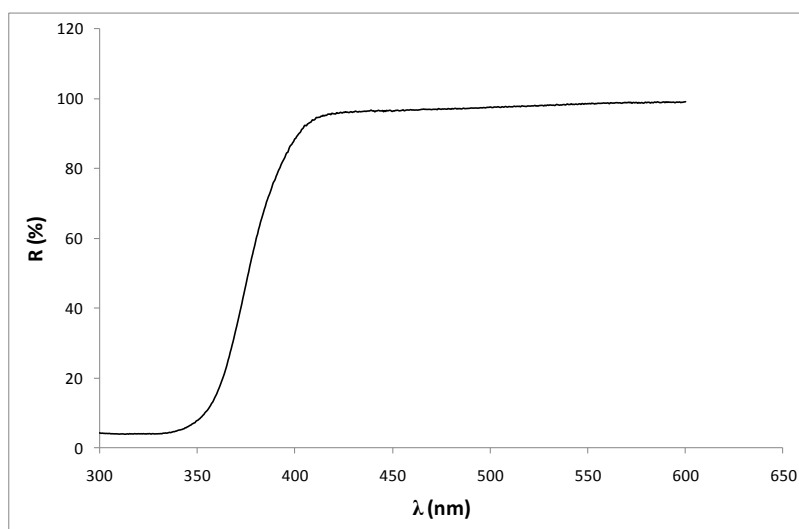


Figure 4.13 TEM micrograph of Degussa P25 [Cho and Kim, 2003]

### 4.2.4 Diffuse reflectance UV-VIS spectroscopy

For anatase AlfaAesar 036199 we have performed diffuse reflectance UV-VIS spectroscopy (Figure 4.14) and we have estimated the bandgap using Kubelka-Munch function (Figure 4.15). As we have described in the appendix 2, the photoinduced transfer of an electron from the valence band to the conduction band can be direct or indirect, corresponding to a direct or an indirect bandgap. In the appendix 2 we have shown that data treated with hypothesis of an indirect transition gives bandgap value of  $3.25 \pm 0.10$  eV, which is typical value reported for anatase in the literature. In the following (i.e. for all the different samples), the bandgap has been estimated considering an indirect transition.



**Figure 4.14** Diffuse reflectance spectrum of commercial anatase AlfaAesar (036199)

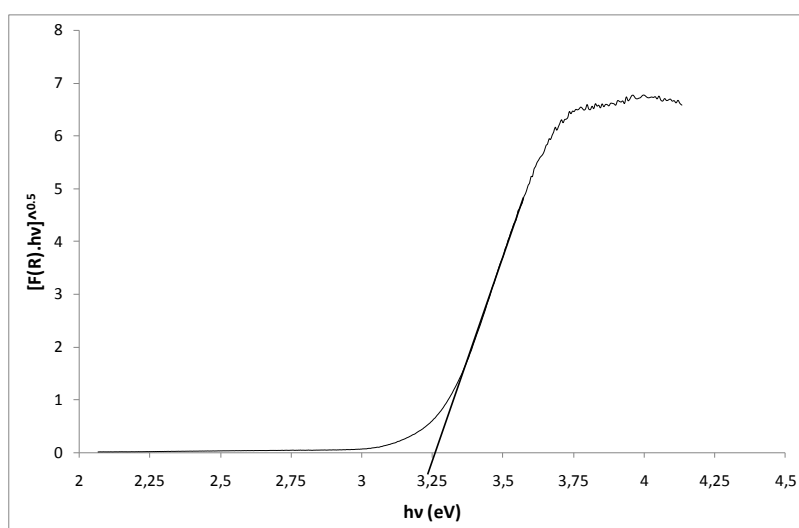


**Figure 4.15** Bandgap evaluation of commercial anatase Alfa Aesar (036199)

Yeredla et al. [Yeredla and Xu, 2008] estimated the bandgap of Degussa P25 (Figure 4.16 and 4.17): the value they found is 3.2 eV.

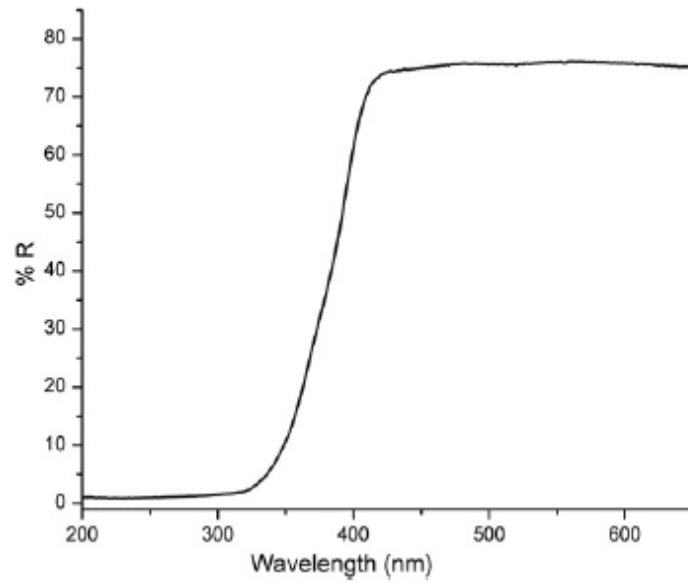


Figure 4.16 Diffuse reflectance spectrum of Degussa P25 [Yeredla and Xu, 2008]

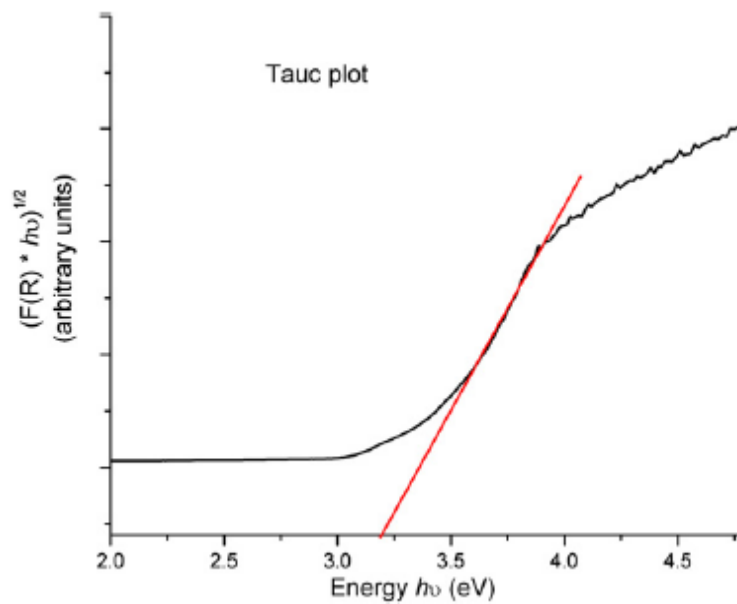


Figure 4.17 Bandgap evaluation of Degussa P25 [Yeredla and Xu, 2008]

### 4.3 Optical characterization of nanoparticles, nanotubes, aerogels and xerogels samples

### 4.3.1 Nanoparticles

The bandgap has been determined using the method described in the appendix 2, starting from reflectance data obtained via Diffuse reflectance UV-VIS spectroscopy (Figure 4.18). Since for all the nanoparticles the main phase is anatase and the characteristic particles size is almost constant, the bandgap has been only estimated for SN-10-150 sample (Figure 4.19). The value obtained for the bandgap is  $3.20 \pm 0.15$  eV, which is the characteristic value of anatase [Earle, 1942]<sup>60</sup>.

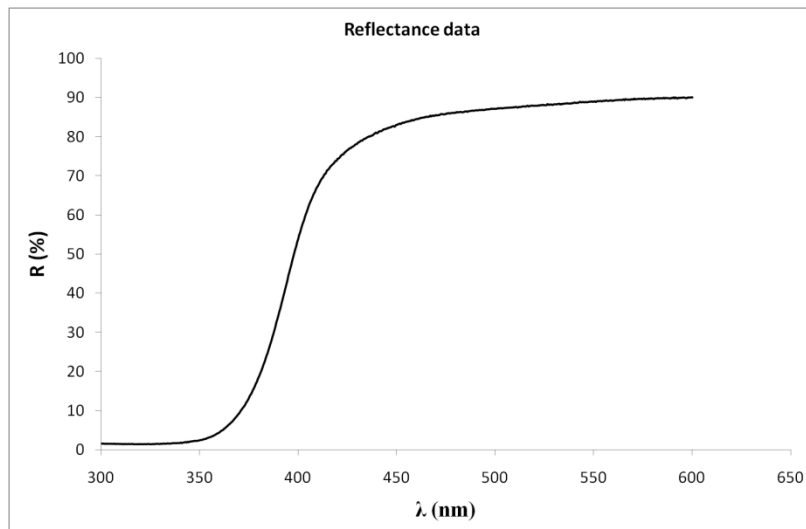


Figure 4.18. Diffuse Reflectance spectrum of SN-10-150 nanoparticles

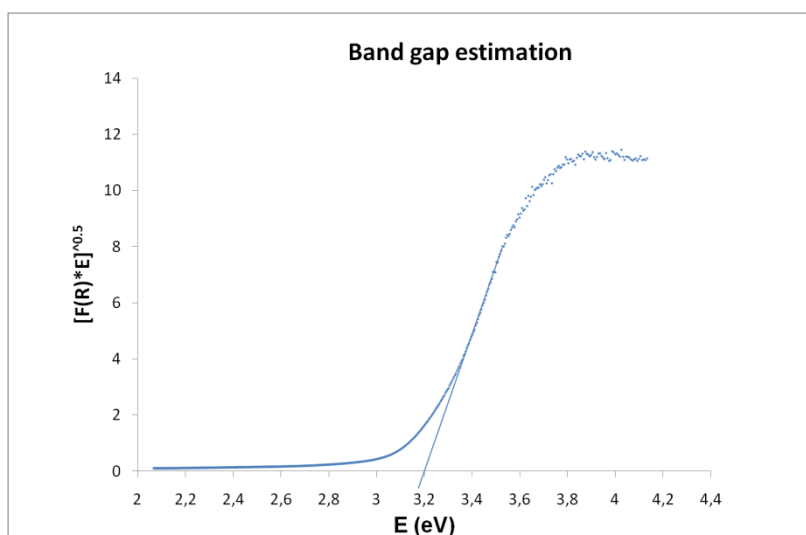
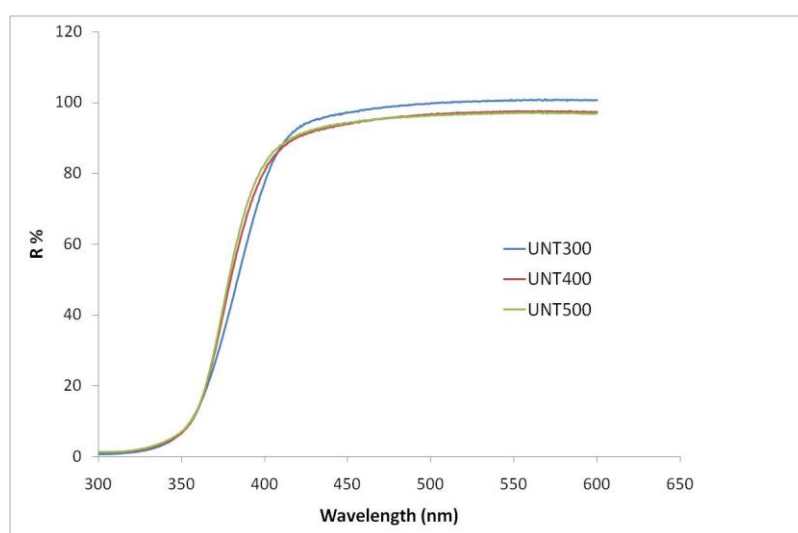


Figure 4.19. Bandgap estimation of SN-10-150 nanoparticles

<sup>60</sup> Considering the family of straight lines that approximate the tangent to the curve in the quasi linear domain, the wavelength value is obtained as average of the intersection points of these lines with the x-axis.

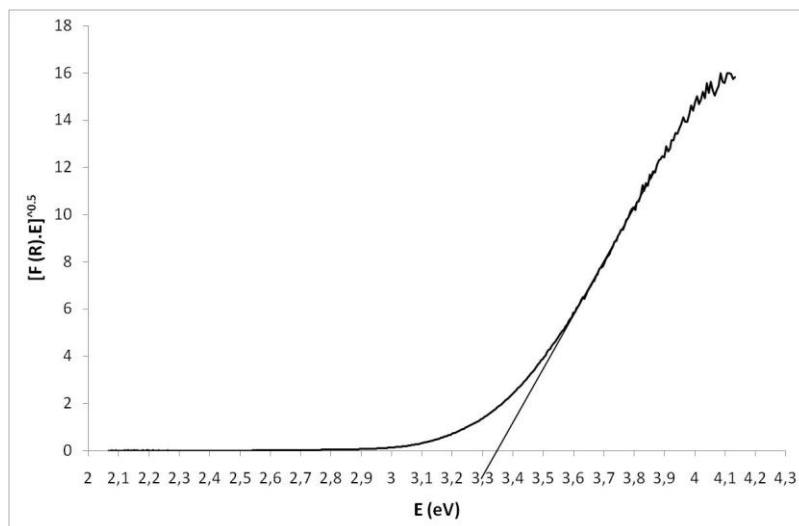
### 4.3.2 Nanotubes

Figure 4.20 shows reflectance analysis results of nanotubes UNT300, UNT400 and UNT500. These data have been treated using Kubelka-Munch function as described in Annex 2, in order to estimate the bandgap of the nanomaterials (Figures 4.21, 4.22 and 4.23). The bandgap seems to decrease by increasing calcination temperature: it is  $3.35 \pm 0.12$  eV for UNT300,  $3.27 \pm 0.14$  for UNT400 and it becomes  $3.25 \pm 0.15$  eV for UNT500. These values and the corresponding errors have been calculated using the method described in the previous paragraph. XRD and TEM characterizations (presented in the second chapter) prove that UNT300 is mostly  $\text{TiO}_2\text{-B}$ , UNT400 a mixture of  $\text{TiO}_2\text{-B}$  and anatase<sup>61</sup> and UNT500 mostly anatase. The bandgap evolution could be linked to this phase evolution: increasing the anatase amount seems to lead to a reduction of the bandgap. However, it must be underlined here that more accurate treatments are necessary to quantify more precisely bandgap values and to confirm this first evaluation.



**Figure 4.20 Diffuse Reflectance spectra of UNT300, UNT400 and UNT500 nanotubes**

<sup>61</sup> In the previous chapter, we have calculated, using Raman spectra, that for nanotubes calcined at 400 °C the weight percentage of  $\text{TiO}_2\text{-B}$  is 20% and of anatase is 80%.



**Figure 4.21. Bandgap estimation of UNT300 nanotubes**

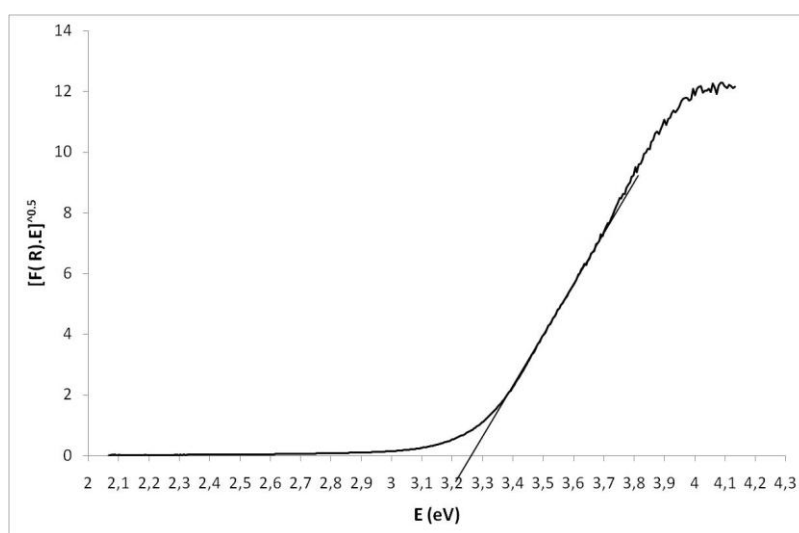


**Figure 4.22. Bandgap estimation of UNT400 nanotubes**

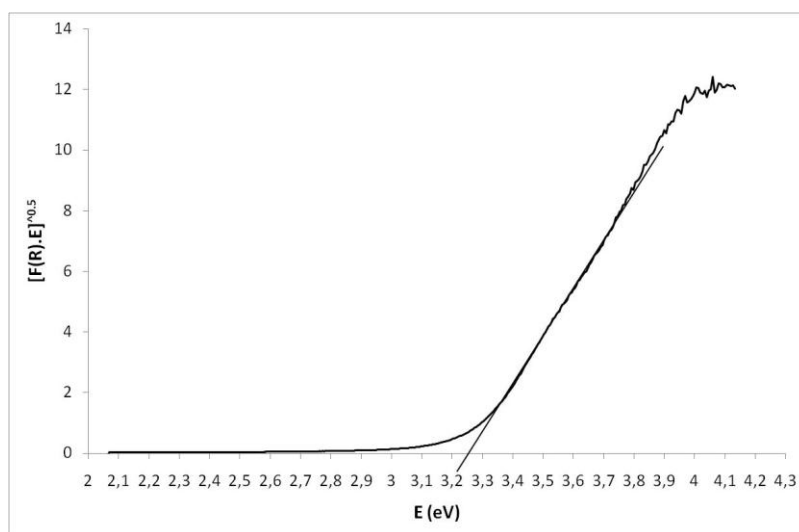


**Figure 4.23. Bandgap estimation of UNT500 nanotubes**

### 4.3.3 Aerogels

Aerogels (samples AA<sup>62</sup> and A500) have been characterized by Diffuse Reflectance UV-VIS spectroscopy. The Figure 4.24 presents the diffuse reflectance spectra of AA and A500 aerogels, the figure 4.25 presents the associated results coming from the Kubelka-Munch treatment.

For amorphous AA sample (as-prepared), the estimated bandgap value is  $3.5 \pm 0.02$  eV and for crystallized A500 (calcined at 500 °C), it is  $3.25 \pm 0.16$  eV, as expected for anatase.

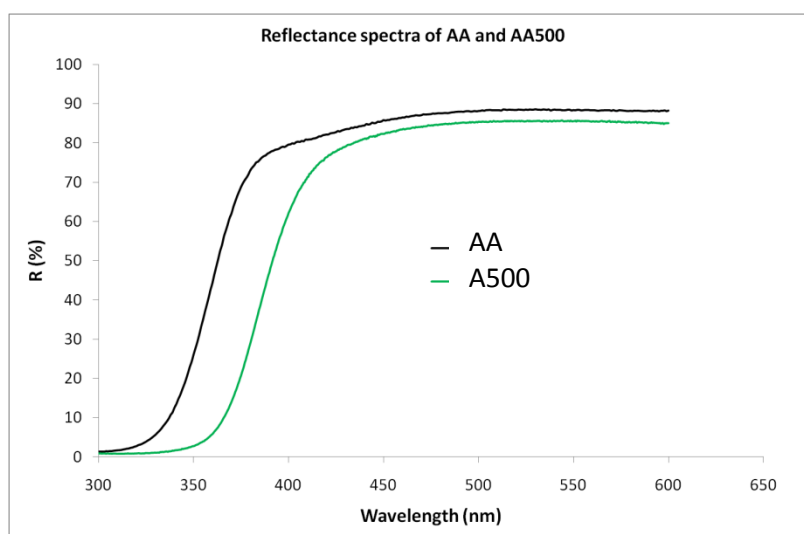


Figure 4.24. Diffuse Reflectance spectra of AA and A500 aerogels

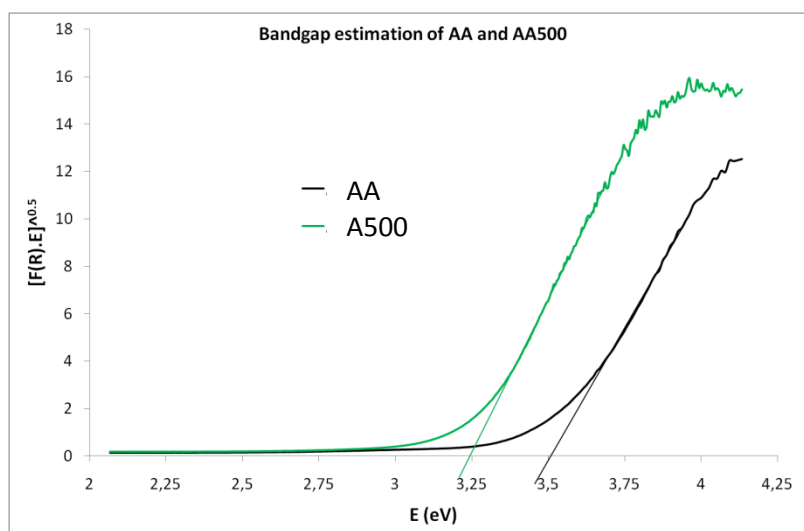


Figure 4.25. Bandgap estimation of AA and A500 aerogels

<sup>62</sup> Note that AA is the TiO<sub>2</sub> aerogel before calcination (confer chapter 2).

#### 4.3.4 Nitrogen-doped aerogels

Figure 4.26 shows diffuse reflectance UV-VIS results of undoped and nitrogen-doped aerogels<sup>63</sup>. This chart illustrates that the more doped is the material, the more it absorbs in the visible domain. Of course this clearly explains the coloration evolution of the materials reported in the Figure 3.17 of the third chapter. In particular we can observe that there is a strong optical modification for the AN1 sample, with the presence of an absorption band at 450 nm. Sato [Sato, 1984], Asahi [Asahi et al., 2001] and Di Valentin [Valentin et al., 2007] observed the same phenomenon on their samples: their nitrogen-doped materials are pale yellow and absorb more in the visible light range.

The Figure 4.26 displays the curves of the diffuse reflectance spectra. The Figures 4.27- 4.29 display the curves of the Kubelka-Munch function, the Table 4.2 sums up results of bandgap estimation. A500 has a bandgap of  $3.25 \pm 0.16$ , AN0.25 has a bandgap of  $3.38 \pm 0.25$  eV, AN0.5 of  $3.35 \pm 0.25$ , while AN1 has a bandgap of  $3.25 \pm 0.35$  eV. We must underline that the Kubelka-Munch treatment on AN0.25 and AN0.5 shows two linear parts, maybe associated to the different absorption bands. For these two samples we have estimated the bandgap considering one of these two parts.

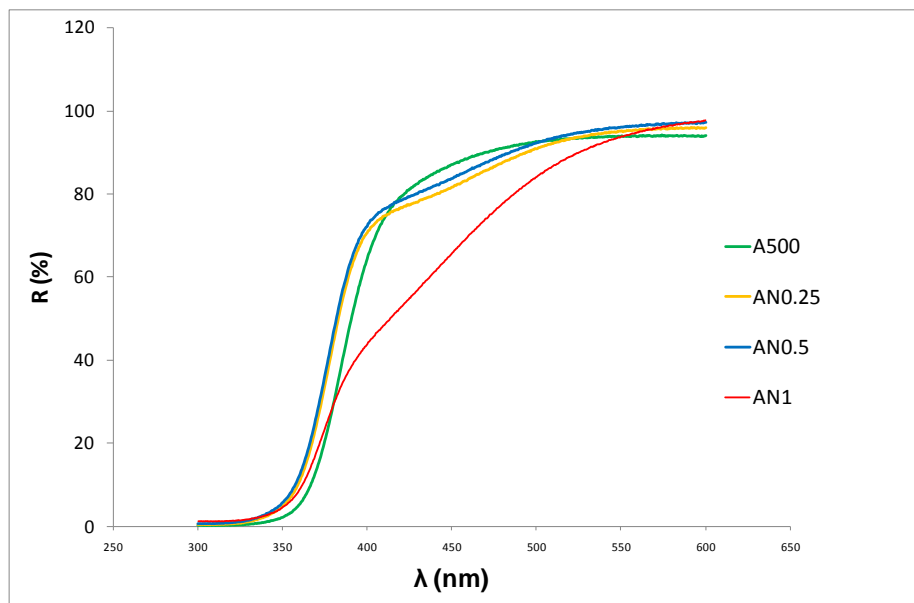


**Figure 4.26. Diffuse reflectance spectra of AN0, AN0.25, AN0.5 and AN1 aerogel samples**

<sup>63</sup> The diffuse reflectance UV-vis spectrum and the corresponding Kubelka-Munch treatment of A500 is presented in the paragraph 4.3.3.

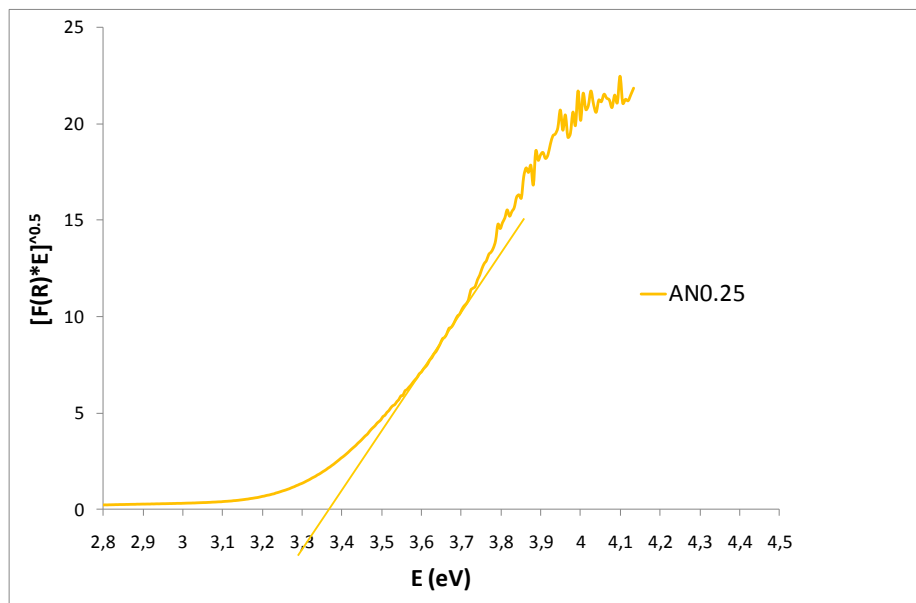


Figure 4.27. Bandgap estimation of AN0.25 aerogel sample

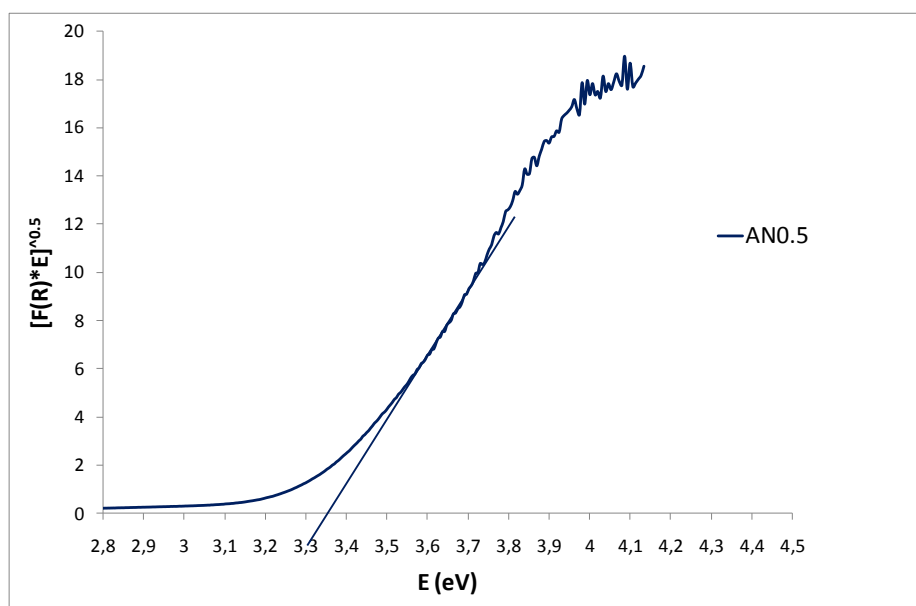


Figure 4.28. Bandgap estimation of AN0.5 aerogel sample

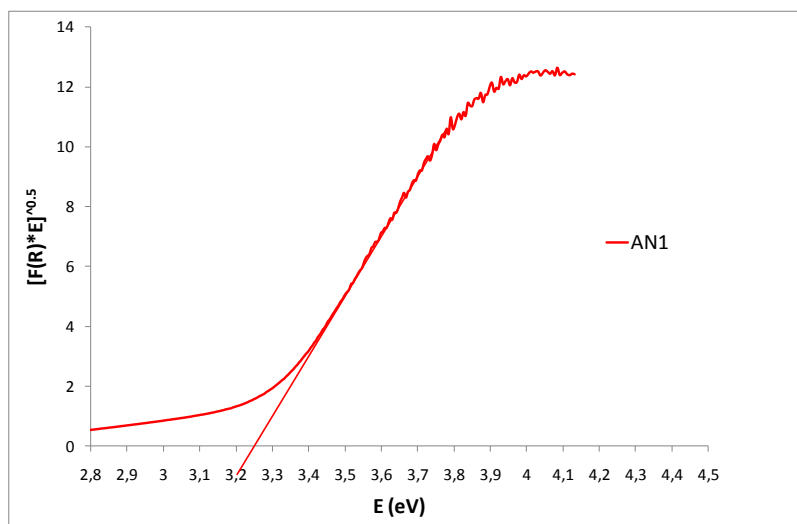


Figure 4.29. Bandgap estimation of AN1 aerogel sample

Sample	Bandgap (eV)
A500	3.25 ± 0.16
AN0.25	3.38 ± 0.25
AN0.5	3.35 ± 0.25
AN1	3.25 ± 0.35

Table 4.2 Bandgap estimation of A500, AN0.25, AN0.5 and AN1 aerogel samples from Kubelka-Munk treatment of diffuse reflectance UV-VIS spectra (assuming an indirect bandgap)

#### 4.3.5 Nitrogen-doped xerogels

Figure 4.30 and Figure 4.31 show the reflectance results and the associated bandgap evaluation of nitrogen-doped xerogels. Both graphs illustrate an increasing of the visible light absorption for the nitrogen-doped materials. Still using the same treatment, I have evaluated the bandgap for XN0.25 and XN0.5 samples:  $2.9 \pm 0.02$  and  $3.1 \pm 0.025$  eV. Although XN1 xerogel seems to absorb in the visible light, the estimation of its bandgap with simple methods could lead to severe mistakes. Indeed, the Kubelka-Munk function on X1 sample, in fact, shows two distinct linear parts.

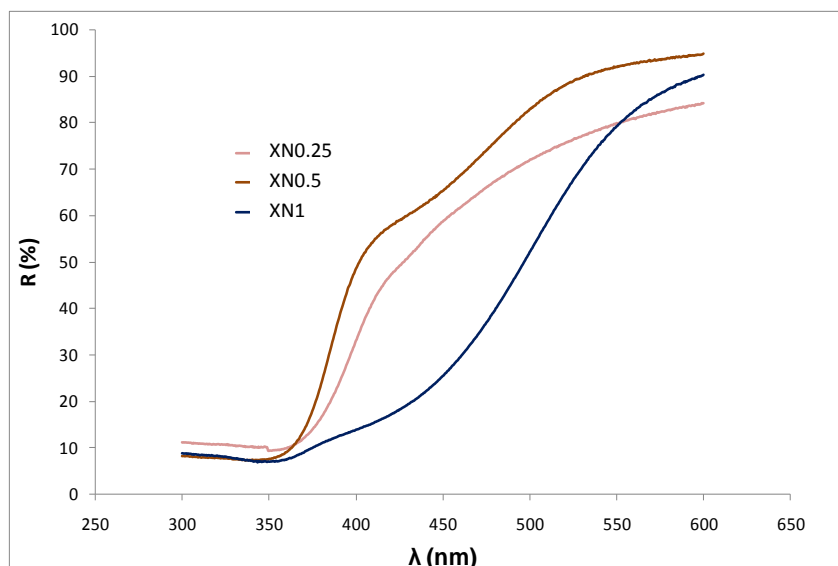


Figure 4.30. Diffuse reflectance spectra of nitrogen-doped xerogels

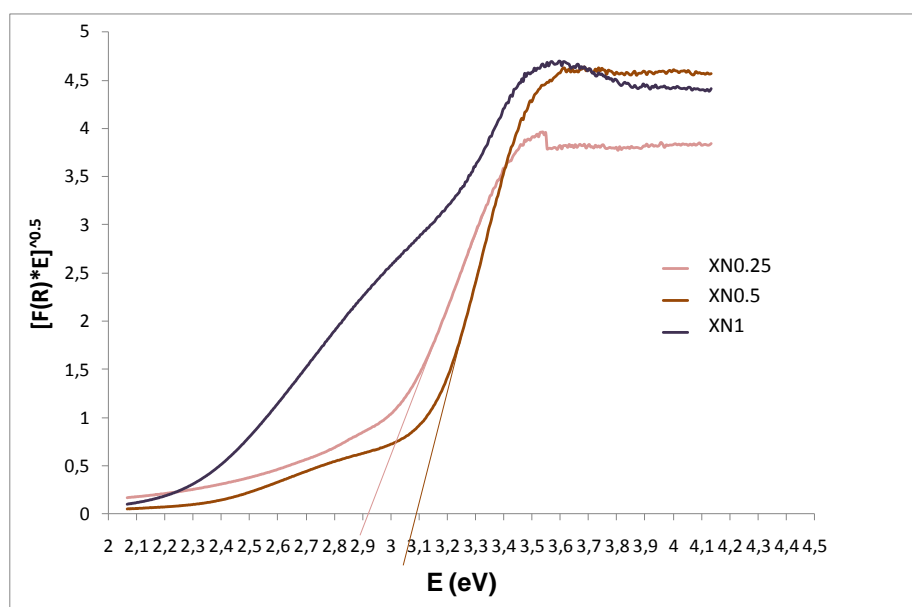


Figure 4.31. Bandgap estimation of nitrogen-doped xerogels from Kubelka-Munck treatment

## 4.4 Hydrogen evolution

### 4.4.1 List of the tested samples

Table 4.3 sums up the features of the tested samples. They have been deeply described in the previous chapters.

Sample	Phase	$S_{BET}$	D	Bandgap
--------	-------	-----------	---	---------

		(m <sup>2</sup> .g <sup>-1</sup> )	(nm)	(eV)
<b>Degussa P25</b>	A (80%), R(20%)	46	30	3.24
<b>Anatase AlfaAesar 036199</b>	A	7.4	180	3.25
<b>ST-01</b>	A	320*	5*	3.25*
<b>SN-10-150</b>	A	143	10	3.25
<b>UNT300</b>	B	246	40 × 9**	3.35
<b>UNT400</b>	A (80%), B(20%)	117	115 × 9**	3.28
<b>UNT500</b>	A, traces B	90	-.***	3.25
<b>A500</b>	A	83	12	3.25
<b>AN0.25</b>	A	60	12	3.38
<b>AN0.5</b>	A	107	10	3.35
<b>AN1</b>	A	78	13	3.25
<b>X500</b>	A	-	14	-
<b>XN0.25</b>	A	-	-	2.90
<b>XN0.5</b>	A	-	-	3.10
<b>XN1</b>	A	-	-	-

**Table 4.3 Summary of the principal characteristics of photocatalysts tested for water splitting. A is anatase, R is rutile and B is TiO<sub>2</sub>-B. D is the characteristic particles diameter from geometric formula ( $D = 6/(S_{BET} \cdot \rho_s)$ ). \* Features of Anatase ST-01 are issued from the Ishihara Co.Ltd website; \*\*  $l(\text{length}) \times \varphi$  (diameter); \*\*\* as explained in the second chapter, we cannot calculate the length and the diameter of UNT500**

For practical reasons, we could not test all the samples without and with Pt loading. So we have first tested all the samples without Pt. Then, we have identified the most photoactive materials and we have loaded them with Pt for subsequent water splitting evaluation.

## 4.4.2 Testing of undoped samples

### 4.4.2.1 Evaluation of nanoparticles

I have performed photocatalytic tests on SN-10-150, Degussa P25 and anatase AlfaAesar 036199 samples in LMSPC. These samples were not Pt-loaded.

Our nanoparticles show a higher activity than AlfaAesar product but a weaker one compared to Degussa P25. Figure 4.32 shows the corresponding results.

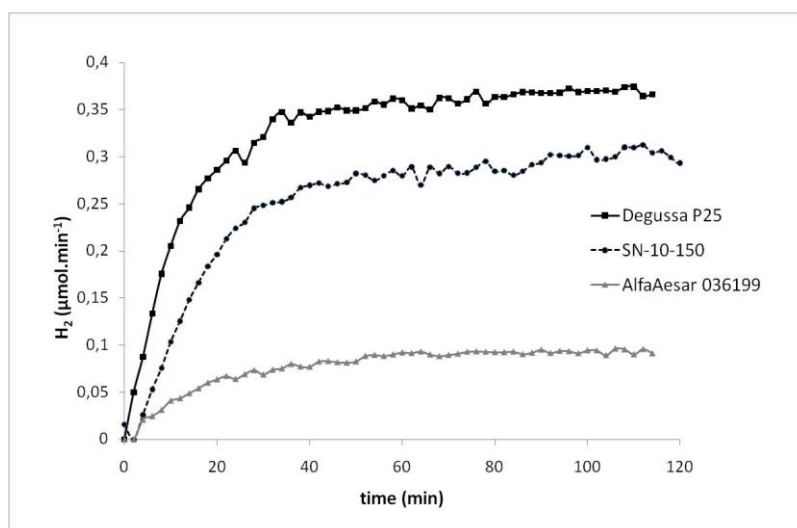


**Figure 4.32. H<sub>2</sub> evolution of Degussa P25, SN-10-150 nanoparticles and Anatase AlfaAesar samples, (150 W metal halide lamp, 900 ml water + 100 ml MeOH, 0.7 g samples, LMSPC Strasbourg)**

The wavelength range of the lamp used for these experiments is mainly between 400 and 700 nm, and almost no wavelengths are in the UV region, as the spectrum of metal-halide lamp shows (Figure 4.2). Since SN-10-150 is anatase, with a band gap of 3.25 eV, it absorbs light at wavelengths inferior to 381nm. Maybe the weak energy of the metal-halide lamp in the UV region is not enough to excite this photocatalyst. Degussa P25, instead, absorbs the visible light at wavelengths inferior to 387 nm, due to the presence of rutile. Moreover it is also known that Degussa P25 has higher photoactivity than anatase thanks to its interface anatase-rutile that enhances charges separation [Hurum et al., 2003] and enhances the hydrogen evolution.

SN-10-150, instead, is significantly more active than AlfaAesar 036199. Our sample, in fact, has smaller particles compared to AlfaAesar 036199 (10 nm vs 180 nm) and higher surface area (143 m<sup>2</sup>.g<sup>-1</sup> vs 7.4 m<sup>2</sup>.g<sup>-1</sup>), while bandgap has the same value. The difference in nanoparticles size and surface area could permit to explain the difference concerning photoactivity of the two samples. Studies devoted to the H<sub>2</sub> production testing are performed with TiO<sub>2</sub> nanoparticles loaded with noble metals [Nada et al., 2005], [Al-Mazroai et al., 2007], [Nishijima et al., 2007], [Suzuki2007], [Rosseler et al., 2010], so we cannot directly compare these bibliographic results with ours.

#### 4.4.2.2 Evaluation of nanotubes

The UNT300, UNT400 and UNT500 nanotubes samples, their TiO<sub>2</sub> precursor AlfaAesar 036199 and Degussa P25 have been tested at LMSPC. Moreover, the sample UNT400 and Degussa P25 have also been tested at ISS. In both experiments series the samples are not Pt-loaded. Figures 4.33 and 4.35 illustrate results obtained at LMSPC and ISS respectively.

## • Tests realized at LMSPC

In this section I will show and discuss the results of the tests carried out at LMSPC.

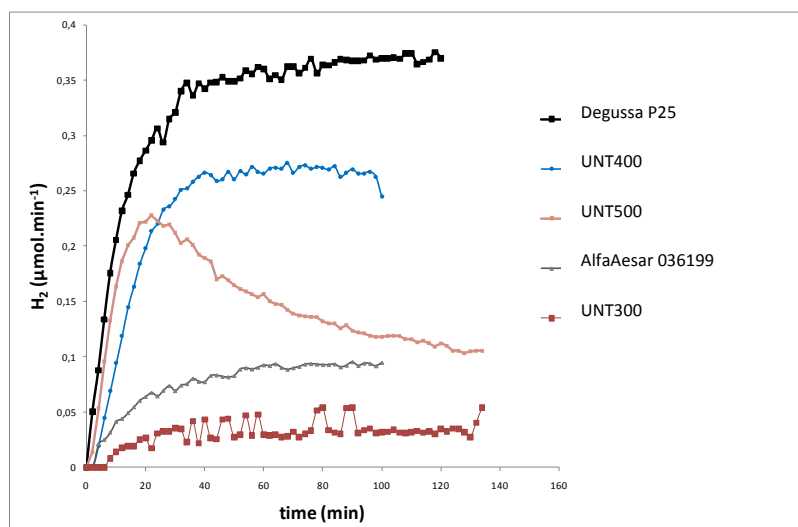


**Figure 4.33 H<sub>2</sub> evolution of nanotubes (UNT300, UNT400 and UNT500), Degussa P25 and AlfaAesar 036199 samples (150 W metal halide lamp, 900 ml water + 100 ml MeOH, 0.7 g samples, - LMSPC Strasbourg)**

Among the three nanotubes samples, UNT400 has the highest photoactivity versus H<sub>2</sub> evolution. It is more active than Anatase AlfaAesar 036199 but less than Degussa P25. XRD and TEM characterizations of UNT400 (Figure 2.27 and 2.30) have shown that this sample is composed of anatase and TiO<sub>2</sub>-B. Interface between these two phases could contribute to explain the higher activity than AlfaAesar 036199 anatase particles. The interface between TiO<sub>2</sub>-B and anatase is a zone where potential charge separation could occur. Since the energetic level of the bottom of the CB of the anatase is - 0.25 eV and that one of TiO<sub>2</sub>-B is 0.35 eV, I hypothesize here that the same mechanism observed by Hurum et al. [Hurum et al., 2003] for the anatase-rutile interface occurs: when sample is irradiated, electron jumps from the CB of the phase that has been excited (TiO<sub>2</sub>-B in our case) to the CB of the other phase (anatase in our case). As for SN-10-150, wavelengths range of halide lamp could explain the higher photoactivity of Degussa P25 than UNT400.

UNT300 has the weakest activity, compared to all the materials analyzed in this experimental serie. XRD and TEM characterizations presented in the second chapter have proved that this sample is TiO<sub>2</sub>-B without anatase. This result is consistent with literature where several articles also report that photoactivity of TiO<sub>2</sub>-B for H<sub>2</sub> generation is weaker than anatase alone or composites of TiO<sub>2</sub>-B and anatase [Kuo et al., 2007], [Jitputti et al., 2007], [Lin et al., 2008].

Finally activity of UNT500 sample for the first twenty minutes follows the profile of UNT400, but later dramatically drops. TEM analyses of UNT500 have been performed after H<sub>2</sub> evolution testing, in order to check if any significant transformation of the material occurred. Figure 4.34 shows the related TEM observation. A large fraction of initial nanotubes appears decomposed in nanoparticles. Before testing, sample was not as decomposed as after H<sub>2</sub> evolution testing. We hypothesize that this transformation of nanotubes in nanoparticles during the H<sub>2</sub> production could be a reason of the dramatic decrease of the UNT500 photogeneration rate. 1D structure, in fact, seems to improve the electron transport for reacting with molecule of reagent adsorbed on the material surface [Jitputti et al., 2007], their disappearance could be prejudicial to watersplitting.

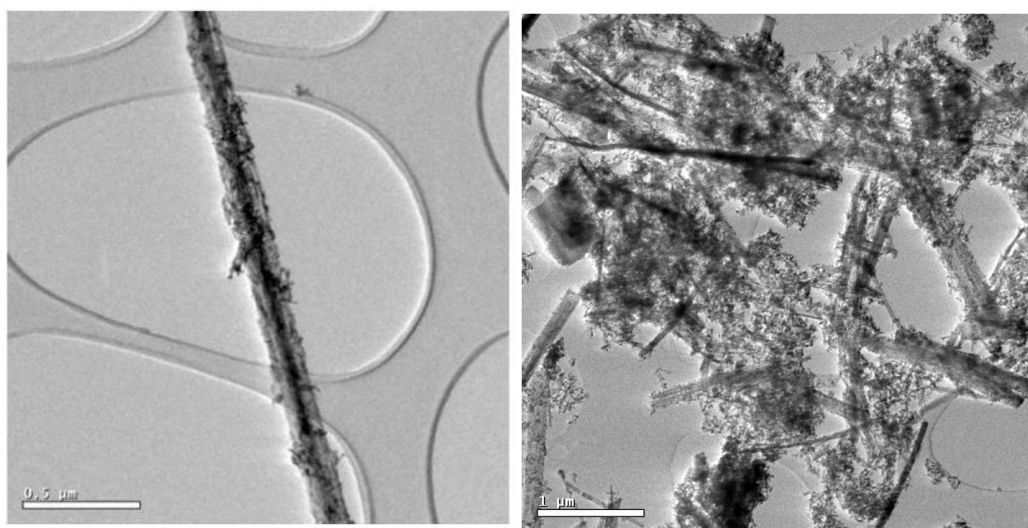


**Figure 4.34. TEM analysis on UNT500 sample before (left) and after (right) H<sub>2</sub> evolution testing at LMSPC**

#### **•Tests realized at ISS**

Figure 4.35 shows the results of the tests carried out at ISS.

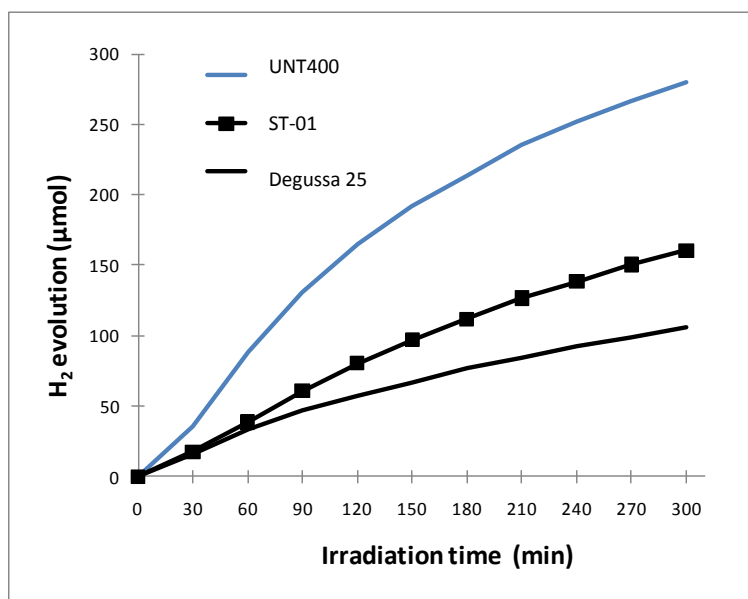


**Figure 4.35. H<sub>2</sub> evolution of nanotube UNT400, Degussa P25 and commercial anatase nanoparticles ST-01 samples.**

**(450 W Hg lamp, 700 ml water + 100 ml MeOH, 0.8 g samples, – ISS, Kyoto)**

The Figure 4.35 illustrates that UNT400 presents a higher photoactivity than Degussa P25. This can be due to the higher activity of the interface anatase-TiO<sub>2</sub>-B under UV radiation than anatase-rutile. Anatase and TiO<sub>2</sub>-B have bandgap of 3.25 and 3.38 eV respectively, so these phases can be excited by UV light. So UNT400 is very active under Hg lamp, which has its strongest relative intensity in the UV range (as shown in Figure 4.2). The second reason is that 1 D morphology seems to be more active than particulate network. Our result on the morphology and interface agrees with what reported in literature [Kuo et al., 2007], [Suzuki et al., 2008]. Both works demonstrate that under UV light 1D structures (nanotubes in Kuo's study and nanowires in Suzuki's one) have higher photoactivity in the photocatalytic generation of H<sub>2</sub> than the benchmark Degussa P25.

Despite the high surface area of the commercial anatase nanoparticles ST-01 (320 m<sup>2</sup>.g<sup>-1</sup>) compared to UNT400 (117 m<sup>2</sup>.g<sup>-1</sup>), this industrial product has a lower photoactivity in our specific testing conditions. This result tends to confirm that the morphology and the interface TiO<sub>2</sub>-B/anatase have an impact stronger than the surface area on the H<sub>2</sub> photocatalytic generation.

#### •Comparison between water splitting tests realized at LMSPC and ISS

In these two different experiments series I have compared the photoactivity of our own home-made TiO<sub>2</sub> samples with different commercial products. In order to compare the H<sub>2</sub> evolution of the same sample in the two systems, I have calculated the amount of hydrogen produced when the stable value is obtained at LMSPC (i.e. at 120 minutes). Then I have compared this value with the H<sub>2</sub> quantity produced in ISS laboratory for the same duration (i.e. after 120 minutes). Table 4.4 sums up these results for comparison purpose.

Sample	H <sub>2</sub> evolution	
	(μmol produced after 120 min)	
	LMSPC	ISS
Degussa P25	42	57
Commercial anatase*	21	80
UNT400	31	165

**Table 4.4. Comparison of H<sub>2</sub> evolution results obtained at LMSPC and at ISS (\*commercial anatase nanoparticles are AlfaAesar 036199 in the case of LMSPC and ST-01 for ISS, their structure differ strongly as summed-up in table 4.3)**

Table 4.4 clearly underlines that the three samples generate more H<sub>2</sub> when experiments are carried out at ISS. For all samples, it must be underlined here that reactor cooling temperature (30 °C for ISS and 15 °C for LMSPC), the lamp power (450 W for ISS and 150 W for LMSPC), the reactor type (batch for ISS and semi-batch for LMSPC) are different. This parameter could play a certain role on the results. However, the main hypotheses are probably to be found elsewhere.

Difference in photoactivity of Degussa P25 is rather small: 42 vs 57 μmol. The main phase of Degussa P25 is anatase that needs UV radiation to be activated. The absence of UV light in the metal-halide lamp spectrum can explain the lower photoactivity of Degussa P25 in the experiments realized at LMSPC.

Commercial anatase nanoparticles tested at ISS have photoactivity four times higher than at LMSPC. Sample tested at LMSPC (AlfaAesar 36199) has a lower surface area than sample tested at ISS (ST-01): 8.6 m<sup>2</sup>.g<sup>-1</sup> vs 320 m<sup>2</sup>.g<sup>-1</sup>. It is well known that high surface area improves the activity of the photocatalyst. Moreover, like for Degussa P25, the presence of UV radiation of the Hg lamp increases the yield of H<sub>2</sub> generated at ISS.

The lamp source is also an important point to explain the photocatalytic behavior of the UNT400 sample. This material is a composite of anatase and TiO<sub>2</sub>-B, phases inactive under visible light, which is the radiation range of the metal-halide lamp at LMSPC.

Another interesting point is the different behavior of anatase in the two systems. Although both photocatalysts have the same content of anatase (80% in UNT400 and P25), the morphology, the radiation source and the other phase of the composite clearly play a strategic role on the performance of the material. For example the position of the conduction band of  $\text{TiO}_2\text{-B}$  is 0.35 eV, of anatase 0.2 eV. If radiation source is UV-light, electron can jump from the conduction band of  $\text{TiO}_2\text{-B}$  to that one of anatase, improving significantly the charge separation. This effect can be enhanced by the nanotubular morphology of the material. This consideration suggests that the choice of the test conditions, of the interface and of the morphology can permit to “tune” the hydrogen photoproduction.

#### 4.4.2.3 Evaluation of aerogels

I have performed photocatalytic tests on aerogel A500, Degussa P25 and anatase AlfaAesar 036199 samples, both in LMSPC and ISS. These samples were not Pt-loaded.

##### •Tests realized at LMSPC

Figure 4.36 illustrates results concerning the photoactivity of aerogel A500, Degussa P25 and Anatase AlfaAesar 036199 as characterized at LMSPC.

As already obtained for SN-10-150 and UNT400, A500 has higher photoactivity than anatase AlfaAesar 036199, due to the difference in the surface area ( $84 \text{ m}^2.\text{g}^{-1}$  for A500 vs  $8.5 \text{ m}^2.\text{g}^{-1}$  for anatase AlfaAesar 036199).

Among all our materials tested in these conditions, A500 is the only one that generates more hydrogen than the benchmark Degussa P25. As previously shown, in these operating conditions, P25 is more active than commercial anatase. So, since A500 is just anatase this encouraging result should be linked to structural and optical properties of the A500 aerogel, as I will discuss later in the section 4.4.5.5.

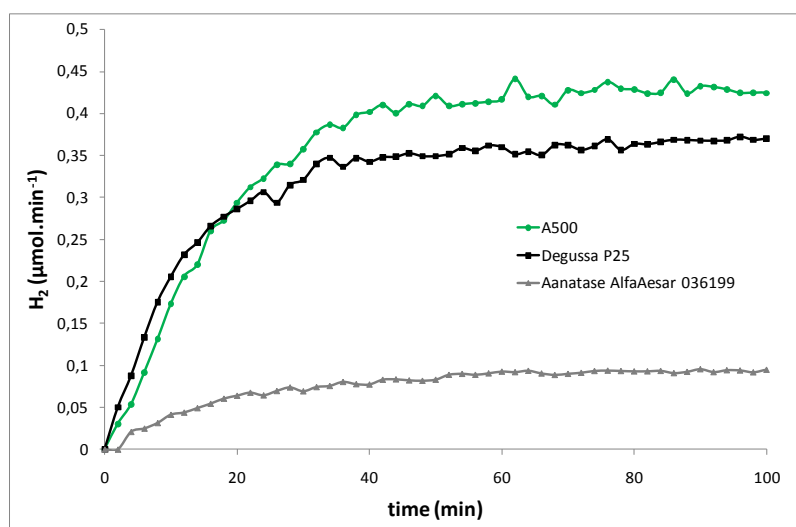


Figure 4.36.  $\text{H}_2$  evolution of aerogel A500, Degussa P25 and anatase AlfaAesar 036199 samples (150 W metal halide lamp, 900 ml water + 100 ml MeOH, 0.7 g samples – LMSPC, Strasbourg)

### •Tests realized at ISS

The only aerogel sample tested at ISS in comparison with Degussa P25 is A500. Associated results are shown at Figure 4.37. Photoactivity of aerogel A500 is twice higher than Degussa P25 (Cf table 4.5). In this case the synergy of optical and structural features of the materials improves the H<sub>2</sub> generation.

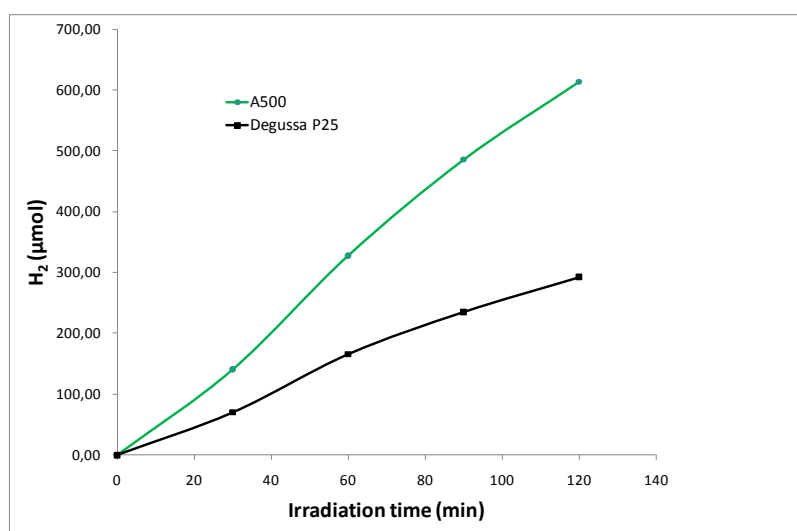


Figure 4.37. H<sub>2</sub> evolution of aerogel A500 and Degussa P25 samples

(450 W Hg lamp, 700 ml water + 100 ml MeOH, 0.8 g samples, ISS, Kyoto)

### •Comparison of tests realized at LMSPC and ISS

Results obtained at LMSPC and ISS have been compared according the same technique as the one used for nanotubes (*confer* paragraph 4.4.2.2). Comparisons are summarized in table 4.5. In both experiments series, A500 generates more hydrogen than Degussa P25. However, the difference is strongest for the tests performed at ISS. Numerous are the differences between the two experimental testings: the reactor (semi-batch at LMSPC and batch at ISS), the reactor cooling water temperature (15 °C at LMSPC and 30°C at ISS), the radiation source (halide lamp at LMSPC and Hg at ISS), the lamp power (150 W for LMSPC and 450 W for ISS) and the concentration of the suspension (0.7 g.l<sup>-1</sup> at LMSPC and 1 g.l<sup>-1</sup> at ISS). A500 is anatase and needs UV light to photogenerate electron/hole couples. Consequently, the radiation range of Hg lamp at ISS has more energy than metal-halide lamp at LMSPC to excite the sample.

---

Sample

H<sub>2</sub> evolution

	(μmol produced after 120 min)	
	LMSPC	ISS
Degussa P25	42	292
A500	52	613

**Table 4.5. Comparison of H<sub>2</sub> evolution results obtained at LMSPC and at ISS.**

#### 4.4.2.4 Evaluation of Pt-loaded aerogels and xerogels

Since aerogel A500 has shown encouraging results, I have decided to load A500 and Degussa P25 samples as well as X500 (for comparison purpose) with Pt (0.3 wt% Pt/TiO<sub>2</sub>) in order to enhance the H<sub>2</sub> evolution [Rosseler et al., 2010]. Figure 4.38 shows the associated results obtained at LMSPC: the green curve describes the photoactivity profile of A500 sample, the black line is related to Degussa P25 and the purple line to X500.

First of all, it appears clearly that the presence of platinum on these materials has a positive effect on the H<sub>2</sub> evolution. In our conditions, the platinization increases the activity of P25 from 0.35 μmol.min<sup>-1</sup> to 3 μmol.min<sup>-1</sup>, while the activity of A500 goes from 0.45 μmol.min<sup>-1</sup> to 9 μmol.min<sup>-1</sup>. Second, it is remarkable that Pt loading significantly enhances the difference in photoactivity between Degussa P25 and A500. The photoactivity of A500-Pt-0.3 wt% is now three times higher than Degussa P25-Pt-0.3.wt%. Finally, it must also be noticed that the photoactivity of sample X500-Pt-0.3 wt.% is the lowest one. This latter result could be ascribed to its low crystallinity and anatase content, coupled with a strong particles agglomeration. Our data completely agree with the literature on this point [Boujday et al., 2004].

Emilio et al. [Emilio et al., 2006] have already underlined the difference in photoactivity of Degussa P25 and some commercial anatase products with and without Pt loading. Studying the photocatalytic degradation of phenol in TiO<sub>2</sub> aqueous suspensions, they observed that the impact of Platinum depends on the substrates: photocatalytic activity of P25 decreased while the one of anatase increased. They followed the charge-carrier dynamics of the materials before and after platinization by Time-Resolved Microwave Conductivity (TRMC) and they tried to correlate the influence of Pt on the photoactivity with TRMC results. They stated that the influence on P25 might be considered as a balance between negative effects of platinization (photons absorption and promotion of carriers recombination) as well as positive effects of platinum deposit (deep electrons traps) together with the specific composition of P25 (enhancement of charge separation due to rutile-anatase interfaces). In their study, they found that, unlike our watersplitting results, the negative effects of the platinization are dominant. However, we observed like Emilio et al. a differential effect of platinization depending on the nature of the substrates : indeed, our platinization seems to have a more positive effect on A500 than on Degussa P25 regarding our watersplitting conditions.

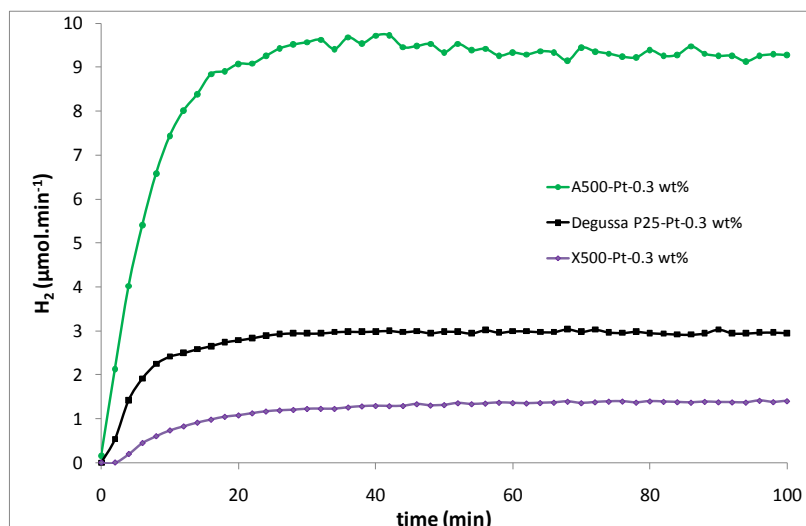


**Figure 4.38. H<sub>2</sub> evolution of of Pt-loaded aerogel A500 and xerogel X500 compared to Pt-loaded Degussa P25 (150 W metal halide lamp, 900 ml water + 100 ml MeOH, 0.7 g samples, Pt/TiO<sub>2</sub>=0.3 wt%, – LMSPC, Strasbourg)**

In order to check the presence of the Pt on the aerogel A500, Scanning Transmission Electron Microscopy-High Angular Annular Dark Field (STEM-HAADF) has been performed at the Centre des Matériaux (Mines ParisTech, Evry) by Dr. Marie-Hélène Berger. Figures 4.39 and 4.40 illustrate the main results of this analysis. The HAADF has highlighted the presence of Pt nanoparticles on the aerogel and the Energy dispersive X-ray spectroscopy (EDX) has permitted to “check” the chemical composition of the considered zone (Figure 4.39), showing that Pt is on the surface of the sample. Figure 4.33 highlights three Pt nanoparticles and allows an estimation of the size of their characteristic size Pt around 5 nm.

The differential effect of platinum on the photoactivity of A500 and P25 can partly come from different dispersion of Pt. A STEM-HAADF study should be carried out on platinized P25 in order to check this hypothesis.

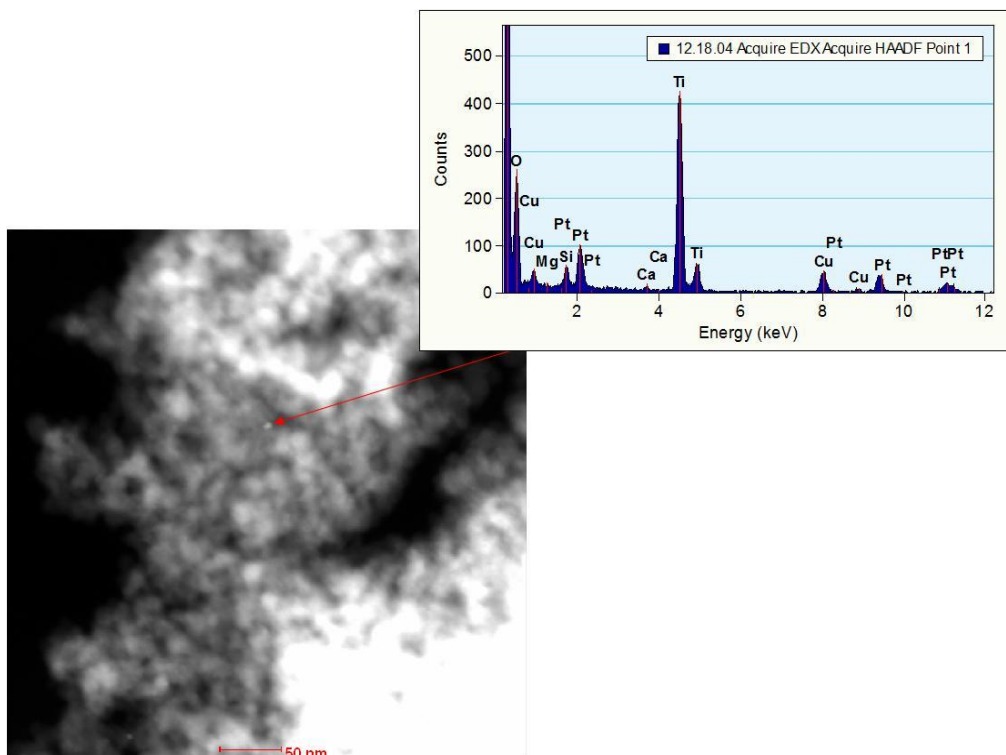


Figure 4.39. STEM-HAADF and EDX on aerogel A500-Pt/TiO<sub>2</sub>=0.3 wt%<sup>64</sup>

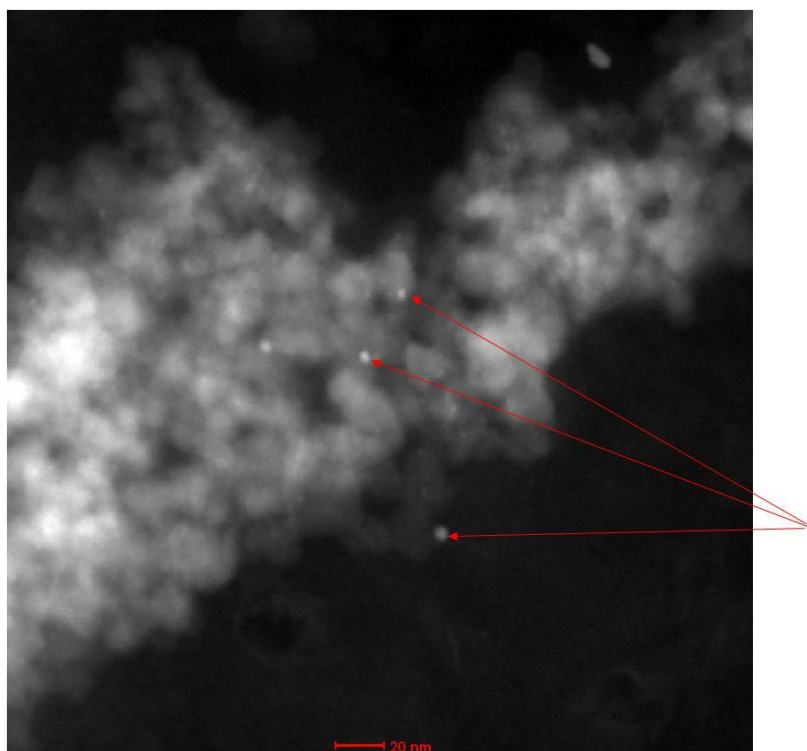


Figure 4.40. STEM-HAADF on aerogel A500 sample - Pt/TiO<sub>2</sub>=0.3 wt% (red arrows indicate Pt nanoparticles)

<sup>64</sup>Cu comes from the grid, Ca, Mg and Si are pollutions.

Finally, X500-Pt-0.3 wt.% has lower activity than A500-Pt-0.3 wt.%, first of all because of the lower crystallinity degree and surface area, two crucial points for the photocatalytic behavior of materials. Moreover, as shown in the chapter 2, particulate network of xerogel is more agglomerated than aerogel and it is well known that an increase of agglomeration causes a decrease of photoactivity.

#### 4.4.2.5 Discussion

These experiments mainly underline two significant points considering H<sub>2</sub> evolution:

- A500 is more active than Degussa P25, in any of our testing conditions,
- Photoactivity of A500-Pt-0.3wt.% is higher than A500 and X500-Pt-0.3. wt%.

First of all, Boujday et al. [Boujday et al., 2004] have already reported higher activity for aerogel than xerogel versus photodegradation of phenol in water. This article underlines that thanks to their high surface area and small crystallites size, aerogels have a photocatalytic activity up to ten times higher than xerogels, despite the higher charge lifetimes observed for xerogels. Although the photocatalytic application is different, our experimental results agree with Boujday's one: aerogel (A500-Pt-0.3wt.%) produces about 10  $\mu\text{mol}\cdot\text{min}^{-1}$  of H<sub>2</sub>, xerogel (X500-Pt-0.3wt.%) about 1  $\mu\text{mol}\cdot\text{min}^{-1}$ . Our structural characterizations clearly show that aerogel has better crystallization and higher surface area which could also be considered as positive features versus H<sub>2</sub> evolution.

Let's discuss now about comparison with Degussa P25. This commercial reference has a higher crystallinity degree than A500 (cf. XRD patterns of P25 in Figure 4.7 in this chapter and XRD of A500 in Figure 2.51 in chapter 2). Furthermore, the fraction of rutile present in P25 is known to improve its absorption in the visible range as well as charge separation [Hurum et al., 2003]. However, aerogel A500 is more active in our specific experimental conditions. So, at this stage, one can wonder why this TiO<sub>2</sub> aerogel presents significantly better photoactivity towards H<sub>2</sub> photogeneration than P25.

First, the specific surface area of A500 aerogel is twice the one of Degussa P25. Secondly, we could hypothesize that the remarkable structure of aerogel materials also contributes to this higher performance. Actually, it is not "a bed" of particles like P25 is, but a continuous interconnected nanostructured network, made up of clusters and aggregates of anatase particles linked together by covalent bonds. We hypothesize that this particular internal structuration could participate to a certain enhancement of the charge (holes and electrons) separation. Using Time Resolved Microwave Conductivity in the same conditions, Emilio et al. [Emilio et al., 2006] studied the behavior of Degussa P25 and Boujday et al. [Boujday et al., 2004] studied TiO<sub>2</sub> aerogels (prepared with nitric acid as catalyst and calcined at 550 °C). After comparison of these two articles, we can stress that aerogel still generates the highest number of charge-carriers with the highest lifetimes compared to P25. Our hypothesis could be consistent with this literature experimental conclusion and could explain the higher photoactivity of aerogel A500 than Degussa P25. Besides, directly linked with the sol-gel synthesis, few hydroxyl groups coming from the titanols  $\equiv\text{Ti-OH}$ , might probably remain

after calcinations at the surface of the anatase particles constituting the solid TiO<sub>2</sub> network (Figure 4.41). Some of them can also come from posterior hydroxylation of the surface. An accurate measurement of the -OH groups is necessary to consolidate this hypothesis and could, for example, be given by chemical analysis like complexation with iron acetylacetonate in toluene [Vanveen et al., 1985], [Znaidi et al., 2001]. Anyway, at this stage, we hypothesize that a certain concentration of hydroxyl groups is present on the surface of our TiO<sub>2</sub> aerogels and probably promotes water adsorption. The study of the surface chemistry of these materials is of high interest to verify this hypothesis but could not be carried out because of the thesis time limitation.

In his article Augugliaro [Augugliaro et al., 1999] shows that adding water vapours to the toluene feed increases the conversion of toluene to benzaldehyde in shorter time compared to a feed without water vapours. FTIR spectroscopy investigations indicate that free hydroxyl groups created on the surface of TiO<sub>2</sub>, thanks to the presence of water, act as effective Lewis adsorption sites for toluene. The results achieved by Augugliaro can partly contribute to explain the encouraging water splitting result obtained with our aerogels. As in Augugliaro's study, we could assume that hydroxyl groups on the surface of our photocatalysts could play a positive role on the adsorption of reagents (H<sub>2</sub>O and/or MeOH) and, consequently on the resulting H<sub>2</sub> photogeneration.

#### **4.4.2.6 Complementary studies**

Since A500 aerogel presented promising results, we have tried to broaden the study of the photoactivity of this materials family by comparing amorphous samples (so-called as-prepared, in the figure 4.41) and samples calcined at different temperatures (400, 500 and 600 °C). The figure 4.41 shows profiles of the photoactivity of these materials versus H<sub>2</sub> evolution. This set of curves show that the calcination temperature increases the crystallinity which improves the photoactivity, despite the decrease of both the specific surface area and the crystallites size (as XRD, N<sub>2</sub> physisorption isotherms and TEM investigations have already underlined in chapter 2). These results show that surface area has not “the” key role in the photocatalytic H<sub>2</sub> evolution. High crystallinity degree of anatase (samples calcined at 400 and 500 °C) and/or creation of anatase-rutile interface (sample calcined at 600 °C), seem to have a more crucial role for our targeted application. In the sample calcined at 600 °C, in fact, UV light excites the anatase and the photogenerated electron goes from the bottom of the anatase conduction band to the bottom of the rutile conduction band.

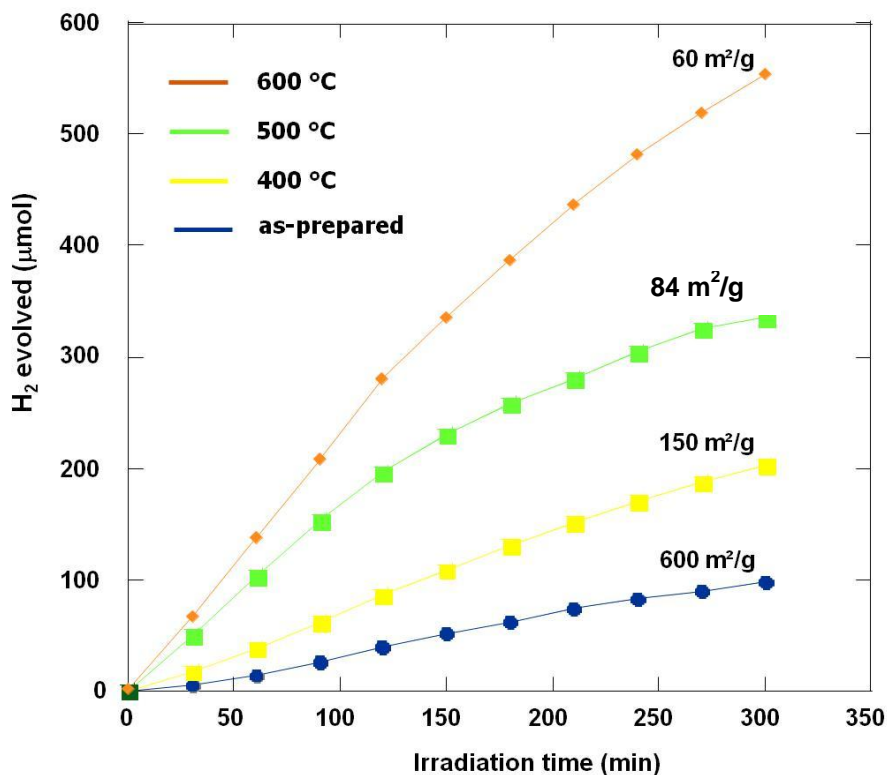


Figure. 4.41 H<sub>2</sub> evolution of TiO<sub>2</sub> aerogels with calcinations temperatures: amorphous so-called “as-prepared” ( $S_{\text{BET}} \sim 600 \text{ m}^2\text{g}^{-1}$ ) and calcined at 400 °C ( $S_{\text{BET}} \sim 150 \text{ m}^2\text{g}^{-1}$ ), 500 °C ( $S_{\text{BET}} \sim 84 \text{ m}^2\text{g}^{-1}$ ) and 600 °C ( $S_{\text{BET}} \sim 60 \text{ m}^2\text{g}^{-1}$ )

(450 W Hg lamp, 900 ml water + 100 ml MeOH, 1 g samples, - ISS, Kyoto)

### 4.4.3 Testing of nitrogen-doped samples

#### 4.4.3.1 Evaluation of aerogels

The Figure 4.42 shows results of photoactivity tests performed at LMSPC on Degussa P25, undoped and nitrogen-doped aerogels versus H<sub>2</sub> evolution. All these samples have been loaded with Pt in order to enhance the H<sub>2</sub> evolution (0.3 wt. % Pt/TiO<sub>2</sub>). The photoactivity of nitrogen-doped samples is slightly higher than that of Degussa P25, while the photoactivity of undoped aerogel A500 (so-called AN0 in the corresponding figure) remains significantly higher.

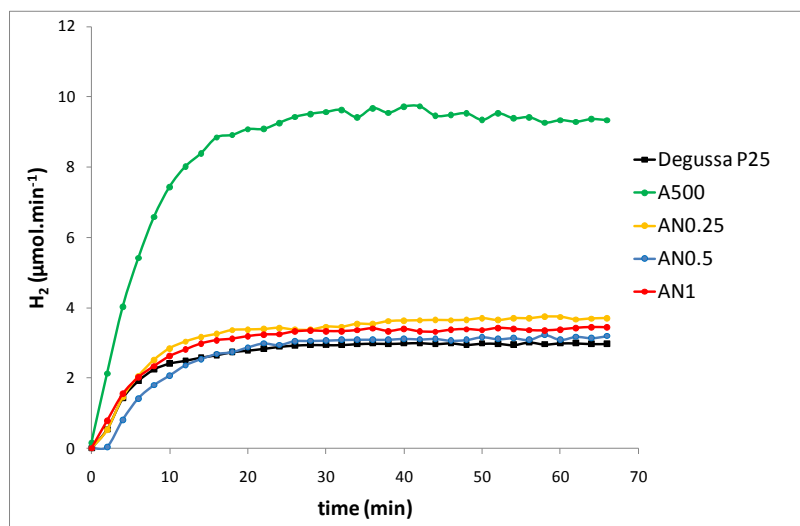


**Figure 4.42. Photoactivity of undoped (A500), nitrogen-doped (AN0.25, AN0.5 and AN1) aerogels Pt-0.3 wt.% and Degussa P25 Pt-0.3 wt.% (150 W metal halide lamp, 900 ml water + 100 ml MeOH, 0.7 g samples – LMSPC, Strasbourg)**

Characterisations of samples presented in the third chapter have shown that structures of undoped and of nitrogen-doped materials are very close: crystallites and particles sizes, specific area as well as crystallinity are rather similar. Consequently, the low activity of nitrogen-doped aerogels could probably due to the electronic modifications observed by XPS. Actually, XPS spectra tend to indicate that the processed nitrogen-doping is interstitial. In addition our XPS investigations on the valence band indicate that doping has induced energetic states in the gap above the valence band, as the absorption at 450 nm observed by UV-vis spectroscopy suggest. Such mid-gap levels [Asahi et al., 2001, Beranek et al., 2006] could act as charge recombination during the photocatalysis process and might cause the low activity of the nitrogen-doped samples compared to undoped sample.

#### 4.4.3.2 Evaluation of xerogels

Figure 4.44 shows the results of H<sub>2</sub> evolution performed at LMSPC on nitrogen-doped xerogels and Degussa P25, without Pt-loading. The three xerogels samples have a lower activity than the commercial reference. These samples have low crystallinity and bigger anatase particles. These features evidently participate to the general decrease of the photoactivity.

The Figure 4.43 clearly indicates that photoactivity of the samples decrease with the increase of the doping rate: the less doped sample (XN0.25) is the most active. Further investigations should be carried out in order to confirm and explain this result which tends to confirm the hypothesis expressed above on creation of mid-gap levels.

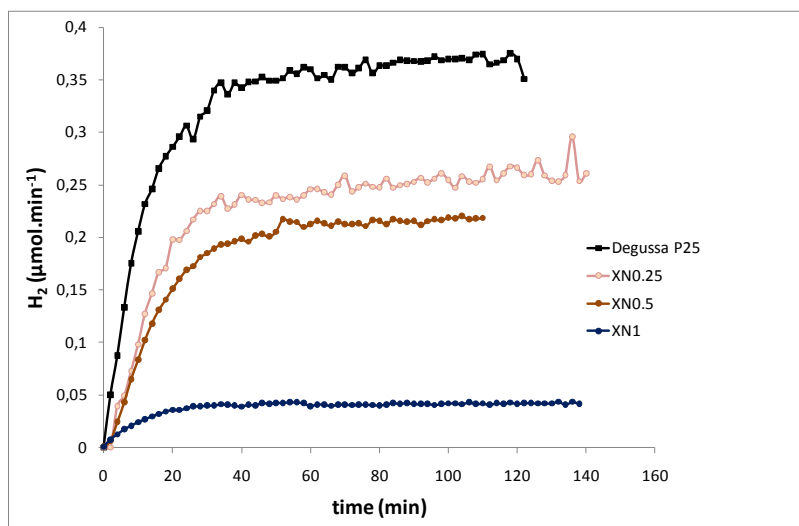


**Figure 4.43. Photoactivity of nitrogen-doped (XN0.25, XN0.5 and XN1) xerogels Pt-0.3 wt.% and Degussa P25 Pt-0.3 wt.%**

(150 W metal halide lamp, 900 ml water + 100 ml MeOH, 0.7 g samples - LMSPC Strasbourg)

Figure 4.44 displays the photoactivity of X500, XN0.25 and XN0.5 xerogel samples loaded with Pt (Pt/TiO<sub>2</sub> = 0.3 wt. %). Due to experimental reasons, the measurements of H<sub>2</sub> evolution at the beginning of the test have given abnormal point (particularly for XN0.25 sample).

The activity of xerogels increases with the increase of the doping rate: X0.5-Pt 0.3% is this time the most active sample. This sample also produces more hydrogen than Degussa P25 loaded with the same theoretical amount of Pt. As for not-loaded xerogels, further investigations are to be initiated to confirm and explain this interesting result.

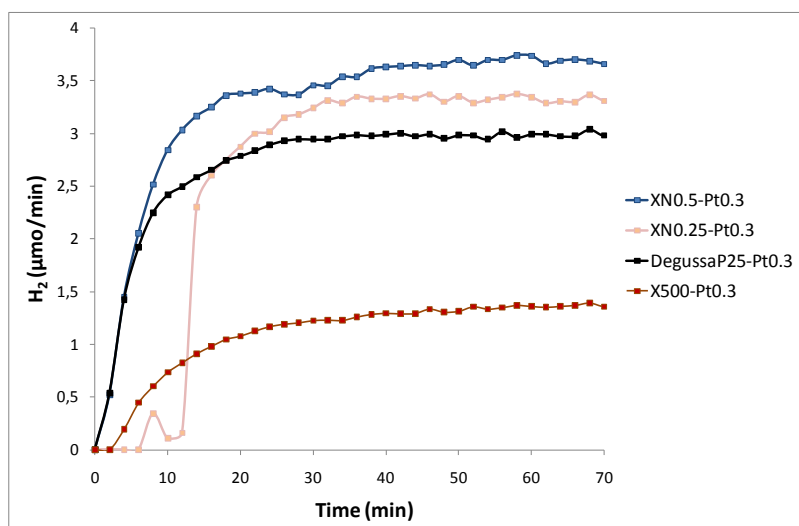


**Figure 4.44. Hydrogen tests on nitrogen-doped xerogels Pt-0.3 wt.% (X500, XN0.25 and XN0.5 samples) and Degussa P25 Pt-0.3 wt.%**

(150 W metal halide lamp, 900 ml water + 100 ml MeOH, 0.7 g samples, - LMSPC Strasbourg)

## 4.5 Conclusions

In this chapter I have summarized the H<sub>2</sub> evolution results obtained on the different TiO<sub>2</sub> morphologies I have elaborated: nanoparticles, nanotubes, aerogel and xerogel materials. Moreover the influence of the nitrogen-doping via sol-gel has also been studied on the latter two morphologies: aerogels and xerogels. Samples have been tested in different conditions using two different devices at LMSPC (Strasbourg University) and ISS (Kyoto University),

The photoactivity of these nanomaterials appears strongly affected by their morphology, cristallinity and specific surface area whatever the testing conditions.

### • *Main conclusions on undoped materials tested with a metal halide lamp at LMSPC*

The Figure 4.45 sums up most significant photoactivity results obtained with the three undoped morphologies (SN-10-150 nanoparticles, UNT400 nanotubes, and A500 aerogels samples) compared to two commercial products used as reference (anatase AlfaAesar 036199 and Degussa P25).

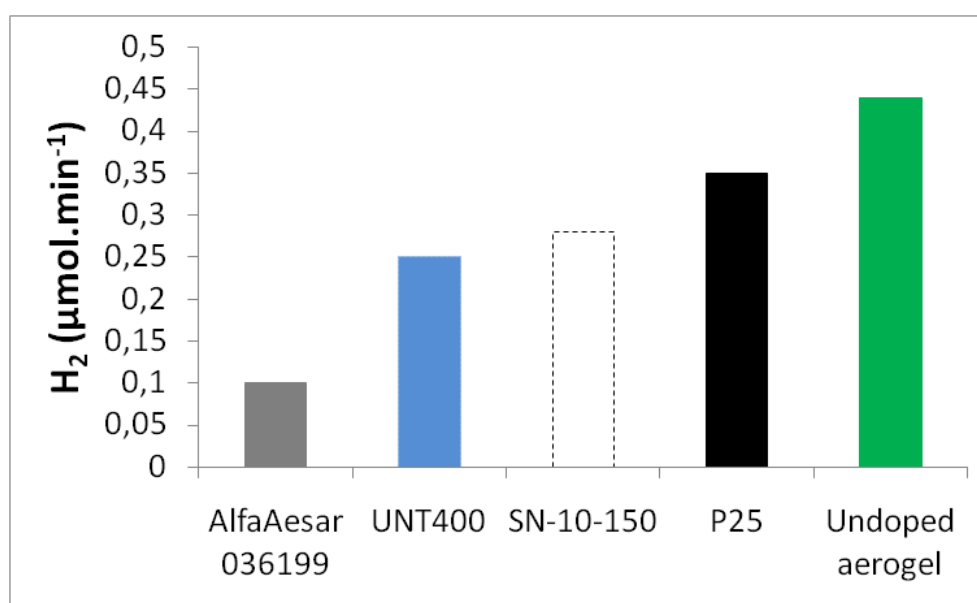


**Figure 4.5.** Photoactivity of Degussa P25 and AlfaAesar anatase nanoparticles, undoped aerogel (A500), anatase nanoparticles (SN-10-150) and undoped nanotubes calcined at 400 °C (UNT400) (150 W metal halide lamp, 900 ml water + 100 ml MeOH, 0.7 g samples, – LMSPC, Strasbourg)

The three photocatalysts we have synthesized are more active than AlfaAesar 031699.

SN-10-150 sample is made up of anatase nanoparticles, as AlfaAesar 036199. However nanoparticles of SN-10-150 are smaller than that of AlfaAesar 036199 and consequently the associated specific area is larger. This result underlines that, for a well-defined family of materials (here anatase particles), specific area has a significant influence.

UNT400 sample, instead, has different morphology and phase compared to anatase AlfaAesar 036199. I hypothesize that its tubular shape together with the coexistence of two different phases could improve charge separation and, consequently, photoactivity.

Although UNT400 and SN-10-150 are more active than AlfaAesar 036199, their H<sub>2</sub> production ability is lower than Degussa P25.

A500 aerogel, instead, is more active than Degussa P25. I have hypothesized that the particular tridimensionnal architecture of the aerogel widely improves charge separation and thus enhances H<sub>2</sub> photoproduction.

• ***Main conclusions on undoped materials tested with a mercury lamp at ISS***

At ISS, photoactivity of A500 aerogel (without Pt loading) is twice the one of Degussa P25 and photoactivity of UNT400 is three times higher than the one of Pt loaded P25. If we compare these results with those obtained in LMSPC, we can observe that UNT400 and A500 samples are much more active in ISS than in LMSPC, always keeping Degussa P25 as the reference material. Amongst other reasons, this increase of the performance is probably coming from the nature of the lamp. Since A500 and UNT500 samples are mostly made up of anatase, they need a lamp with a wavelength in the range of UV light. This is the working range of lamp in ISS, while lamp in LMSPC has main part of its spectrum in the visible light region.

• ***Main conclusions on nitrogen-doped materials tested with a halide lamp at LMSPC***

I have checked the influence of nitrogen-doping on aerogels and xerogels because, within the frame of this study, they appear as the most promising undoped samples for water splitting.

In the case of aerogels, the nitrogen-doping decreases dramatically the activity of the initial material. Pt loaded nitrogen-doped aerogels have an activity similar to that of Degussa P25. XPS investigations on the valence band have revealed that such a doping route has probably created mid-gap levels in the gap. These localized states can trap the carriers and thus limit drastically the H<sub>2</sub> evolution of the doped samples comparing to the undoped one.

However, Pt loaded nitrogen-doped xerogels are more active than not-modified corresponding xerogel. As reflectance data show, they absorb more visible light than their aerogels counterparts. This data could explain the radically different evolution of the performances of the xerogels with level of nitrogen-doping. However, since we do not have any investigation on their valence band by XPS, we cannot strongly support this hypothesis. Moreover, the behaviour of unloaded nitrogen-doped xerogels, less active than undoped ones, is questioning and must be repeated.

Finally, this study on the hydrogen photoproduction underlines that morphology has a strong impact on the hydrogen evolution: although the phase is the same and the surface area similar,

aerogel (A500) is significantly more active than particles (SN-10-150). Interface TiO<sub>2</sub>-B/anatase (UNT400) and tubular morphology also play a strategic role on the hydrogen production. Our anionic doping on aerogels (as well as our cationic doping on nanotubes as presented in Appendix 1), instead, seem not to be a good strategy for improving the activity of undoped materials.



## 5. General conclusion and some perspectives

TiO<sub>2</sub> is a well-spread material among others for superhydrophilic surfaces, degradation of pollutants and several applications in the energy field. In the last decade increasing energy demand has pushed research to reconsider TiO<sub>2</sub> as a promising photocatalyst for clean hydrogen (H<sub>2</sub>) production [Fujishima et al., 2008]. Directly related to this topic, this document reports the most significant results of my Ph-D thesis on the elaboration, characterization and study of different TiO<sub>2</sub> nanostructures for H<sub>2</sub> production via water photolysis (so-called water splitting).

### • Summary

First, I have elaborated and characterized three different TiO<sub>2</sub> (nano)structures in order to underline the impact of their specific morphology on H<sub>2</sub> evolution: nanoparticles, nanotubes (1D structure), aerogels and xerogels (3D continuous networks).

- Nanoparticles have been synthesized starting from a precursor issued from the precipitation of TiCl<sub>4</sub> and NaOH at pH 2 in batch conditions at 25 °C and atmospheric pressure. At the end of this stage, we have obtained an amorphous product. This product has been crystallized in hydrothermal conditions at different pH and temperatures. I have chosen pH 2 and 10, temperatures 150 and 250 °C. This technique permits to obtain a wide range of nanoparticles, different in size as well as surface area. The smallest nanoparticles have a diameter of 9 nm (surface area 164 m<sup>2</sup>.g<sup>-1</sup>), 37 nm for the biggest (surface area 17 m<sup>2</sup>.g<sup>-1</sup>). Generally, I have observed that low temperatures of crystallization allow the germination of anatase without significant growth of nanoparticles, conducting to TiO<sub>2</sub> photocatalyst with a rather high surface area. At high temperatures, Ostwald ripening is more sensitive and leads to bigger particles.

- Nanotubes have been elaborated using the Kasuga method. A solution of commercial anatase nanoparticles and NaOH 10 M has been put in autoclave and heated up to 150 °C for 72 h. At the end of this step, ion-exchange treatment has given nanotubes of protonated titanate. After this stage, calcinations treatment at 300, 400 and 500 °C temperatures has led to elaboration of three specific materials, differing in shape and phase. XRD patterns state that at 300 °C sample made of TiO<sub>2</sub>-B has been obtained, at 400 °C a mixture of TiO<sub>2</sub>-B and anatase is formed and at 500 °C almost pure anatase is elaborated. TEM analysis states that TiO<sub>2</sub>-B phase is associated with nanotubular structure and anatase with nanoparticles (short rods). So no pure-anatase nanotubes have been elaborated, but mixture of phases (TiO<sub>2</sub>-B and anatase) and structures (nanoparticles and nanotubes). Results of N<sub>2</sub> physisorption investigations report a drop of surface area when calcination temperature is 400 °C or 500 °C due to a transformation of tubes in particles. Nevertheless, we considered that such mixed structures deserved testing for hydrogen photoproduction and we did not try to further improve the whole process to get pure anatase nanotubes or nanowires.

- Finally aerogels and xerogels have been elaborated from gels synthesized in isopropanol using HNO<sub>3</sub> as catalyst and titanium tert-butoxide as precursor in presence of water for hydrolysis. Gels have been synthesized according to a formulation of reference

selected from literature with a molar ratio equal to  $\text{Ti}(\text{OtBu})_4 : \text{iPrOH} : \text{HNO}_3 (2\text{M}) : \text{H}_2\text{O} = 1 : 18 : 0.08 : 3$ . After gelation, syneresis and washing, gels have been dried. Two drying routes have been followed: supercritical  $\text{CO}_2$  and evaporation dryings. Once dried, the aerogels and xerogels have been calcined in order to generate anatase. First, a study of the calcinations temperatures of aerogels has shown that at  $500\text{ }^\circ\text{C}$  well crystallized anatase is present without rutile. In parallel, it has been shown that xerogels calcined in the same conditions are also formed of anatase but are less crystallized than their aerogels counterparts and thus necessitate longer calcinations duration to reach an equivalent degree of crystallization. The anatase aerogels calcined at  $500^\circ\text{C}$  appear constituted of particles of around  $15\text{ nm}$  and present specific area close to  $100\text{ m}^2/\text{g}$  as measured by BET. The xerogels are much more compact and are composed of significantly bigger particles.

After this first elaboration step, I have studied doping of nanotubes with vanadium and aerogels/xerogels with nitrogen, in order to shift the photoresponse of these materials in the visible-light range.

- Vanadium-doped nanotubes have been elaborated by wet impregnation of titanate with  $\text{VO}(\text{acac})_2$  water solution. I have chosen three doping V/Ti atomic% : 0.5, 1 and 2. After complete evaporation of water, I have calcined the resulting samples. It has been observed that vanadium has two main effects on the elaboration protocol:

- anatase appears at higher temperature and rutile appears at lower temperature comparing to undoped nanotubes,
- $\text{TiO}_2\text{-B}$  remains present at high temperature (here,  $500$  and  $600\text{ }^\circ\text{C}$ ).

In order to quantify the anatase/ $\text{TiO}_2\text{-B}$  ratio, Raman spectroscopy has been used. It has been found that in undoped sample calcined at  $400\text{ }^\circ\text{C}$  anatase is  $80\text{ wt}\%$  and  $\text{TiO}_2\text{-B}$  is  $20\text{ wt}\%$ . Anatase percentage dramatically drops for  $0.5\%$  sample calcined at  $400\text{ }^\circ\text{C}$  ( $2\%$ ),  $1\%$  calcined at  $500\text{ }^\circ\text{C}$  ( $9\%$ ) and  $2\%$  calcined at  $600\text{ }^\circ\text{C}$  ( $4\%$ ). As a consequence,  $\text{V}^{4+}$  impregnation is detrimental to formation of anatase nanotubes and would require a severe optimization study. Considering these experimental issues it has been decided not to insist on this first way.

- After these tries to get vanadium-doped nanotubes, I have tried to elaborate nitrogen-doped aerogels and xerogels, using urea as a potential source of nitrogen directly incorporated in the sol. Such a process reveals no change regarding structural features of the final aerogels and xerogels. Not-modified and nitrogen-modified samples show similar anatase crystallization degree and crystallites size (as characterized by XRD), surface area (as evaluated by BET treatment of  $\text{N}_2$  sorption isotherms) and particles size (as observed by TEM). This chemical treatment does not seem to induce significant modifications in position and shape of the Ti 2p and O 1s peaks, as XPS results show. XPS has first permitted to set off that the samples have been doped and then allowed to make some hypothesis on the nature of doping in the matrix. Indeed, literature seems to agree that a nitrogen signal at about  $400\text{ eV}$  (in our case is  $400.3\text{ eV}$ ) is representative of interstitial doping.

Once elaborated, a short selection of materials has been tested versus water splitting in two laboratories: Institute of Sustainability Science (ISS) at Kyoto University and Laboratory of Materials, Surfaces and Processes for the Catalysis (LMSPC) at University Louis Pasteur in Strasbourg. The principal difference between the two testing benches concerns the nature of the

light source. At ISS a Hg lamp is used instead of a metal-halide lamp at LMSPC which induces some rather different irradiation conditions. In order to easily compare the results obtained with these two specific devices, Degussa P25 has been used as the reference TiO<sub>2</sub> material.

- The main two results obtained at the LMSPC are: for one hand, undoped anatase aerogels calcined at 500 °C are three times more active than Degussa P25 and for the other hand undoped nanotubes calcined at 400 °C and anatase nanoparticles (SN-10-150) appear less active than Degussa P25. At ISS, instead, hydrogen evolutions of both aerogel calcined at 500 °C and nanotubes calcined at 400 °C are at least twice as high as those of Degussa P25. First of all, this difference is probably due to the specificities of the lamps. Indeed, Hg lamp spectrum is located in the UV range, where the TiO<sub>2</sub>-B and anatase are activated. On the contrary, the metal-halide lamp has a spectrum mainly in the visible light, in which TiO<sub>2</sub>-B and anatase are not excited. Since the undoped nanotubes calcined at 400 °C are a mixture of anatase and TiO<sub>2</sub>-B, I hypothesize that this photocatalyst is more efficiently excited by Hg lamp. In parallel, good results obtained with aerogels are probably coming from the particular structure of the material. Aerogel, in fact, is a tridimensionnal continuous network in which particles are linked all together with covalent necks. We hypothesize that this feature is susceptible to improve the charge separation and, consequently, the hydrogen production. This first set of experiments performed within this work confirms that morphology can have a strong impact on the hydrogen photogeneration. As a preliminary conclusion on performances, hydrogen tests have revealed two rather promising photocatalysts versus H<sub>2</sub> photoevolution: undoped aerogel calcined at 500 °C and undoped nanotubes calcined at 400 °C. It can also be stressed here that Pt loading of Degussa P25 and aerogel enhances significantly the difference in photoactivity of these two samples.

- Finally, nitrogen-doped aerogels, instead, have an activity similar to that of Degussa P25 (as obtained at LMSPC). This result could be partly explained thanks to the XPS study of the valence band. These XPS investigations have stated that nitrogen-doping has induced levels in the bandgap without inducing a reduction of the bandgap value. It has been hypothesized on this basis that these localized energy levels could trap the photogenerated carriers and thus limit the hydrogen production.

As a general conclusion on experimental results, we can state that i) undoped materials have a significantly higher activity than doped materials and ii) among the undoped samples, nanotubes calcined at 400 °C and aerogels calcined at 500 °C are the most interesting for further research on water splitting.

### • To go further

This Ph-D work is the *first stone* for further researches at CEP / MINES ParisTech on this “hot” topic. Obviously, it can be set off here that further researches are necessary to improve the efficiency of TiO<sub>2</sub> aerogels and nanotubes materials for the targeted water splitting application.

As far as undoped materials are concerned, we could underline that i) optimizing the hydrothermal and post-treatment transformation parameters of nanotubes could lead to the preparation of anatase nanotubes with activity higher than TiO<sub>2</sub>-B/anatase nanotubes and ii)

for their part, anatase  $\text{TiO}_2$  xerogels must be studied with deeper attention because they could represent interesting materials. Indeed, calcinated in adequate conditions, they could permit to avoid supercritical drying without degrading *too much* their water splitting efficiency.

As far as doped materials are concerned XPS characterizations let us think that activity of nitrogen-doped aerogels could be improved by increasing the set of doping states localized near the edge of the valence band in order to narrow the bandgap [Serpone, 2006]. Literature shows that bandgap reduction can be achieved by increasing the concentrations of the dopants [Serpone, 2006]. A heat treatment at low temperature (in the range 300-400 °C) under  $\text{NH}_3$  flow (usually  $\text{NH}_3/\text{Ar}$  or  $\text{NH}_3/\text{N}_2$  flow) of the urea-modified aerogels could permit to increase the doping ratio in the  $\text{TiO}_2$  matrix [Horikawa et al., 2008]. Another technique to dope nanotubular structures as well as aerogels and xerogels is the non-equilibrium nitrogen DC-Arc plasma treatment. This tool has already been used in our research Center with preliminary promising results [Suzuki et al., 2008].

Of course many other perspectives of continuation could be listed here. Among others, it is of high interest to initiate works on morphological and/or allotropic interfaces to enhance charges separation for example through the synthesis of aerogel / nanotubes composites [Suzuki et al., 2008].



## APPENDIX 1.

### Vanadium doping: High Temperature X-Rays Diffraction study and photocatalytic test for hydrogen evolution

High temperature X-ray diffraction (HT-XRD) has been used to investigate the thermal stability of the doped vanadium anatase nanotubes. These analyses have been carried out by Prof. Suzuki from Kyoto University. For the undoped sample (Figure A1.1) the anatase disappears at 900 °C, as known in the literature [Czanderna1958]. For 0.5, 1 and 2% doped samples the anatase disappears at 800, 700 and 600 °C respectively (Figure A1.2, Figure A1.3 and Figure A1.4). Our results agree with literature [Banares1996]. Following HT-XRD results V0.5 should be anatase after calcination at 500 °C, V1 and V2 after a treatment at 600 °C. However, Raman Spectroscopy shows that they are TiO<sub>2</sub>-B. Difference in conditions of the high temperature X-ray diffraction analyses from the calcination conditions of our materials can explain these results. The heating rate of the calcinations procedure is 2 °C/min, while that of the HT-XRD is 10 °C/min. This is why even though the 2% doped sample has been calcined at 600 °C, it has not lost the 1 D morphology but it still is TiO<sub>2</sub>-B. Slow heating rate keep the phase and the corresponding morphology.

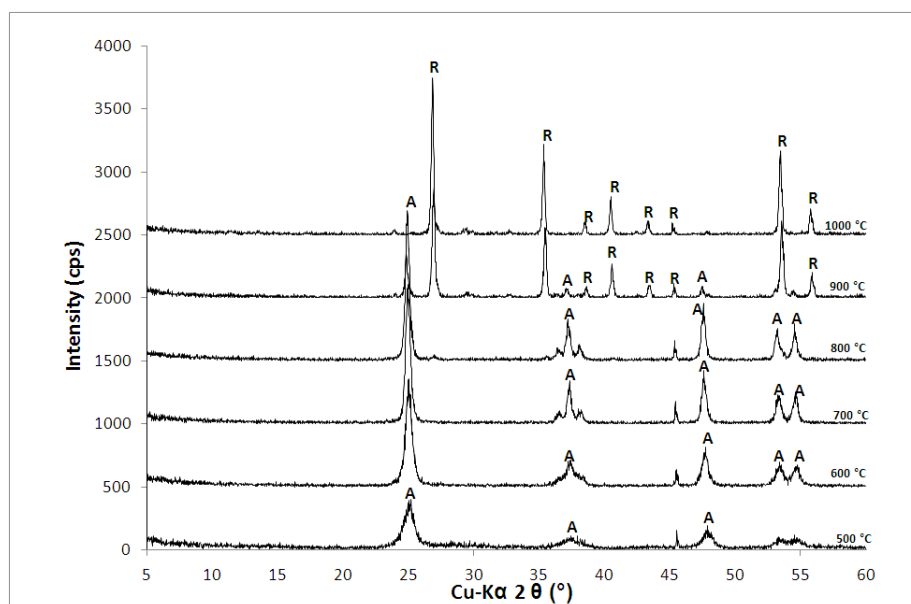
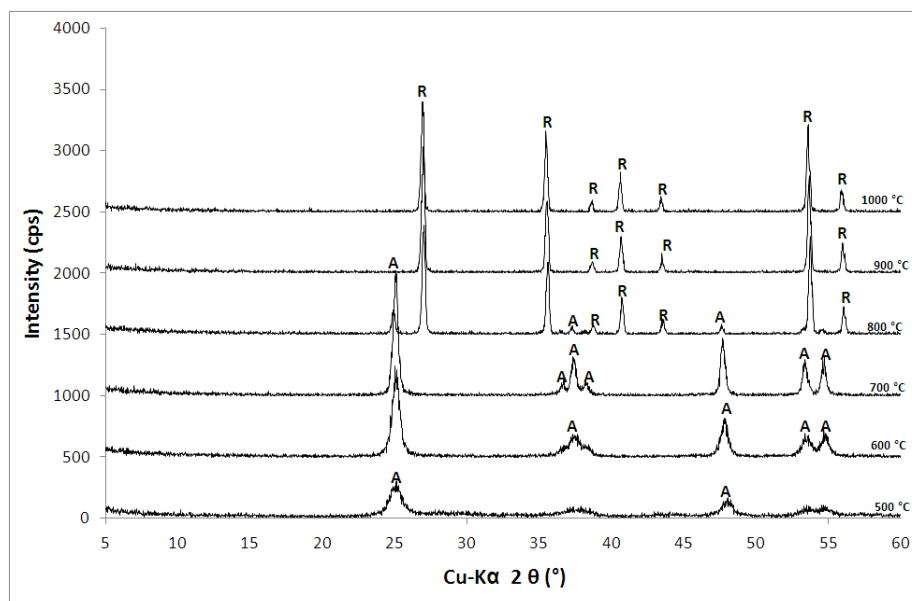
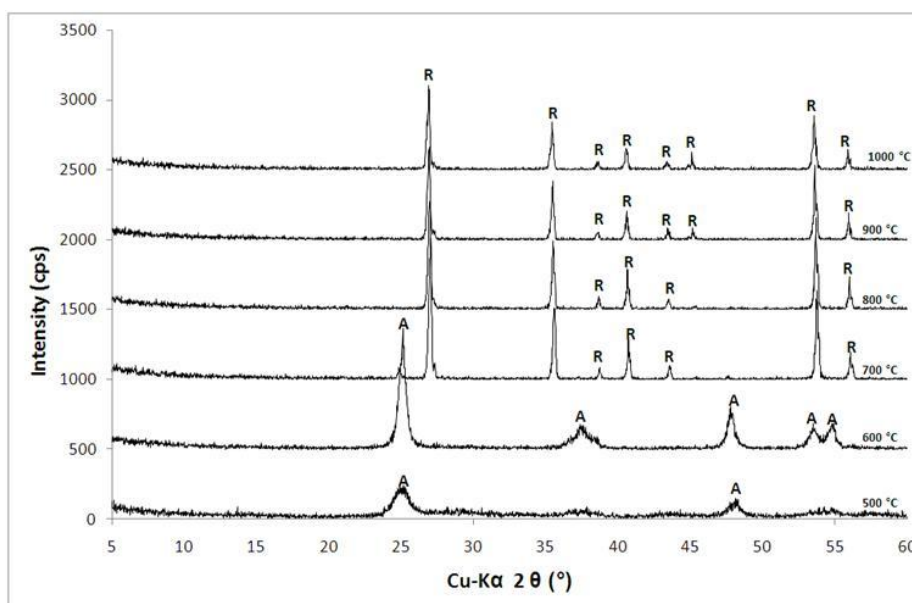


Figure A1.1 HT-XRD of undoped nanotubes (A=anatase, R=rutile)



**Figure A1.2 HT-XRD of V0.5 (A=anatase, R=rutile)**



**Figure A1.3 HT-XRD of V1 (A=anatase, R=rutile)**

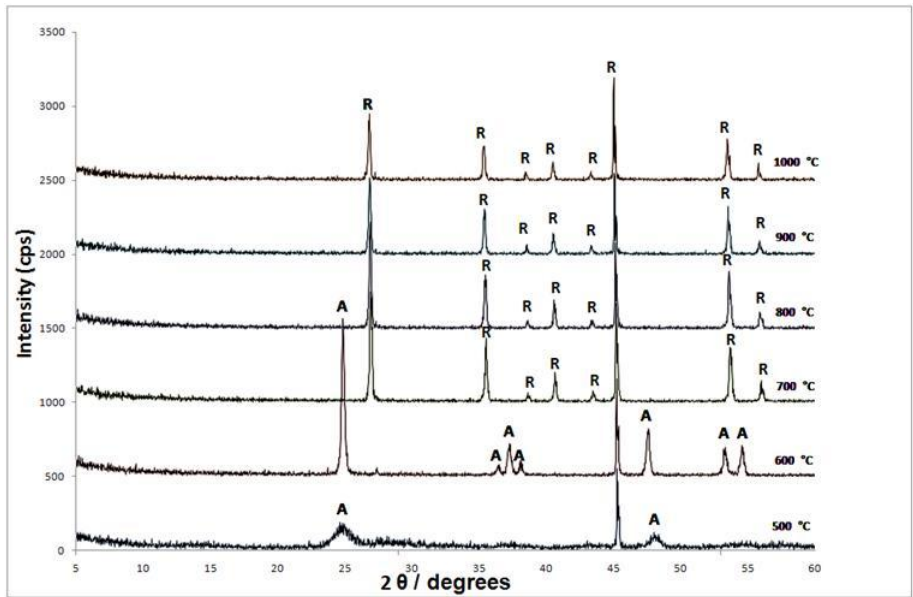


Figure A1.4 HT-XRD of V2 (A=anatase, R=rutile)

Figure A5 gathers spectra taken at 700 °C, highlighting that at this temperature 0 and 0.5% samples are still anatase, 1% almost all rutile, 2% all rutile. This analysis give significant results: vanadium reduces the existing range of anatase. In doped samples anatase, in fact, appears at higher temperatures and turns into rutile at lower temperatures, comparing to undoped material.

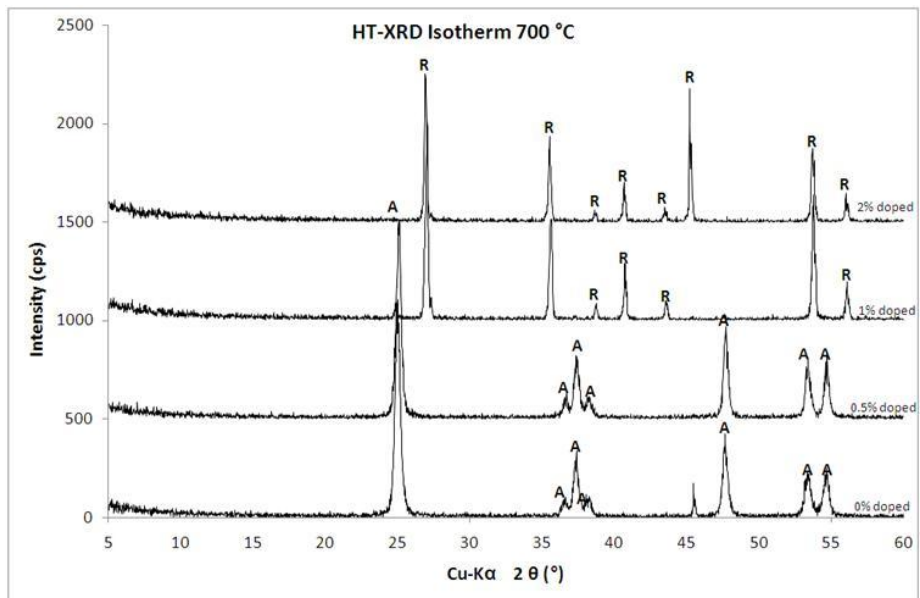


Figure A1.5. Diffractograms at 700 °C

The photocatalytic tests have been performed on doped and undoped nanotubes (Figure 1.6).

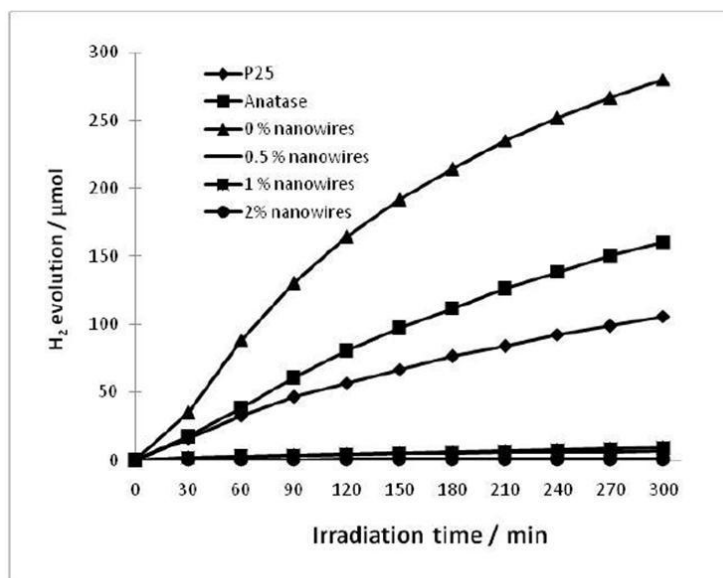


Figure A1.6. Hydrogen evolution

Degussa P25 (ref: Aerosil Evonik Degussa Co., Ltd.) and commercial anatase particles ST-01 (ref: ST-01, Ishihara Sangyo Co., Ltd.) have been tested as reference materials

With our experimental conditions the photoactivity of the tested materials ranges as follows:

Undoped nanotubes >> Commercial anatase ST-01 > Degussa P25 >> doped nanotubes

It is noteworthy that the most active materials are the undoped nanotubes, according to the literature (Yoshikazu 2008, Catalysis Communications). Such an increase of photoactivity is probably due to the better crystalline structure of 1 D materials. Photoactivity of nanotubes seems to be also more efficient in other applications (Aimin Yu et al., 2009, Catalysis Letters).

Despite this exciting behavior of undoped nanotubes, vanadium doped nanotubes have a very low activity. Indeed, although their band gap is narrower than that of undoped samples, their photoactivity has dramatically decreased which wipes out any hope to use them as visible light photocatalyst for water splitting.

Recent studies have actually demonstrated that cation doping can significantly lower the flat band potential of the conduction band of titania, under the critical value of 0 eV (NagaveniK. Et al. 2004, J. Phys. Chem. B).

In addition, possible mid-gap levels in the band gap can be introduced and act as recombination centers of electron/hole couples.

Finally, we assume that vanadium doped semiconductors can photocatalyse the competitive backward reaction (that produces water from H<sub>2</sub> and O<sub>2</sub> produced), as already demonstrated for ethanol degradation (ref. Masih: Applied Catalysis A: General 325 (2007) 276–282).

Photoactivity of TiO<sub>2</sub> based nanomaterials depends also on testing conditions. Li L. (Li L. 2009, Materials Chemistry and Physics) reports that undoped catalysts are active under UV light, while vanadium doped materials are more active under visible light. Our tests have always been performed using a Hg lamp without wavelengths filters. This operating condition may also explain the low activity of doped samples.



## APPENDIX 2. Opto-electronic characterisations

Two important features of our materials have to be determined with respect to the sunlight conversion to hydrogen :

- the bandgap because it will govern the light absorption
- the conduction band energy level, on which depends the hydrogen formation

The determination of the valence band energy level may also help to the determination of the aforementioned features, provided that at least one of them is available. As a matter of fact, knowing the valence band energy level and either the bandgap or the conduction band energy level will allow to respectively determine the conduction band energy level or the bandgap, the latter corresponding to the energy difference between the conduction and the valence bands.

To this end, we have used UV-Vis Diffuse Reflectance and UPS-XPS.

### A.2.1 UV-Vis Diffuse Reflectance

Diffuse reflectance is a very useful technique to determine the optical absorption properties of powdered materials, what cannot be done with standard UV-Vis spectroscopy developed for non opaque samples. It can in particular be used to determine the bandgap of semiconducting materials such as TiO<sub>2</sub>.

In standard transmission UV-Vis spectroscopy, the fading (figure A2.1) of a monochromatic beam, of intensity  $I_0$ , through a sample of thickness  $x$ , is represented by the equation:

$$I = I_0 \cdot \exp(-\alpha x) \quad \text{eq.A2.1}$$

with  $\alpha$  the absorption coefficient of the material.

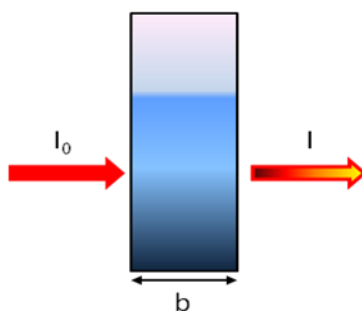


Figure A2.1

The transmittance (T) is defined as:

$$T = I/I_0 \quad \text{eq.A2.2}$$

The absorbance (A) or optical density (OD) is defined as:

$$A = -\log(I/I_0) = \log(1/T) \quad \text{eq.A2.3}$$

This technique may be used for powdered materials provided that a stable suspension can be prepared. Nevertheless, the scattering due to the solid particles makes the interpretation more difficult. Diffuse reflectance spectroscopy is actually more dedicated to the analysis of powdered samples.

In that case, the part of the incident beam that has not been absorbed by the sample is reflected in a diffuse manner by the powder. The thickness of material interacting with the monochromatic beam is difficult to estimate but the absorption coefficient remains proportional to the absorbance. The reflectance R is assimilated to the transmittance so that:

$$A = \log(1/R) \quad \text{eq.A2.4}$$

The bandgap of semiconductors can moreover be estimated looking at the absorption edge on UV-Vis spectra obtained in diffuse reflectance mode (figure A2.2).

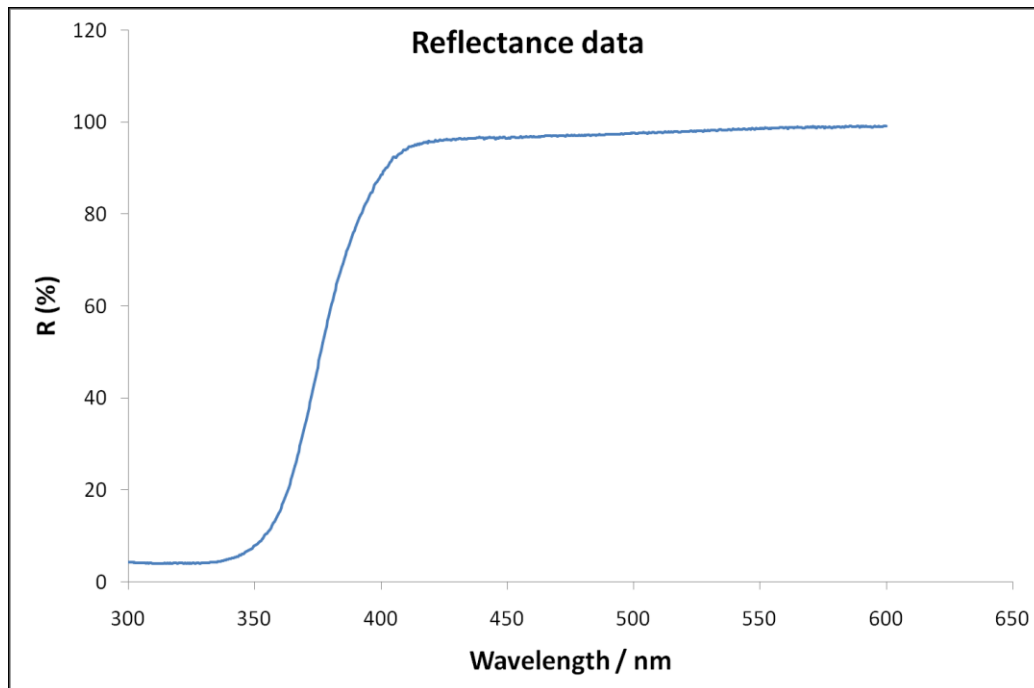


**Figure A2.2: Reflectance data of commercial anatase particles (AlfaAesar 036199)**

This absorption edge corresponds indeed to the photoinduced transfer of an electron from the highest level of the valence band to the lowest level of the conduction band (figure A2.3). Such a transition can be direct or indirect, corresponding to a direct or an indirect bandgap, depending on the conservation or not of the momentum during the transition.

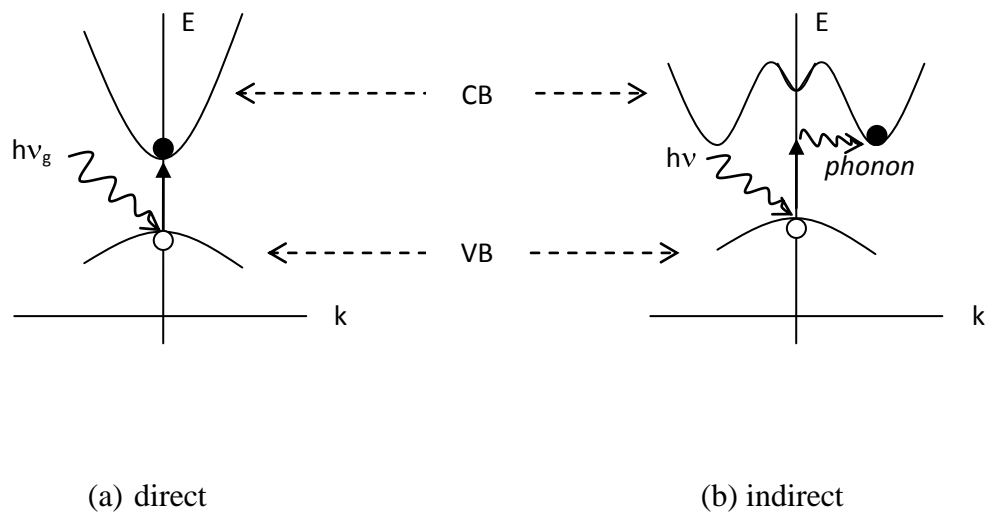


**Figure A2.3. Photoinduced transfer of an electron from the valence band the conduction band**

The reflectance essentially depends on three parameters: the absorption coefficient, the scattering coefficient and the thickness of the sample. It is given by the formula:

$$R = (1 - R_g(a - b \coth(bSx)))/(a - R_g + b \coth(bSx)) \quad \text{eq.A.2.5}$$

where

- $K$  = absorption coefficient
- $S$  = scattering coefficient
- $x$  = thickness
- $a = 1 + K/S$
- $b = (a^2 - 1)^2$  or  $\sqrt{(a^2 - 1)}$
- $R_g$  = reflectance of the support

In the case of a thick powder bed, the sample holder (support) has no effect on the reflectance of the sample, which can then be simplified as:

$$R_{\infty} = 1 + K/S - [(K/S)^2 + 2K/S]^{1/2} \quad \text{eq.A2.6}$$

where  $R_{\infty}$  is the reflectance at infinite thickness.

Solving this equation for  $(K/S)$  gives the Kubelka-Munk function:

$$F(R) = K/S = (1 - R_{\infty})^2 / 2R_{\infty} \quad \text{eq.A2.7}$$

The absorption coefficient  $K$  can be expressed [Pankove, 1971]:

$$K \propto (h\nu - E_g)^n / (h\nu) \quad \text{eq.A2.8}$$

$n = 0.5$  for a direct bandgap /  $n = 2$  for an indirect bandgap

where

- $h$  = Planck's constant
- $\nu$  = wave number ( $\text{cm}^{-1}$ )
- $E_g$  = bandgap energy value (eV)

Making the assumption that the Kubelka-Munk function  $F(R)$  is proportional to the absorption coefficient, we have:

- $[F(R) \cdot h\nu]^{0.5} \propto (h\nu - E_g)$  for an indirect bandgap
- $[F(R) \cdot h\nu]^2 \propto (h\nu - E_g)$  for a direct bandgap

The absorption edge gives a rough estimation of the bandgap. Plotting  $(Kh\nu)^{1/n}$  as a function of  $h\nu$ , allows to more precisely determine the value of the bandgap that is equal the x-intercept of the extrapolated linear part of the plot. Fig. A2.3 and A2.4 show curves for bandgap estimation assuming direct and indirect transition. Elaborating data with hypothesis of indirect transition gives bandgap value of 3.25 eV, as known in the literature. So we can

state that electron transition is indirect in anatase form. Since in this thesis synthesised materials are anatase based, bandgap has been evaluated assuming direct transition.

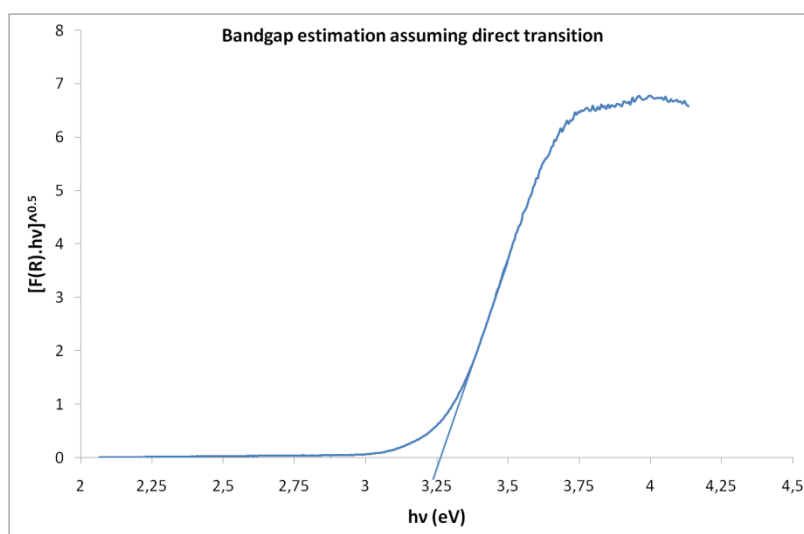


**Figure A2.4 Estimation of the band gap of commercial anatase nanoparticles assuming indirect transition (AlfaAesar 036199)**

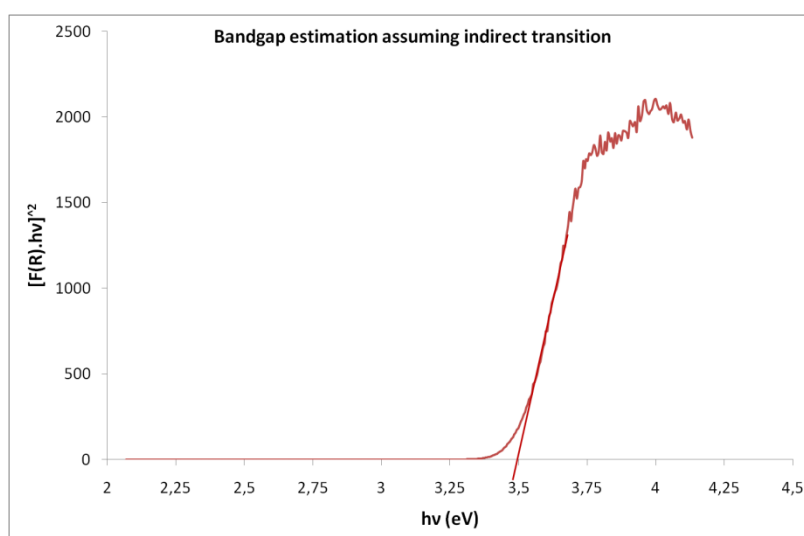


**Figure A2.5 Estimation of the bandgap of commercial anatase nanoparticles (AlfaAesar 036199) assuming direct transition**

### *Equipment*

For the analyses, we have used the Cary 500 UV-VIS-NIR spectrophotometer (Figure A2.6) from the LPMC (Laboratoire de Physique de la Matière Condensée) at Nice University.

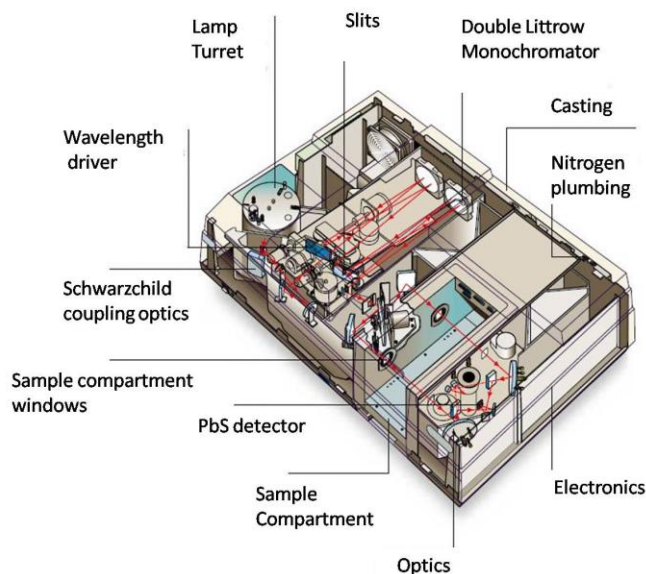


**Figure A2.6: Cary 500 UV-Vis N-IR**

This spectrophotometer measures the reflectance as a function of the wavelength (nm) in the range [190 nm; 3200 nm]. Actually, data are really reliable above 250 nm.

A calibration procedure, consisting in analyzing two reference samples (one absorbing all the light (black reference) the other reflecting it all (white reference)) is steadily followed, to correct any drift that could occur with time.

In order to collect at maximum the reflected light, an integration sphere equipped with a photodetector is placed around the sample (figure A2.7) so that multiple reflections lead to a fairly high optical intensity inside the sphere and consequently to a high optical efficiency.

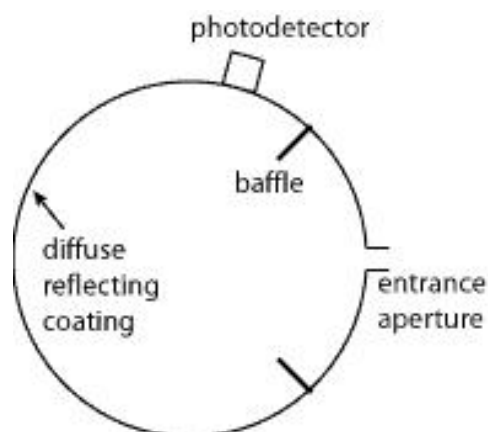


**Figure A2.7 Integrating sphere of a spectrophotometer**

Two baffles act as light barriers to prevent any direct illumination of the detector by the light source. Ideally, the coating on the inner side of the integrating sphere has a very high reflectivity over the required wavelength range.

## A2.2 UPS and XPS

Photoelectron Spectroscopy was developed in 1967 by Kai Siegbahn, to identify chemical elements on the surface of catalysts. Photons produced by an energy source are sent to the sample. After they collide with the matter, electrons are emitted. Photoelectron spectroscopy analyses the kinetic energy distribution of the emitted photoelectrons to study the composition and the components electronic state of the surface region of a sample.

Photons can be produced by:

- X-rays, using soft-rays with a photon energy of 200-2000 eV **to examine core-levels (XPS)**
- Ultra-violet, using vacuum UV radiation with a photon energy of 10-45 eV **to examine valence levels (UPS)**

In XPS the photon is absorbed by an atom in a molecule or a solid, leading to the ionization and the emission of a core (inner shell) electron. By contrast, in UPS the photon interacts with valence levels of the molecule or solid, leading to ionization by removal of one of these valence electrons. The kinetic energy distribution of the emitted photoelectrons (i.e. the number of emitted photoelectrons as a function of their kinetic energy) can be measured using any appropriate electron energy analyzer and a photoelectron spectrum can thus be recorded.

Photoelectron spectroscopy is similar to Auger spectroscopy. The difference is the exciter source : electrons for Auger, photons for photoelectron spectroscopy. Photoelectron spectroscopy uses monochromatic sources of irradiation (i.e. photons of fixed energy).

Physical principles of photoelectron spectroscopy are schematically represented in Figure A2.8:

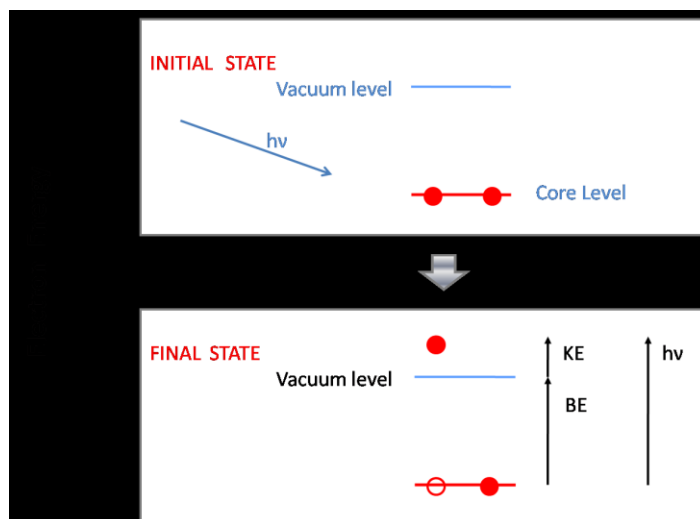


**Figure A2.8 Mechanism of photoemission**

Photons with energy  $h\nu$  are sent to the sample and excite electrons. Once excited, electrons pass from the core level to the vacuum level. The Binding Energy (BE) is taken to be a direct measure of the energy required to just remove the electron concerned from its initial level to the vacuum level and the Kinetic Energy (KE) of the photoelectron is given by:

$$KE = h\nu - BE \quad (A2.9)$$

where  $h\nu$  is the photons energy

The equipment for a photoemission experiment (XPS or UPS) is made up of:

- a source of fixed-energy radiation
- an electron energy analyser
- a high vacuum environment

Figure A2.9 illustrated the required system:

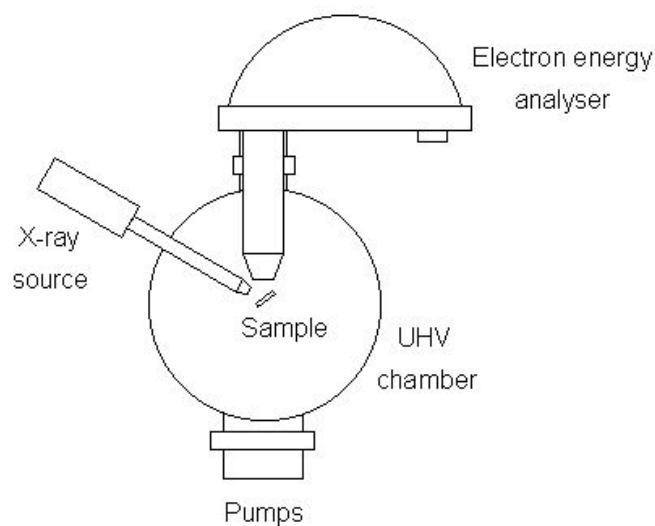


**Figure A2.9** Experimental system for photoemission analyses

The vacuum environment avoids any collision with the gas during the analysis of emitted photoelectrons.

The energy of the emitted electrons is a feature of the emitting atom. Each core atomic orbital give a characteristic photoelectron spectrum at kinetic energies determined by the photon energy and the respective binding energies. Second information we have from photoemission are on the quantum number of the emitting atoms.

Table A2.1 correlates notation in photoemission spectroscopy with atomic quantum numbers.

XPS/UPS notation	Quantum numbers		
	n	l=0 to n-1	j=1 +/- 1=2
1s	1	0	1/2
2s	2	0	1/2
2p <sub>1/2</sub>	2	1	1/2
2p <sub>3/2</sub>	2	1	3/2
3s	3	0	1/2
3p <sub>1/2</sub>	3	1	1/2
3p <sub>3/2</sub>	3	1	3/2
3d <sub>3/2</sub>	3	2	3/2
3p <sub>5/2</sub>	3	2	5/2

**Table A2.1 Notation in XPS/UPS and quantum numbers**



# Elaboration et étude de nanostructures de $\text{TiO}_2$ pour la production d'hydrogène par photolyse de l'eau

Daniela D'Elia

## 1. Introduction et état de l'art

Face à la demande énergétique croissante, la société se trouve aujourd'hui confrontée à deux défis majeurs :

- un défi environnemental, consistant à produire de l'énergie selon des procédés propres et « durables »;
- un défi économique, consistant à rendre ce nouveau type de production compétitif par rapport aux procédés classiques (exploitant notamment les ressources fossiles).

Une solution actuellement proposée est de produire de l'énergie à partir de sources renouvelables intermittentes, comme l'éolien ou le solaire. Une solution alternative est de stocker l'énergie via un vecteur énergétique, dont l'un des exemples particulièrement prometteurs est l'hydrogène. Actuellement, 95% de l'hydrogène sont produits par des ressources fossiles ; les 5% restants sont issus de procédés électrolytiques ou basés sur l'exploitation de la biomasse. Une voie séduisante est le procédé de production d'hydrogène par photolyse de l'eau à partir du rayonnement solaire.

Les principes théoriques à la base de ce procédé reposent sur la capacité d'oxydoréduction des semi-conducteurs. Un semi-conducteur est un matériau caractérisé par une bande interdite, qui est une différence d'énergie entre une bande permise et pleine, la bande de valence, et une bande vide la bande de conduction. Lorsque le semi-conducteur absorbe une radiation lumineuse dont l'énergie est supérieure ou égale à celle de sa bande interdite, il est capable de photo-générer un couple électron-trou: l'électron « saute » de la bande de valence à celle de conduction. Pour qu'un semi-conducteur puisse photo-catalyser la réaction de photolyse de l'eau il faut que la limite énergétique inférieure de sa bande de conduction soit supérieure ou égale à 0 eV, et que la limite énergétique supérieure de sa bande de valence soit inférieure ou égale à -1.23 eV (Figure 1).

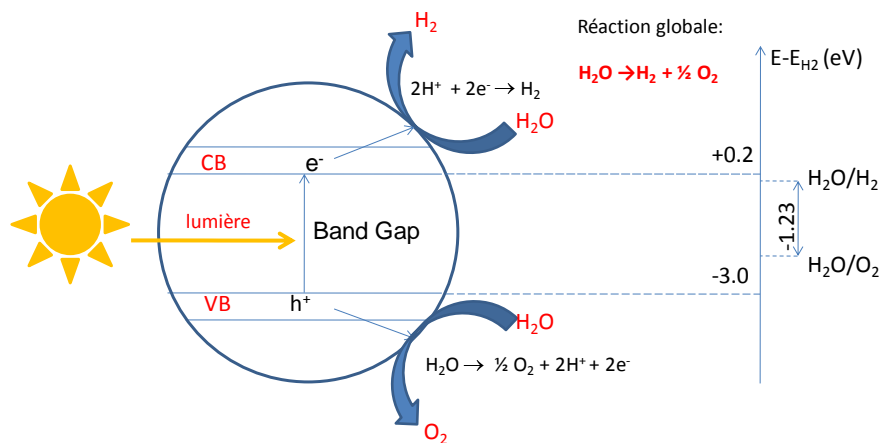


Figure 1 : Représentation schématique de la réaction de photolyse de l'eau à la surface d'une particule de dioxyde de titane ( $\text{TiO}_2$ )

Plusieurs candidats satisfont à cette condition (voir figure ci-dessous), comme par exemple l'oxyde de zinc. Les composés de cadmium sont aussi très efficaces, mais ce sont de forts polluants environnementaux. Les semi-conducteurs à base de gallium sont également très performants, mais ils sont malheureusement très instables. Le dioxyde de titane ( $\text{TiO}_2$ ) est l'un des meilleurs candidats en raison de la position de ses bandes, de sa forte stabilité chimique, et de son abondance qui en fait un matériau peu cher.

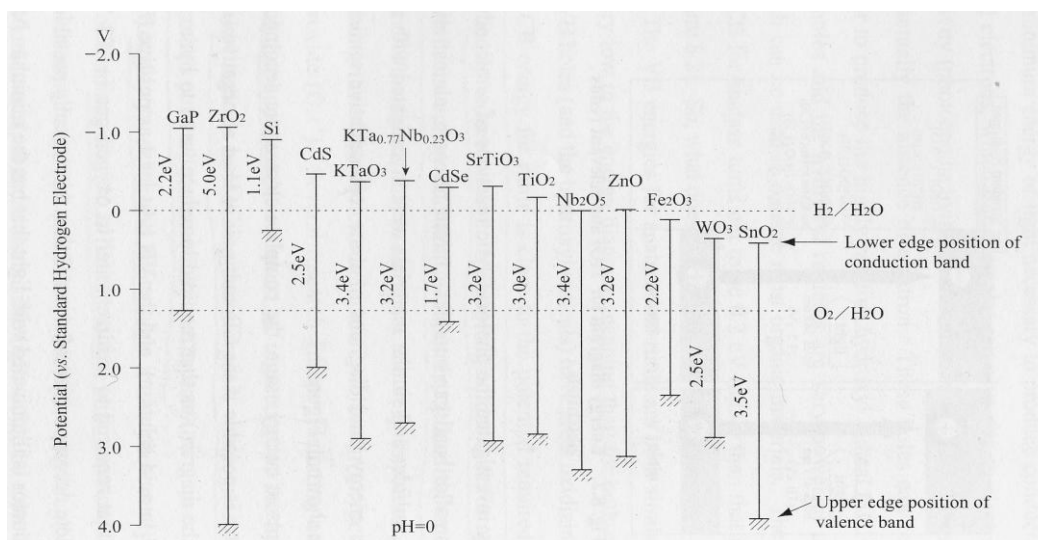


Figure 2 : Diagramme des potentiels de quelques semi-conducteurs

Le dioxyde de titane peut se présenter sous différentes formes, parmi lesquelles les plus utilisées en photo-catalyse sont le  $\text{TiO}_2$ -B, l'anatase, le rutile et la brookite. Le  $\text{TiO}_2$ -B est la forme monoclinique du  $\text{TiO}_2$ , la brookite sa forme orthorhombique, l'anatase et le rutile ses formes tétragonales (Tableau 1).

Form	a (Å)	b (Å)	c (Å)	$\beta$ (°)
$\text{TiO}_2$ -B	12,163	3,735	6,513	107,29
Anatase	3,777	3,777	9,501	90
Brookite	9,174	5,449	5,138	90
Rutile	4,594	4,594	2,9586	90

Tableau 1 : Paramètres des cellules élémentaires des formes allotropiques du  $\text{TiO}_2$  les plus communes

Par rapport à l'anatase, le rutile présente des lacunes d'oxygène. Pour la photolyse de l'eau, l'anatase est la forme la mieux adaptée car le bas de sa bande de conduction est à + 0.2 eV, alors que celui du rutile est à 0 eV.

L'objectif principal de cette thèse était d'améliorer l'efficacité de l'anatase, car avec un band gap de 3.2 eV son efficacité énergétique actuelle est de l'ordre de 1%. Selon une estimation du Département Énergétique des États-Unis, on considère que le procédé de photolyse de l'eau ne peut être compétitif économiquement qu'à partir d'une efficacité énergétique de 10% et une durée de fonctionnement de 1000 heures.

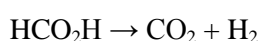
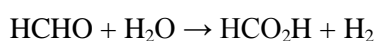
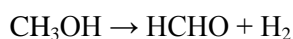
Les problèmes à la base de la faible performance de l'anatase sont multiples:

- absorption de la lumière sur une faible partie du spectre, (seulement les longueurs d'onde inférieures à 382 nm) ;
- rapide recombinaison du couple électron-trou ;
- vitesse de la réaction inverse, thermodynamiquement favorisée, qui à partir de l'hydrogène et de l'oxygène donne de l'eau.

Différentes solutions sont proposées dans la littérature pour palier ces problèmes majeurs :

1. ajout de donneurs d'électrons [Nada et al., 2005], comme l'éthanol ou le méthanol ;
2. ajout de sels de carbonates [Arakawa et al., 2000], comme le  $\text{Na}_2\text{CO}_3$  ;
3. enrobage avec des métaux nobles [Sakthivel et al., 2004], comme le Pt, le Pd, ou l'au ;
4. dopage cationique [Choi et al., 1994] ou anionique [Asahi et al., 2001] ;
5. sensibilisation avec des colorants [Dhanalakshmi et al., 2001] ;
6. jonction de semi-conducteurs [So and ans SJ Moon, 2004] ;
7. implantation ionique avec des métaux et des non-métaux [Anpo et al., 2001].

Les solutions (1), (3), (5), (6), (7) peuvent permettre d'éviter la recombinaison électron-trou, la (2) permet d'éviter la réaction inverse, la (4) peut permettre d'augmenter la gamme d'absorption de la lumière. On peut noter ici que le méthanol peut aussi être considéré comme une source de génération d'hydrogène :



Les solutions adoptées dans ce travail de thèse sont l'ajout de méthanol en solution, le dépôt de nanoparticules de Pt en surface des particules de  $\text{TiO}_2$  et le dopage, cationique et anionique de ces dernières. Avant de présenter les travaux réalisés, rappelons tout d'abord quelques aspects de l'impact théorique du dopage.

Dans le schéma suivant proposé par Serpone [Serpone, 2006](Figure 3), les modifications induites par le dopage sont représentées. La partie gauche représente une bande interdite non modifiée. Sur la partie centrale, on peut voir que si le dopage est cationique, on a la formation de niveaux discrets proches de la bande de conduction, tandis que s'il est anionique, les niveaux sont proches de la bande de valence. Une vraie réduction du bandgap est obtenue lorsqu'il y a superposition des bandes idoines. La position et l'effet du dopage dépendent donc de la nature et de la quantité du dopant.

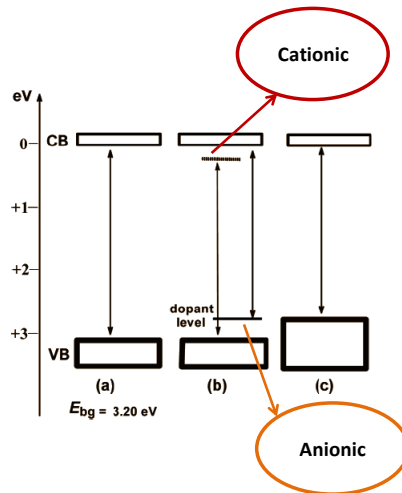


Figure 3 : Effet théorique des dopages cationique et anionique sur la bande interdite

Un des aspects les plus originaux de cette thèse était d'étudier l'impact des interfaces sur la photolyse de l'eau. L'idée sous-jacente repose sur les « bonnes » propriétés du Degussa P25. Ce matériau commercial est un mélange à 80 %<sub>massique</sub> d'anatase et 20 %<sub>massique</sub> de rutile. On rappelle que le bas de la bande de conduction de l'anatase est à + 0.2 eV et celui du rutile à 0 eV. Lorsque l'anatase est excité, l'électron « saute » de la bande de valence à celle de conduction de l'anatase. L'électron peut ultérieurement « sauter » sur le rutile (Figure 4). Ce cheminement de l'électron participe à l'amélioration de la séparation des charges photo-générées. Le Degussa P25 est aussi capable d'absorber plus de lumière car l'anatase absorbe dans la région de l'ultra-violet tandis que le rutile absorbe dans le visible violet.

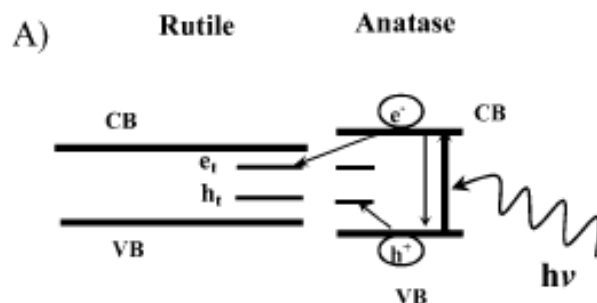
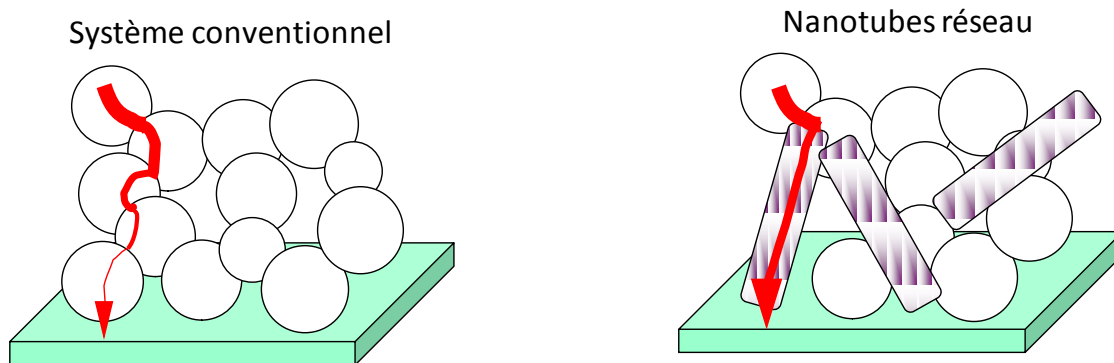


Figure 4 : Représentation schématique de la séparation des charges du Degussa P25 [Hurum et al., 2003]

L'autre aspect original de ce travail était l'étude de l'impact des morphologies sur la photolyse de l'eau. Le travail de Yoshikazu Suzuki [Suzuki et al., 2005] a en effet montré que pour les cellules solaires, un réseau d'objets ponctuels « 0D » provoque un transport pauvre d'électrons, alors qu'un réseau d'objets allongés « 1D » a un effet « autoroute » pour le transfert des charges (Figure 5). Nous voulions savoir si un effet morphologique analogue pouvait être identifié dans le cadre de la photolyse de l'eau. C'était un des objectifs de ce travail de thèse sur les morphologies de TiO<sub>2</sub> nanostructuré.



**Figure 5 : Représentation schématique du cheminement des électrons à travers un système colloïdal conventionnel ou au travers d'un réseau de nanotubes**

En résumé, les objectifs de cette thèse étaient les suivants. L'objectif principal était d'améliorer la performance du  $\text{TiO}_2$  pour la photodissociation de l'eau en améliorant ses propriétés optiques par la technique du dopage, et en évitant la recombinaison des charges via un travail sur les morphologies et les interfaces. Un autre objectif, plus théorique mais tout autant important pour identifier les voies de recherche futures, était de mieux comprendre les phénomènes mis en jeu dans la photogénération de l'hydrogène.

Pour atteindre ces objectifs, différentes techniques d'élaboration ont été utilisées :

- Précipitation en batch et sol-gel pour élaborer des objets ponctuels (*i.e.* des particules) et tridimensionnels (*i.e.* des aérogels) ;
- Transformation hydrothermale pour obtenir des nanotubes.

## 2. Elaboration des nanostructures non modifiées

• Dans un premier temps, nous avons synthétisé des particules en batch en précipitant  $\text{TiCl}_4$  et  $\text{NaOH}$  à  $25\text{ }^\circ\text{C}$ , à pH 2 pendant 1h. Quatre parties de ce précipité ont été cristallisées en autoclave, à deux températures et deux pH différents :  $150\text{ }^\circ\text{C}$ , pH 2 et  $250\text{ }^\circ\text{C}$ , pH 10. Une autre partie a été pré-traitée à  $80\text{ }^\circ\text{C}$  pendant 30 heures à pH 10. Ce produit a été ultérieurement divisé en deux parties : une a été cristallisée en autoclave à  $150\text{ }^\circ\text{C}$ , une autre à  $250\text{ }^\circ\text{C}$ , le pH a été maintenu à 10 (Figure 6).

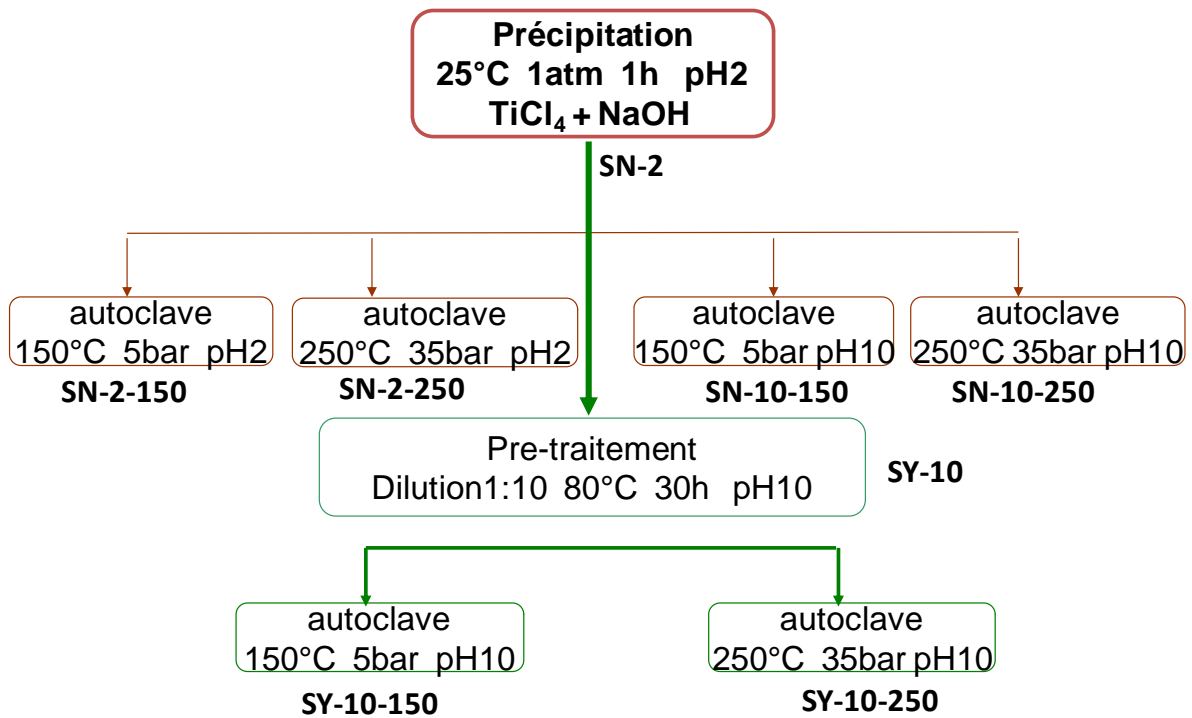


**Figure 6 : Schéma de la synthèse de nanoparticules de TiO<sub>2</sub>**

Dans chaque cas, de l'anatase a été obtenu, excepté pour l'échantillon non prétraité et cristallisé à pH 2 et à 150 °C pour lequel on a pu observer un mélange d'anatase et rutile. Ceci peut être expliqué par les conditions thermodynamiques et cinétiques qui étaient favorables à la croissance du rutile. La taille des cristallites, calculée à partir des diffractogrammes rayon X, et la taille des particules, analysée par microscopie à transmission électronique, se corrélient à la surface spécifique, estimée par physisorption d'azote : à une augmentation des tailles des cristallites et des particules correspond une diminution de la surface spécifique (Tableau 2).

Entry	XRD L(nm)	TEM l(nm)	S <sub>BET</sub> (m <sup>2</sup> .g <sup>-1</sup> )
SN-2	-	Germe anatase	-
SN-2-150	7	8	148
SN-2-250	11, 28*	8, 27*	88
SN-10-150	9	10	143
SN-10-250	42	85	17
SY-10	6	4	8
SY-10-150	14	7	164
SY-10-250	9	9	40

**Tableau 2 : Résultats des caractérisations structurales des nanoparticules de TiO<sub>2</sub>. (\* est le rutile)**

La microscopie à transmission électronique (Figure 7) nous indique aussi qu'on n'a pas obtenu d'agrégats ou d'amas et que les particules sont assez bien distinctes les unes des autres.

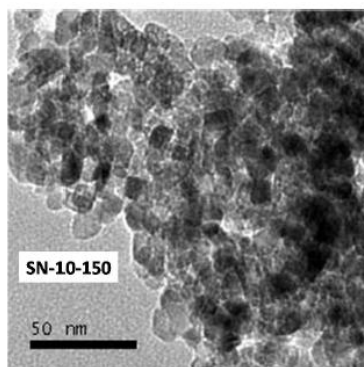


Figure 7 : Image MET (microscopie à transmission électronique) de l'échantillon SN-10-150

• Dans un second temps, nous avons élaboré des nanotubes de  $\text{TiO}_2$  par la méthode Kasuga [Kasuga et al., 1998a]. En conditions hydrothermales très basiques ( $\text{NaOH}$  10 M), à température modérée ( $150^\circ\text{C}$ ), des particules d'anatase commerciales donnent des feuillets de titanate de sodium ( $\text{Na}_2\text{Ti}_2\text{O}_5$ ) qui, après protonation avec du  $\text{HCl}$ , se déroulent en nanotubes titanate ( $\text{H}_2\text{Ti}_2\text{O}_5 \cdot \text{H}_2\text{O}$ ). Ce matériau a été enfin calciné à trois températures différentes :  $300^\circ\text{C}$ ,  $400^\circ\text{C}$  et  $500^\circ\text{C}$  (Figure 8).

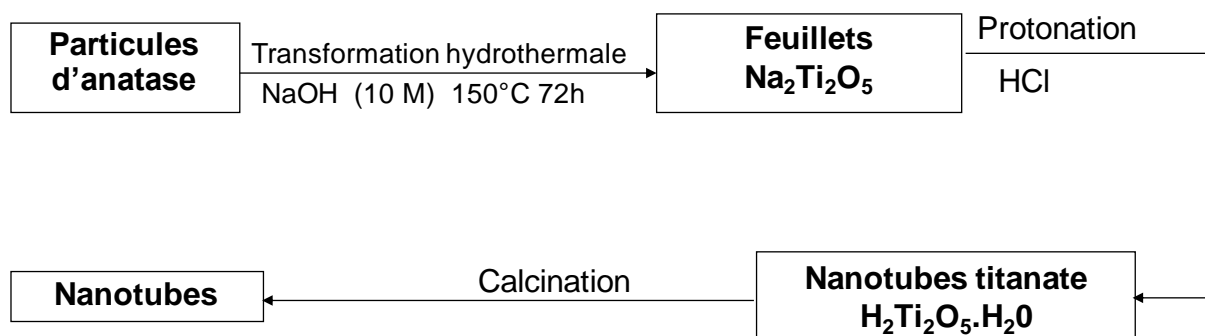


Figure 8 : Schéma du procédé de synthèse des nanotubes de  $\text{TiO}_2$

La caractérisation DRX montre que les nanotubes non dopés sont bien des titanates, dont la formule brute peut être écrite comme  $\text{H}_2\text{Ti}_2\text{O}_5 \cdot \text{H}_2\text{O}$ . Après calcination à  $300^\circ\text{C}$ ,  $400^\circ\text{C}$  et  $500^\circ\text{C}$ , on obtient respectivement du  $\text{TiO}_2$ -B, un mélange  $\text{TiO}_2$ -B/anatase, et de l'anatase uniquement (Figure 9).

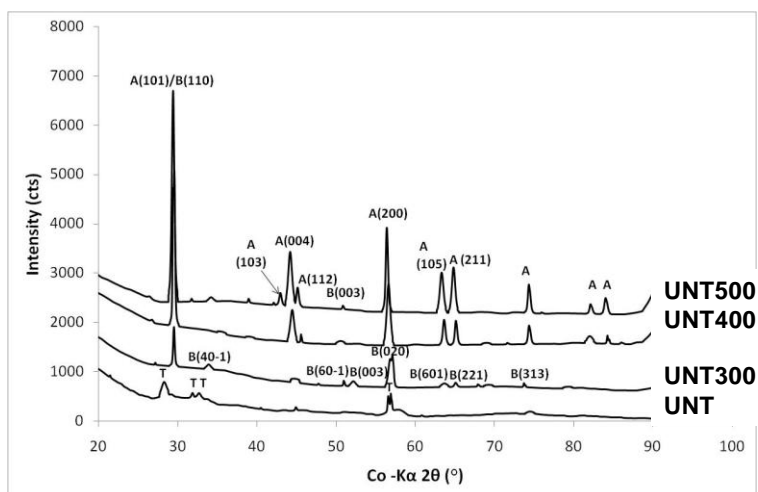


Figure 9 : DRX des nanotubes de TiO<sub>2</sub>

La DRX ne peut nous donner aucune information sur la morphologie de cette phase, qui a été analysée par MET. Les produits calcinés à 300 °C ont une forme tubulaire. Alors qu'à 400 °C le TiO<sub>2</sub>-B est toujours tubulaire, l'anatase, en revanche, se présente sous forme de particules. Ces analyses nous montrent que la phase TiO<sub>2</sub>-B est toujours associée à une morphologie 1D, l'anatase à des nanoparticules (0D) (Figure 10).

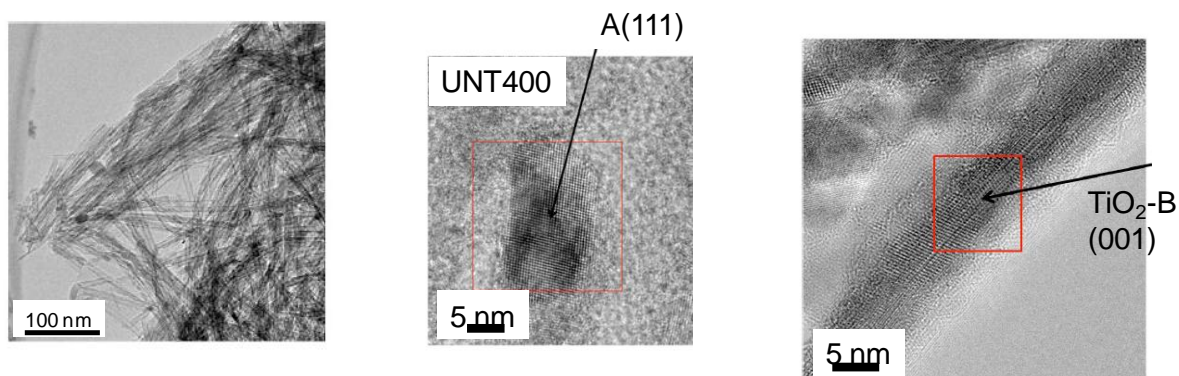
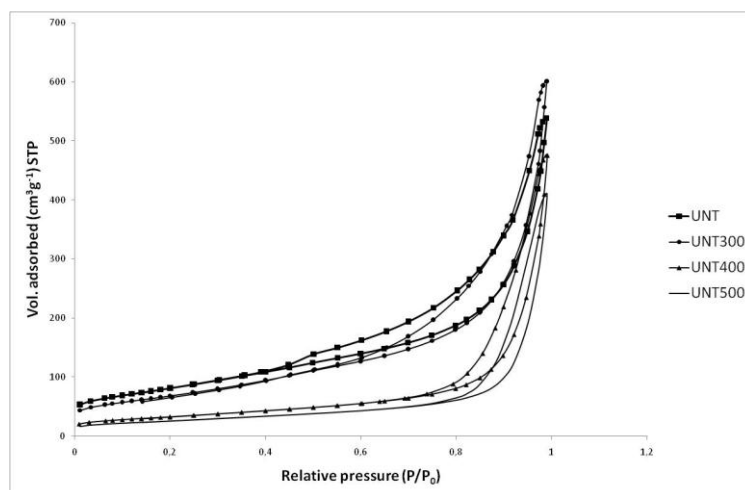


Figure 10 : MET des nanotubes de TiO<sub>2</sub>

Ce résultat est confirmé par les mesures de physisorption d'azote. Tout d'abord les isothermes nous indiquent qu'en augmentant la température, la surface spécifique se réduit sensiblement, en particulier quand l'anatase apparaît, aux environs de 400 °C (Figure 11).



**Figure 11 : Isothermes de physisorption d'azote**

Pour tous les échantillons, la distribution des pores indique une population de pores dont le diamètre est centré à 3 nm. Pour les nanotubes calcinés à 400 et 500 °C, une deuxième population apparaît, centrée à 22nm pour une calcination à 400 °C, et à 46nm pour une calcination à 500 °C (Figure 12).

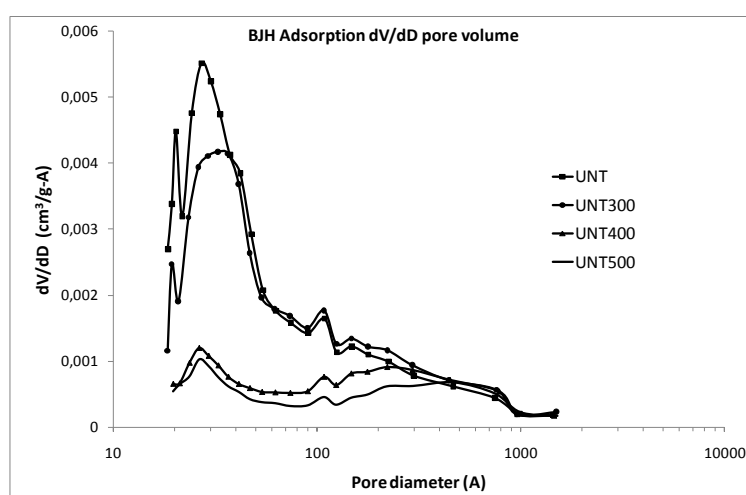


**Figure 12 : Distribution de la taille des pores des nanotubes**

La première population de pores, commune à tous les matériaux, est associée à une porosité interne, c'est-à-dire à la porosité des tubes, la deuxième est liée à une porosité externe, c'est-à-dire à la porosité interparticulaire [Beuvier]. Donc les mesures de physisorption d'azote confirment que les matériaux non calcinés ou calcinés à 300 °C sont des tubes, tandis que ceux calcinés à 400 et 500 °C sont un mélange de tubes et de particules. Les résultats des mesures de physisorption d'azote sont résumés dans le Tableau 3.

Entry	$S_{\text{BET}}$ ( $\text{m}^2\text{g}^{-1}$ )	$\delta_1$ (nm)	$\delta_2$ (nm)	$V_p$ ( $\text{cm}^3\text{g}^{-1}$ )
UNT	292	3	-	0.65
UNT300	246	3	-	0.71
UNT400	117	3	22	0.52
UNT500	90	3	46	0.42

Tableau 3 : Résultats des mesures de physisorption d'azote

• La troisième et dernière morphologie élaborée était les structures 3D, telles que l'aérogel et le xérogel. Nous avons suivi un protocole expérimental très similaire à celui adopté par Boujday et al. [Boujday2004], représenté sur la Figure 13. Deux solutions ont été mélangées sous agitation mécanique. La première contient le butoxyde de titane  $\text{Ti}(\text{OBU})_4$ , précurseur de l'oxyde métallique, et l'isopropanol (iPrOH). La deuxième contient également de l'isopropanol, de l'acide nitrique ( $\text{HNO}_3$ ), catalyseur de la réaction sol-gel, et de l'eau. Après transition sol-gel, le gel a été vieilli pendant 4 jours à température ambiante. Une partie a été séchée par simple évaporation à pression atmosphérique pour avoir des xérogels, une autre a été séchée en conditions supercritiques du  $\text{CO}_2$  pour avoir des aérogels. Ces derniers ont été calcinés à 400, 500, 600 et 700 °C pendant deux heures pour identifier la température de calcination nécessaire pour avoir de l'anatase bien cristallisée sans présence de rutile.

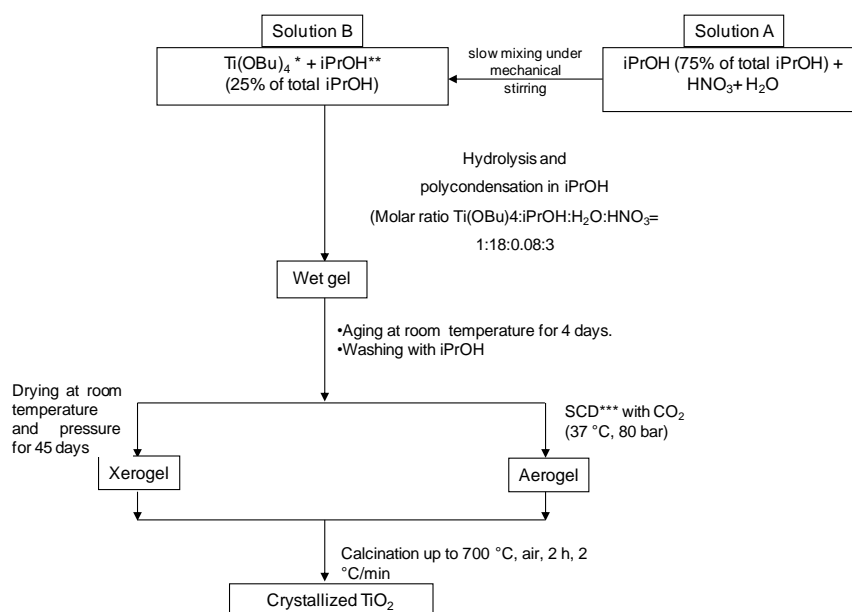


Figure 13 : Schéma du protocole d'élaboration des aérogels/xérogels

Les diffractogrammes à rayons X (Figure 14) nous montrent que nous avons obtenu de l'anatase pour les échantillons calcinés à 400, 500 et 600 °C. Concernant l'échantillon calciné à 600 °C, on peut aussi observer un pic de rutile. En utilisant la formule de Scherrer, nous avons pu calculer la composition de cet échantillon : 90% d'anatase et 10% de rutile. Donc, dans notre cas, la température

qui permet de synthétiser de l'anatase bien cristallisé sans avoir du rutile est de 500 °C. A 700°C, on obtient uniquement du rutile. Le xérogel a été aussi calciné à 500 °C. En comparant la DRX de l'aérogel et du xérogel calcinés (Figure 15), on remarque que ce dernier est moins cristallin que le premier. La taille des cristallites, calculée par la formule de Scherrer, nous montre qu'en augmentant la température de calcination la taille des cristallites augmente également.

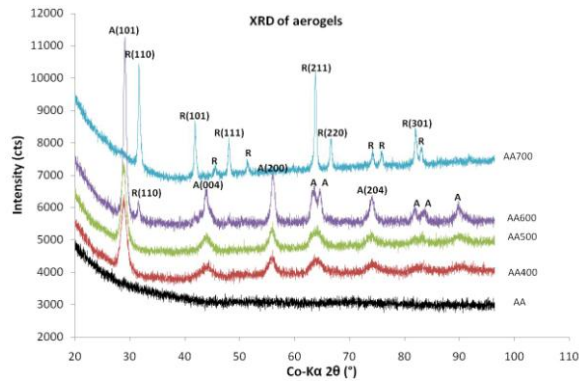


Figure 14 : DRX des aérogels

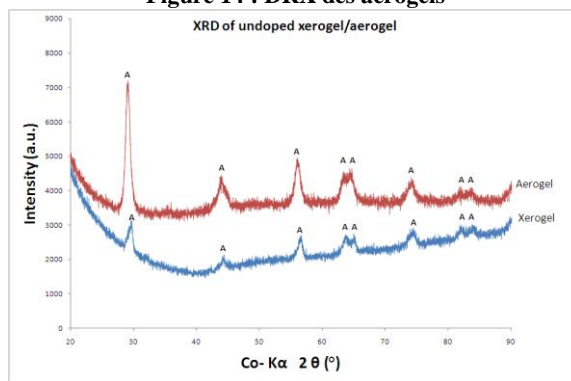


Figure 15 : DRX de l'aérogel et du xérogel calcinés à 500 °C

Les isothermes de physisorption d'azote nous montrent que l'aérogel amorphe a une surface spécifique élevée (568 m<sup>2</sup>.g<sup>-1</sup>), et que si l'on augmente la température de calcination, la surface spécifique diminue ainsi que le volume poreux (Tableau 4). Tous les échantillons présentent deux populations de pores, une dont le diamètre est centré autour de 3 nm, l'autre autour de 22 nm (Figure 16). Pour l'échantillon calciné à 700 °C, le diamètre de la deuxième population est décalé vers 46 nm (Figure 17).

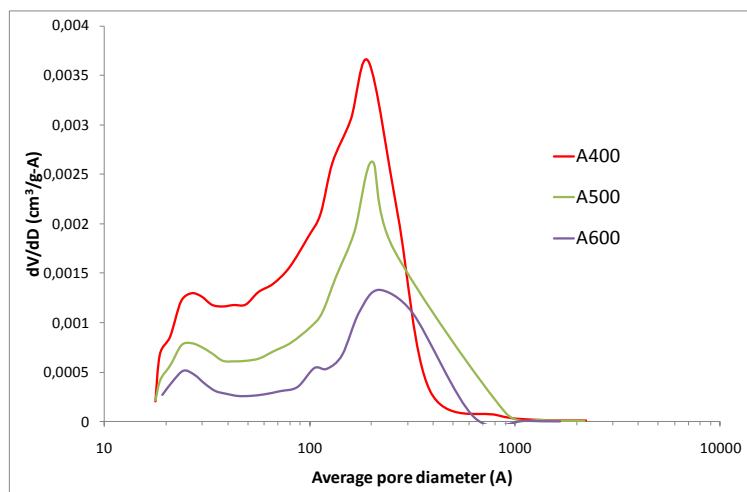


Figure 16 : Distribution de la taille des pores de AA, A400, A500 et A600

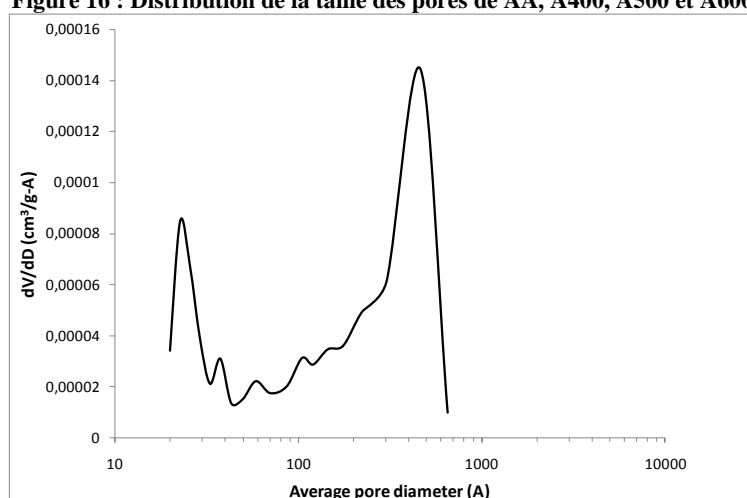


Figure 17 : Distribution de la taille des pores d'A700

Entry	$S_{BET}$ ( $m^2g^{-1}$ )	D (nm)	$\delta_1$ (nm)	$\delta_2$ (nm)	$V_p$ ( $cm^3g^{-1}$ )
AA	568	3	-	-	-
A400	158	10	3	20	0.63
A500	97	16	3	20	0.43
A600	59	26	3	22	0.27
A700	6	232	3	46	0.05

Tableau 4 : Résultats de caractérisation des aérogels par physisorption d'azote

Par microscopie à transmission électronique (Figure 18), on peut remarquer que l'aérogel amorphe est moins dense que le xérogel *parent*. Cette même différence peut être observée sur les produits calcinés : l'aérogel présente des particules plus petites et moins d'agrégats que le xérogel. La transformé de Fourier inverse nous confirme pour sa part que l'on a obtenu de l'anatase.

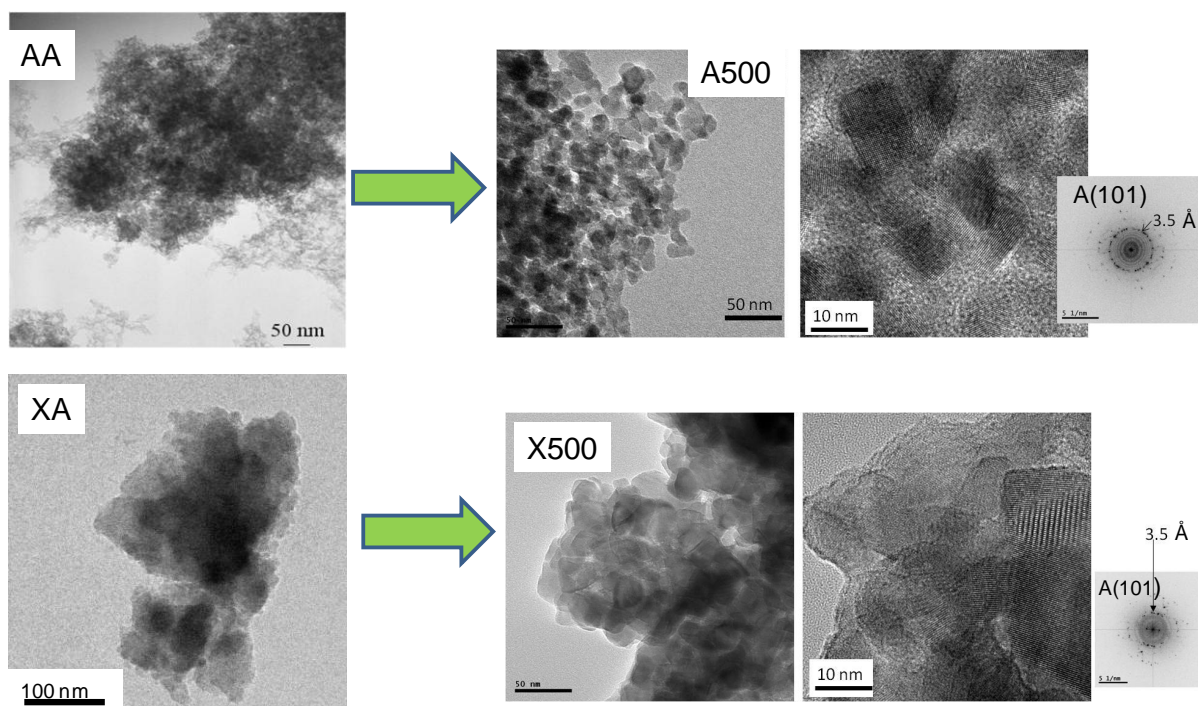


Figure 18 : MET de l'aérogel et xérogel amorphe (AA et XA) et des deux matériaux calcinés à 500 °C (A500 et X500)

### 3. Elaboration d'aérogels/xérogels dopés à l'azote

Une fois les nanostructures d'anatase pure élaborées, nous avons décidé de doper à l'azote les aérogels et les xérogels. Le procédé d'élaboration est très similaire à celui adopté pour l'élaboration des aérogels/xérogels non dopés. Comme source d'azote nous avons utilisé l'urée en trois concentrations différentes et les produits séchés amorphes ont été calcinés à 500 °C (Figure 19).

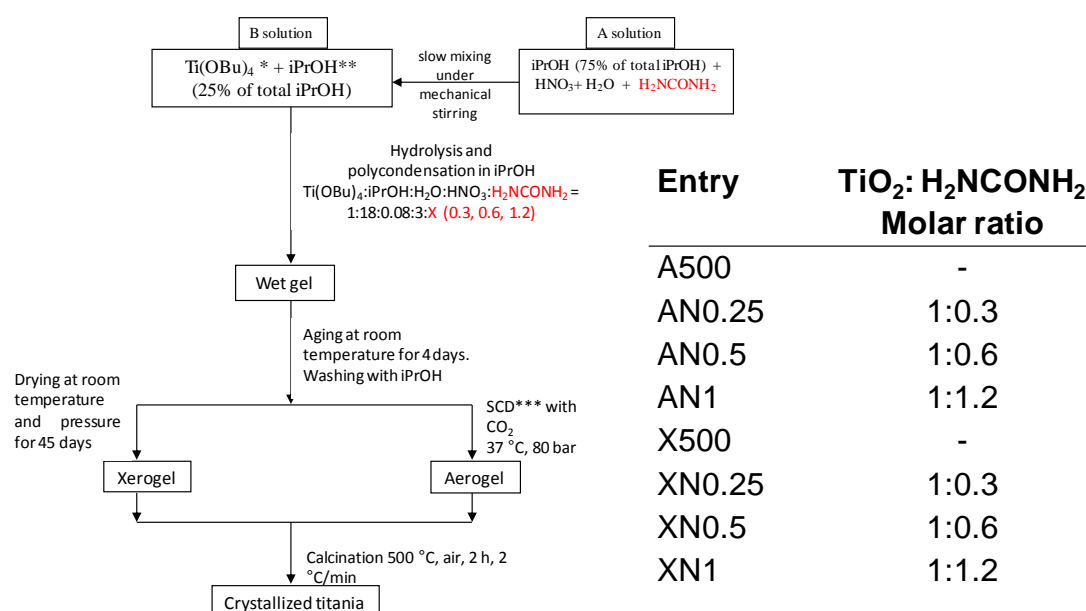


Figure 19 : Procédé de synthèse des aérogels : xérogels dopés à l'azote et rapports molaires TiO<sub>2</sub>/urée utilisés

En comparant les DRX des matériaux non dopés et dopés (Figure 20), on peut remarquer que les produits non dopés et leurs correspondants dopés ont une cristallinité très proche, et que les aérogels sont « mieux » cristallisés que les xérogels (Figure 21).

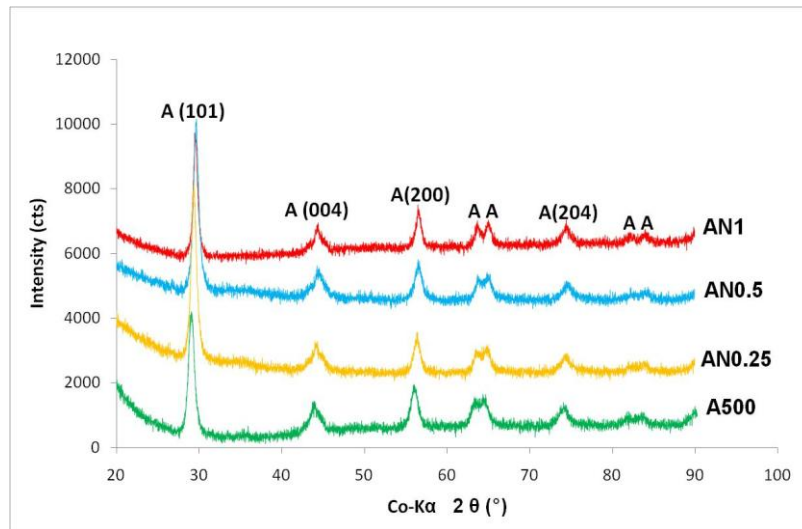


Figure 20 : DRX des aérogels dopés à l'azote

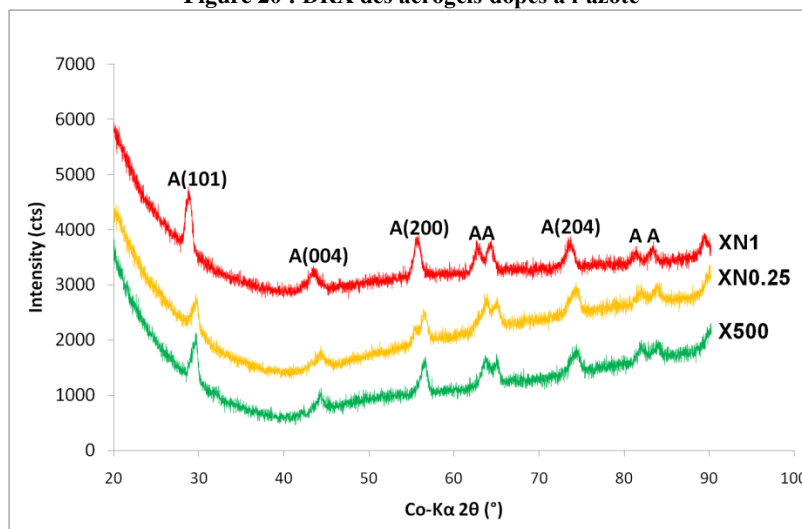


Figure 21 : DRX des xérogels dopés à l'azote

Les caractérisations effectuées sur les échantillons dopés (Figure 22) montrent que le dopage n'a pas induit de modifications structurales significatives. En effet, la taille des cristallites se situe entre 14 et 17 nm, celle des particules entre 10 et 13 nm, et la surface spécifique entre 60 et 101 m<sup>2</sup>.g<sup>-1</sup>. Par analyse élémentaire, l'azote a été détecté seulement dans l'aérogel et le xérogel dont le gel a été synthétisé avec le plus haut taux de dopant en solution.

Entry	XRD L(nm)	TEM l (nm)	S <sub>BET</sub> (m <sup>2</sup> g <sup>-1</sup> )	D (nm)	N (% wt.)
A500	17 <sup>A</sup>	12 <sup>A</sup>	97	16	< 0.10
AN0.25	14 <sup>A</sup>	12 <sup>A</sup>	60	25	< 0.10
AN0.5	17 <sup>A</sup>	10 <sup>A</sup>	107	14	< 0.10
AN1	14 <sup>A</sup>	13 <sup>A</sup>	78	19	0.17
X500	14 <sup>A</sup>	-	-	-	< 0.10
XN0.25	14 <sup>A</sup>	-	-	-	< 0.10
XN0.5	-	-	-	-	< 0.10
XN1	14 <sup>A</sup>	-	-	-	0.13

**Figure 22 : Résultats des caractérisations effectuées sur les matériaux dopés à l'azote**

Le dopage, par contre, modifie sensiblement les propriétés optiques des semi-conducteurs. Pour les analyser, nous avons entamé une collaboration avec le Dr. Yannick Fagot-Revurat de l'Université de Nancy afin de réaliser des mesures de spectrométrie photoélectronique à rayon X (XPS).

Tout d'abord, le spectre du Ti 2p (Figure 23) révèle deux pics, l'un à 459,4 eV et l'autre à 465,2 eV correspondant à Ti<sup>4+</sup>. Le spectre du O 1s (Figure 23) révèle un pic à 530,7 eV. On peut remarquer une superposition presque parfaite des spectres de Ti 2p et O 1s de l'échantillon non dopé (A500) avec ceux des échantillons chimiquement modifiés (AN0.5 et AN1). Sur le spectre Ti 2p, aucun épaulement à 455 eV, attribué dans la littérature à la présence de Ti<sup>3+</sup> [Batziil et al., 2006], n'a été observé. Par conséquent, la modification chimique de ces échantillons ne semble pas induire la présence de Ti<sup>3+</sup>.

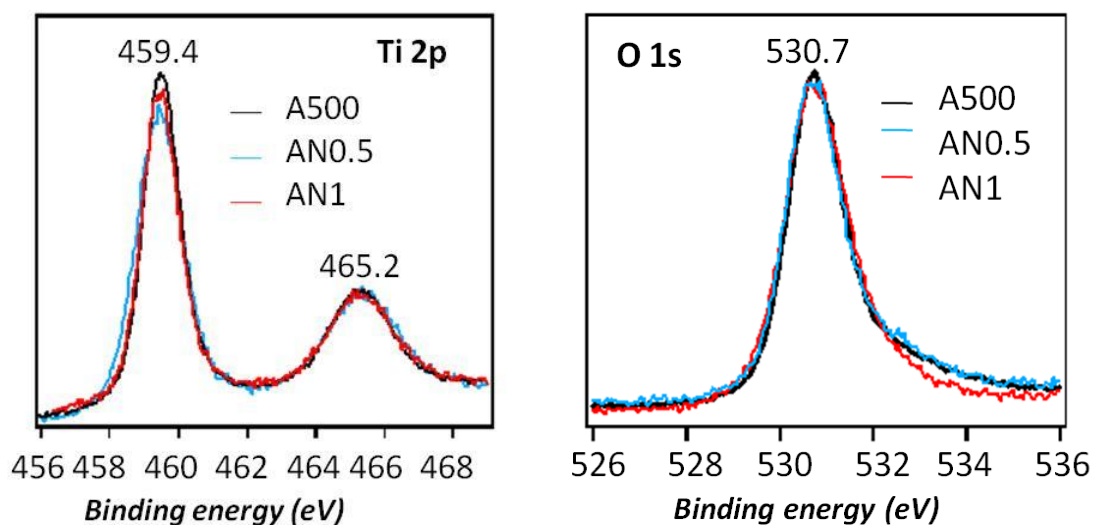


**Figure 23 : Spectres XPS de Ti 2p et O 1s des aérogels A500, AN0.5 et AN1 (Mg-K $\alpha$ ; hv = 1254,6 eV)**

Ces mesures nous ont ainsi permis d'identifier la nature du dopage pratiqué (Figure 24). La littérature attribue en effet le pic 1s N à environ 396 eV à un dopage substitutionnel, et le pic N 1s à 400 eV à un dopage interstitiel, assigné à la présence de composés azotés dans la matrice TiO<sub>2</sub>, responsables de la formation de niveaux discrets dans le gap.

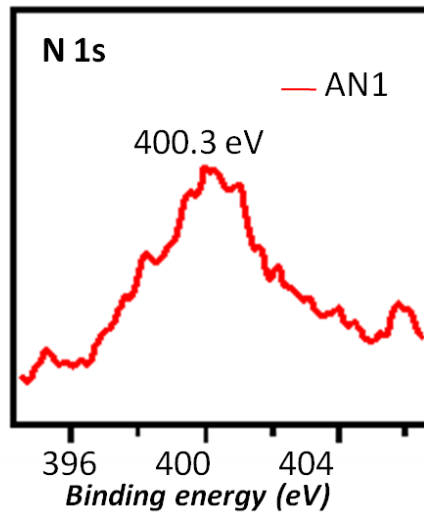


Figure 24 : Spectre XPS sur N 1s XPS de l'aérogel AN1(Mg-K $\alpha$  ;  $h\nu = 1254,6$  eV)

Cette étude nous a aussi fourni des informations précieuses sur les modifications induites par le dopage sur la bande de valence (Figure 25). Tout d'abord, ces mesures XPS nous montrent que le dopage n'a pas entraîné la formation de lacunes d'oxygène, car aucun pic à 1 eV n'a été révélé, confirmant qu'aucun  $Ti^{3+}$  n'a été formé. L'azote, par contre, induit la formation de niveaux discrets proches de la bande de valence, qui semblent décaler sa limite énergétique supérieure à 1 eV. Entre 1 et 3 eV. Takahashi et al. [Takahashi et al., 2008] attribuent ce changement à la présence de faibles états de la bande interdite, assignés à des états dérivés associés à N 2p. En conclusion, l'XPS nous permet de dire que notre dopage est de type interstitiel, que l'on a formé des niveaux discrets dans la bande de valence et qu'aucune lacune d'oxygène ne s'est créée.

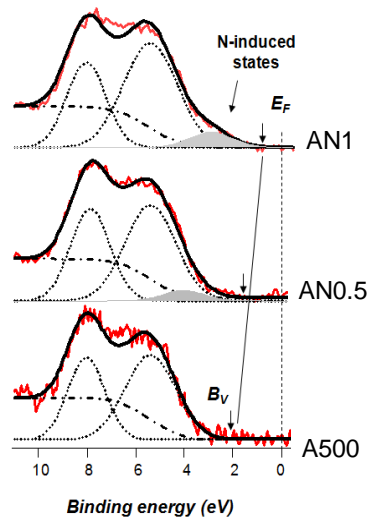


Figure 25 : Analyse de l'influence de l'azote sur la bande de valence des échantillons A500, AN0.5 et AN1 (Mg-K $\alpha$ ;  $h\nu=1254.6$  eV)

## 4. Evaluation de la photogénération d'hydrogène

Certains des produits élaborés, listés dans le Tableau 5 ont été testés pour évaluer leur activité dans la production d'hydrogène. Pour ces matériaux, le bandgap a été mesuré par la spectroscopie UV-vis autour de 3.25 eV, ce qui correspond à la valeur que l'on peut trouver dans la littérature.

Sample	Phase	S <sub>BET</sub> (m <sup>2</sup> .g <sup>-1</sup> )	TEM l (nm)	Bandgap (eV)
<b>Degussa P25</b>	A (80%), R(20%)	46	30	3.24
<b>Anatase α- Aesar 036199</b>	A	7.4	180	3.25
<b>Anatase ST-01</b>	A	320	5	3.25
<b>SN-10-150</b>	A	143	10	3.25
<b>UNT300</b>	B	246	40*9	3.35
<b>UNT400</b>	A (80%), B(20%)	117	115*9	3.28
<b>UNT500</b>	A, traces B	90	-	3.25
<b>A500</b>	A	83	12	3.25
<b>AN0.25</b>	A	60	12	3.38
<b>AN0.5</b>	A	107	10	3.35
<b>AN1</b>	A	78	13	3.25
<b>X0.25</b>	A	-	-	2.90
<b>X0.5</b>	A	-	-	3.10
<b>X1</b>	A	-	-	-

**Tableau 5 : Résumé des caractéristiques principales des photocatalyseurs testés dans ce travail pour la photolyse de l'eau. A est l'anatase, R est le rutile et B est le TiO<sub>2</sub>-B.**

Deux photo-réacteurs ont été utilisés : un réacteur batch doté d'une lampe à mercure dont le spectre d'absorption est centré dans la région des ultraviolets, et un réacteur semi-batch doté d'une lampe halogène dont le spectre d'absorption est centré dans la région du visible. Dans les deux cas, la lampe est positionnée selon l'axe du système de révolution cylindrique. Les expérimentations avec le photo-réacteur batch ont été réalisées par le Dr. J. Jitputti et le Prof. Y. Suzuki à l'Université de Kyoto, celles avec le photo-réacteur semi-batch par moi-même, sous la supervision des Dr. N. Keller et V. Keller-Spitzer à l'Université de Strasbourg (Figure 26).

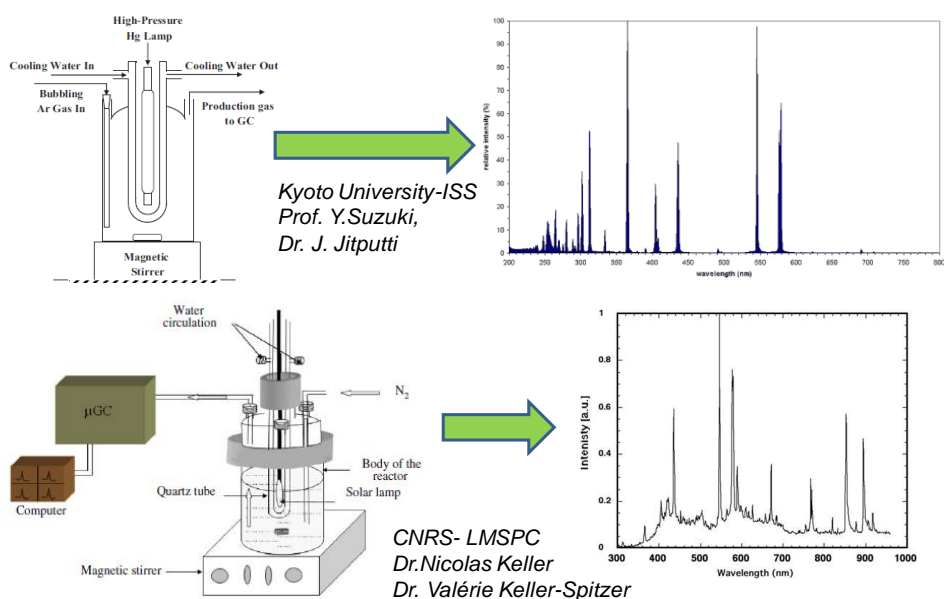


Figure 26 : Réacteurs et spectres des lampes utilisés pour les tests de photolyse

Le Degussa P25, l'anatase commercial  $\alpha$ -Aesar et les nanotubes calcinés (UNT300, UNT400, UNT500) ont été testés avec le système strasbourgeois en utilisant un litre de solution aqueuse à 10 volume% de méthanol contenant 0.7 g de catalyseur. La température du bain est maintenue constante à 25 °C.

Parmi les nanotubes, l'échantillon le plus actif est l'UNT400 qui a une performance plus élevée que l'anatase AlfaAesar 036199, mais plus faible que le Degussa P25.

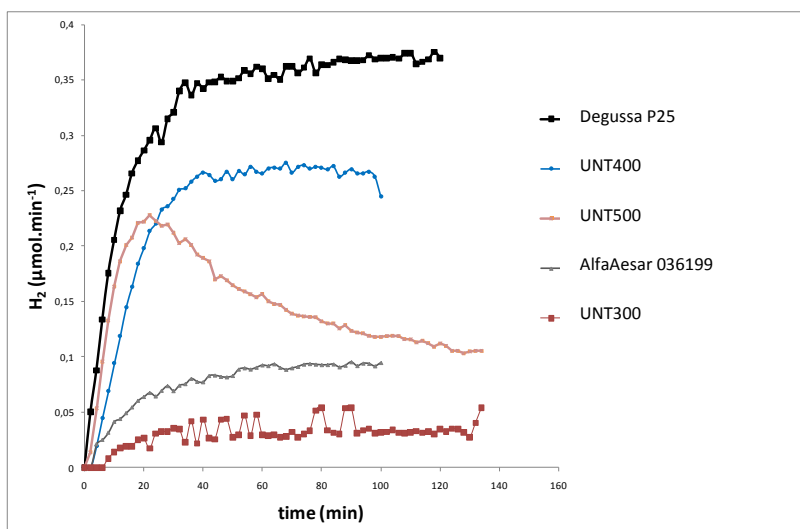
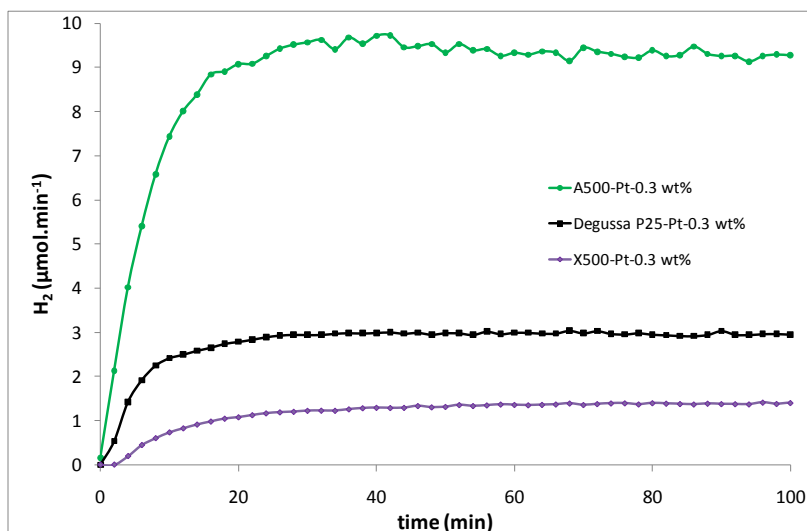


Figure 27 : Photoactivité des nanotubes (UNT300, UNT400 et UNT500), de l'anatase commercial AlphaAesar 036199 et du Degussa P25 testés à l'Université de Strasbourg

Les caractérisations DRX et MET ont montré que ce matériaux est un mélange d'anatase et de  $\text{TiO}_2\text{-B}$ . L'interface de ces deux phases pourrait permettre la séparation des charges, et donc expliquer l'activité plus élevée que l'anatase commercial et les nanotubes calcinés à 300 °C qui sont du  $\text{TiO}_2\text{-B}$  pure. L'anatase et le  $\text{TiO}_2\text{-B}$  sont actifs sous irradiation UV, alors que le rutile est actif sous irradiation

visible. Cette différence pourrait être à la base de la plus grande activité du Degussa P25 dans ces conditions de test. L'échantillon UNT500 a une activité similaire à celle de l'UNT400 pour les vingt premières minutes, mais elle chute ensuite. Des analyses MET effectuées sur l'échantillon après le test ont mis en évidence une décomposition importante des nanotubes en nanoparticules. Nous faisons l'hypothèse que cette transformation est à la base du changement de photoactivité du matériau.

L'aérogel calciné à 500 °C, le xérogel, et le Degussa P25 ont aussi été testés à Strasbourg, après avoir été « enrobés » avec du platine par imprégnation. L'aérogel est 10 fois plus actif que le xérogel et 3 fois plus que le Degussa P25.



**Figure 28 : Photoactivité de l'aérogel et du xérogel non dopés (A500 et X500) et du Degussa P25 « enrobés » avec du platine testés à l'Université de Strasbourg**

Cette première série d'expériences nous a ainsi permis d'identifier deux matériaux clés pour la photo-production d'hydrogène: l'aérogel calciné à 500 °C et les nanotubes calcinés à 400 °C.

Ces deux semi-conducteurs ont aussi été testés dans le réacteur batch de l'Université de Kyoto, sous lampe à mercure, dont on rappelle que le spectre est centré dans la région de l'ultraviolet. Dans ces conditions, l'UNT400 produit trois fois plus d'hydrogène que le Degussa P25, car l'anatase et le TiO<sub>2</sub>-B sont plus actifs sous ultraviolet que sous lumière visible. L'A500 produit deux fois plus d'hydrogène que le Degussa P25.

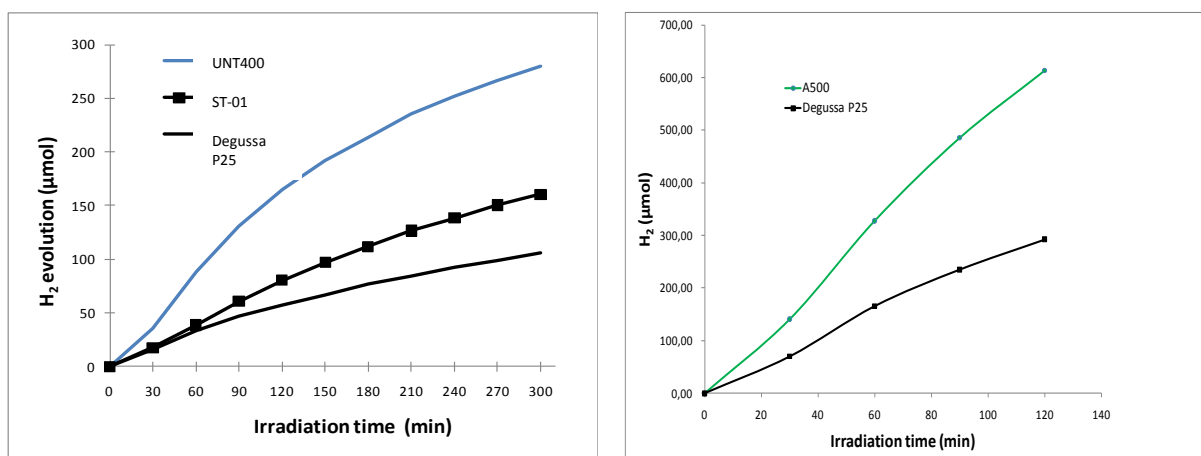


**Figure 29 : Photoactivité des nanotubes calcinés à 400 °C (UNT400) et de l'anatase commercial ST-01 (à gauche) et de l'aérogel non dopé (A500) (à droite), caractérisée dans le réacteur de Kyoto (sous lampe à mercure) . Comparaison avec le Degussa P25**

Cette « forte » activité de l'échantillon A500 doit être recherchée dans sa structure morphologique, plutôt que dans sa structure cristalline ou de sa bande interdite. Pour expliquer ce comportement, il faut remarquer que l'aérogel A500 n'est pas un lit de particules comme le P25, mais un réseau continu nanostructuré, composé d'agrégats et de « grappes » de particules liés entre eux par des liaisons covalentes. Nous faisons l'hypothèse que cette structure interne particulière pourrait améliorer la séparation des charges (électrons /trous). Par ailleurs, conséquence directe du procédé sol-gel, des groupes hydroxyles provenant des titanols Ti-OH auraient pu rester après calcination sur la surface des particules constituant le réseau d'anatase. Ces groupes pourraient accroître l'hydrophilie du TiO<sub>2</sub>, et donc l'adsorption d'eau sur la surface du matériau.

Après avoir testé la photoactivité des matériaux non dopés, nous avons aussi évalué la performance des matériaux dopés à l'azote. Il s'avère que ces échantillons dopés à l'azote ont une activité très similaire à celle du Degussa P25, donc plus faible que l'aérogel non dopé. Ce comportement photocatalytique pourrait être lié à la présence de niveaux discrets dans la bande de valence, analysée par XPS. Ces défauts pourraient être des centres de recombinaison des charges, et donc responsables de la diminution d'activité des matériaux non dopés par rapport à l'aérogel non dopé. A ce stade, il s'agit encore d'hypothèses à vérifier.

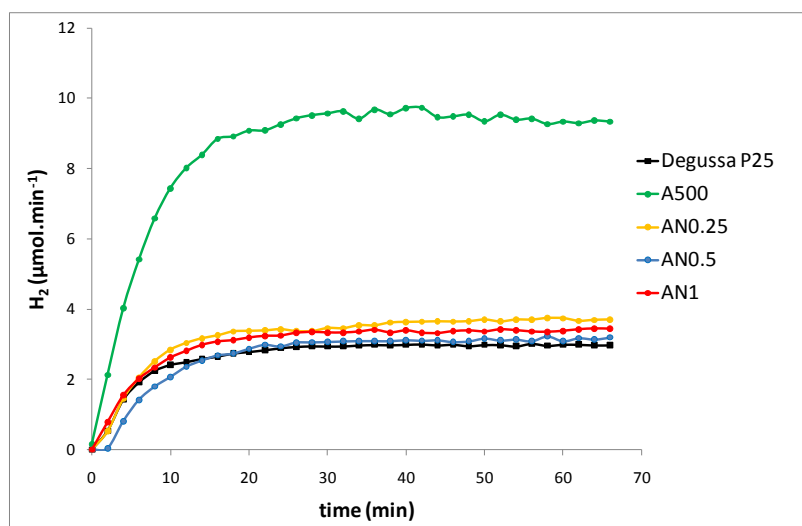


Figure 30 : Photoactivité des aérogels dopés (A500, AN0.25, AN0.5 et AN1) et du Degussa P25 où on a déposé du Pt

## 5. Conclusions et perspectives

Les conclusions principales de ce travail de thèse peuvent être résumées ainsi. En ce qui concerne les nanostructures non dopées nous avons obtenu de l'anatase pour les particules précipitées et les aérogels. Les nanotubes, en revanche, sont des mélanges d'anatase et de TiO<sub>2</sub>-B. Le résultat le plus intéressant de l'étude sur les aérogels dopés à l'azote concerne l'état de sa bande de valence dans laquelle les mesures de spectroscopie en photoémission ont révélé des niveaux discrets. Les tests d'hydrogène nous ont montré que les deux échantillons les plus performants sont les nanotubes calcinés à 400 °C et l'aérogel non dopé calciné à 500 °C. Les mesures d'évaluation de production d'hydrogène nous ont aussi démontré que la photoactivité des catalyseurs dépend des conditions de tests, plus particulièrement du type de lampe et de sa puissance.

A partir de ces conclusions on peut souligner des perspectives pour la suite de ce travail de recherche initié au CEP avec cette thèse. Tout d'abord, l'amélioration des paramètres de synthèse de nanotubes pourrait permettre d'avoir des nanostructures d'anatase pure. Ensuite, en augmentant la durée de calcination des xérogels, on peut envisager une amélioration de la cristallinité des xérogels et peut-être de leur performance vis-à-vis de la photoproduction d'hydrogène. Introduire plus de dopant (azote) dans les aérogels accroîtrait l'activité, déjà très prometteuse, des aérogels. Pour atteindre cet objectif on pourrait utiliser des techniques différentes de celle utilisées dans cette thèse, comme par exemple celle du plasma froid.

## References

- [**Ackerman et al., 2001**] Ackerman, W. C., Vlachos, M., Rouanet, S., and Freundt, J. (2001). Use of surface treated aerogels derived from various silica precursors in translucent insulation panels. *Journal of Non-Crystalline Solids*, 285:264–271.
- [**Addamo et al., 2005**] Addamo, M., Vincenzo Augugliaro, di Paola, A., Garcia-Lopez, E., Loddo, V., Marci, G., and Palmisano, L. (2005). Preparation and photoactivity of nanostructured TiO<sub>2</sub> particles obtained by hydrolysis of TiCl<sub>4</sub>. *Colloids and Surfaces A*, 265:23–31.
- [**Al-Mazroai et al., 2007**] Al-Mazroai, L. S., Bowker, M., Davies, P., Dickinson, A., Greaves, J., James, D., and Millard, L. (2007). The photocatalytic reforming of methanol. *Catalysis Today*, 122:46–50.
- [**Alviso and Pekala, 1991**] Alviso, C. and Pekala, R. (1991). Melamine formaldehyde aerogels. *Polymers Preparation*, 32:242–243.
- [**Andersson and Wadsley, 1966**] Andersson, S. and Wadsley, A. D. (1966). Crystallographic shear and diffusion paths in certain higher oxides of niobium, tungsten, molybdenum and titanium. *Nature*, 211:581–583.
- [**Anpo et al., 2001**] Anpo, M., Kishiguchi, S., Ichihashi, Y., Takeuchi, M., Yamashita, H., (2001). The design and development of second-generation titanium dioxide photocatalysts able to operate under visible light irradiation by applying a metal ion-implantation method. *Research on Chemical Intermediates*, 27:459–467.
- [**Ananpattarachai et al., 2009**] Ananpattarachai J., K Puangrat and S. Supapan (2009) Visible light absorption ability and photocatalytic oxidation activity of various interstitial N-doped TiO<sub>2</sub> prepared from different nitrogen dopants. *Journal of Hazardous Materials* 168, 253–261
- [**Arakawa and Sayama, 2000**] Arakawa, H. and Sayama, K. (2000). Solar hydrogen production: significant effect of Na<sub>2</sub>CO<sub>3</sub> addition on water splitting using simple oxide semiconductor photocatalysts. *Catalysis Surveys Japan*, 4:75–80.
- [**Asahi et al., 2001**] Asahi, R., Morikawa, T., Ohwaki, T., Y. K. A., and Y. T. (2001). Visible-light photocatalysis in nitrogen-doped titanium oxides. *Science*, 293:269–271.
- [**Ashokkumar, 1998**] Ashokkumar, M. (1998). An overview on semiconductor particulate systems for photoproduction of hydrogen. *International Journal of Hydrogen Energy*, 23:427–438.

- [Augugliaro et al., 1999]** Augugliaro, V., Coluccia, S., Loddo, V., Marcheseb, L., Martra, G., Palmisano, L., and Schiavelloa, M. (1999). Photocatalytic oxidation of gaseous toluene on anatase TiO<sub>2</sub> catalyst: mechanistic aspects and FT-IR investigation. *Applied Catalysis B: Environmental*, 20:15–27.144
- [Baia et al., 2006]** Baia, L., Peter, A., Cosoveanu, V., Indrea, E., Baia, M., Popp, J., and Danciu, V. (2006). Synthesis and nanostructural characterization of TiO<sub>2</sub> aerogels for photovoltaic devices. *Thin Solid Films* 511/512, 511-512:512–516.
- [Bamwenda et al., 1995]** Bamwenda, G., Tsubota, S., and Haruta, T. N.M. (1995). Photoassisted hydrogen production from a water ethanol solution: a comparison of activities of Au-TiO<sub>2</sub> and Pt-TiO<sub>2</sub>. *Journal of Photochemistry and Photobiology A: Chemistry*, 89:177–189.
- [Bhattacharyya et al., 2009]** K. Bhattacharyya, S. Varma, A. K. Tripathi, S. R. Bharadwaj, and A. K. Tyagi. Mechanistic Insight by *in Situ* FTIR for the Gas Phase Photo-oxidation of Ethylene by V-Doped Titania and Nano Titania. *J. Phys. Chem. B* 2009, 113, 5917–5928
- [Batzill et al., 2006]** Batzill, M., Morales, E. H., and Diebold, U. (2006). Influence of nitrogen doping on the defect formation and surface properties of TiO<sub>2</sub> rutile and anatase. *Physical Review Letters*, 96:026103.
- [Bavykin et al., 2006]** Bavykin, D. V., Friedrich, J. M., and Walsh, F. C. (2006). Protonated titanates and TiO<sub>2</sub> nanostructured materials: Synthesis, properties, and applications. *Advanced Materials*, 18:1–19.
- [Bavykin et al., 2004]** Bavykin, D. V., Parmon, V. N., Lapkina, A. A., and Walsh, F. C. (2004). The effect of hydrothermal conditions on the mesoporous structure of TiO<sub>2</sub> nanotubes. *Journal of Materials Chemistry*, 14:3370–3377.
- [Benfer and Knzinger, 1999]** Benfer, S. and Knzinger, E. (1999). Structure, morphology and surface properties of nanostructured ZrO<sub>2</sub> particles. *Journal of Materials Chemistry*, 9:1203–1209.
- [Beranek and Kisch, 2007]** Beranek, R. and Kisch, H. (2007). Surface-modified anodic TiO<sub>2</sub> films for visible light photocurrent response. *Electrochemistry Communications*, 9:761–766.
- [Bettinelli et al., 2007]** Bettinelli, M., Dallacasa, V., Falcomer, D., Fornasiero, P., Gombacc, V., Montini, T., Romano, L., and Speghini, A. (2007). Photocatalytic activity of TiO<sub>2</sub> doped with boron and vanadium. *Journal of Hazardous Materials*, 146:529–534.
- [Beuvier, 2009]** Beuvier, T. (2009). Des nanotitanates de sodium aux dioxydes de titane: électrode négative base de TiO<sub>2</sub>(B) nanométrique pour accumulateur lithium-ion. PhD thesis, Université de Nantes.

**[Bisson et al., 2003]** Bisson, A., Rigacci, A., Lecomte, D., Rodier, E., and Achard, P. (2003). Drying of silica gels to obtain aerogels: Phenomenology and basic techniques. *Drying Technology*, 21:593–628.

**[Bosch and F.Janssen, 1988]** Bosch, H. and F.Janssen (1988). Catalytic reduction of nitrogen oxides: a review on the fundamentals and technology. *Catalysis Today*, 2:369.

**[Boujday et al., 2004]** Boujday, S., Wunsch, F., Portes, P., Bocquet, J.-F., and Colbeau-Justin, C. (2004). Photocatalytic and electronic properties of TiO<sub>2</sub> powders elaborated by solgel route and supercritical drying. *Solar Energy Materials & Solar Cells*, 83:421–433.

**[Bradley et al., 1978]** Bradley, D., Mehrotra, R., and Gaur, D. (1978). *Metal Alkoxides*. Academic Press. 145

**[Brinker and Scherer, 1990]** Brinker, C. J. and W. Scherer, G. (1990). *SOL GEL SCIENCE. The Physics and Chemistry of Sol-Gel Processing*. Academic Press.

**[Bruce, 2005]** Bruce, P. G. (2005). Energy materials. *Solid State Sciences*, 7:1456–1463.

**[Buisson et al., 2001]** Buisson, P., Hernandez, C., M, M. P., and Pierre, A. (2001). Encapsulation of lipases in aerogels. *Journal of Non-Crystalline Solids*, 285:295–302.

**[Bulushev et al., 2000]** Bulushev, D. A., Kiwi-Minsker, L., Zaikovskii, V. I., and Renken, A. (2000). Formation of active sites for selective toluene oxidation during catalyst synthesis via solid-state reaction of V<sub>2</sub>O<sub>5</sub> with TiO<sub>2</sub>. *Journal of Catalysis*, 193:145–153.

**[Burda et al., 2003]** Clemens Burda, Yongbing Lou, Xiaobo Chen, Anna C. S. Samia, John Stout, and James L. Gole. Enhanced Nitrogen Doping in TiO<sub>2</sub> Nanoparticles. *Nano letters*, 3, 81, 1049-1051.

**[Burnside et al., 1998]** Burnside, S., Shklover, V., Barbe, C., Comte, P., Arendse, F., Brooks, K., and Grtzel, M. (1998). Self-organization of TiO<sub>2</sub> nanoparticles in thin films. *Chemical Materials*, 10:2419–2425.

**[Cassaignon et al., 2007]** Cassaignon, S., Joelsch, M., and Jolivet, J.-P. (2007). Selective synthesis of brookite, anatase and rutile nanoparticles: thermolysis of TiCl<sub>4</sub> in aqueous nitric acid. *Journal of Materials Science*, 42:6689–6695.

**[Chaput et al., 1995]** Chaput, F., Dunn, B., Fuqua, P., and Salloux, K. (1995). Synthesis and characterization of vanadium oxide aerogels. *Journal of Non-Crystalline Solids*, 188:11–18.

**[Cheng et al., 2004]** P. Cheng, J. Qiu, M. Gu, Y. Jin, W. Shangguan (2004). Synthesis of shape-controlled titania particles from a precursor solution containing urea. *Materials Letters* 58, 3751–3755

**[Chen et al., 2005]** X. Chen, Y. Lou, A. C. S. Samia, C. Burda, and J. L. Gole (2005). Formation of oxynitride as the photocatalytic enhancing site in nitrogen-doped titania nanocatalysts: comparison to a commercial nanopowder. *Advanced functional materials* 15,1

**[Chen et al., 2007]** Chen, H., Nambu, A., Wen, W., Graciani, J., Zhong, Z., Hanson, J. C., Fujita, E., and Rodriguez, J. A. (2007). Reaction of  $\text{NH}_3$  with titania: N-doping of the oxide and Ti-N formation. *Journal of Physical Chemistry C*, 111:1366–1372.

**[Cheng et al., 1995]** Cheng, H., Ma, J., Zhao, Z., and Qi, L. (1995). Hydrothermal preparation of uniform nanosize rutile and anatase particles. *Chemistry of Materials*, 7:663–671.

**[Cho et al., 2005]** Cho, C. H., Han, M. H., Kim, D. H., and Kim, D. K. (2005). Morphology evolution of anatase  $\text{TiO}_2$  nanocrystals under a hydrothermal condition (pH = 9.5) and their ultra-high photo-catalytic activity. *Materials Chemistry and Physics*, 92:104–111.

**[Cho and Kim, 2003]** Cho, C. H. and Kim, D. K. (2003). Photocatalytic activity of monodispersed spherical  $\text{TiO}_2$  particles with different crystallization routes. *Journal of the American Ceramic Society*, 86:1138–1145.

**[Choi et al., 1994]** Choi W., Termin A. and R., Hoffmann M. (1994). The role of metal ion dopants in quantum-sized  $\text{TiO}_2$ : correlation between the photoreactivity and charge carrier recombination dynamics. *Journal of Physical chemistry*, 98:13669–13679.

**[Ciambelli et al., 1995]** Ciambelli, P., Lisi, L., Russo, G., and Volta, J. C. (1995). Physico-chemical study of selective catalytic reduction vanadia-titania catalysts prepared by the equilibrium adsorption method. *Applied Catalysis B: Environmental*, 7:1–18.

**[Cong et al., 2007]** Cong, Y., Zhang, J., Chen, F., and Anpo, M. (2007). Synthesis and characterization of nitrogen-doped  $\text{TiO}_2$  nanophotocatalyst with high visible light activity. *Journal of Physical Chemistry C*, 111:6976–6982. 146

**[Cromer and Herrington, 1955]** Cromer, D. and Herrington, K. (1955). The structures of anatase and rutile. *Journal of the American Chemical Society*, 77:4708–4709.

**[Dagan and Tomkiewicz, 1993]** Dagan G. and Tomkiewicz M. (1993).  $\text{TiO}_2$  aerogels for photocatalytic decontamination of aquatic environments. *Journal of physical chemistry*. Vol. 97, 49, 12651-12655.

**[Dhanalakshmi et al., 2001]** Dhanalakshmi, K., Latha, S., Anandan, S., and Maruthamuthu, P. (2001). Dye sensitized hydrogen evolution from water. *International Journal of Hydrogen*

Energy, 26:669–674.

**[Diebold2003]** Diebold Ulrike (2003). The surface science of titanium dioxide. *Surface Science Reports* 48, 53-229.

**[Diwald et al., 2004]** Diwald O., Thompson T. L., Goralski Ed G., Walck S. D., and Yates J. T. (2004) The Effect of Nitrogen Ion Implantation on the Photoactivity of TiO<sub>2</sub> Rutile Single Crystals. *Journal of Physic Chemistry B*, 108, 52-57

**[Dubrovinsky et al., 2001]** Dubrovinsky, L., Dubrovinskaia, N., Swamy, V., Muscat, J., Harrison, N., Ahuja, R., Holm, B., and Johansson, B. (2001). Materials science: The hardest known oxide. *Nature*, pages 653–654.

**[Dvoranova et al., 2002]** Dvoranova, D., Brezova, V., Mazur, M., and Malati, M. (2002). Investigations of metal-doped titanium dioxide photocatalysts. *Applied Catalysis B: Environmental*, 37:91–105.

**[Earle, 1942]** Earle, M. D. (1942). The electrical conductivity of titanium dioxide. *Physical Review*, 61:56–62.

**[Einarsrud et al., 2001]** Einarsrud, M.-A., Nilsen, E., Rigacci, A., Pajonk, G., Buathier, S., Valette, D., Durant, M., Chevalier, B., Nitz, P., and Ehrburger-Dolle, F. (2001). Strengthening of silica gels and aerogels by washing and aging processes. *Journal of Non-Crystalline Solids*, 285:1–7.

**[Emeline et al., 2007]** Emeline, A., Ryabchuk, V., and Serpone, N. (2007). Photoreactions occurring on metal-oxide surfaces are not all photocatalytic. description of criteria and conditions for processes to be photocatalytic. *Catalysis Today*, 122:4091–100.

**[Emilio et al., 2006]** Emilio, C. A., Litter, M. I., Kunst, M., Bouchard, M., and Colbeau-Justin, C. (2006). Phenol photodegradation on platinized-TiO<sub>2</sub> photocatalysts related to charge-carrier dynamics. *Langmuir*, 22:3606–3613.

**[Feist and Davies, 1992]** Feist, T. P. and Davies, P. K. (1992). The soft chemical synthesis of TiO<sub>2</sub> (B) from layered titanates. *Journal of Solid State Chemistry*, 101:275–295.

**[Finnegan et al., 2007]** Finnegan, M. P., Zhang, H., and Banfield, J. F. (2007). Phase stability and transformation in titania nanoparticles in aqueous solutions dominated by surface energy. *Journal of Physical Chemistry C*, 111:1962–1968.

**[Fox and Dulay, 1993]** Fox, M. A. and Dulay, M. T. (1993). Heterogeneous photocatalysis. *Chemical Review*, 93:341–357.

**[Frank and Bard, 1977]** Frank, S. N. and Bard, A. J. (1977). Heterogeneous photocatalytic oxidation of cyanide ion in aqueous solutions at titanium dioxide powder. *Journal of the American Chemical Society*, 99:303–304.

**[Fujishima and Honda, 1972]** Fujishima, A. and Honda, K. (1972). Electrochemical photolysis of water at a semiconductor electrode. *Nature*, 238:37–38.

**[Fujishima et al., 1999]** Fujishima, A., Hashimoto, K., and Watanabe, T. (1999). *TiO<sub>2</sub> photocatalysis: Fundamental and Applications*. BKC Inc. 147

**[Fujishima et al., 2000]** Fujishima, A., Rao, T. N., and Tryk, D. A. (2000). Titanium dioxide photocatalysis. *Journal of Photochemistry and Photobiology C: Photochemistry Reviews*, 1:1–21.

**[Fujishima et al., 2008]** Fujishima, A., Zhang, X., and Tryk, D. A. (2008). TiO<sub>2</sub> photocatalysis and related surface phenomena. *Surface Science Reports*, 63:515–582.

**[Galinska and Walendziewski, 2005]** Galinska, A. and Walendziewski, J. (2005). Photocatalytic water splitting over Pt-TiO<sub>2</sub> in the presence of sacrificial reagents. *Energy Fuels*, 19:1143–1147.

**[Gash et al., 2001]** Gash, A. E., Tillotson, T. M., Jr., J. H. S., Hrubesh, L. W., and Simpson, R. L. (2001). New solgel synthetic route to transition and main-group metal oxide aerogels using inorganic salt precursors. *Journal of Non-Crystalline Solids*, 285:22–28.

**[Gong et al., 2001]** Gong, D., Grimes, C. A., Varghese, O. K., Hu, W., Singh, R., Chen, Z., and Dickey, E. C. (2001). Titanium oxide nanotube arrays prepared by anodic oxidation. *Journal of Materials Research*, 16:331–334.

**[Gopel et al., 1984]** W Göpel, J.A Anderson, D Frankel, M Jaehnig, K Phillips, J.A Schäfer and G Rocker (1984). Surface defects of TiO<sub>2</sub> (110): A combined XPS, XAES AND ELS study. *Surface Science Vol. 139, 2-3, Pages 333-346*

**[Gurunathan et al., 1997]** Gurunathan, K., Maruthamuthu, P., and Sastri, V. (1997). Photocatalytic hydrogen production by dye-sensitized Pt/SnO<sub>2</sub> and Pt/SnO<sub>2</sub>/RuO<sub>2</sub> in aqueous methylviologen solution. *International Journal of Hydrogen Energy*, 22:57–62.

**[Hashimoto et al., 2005]** Hashimoto, K., Irie, H., and Fujishima, A. (2005). TiO<sub>2</sub> photocatalysis: A historical overview and future prospects. *Japanese Journal of applied physics*, 44:8269–8285.

**[Hench and West, 1990]** Hench, L. L. and West, J. K. (1990). The sol-gel process. *Chemical Review*, 90:33–72.

**[Hengerer et al., 2000]** Hengerer, R., Bolliger, B., Erbudak, M., and Grtzel, M. (2000). Structure and stability of the anatase  $\text{TiO}_2$  (101) and (001) surfaces. *Surface Science*, 460:162–169.

**[Herrmann, 1999]** Herrmann, J.-M. (1999). Heterogeneous photocatalysis: fundamentals and applications to the removal of various types of aqueous pollutants. *Catalysis Today*, 53:115–129.

**[Hirashima et al., 1998]** Hirashima, H., Kojima, C., Kohama, K., Imai, H., Balek, V., Hamada, H., and Inaba, M. (1998). Oxide aerogel catalysts. *Journal of Non-Crystalline Solids*, 225:153–156.

**[Hoepfner et al., 2008]** Hoepfner, S., Ratke, L., and Milow, B. (2008). Synthesis and characterisation of nanofibrillar cellulose aerogels. *Cellulose*, 15:121–129.

**[Hoffmann et al., 1995]** Hoffmann, M. R., Martin, S. T., Choi, W., and Bahneman, D. W. (1995). Environmental applications of semiconductor photocatalysis. *Chemical Review*, 95:69–96.

**[Horikawa et al., 2008]** Horikawa, T., Katoh, M., and Tomida, T. (2008). Preparation and characterization of nitrogen-doped mesoporous titania with high specific surface area. *Microporous and Mesoporous Materials*, 110:397–404. 148

**[Huanga et al., 2007]** Huanga, C.-M., Chen, L.-C., Cheng, K.-W., and Pan, G.-T. (2007). Effect of nitrogen-plasma surface treatment to the enhancement of  $\text{TiO}_2$  photocatalytic activity under visible light irradiation. *Journal of Molecular Catalysis A: Chemical*, 261:218–224.

**[Hulteen and Martin, 1997]** Hulteen, J. C. and Martin, C. R. (1997). A general template-based method for the preparation of nanomaterials. *Journal of Material Chemistry*, 7:1075–1087.

**[Hurum et al., 2003]** Hurum, D. C., Agrios, A. G., and Gray, K. A. (2003). Explaining the Enhanced Photocatalytic Activity of Degussa P25 Mixed-Phase  $\text{TiO}_2$  Using EPR. *Journal of Physics Chemistry*, 107:4545–4549.

**[Husing et al., 1999]** Husing, N., Schubert, U., Mezei, R., Fratzl, P., Riegel, B., Kiefer, W., Kohler, D., and Werner (1999). Formation and structure of gel networks from  $\text{Si}(\text{OEt})_4/(\text{MeO})_3\text{Si}(\text{CH}_2)_3\text{NR}_2$  mixtures ( $\text{NR}'_2$ )  $\text{NH}_2$  or  $\text{NHCH}_2\text{CH}_2\text{NH}_2$ ). *Chemistry of Materials*, 11:451–457.

**[Indrea et al., 2009]** Indrea, E., Dreve, S., Silipas, T., Mihailescu, G., and Danciu, V. (2009). Nanocrystalline semiconductor materials for solar water-splitting. *Journal of Alloys and Compounds*, 483:445–449.

[Liu et al., 2009] Song Liu, Tianhua Xie, Zhi Chen and Jiantao Wu. Highly active V–TiO<sub>2</sub> for photocatalytic degradation of methyl orange. *Applied Surface Science* 255 (2009) 8587–8592

[Jitputti et al., 2007] Jitputti, J., Pavasupree, S., Suzuki, Y., and Yoshikawa, S. (2007). Synthesis and photocatalytic activity for water-splitting reaction of nanocrystalline mesoporous titania prepared by hydrothermal method. *Journal of Solid State Chemistry*, 180:1743–1749.

[Jitputti et al., 2008] Jitputti, J., Suzuki, Y., and Yoshikawa, S. (2008a). Synthesis of TiO<sub>2</sub> nanowires and their photocatalytic activity for hydrogen evolution. *Catalysis Communications*, 9:1265–1271.

[Jolivet et al., 2004] Jolivet, J.-P., Froidefond, C., Pottier, A., Chanac, C., Cassaignon, S., Tronc, E., and Euzen, P. (2004). Size tailoring of oxide nanoparticles by precipitation in aqueous medium. a semi-quantitative modelling. *Journal of Materials Chemistry*, 14:3281–3288.

[Jolivet et al., 2008] Jolivet, J.-P., Cassaignon, S., Chaneac, C., Chiche, D., and Tronc, E. (2008). Design of oxide nanoparticles by aqueous chemistry. *Journal of Sol-gel Science and Technology*, 46:299–305.

[Jun et al., 2006] J. Jun, J.-H. Shin, M. Dhaya (2006). Surface state of TiO<sub>2</sub> treated with low ion energy plasma *Applied Surface Science* 252, 3871–3877

[Kang et al., 2007] Kang, I.-C., Zhang, Q., Kano, J., Yin, S., Sato, T., and Saito, F. (2007). Synthesis of nitrogen doped TiO<sub>2</sub> by grinding in gaseous NH<sub>3</sub>. *Journal of Photochemistry and Photobiology A: Chemistry*, 189:232–238.

[Kasuga et al., 1998a] Kasuga, T., Hiramatsu, M., Hoson, A., Sekino, T., and Niihara, K. (1998). Formation of titanium oxide nanotube. *Langmuir*, 14:3160–3163.

[Kasuga et al., 1998b] Kasuga, T., Hiramatsu, M., Hoson, A., Sekino, T., and Niihara, K. (1998). Titania nanotubes prepared by chemical processing. *Advanced Materials*, 11:1307–1311. 149

[Kavan et al., 1996] Kavan, L., Gratzel, M., Gilbert, S., Klemenz, C., and Scheel, H. (1996). Electrochemical and photoelectrochemical investigation of single-crystal anatase. *Journal of the American Chemical Society*, 118:6716–6723.

[Khan et al., 2002] Khan, S., Al-Shahry, M., and Ingler, M. W. (2002). Efficient photochemical water splitting by a chemically modified N-TiO<sub>2</sub>. *Science*, 297:2243–2245.

- [Kim et al., 2007]** Kim, W.-I., Suh, D. J., Park, T.-J., and Hong, I.-K. (2007). Photocatalytic degradation of methanol on titania and titania-silica aerogels prepared by non-alkoxide sol-gel route. *Topics in Catalysis*, 44:499–505.
- [Kistler, 1932]** Kistler, S. (1932). Coherent expanded aerogels. *Journal of Physical Chemistry*, 36:52–64.
- [Kitano et al., 2007]** Kitano, M., Mitsui, R., Eddy, D. R., El-Bahy, Z. M. A., Matsuoka, M., Ueshima, M., and Anpo, M. (2007). Synthesis of nanowire TiO<sub>2</sub> thin films by hydrothermal treatment and their photoelectrochemical properties. *Catalysis Letters*, 119:217221.
- [Klosek and Raftery, 2001]** Klosek, S. and Raftery, D. (2001). Visible light driven V-Doped TiO<sub>2</sub> photocatalyst and its photooxidation of ethanol. *Journal of Physical Chemistry B*, 105:2815–2819.
- [Kolen'ko et al., 2005]** Kolen'ko, Y., Garshev, A., Churagulov, B., Boujday, S., Portes, P., and Colbeau-Justin, C. (2005). Photocatalytic activity of sol-gel derived titania converted into nanocrystalline powders by supercritical drying. *Journal of Photochemistry and Photobiology A: Chemistry*, 17:19–26.
- [Kristensen, 1968]** Kristensen, I. (1968). Semiconductor-to-semiconductor transition in the pseudobinary system TiO<sub>2</sub>-VO<sub>2</sub>. *Journal of Applied Physics*, 39:5341–5342.
- [Kuo et al., 2007]** Kuo, H.-L., Kuo, C.-Y., Liu, C.-H., Chao, J.-H., and Lina, C.-H. (2007). A highly active bi-crystalline photocatalyst consisting of TiO<sub>2</sub> (b) nanotube and anatase particle for producing H<sub>2</sub> gas from neat ethanol. *Catalysis Letters*, 113:1–2.
- [Lazzeri et al., 2001]** Lazzeri, M., Vittadini, A., and Selloni, A. (2001). Structure and energetic of stoichiometric TiO<sub>2</sub> anatase surfaces. *Physical Review B*, 63.
- [Lee et al., 2001]** Lee, S., Lee, S., and Lee, H. (2001). Photocatalytic production of hydrogen from aqueous solution containing CN as a hole scavenger. *Applied Catalysis A: general*, 207:173–181.
- [Lei et al., 2001]** Y. Lei, L. D. Zhang and J. C. Fan. Fabrication, characterization and Raman study of TiO<sub>2</sub> nanowire arrays prepared by anodic oxidative hydrolysis of TiCl<sub>3</sub> *Chemical Physics Letters* Volume 338, Issues 4-6, Pages 231-236
- [Li et al., 2007]** Li, W., Fu, T., Xie, F., Yu, S., and He, S. (2007). The multi-staged formation process of titanium oxide nanotubes and its thermal stability. *Materials Letters*, 61:730–735.
- [Lin et al., 2008]** Lin, C.-H., Chao, J.-H., Liu, C.-H., Chang, J.-C., and Wang, F.-C. (2008). Effect of calcination temperature on the structure of a Pt/TiO<sub>2</sub> (B) nanofiber and its photo-

catalytic activity in generating H<sub>2</sub>. *Langmuir*, 24:9907–9915.

**[LionelVayssieres, 2008]** Lionel Vayssieres (2008). Synthesis, properties and applications of oxide nanomaterials Chapter 2. Editors: Jose A. Rodriguez and Marcos Fernandez-Garcia Publishers: Wiley-VCH, Berlin. Pag. 49-78

**[Liu et al., 2006]** Liu, J., Yang, R., and Li, S. (2006). Preparation and characterization of the TiO<sub>2</sub>-V<sub>2</sub>O<sub>5</sub> photocatalyst with visible-light activity. *Rare metals*, 25-6:636.

**[Livraghi et al., 2006]** S. Livraghi, M. C. Paganini, E. Giamello, A. Selloni, C. Di Valentin, and G. Pacchioni (2006). Origin of Photoactivity of Nitrogen-Doped Titanium Dioxide under Visible Light. *Journal of the American Chemical Society*, VOL. 128, NO. 49

**[Luo et al., 2009]** Luo, L., Cooper, A., and Fan, M. (2009). Preparation and application of nanoglued binary titania-silica aerogel. *Journal of Hazardous Materials*, 161:175–182.

**[Ma et al., 2003]** Ma, R., Bando, Y., and Sasaki, T. (2003). Nanotubes of lepidocrocite titanates. *Chemical Physics Letters*, 380:577–582.

**[Ma et al., 2004]** Ma, R., Bando, Y., and Sasaki, T. (2004). Directly rolling nanosheets into nanotubes. *Journal of Physical Chemistry B*, 108:2115–2119.

**[Malinowska et al., 2003]** Malinowska, B., Walendziewski, J., Robert, D., Weber, J. V., and Stolarski, M. (2003). Titania aerogels: Preparation and photocatalytic tests. *International Journal of Photoenergy*, 5:147–152.

**[Marchand et al., 1980]** Marchand, R., Brohan, L., and Tournoux, M. (1980). TiO<sub>2</sub>(b) a new form of titanium dioxide and the potassium octatitanate K<sub>2</sub>Ti<sub>8</sub>O<sub>17</sub>. *Materials Research Bulletin*, 15:1129–1133.

**[Masmoudi, 2006]** Masmoudi, Y. (2006). Etude du schage au CO<sub>2</sub> supercritique pour l'élaboration de matériaux nanostructurés : application aux arogels de silice monolithiques. PhD thesis, MINES ParisTech.

**[Matejova et al., 2010]** Matejova, L., Cajthaml, T., Matej, Z., Benada, O., Kluson, P., and Solcova, O. (2010). Super/subcritical fluid extractions for preparation of the crystalline titania. *Journal of Supercritical Fluids*, 52:215–221.

**[Mattesini et al., 2004]** Mattesini, M., de Almeida, J., L.Dubrovinsky, Dubrovinskaia, N., Johansson, B., and Ahuja, R. (2004). High-pressure and high-temperature synthesis of the cubic TiO<sub>2</sub> polymorph. *Physical Review B*, 70:115101–115109.

**[Matthews, 1976]** Matthews, A. (1976). The crystallization of anatase and rutile from amorphous titanium dioxide under hydrothermal conditions. *American Mineralogist*, 61:419–424.

- [**Mor et al., 2005**] Mor, G. K., Shankar, K., Paulose, M., Varghese, O. K., and Grimes, C. A. (2005). Enhanced photocleavage of water using titania nanotube arrays. *Nano Letters*, 5:191–195.
- [**Morris et al., 1999**] Morris, C., Anderson, M., Stroud, R., Merzbacher, C., and Rolison, D. (1999). Silica sol as a nanogluue: flexible synthesis of composite aerogels. *Science*, 284:622–624.
- [**Mrowiec-Bialon et al., 1998**] Mrowiec-Bialon, J., Paja, L., Jarzbski, A. B., Lachowskia, A. I., and Malinowski, J. J. (1998). Preparation effects on zirconia aerogel morphology. *Journal of Non-Crystalline Solids*, 225:115–119.
- [**Murphy et al., 2006**] Murphy, A., Barnes, P., Randeniya, L., Plumb, C., Grey, I., Horne, M., and Glasscock, J. (2006). Efficiency of solarwater splitting using semiconductor electrodes. *International Journal of Hydrogen Energy*, 31:1999–2017.
- [**Nada et al., 2005**] Nada, A., Barakat, M., Hamed, H., Mohamed, N., and Veziroglu, T. (2005). Studies on the photocatalytic hydrogen production using suspended modified TiO<sub>2</sub> photocatalysts. *International Journal of Hydrogen Energy*, 30:687–691.
- [**Nagaveni et al., 2004**] Nagaveni, K., Hegde, M. S., and Madras, G. (2004). Structure and photocatalytic activity of Ti<sub>1-x</sub>MxO<sub>2</sub> (M = W, V, Ce, Zr, Fe, and Cu) synthesized by solution combustion method. *Journal of Physical Chemistry B*, 108:20204–20212.
- [**Ni et al., 2007**] Ni, M., Leung, M. K., Leung, D. Y., and Sumathy, K. (2007a). A review and recent developments in photocatalytic water-splitting using TiO<sub>2</sub> for hydrogen production. *Renewable and Sustainable Energy Reviews*, 11:401–425.
- [**Nielsen, 1964**] Nielsen, A. (1964). *Kinetics of precipitation*. Pergamo Press.
- [**Nishijima et al., 2007**] Nishijima, K., Kamai, T., Murakami, N., Tsubota, T., and Ono, T. (2007). Photocatalytic hydrogen or oxygen evolution from water over S- or N-Doped TiO<sub>2</sub> under visible light. *International Journal of Photoenergy*, 2008:173943–173950.
- [**Nosaka et al., 2005**] Nosaka, Y., Matsushita, M., Nishino, J., and Nosaka, A. Y. (2005). Nitrogen-doped titanium dioxide photocatalysts for visible response prepared by using organic compounds. *Science and Technology of Advanced Materials*, 6:143–148.
- [**Nowotny et al., 2007**] Nowotny, J., Bak, T., Nowotny, M., and Sheppard, L. (2007). Titanium dioxide for solar-hydrogen I. functional properties. *International Journal of Hydrogen Energy*, 32:2609–2629.
- [**Pajonk, 1989**] G.M. Pajonk, Drying methods preserving the textural properties, *Journal de Physique Appliquée C4-n°4*, tome 24 (1989) 13-22
- [**Pajonk et al., 1995**] Pajonk, G., Elaloui, E., Achard, P., Chevalier, B., Chevalier, J., and Durrant, M. (1995). Physical properties of silica gels and aerogels prepared with new polymeric

precursors. *Journal of Non-Crystalline Solids*, 186:1–8.

**[Pankove, 1971]** J.I. Pankove, *Optical Processes in semiconductors*, Dover Publications, Inc, New York, 1971

**[Paola et al., 2002]** Paola, A., Marci, G., Palmisano, L., Schiavello, M., Uosaki, K., and et al., (2002). Preparation of polycrystalline TiO<sub>2</sub> photocatalysts impregnated with various transition metal ions: characterization and photocatalytic activity for degradation of 4-nitrophenol. *Journal of Physical Chemistry B*, 106:637–645.

**[Paola et al., 2008]** Paola, A. D., Cufalo, G., Addamo, M., Bellardita, M., Campostrini, R., Ischia, M., Ceccato, R., and Palmisano, L. (2008). Photocatalytic activity of nanocrystalline TiO<sub>2</sub> (brookite, rutile and brookite-based) powders prepared by thermohydrolysis of TiCl<sub>4</sub> in aqueous chloride solutions. *Colloids and Surfaces A: Physicochemical Engineering*, 317:366–376. 152

**[Park et al., 2006]** Park, J. H., Kim, S., and Bard, A. J. (2006). Novel carbon-doped TiO<sub>2</sub> nanotube arrays with high aspect ratios for efficient solar water splitting. *Nano Letters*, 6:24–28.

**[Parker et al., 1990]** Parker, J. C., Geiser, U. W., and Lam, D. J. (1990). Optical properties of the vanadium oxides VO<sub>2</sub> and V<sub>2</sub>O<sub>5</sub>. *Journal of the American Ceramic Society*, 73:3206–3208.

**[Peng et al., 2001]** Du, G., Chen, Q., Che, R., Yuan, Z., and Peng, L. (2001). Preparation and structure analysis of titanium oxide nanotubes. *Applied Physics Letters*, 79:3702–3704.

**[Pekala, 1989]** Pekala, R. (1989). Organic aerogels from polycondensation of resorcinol with formaldehyde. *Journal of Material Science*, 24:3221.

**[Penn and Banfield, 1999]** Penn, R. L. and Banfield, J. F. (1999). Morphology development and crystal growth in nanocrystalline aggregates under hydrothermal conditions: Insights from titania. *Geochimica et Cosmochimica Acta*, 63:1549–1447.

**[Phalippou and Kocon, 2004]** Phalippou, J. and Kocon, L. (2004). *Aerogels : Aspects fondamentaux*. Technical report, Techniques de l'ingénieur,

**[Pierre et al., 1999]** Pierre, A., Begag, R., and Pajonk, G. (1999). Structure and texture of alumina aerogel monoliths made by complexation with ethyl acetoacetate. *Journal of Materials Science*, 34:4937–4944.

**[Pierre and Pajonk, 2002]** Pierre, A. and Pajonk, G. (2002). Chemistry of aerogels and their applications. *Chemistry Review*, 102:4243–4265.

**[Pietron and Rolison, 2001]** Pietron, J. and Rolison, D. (2001). Electrochemically induced surface modification of titanols in a “nanoglued” titania aerogel-silica aerogel composite film. *Journal of Non-crystalline solids* 285, 13-21.

**[Pietron et al., 2002]** Jeremy J. Pietron,<sup>†</sup> Rhonda M. Stroud,<sup>‡</sup> and Debra R. Rolison (2002). Using Three Dimensions in Catalytic Mesoporous Nanoarchitectures. *Nano Letters*, Vol. 2, No 5, 545-549.

**[Pietron and Rolison, 2004]** Pietron, J. and Rolison, D. (2004). Improving the efficiency of titania aerogel-based photovoltaic electrodes by electrochemically grafting isopropyl moieties on the titania surface. *Journal of Non-Crystalline Solids*, 350:107–112.

**[Pietron et al., 2007]** J. J. Pietron, A. M. Stux, R. S. Compton, D. R. Rolison. Dye-sensitized titania aerogels as photovoltaic electrodes for electrochemical solar cells. *Solar Energy Materials & Solar Cells* 91, 1066–1074.

**[Piotrowska and Walendziewski, 2005]** Piotrowska, A. and Walendziewski, J. (2005). The photocatalytic hydrogen production from the water over titania aerogels under uv irradiation. In *Proceedings International Hydrogen Energy Congress and Exhibition IHEC*.

**[Popa et al., 2010]** Popa, M., Marcovei, D., Indrea, E., Mercioniu, I., Popescu, I., and Danciu, V. (2010). Synthesis and structural characteristics of nitrogen doped TiO<sub>2</sub> aerogels. *Microporous and Mesoporous Materials*, 132:80–86.

**[Pottier et al., 2003]** Pottier, A., Cassaignon, S., Chanac, C., Villain, F., Tronc, E., and Jolivet, J.-P. (2003). Size tailoring of TiO<sub>2</sub> anatase nanoparticles in aqueous medium and synthesis of nanocomposites. Characterization by raman spectroscopy. *Journal of Materials Chemistry*, 13:877–882.

**[Prokes et al., 2005]** S.M. Prokes, J.L. Gole, X. Chen, C.Burda, and W. Carlos (2005). Defect related optical behavior in surface-modified TiO<sub>2</sub> nanostructures. *Advanced functional materials*, 15, 1

**[Ramamoorthy et al., 1994]** Ramamoorthy, M., Vanderbilt, D., and King-Smith, R. (1994). First-principles calculations of the energetics of stoichiometric tio2 surfaces. *Physical Review B*, 49:1672116727.

**[Rao et al., 2004]** Rao, A. V., Pajonk, G., Bhagat, S., and Barboux, P. (2004). Comparative studies on the surface chemical modification of silica aerogels based on various organosilane compounds of the type R<sub>n</sub>Si<sub>x4-n</sub>. *Journal of Non-Crystalline Solids*, 350:216–223.

**[Rigacci et al., 2004]** Rigacci, A., Marechal, J., Repoux, M., Moreno, M., and Achard, P. (2004). Preparation of polyurethane-based aerogels and xerogels for thermal superinsulation. *Journal of Non-Crystalline solids*, 350:372.153

**[Rolison et al., 1997]** Karen E. Swider, Celia I. Merzbacher, Patrick L. Hagans, and Debra R. Rolison. Synthesis of Ruthenium Dioxide-Titanium Dioxide Aerogels: Redistribution of Electrical Properties on the Nanoscale. *Chem. Mater.*, 9, 1248-1255

**[Rosseler et al., 2010]** Rosseler, O., Shankar, M., Du, M., Schmidlin, L., Keller, N., and Keller, V. (2010). Solar light photocatalytic hydrogen production from water over Pt and Au/TiO<sub>2</sub> (anatase/rutile) photocatalysts: Influence of noble metal and porogen promotion. *Journal of Catalysis*, 269:179–190.

**[Rouquerol et al., 1999]** Rouquerol, F., Rouquerol, J., and Sing, K. (1999). Adsorption by powders and porous solids. Academic Press.

**[Rouquerol et al., 2003]** Rouquerol, F., Luciani, L., Llewellyn, P., Denoyel, R., and Rouquerol, J. Texture des matériaux pulvulents ou poreux. Technical report, Techniques de l'Ingénieur.

**[Sakthivel et al., 2004]** Sakthivel, S., Shankar, M., Palanichamy, M., Arabindoo, B., Bahnemann, D., and Murugesan, V. (2004). Enhancement of photocatalytic activity by metal deposition: characterization and photonic efficiency of Pt, Au and Pd deposited on TiO<sub>2</sub> catalyst. *Water Research*, 38:3001–3008.

**[Sato, 1986]** Sato, S. (1986). Photocatalytic activity of NO<sub>x</sub>-doped TiO<sub>2</sub> in the visible-light region. *Chemical Physics Letters*, 123:126–128.

**[Scherer, 1990]** Scherer, G. W. (1990). Theory of drying. *Journal of American Ceramic Society*, 73:3–14.

**[Schleicher and Walter, 1997]** Schleicher, D. M. and Walter, B. (1997). Formation of titania nanoparticles by vapor phase reactions of titanium tetrakisopropoxide in oxygen/ozone containing atmospheres. *Nanostructured Materials*, 8:579–586.

**[Sene et al., 2002]** Jeosadaque J. Sene, Walter A. Zeltner, and Marc A. Anderson. Fundamental Photoelectrocatalytic and Electrophoretic Mobility Studies of TiO<sub>2</sub> and V-Doped TiO<sub>2</sub> Thin-Film Electrode Materials. *J. Phys. Chem. B* 2003, 107, 1597-1603

**[Serpone, 2006]** Serpone, N. (2006). Is the band gap of pristine TiO<sub>2</sub> narrowed by anion- and cation-doping of titanium dioxide in second-generation photocatalysts? *Journal of Physical Chemistry B*, 110:24287–24293.

**[Shimoyama et al., 2010]** Shimoyama, Y., Ogata, Y., Ishibashi, R., and Iwai, Y. (2010). Drying processes for preparation of titania aerogel using supercritical carbon dioxide. *Chemical Engineering Research and Design*, In press

**[Shklover et al., 1997]** Shklover, V., Nazeeruddin, M., Zakeeruddin, S., Barbe, C., Kay, A., Haibach, T., Steurer, W., Hermann, R., Nissen, H., and Grätzel, M. (1997). Structure of

nanocrystalline TiO<sub>2</sub> powders and precursor to their highly efficient photosensitizer. *Chemistry of materials*, 9:430–439.

**[Silipas et al., 2009]** Silipas, T., Indrea, E., Dreve, S., Suci, R.-C., Rosu, M., Danciu, V., Cosoveanu, V., and Popescu, V. (2009). TiO<sub>2</sub>-based systems for photoelectrochemical generation of solar hydrogen. *Processes in Isotopes and Molecules, Journal of Physics: Conference Series*, 182:012055. 154

**[Silversmit et al., 2005]** Silversmit, G., Poelman, H., Depla, D., Barrett, N., Marin, G. B., and Gryse, R. D. (2005). A fully oxidized V<sub>2</sub>O<sub>5</sub>/TiO<sub>2</sub>(001)-anatase system studied with in situ synchrotron photoelectron spectroscopy. *Surface Science*, 584:179–186.

**[Simonsen and Sogaard, 2010]** Simonsen, E. M. and Sogaard, E. G. (2010). Sol-gel reaction of titanium alkoxides and water: influence of pH and alkoxy group on cluster formation and properties of the resulting products. *Journal of Sol-Gel Science and Technology*, 53:485–497.

**[Sing, 1982]** Sing, K. S. W. (1982). Reporting physisorption data for gas/solid systems, with special reference to the determination of surface area and porosity. Technical report, International union of pure and applied chemistry

**[So and SJ Moon, 2004]** So, W. and SJ Moon, K. K. (2004). Photo-production of hydrogen over the CdS-TiO<sub>2</sub> nano-composite particulate films treated with TiCl<sub>4</sub>. *International Journal of Hydrogen Energy*, 29:229–234.

**[Sreethawong et al., 2005]** Sreethawong, T., Suzuki, Y., and Yoshikawa, S. (2005). Photocatalytic evolution of hydrogen over nanocrystalline mesoporous titania prepared by surfactant-assisted templating sol-gel process. *Catalysis Communication*, 6:119–124.

**[Sreethawong and Yoshikawa, 2006]** Sreethawong, T. and Yoshikawa, S. (2006). Enhanced photocatalytic hydrogen evolution over Pt supported on mesoporous TiO<sub>2</sub> prepared by single-step sol-gel process with surfactant template. *International Journal of Hydrogen Energy*, 31, 786–796.

**[Sreethawong et al., 2007]** Sreethawong, T., Puangpetch, T., Chavadej, S., and Yoshikawa, S. (2007). Quantifying influence of operational parameters on photocatalytic H<sub>2</sub> evolution over Pt-loaded nanocrystalline mesoporous TiO<sub>2</sub> prepared by single-step sol-gel process with surfactant template. *Journal of Power Source*, 165:861–869.

**[Sunada et al., 1998]** Sunada, K., Kikuchi, Y., Hashimoto, K., and Fujishima, A. (1998). Bactericidal and detoxification effects of TiO<sub>2</sub> thin film photocatalysts. *Environmental Science and Technology*, 32:726–728.

[**Suzuki et al., 2008**] Suzuki, Y., Gonzalez-Aguilar, J., Traisnel, N., Berger, M.-H., Repoux, M., and Fulcheri, L. (2008). Non-equilibrium nitrogen dc-arc plasma treatment of TiO<sub>2</sub> nanopowder. *Journal of Nanoscience and Nanotechnology*, 8:1–5.

[**Takahashi et al., 2008**] I. Takahashi, D.J. Payne, R.G. Palgrave, R.G. Egdell (2008). High resolution X-ray photoemission study of nitrogen doped TiO<sub>2</sub> rutile single crystals. *Chemical Physics Letters* 454, 314–317

[**Teichner et al., 1976**] Teichner, S., Nicolaon, G., Vicarini, M., and Gardes, G. (1976). Inorganic oxide aerogels. *Advances in colloid and interface Sciences*, 5:3:245–273.

[**Tewari et al., 1985**] Tewari, P., Hunt, A., and Lofftus, K. (1985). Ambient-temperature supercritical drying of transparent silica aerogels. *Materials Letters*, 3:363–367.

[**Tsai and Teng, 2004**] Tsai, C.-C. and Teng, H. (2004). Regulation of the physical characteristics of titania nanotube aggregates synthesized from hydrothermal treatment. *Chemistry of Materials*, 16:4352–4358. 155

[**Tokmakov et al.**] I. V. Tokmakov, S. A., and D. L. Thompson. Urea and Urea Nitrate Decomposition Pathways: A Quantum Chemistry Study. <http://pubs.acs.org>

[**Tursiloadi et al., 2006**] Tursiloadi, S., Yamanaka, Y., and Hirashima, H. (2006). Thermal evolution of mesoporous titania prepared by CO<sub>2</sub> supercritical extraction. *Journal of Sol-Gel Science and Technology*, 38:5–12.

[**Umebayashi et al., 2003**] Umebayashi, T., Yamaki, T., Tanaka, S., and Asai, K. (2003). Visible light-induced degradation of methylene blue on S-doped TiO<sub>2</sub>. *Chemistry Letters*, 32:330–331.

[**Valentin et al., 2007**] Valentin, C. D., Finazzi, E., Pacchioni, G., Selloni, A., Livraghi, S., Paganini, M. C., and Giamello, E. (2007). N-doped TiO<sub>2</sub>: Theory and experiment. *Chemical Physics*, 339:44–56.

[**Valentin et al., 2005**] Valentin, C. D., Pacchioni, G., Selloni, A., Livraghi, S., and Giamello, E. (2005). Characterization of paramagnetic species in N-Doped TiO<sub>2</sub> powders by EPR spectroscopy and DFT calculations. *The Journal of Physical Chemistry B Letters*, 109:11414–11419.

[**Vanveen et al., 1985**] Vanveen, J., Veltmaat, F., and Jonkers, G. (1985). A method for the quantitative determination of the basic, acidic and total hydroxy content of TiO<sub>2</sub>. *Journal of the chemical society-chemical communications*, 23:1656–1658.

[**Varghese and Grimes, 2008**] Varghese, O. K. and Grimes, C. A. (2008). Appropriate strategies for determining the photoconversion efficiency of water photoelectrolysis cells: A

review with examples using titania nanotube array photoanodes. *Solar Energy Materials and Solar Cells*, 92:374–384.

**[Varghese et al., 2009]** Varghese, O. K., Paulose, M., LaTempa, T. J., and Grimes, C. A. (2009). High-rate solar photocatalytic conversion of CO<sub>2</sub> and water vapor to hydrocarbon fuels. *Nano Letters*, 9:731–737.

**Venkateswara et al., 2005 ]** A. Venkateswara Rao, Manish M. Kulkarni and Sharad D. Bhagat (2005). Transport of liquids using superhydrophobic aerogels. *Journal of Colloid and Interface Science*, Volume 285, Issue 1, 1

**[Vittadini et al., 2009]** Vittadini, A., Casarin, M., and Selloni, A. (2009). Structure and stability of TiO<sub>2</sub>-B surfaces: A density functional study. *The Journal of Physical Chemistry C Letters*, 113:18973–18977.

**[Wei et al., 2008]** Wei, J., Zhao, L., Peng, S., Shi, J., Liu, Z., and Wen, W. (2008). Wettability of urea-doped TiO<sub>2</sub> nanoparticles and their high electrorheological effects. *Journal of Sol-Gel Science and Technology*, 47:311–315.

**[Wilke and Breuer, 1999]** Wilke, K. and Breuer, H. (1999). The influence of transition metal doping on the physical and photocatalytic properties of titania. *Journal of Photochemistry and Photobiology A: Chemistry*, 121:49–53.

**[Wright and Sommerdijk, 2001]** Wright, J. and Sommerdijk, N. (2001). *Sol-Gel Materials Chemistry and Applications*. Gordon and Breach Science Publishers.

**[Wu and Chen, 2004]** Wu, J. C.-S. and Chen, C.-H. (2004). A visible-light response vanadium-doped titania nanocatalyst by solgel method. *Journal of Photochemistry and Photobiology A: Chemistry*, 163:509–515. 156

**[Wu and Lee, 2004]** Wu, N. and Lee, M. (2004). Enhanced TiO<sub>2</sub> photocatalysis by Cu in hydrogen production from aqueous methanol solution. *International Journal of Hydrogen Energy*, 29:1601–1605.

**[Yamashita et al., 2001]** Yamashita, H., Harada, M., Misaka, J., Takeuchi, M., Ichihashi, Y., and Goto, F. (2001). Application of ion beam techniques for preparation of metal ion-implanted tio<sub>2</sub> thin film photocatalyst available under visible irradiation: metal ion-implantation and ionized cluster beam method. *Journal of Synchrotron Radiation*, 8:569–571.

**[Yamashita et al., 2003]** Yamashita, J., Ojima, T., Shioya, M., Hatori, H., and Yamada, Y. (2003). Organic and carbon aerogels derived from polyvinylchloride. *Carbon*, 41:285–294.

**[Yeredla and Xu, 2008]** Yeredla, R. R. and Xu, H. (2008). An investigation of nanostructured rutile and anatase plates for improving the photosplitting of water. *Nanotechnology*, 19.

**[Yeung et al., 2008]** Yeung, K., Leung, W., Yao, N., and Cao, S. (2008). Reactivity and antimicrobial properties of nanostructured titanium dioxide. *Catalysis Today*, 143:218–224.

**[Yoda et al., 2001]** Yoda, S., Suh, D., and Sato, T. (2001). Adsorption and photocatalytic decomposition of benzene using silica-titania and titania aerogels : effect of supercritical drying. *Journal of Sol-Gel Science and Technology*, 22:75–81.

**[Yoshida et al., 2005]** Yoshida, R., Suzuki, Y., and Yoshikawa, S. (2005). Syntheses of TiO<sub>2</sub>(B) nanowires and TiO<sub>2</sub> anatase nanowires by hydrothermal and post-heat treatments. *Journal of Solid State Chemistry*, 178:2179–2185.

**[Yuan et al., 2006]** J. Yuan, M. Chen, J. Shi, W. Shangguan (2006). Preparations and photocatalytic hydrogen evolution of N-doped TiO<sub>2</sub> from urea and titanium tetrachloride. *International Journal of Hydrogen Energy* 31, 1326 – 1331

**[Zacharaki et al., 2008]** Zacharaki, I., Kontoyannis, C., Lycourghiotis, A., and Kordulis, C. (2008). The influence of calcination on the size of nanocrystals, porous structure and acid-base properties of mesoporous anatase used as catalytic support. *Colloids and Surfaces A: Physicochemical and Engineering Aspects*, 324:208–216.

**[Zhang et al., 2000]** Zhang, Q., Gao, L., and Guo, J. (2000). Effects of calcination on the photocatalytic properties of nanosized TiO<sub>2</sub> powders prepared by TiCl<sub>4</sub> hydrolysis. *Applied Catalysis B: Environmental*, 26:207–215.

**[Zhao et al., 2002]** Zhao, G., Han, G., Takahashi, M., and Yokoa, T. (2002). Photoelectrochemical properties of sol-gel derived Ti<sub>1-x</sub>V<sub>x</sub>O<sub>2</sub> solid solution film photoelectrodes. *Thin solid Films*, 410:14–20.

**[Zhao et al., 2004]** Zhao, W., Ma, W., Chen, C., Zhao, J., and Shuai, Z. (2004). Efficient degradation of toxic organic pollutants with Ni<sub>2</sub>O<sub>3</sub>/TiO<sub>2-x</sub> under visible irradiation. *Journal of the American Chemical Society*, 126:4782–4783.

**[Zhao et al., 1999]** Zhao, G., Kozuka, H., Lina, H., and Yokoa, T. (1999). Sol-gel preparation of Ti<sub>1-2x</sub>V<sub>x</sub>O<sub>2</sub> solid solution film electrodes with conspicuous photoresponse in the visible region. *Thin Solid Films*, 339:123–128.

**[Zhou et al., 2009]** Wenfang Zhou, Qingju Liu, Zhongqi Zhu and Ji Zhang Preparation and properties of vanadium-doped TiO<sub>2</sub> photocatalysts . *J. Phys. D: Appl. Phys.* 43, 3

**[Znaidi et al., 2001]** Znaidi, L., Seraphimova, R., Bocquet, J., Colbeau-Justin, C., and Pommier, C. (2001). A semi-continuous process for the synthesis of nanosize TiO<sub>2</sub> powders and their use as photocatalysts. *Materials Research Bulletin*, 36:811–825.



## **Titre : Elaboration et étude de nanostructures de TiO<sub>2</sub> pour la production d'hydrogène par photolyse de l'eau**

**RESUME :** L'hydrogène est considéré comme un vecteur énergétique de très forte potentialité (pour faire face à l'épuisement des ressources fossiles et le réchauffement climatique). Parmi les nombreux points à améliorer, sa production selon un procédé propre mobilise des efforts certains. Le processus de photolyse de l'eau sous irradiation solaire est l'un des plus pertinents (recours aux énergies renouvelables, catalyseur abondant et bon marché, température ambiante, ...). Cependant, son rendement est actuellement encore très faible. L'objectif de cette thèse est d'étudier l'impact de la morphologie et de la nanostructure du semi-conducteur de référence - le dioxyde de titane (TiO<sub>2</sub>) - sur ses performances de production d'hydrogène par photolyse de l'eau. Pour cela, trois types de nanostructures d'anatase radicalement différentes ont été élaborées et finement caractérisées : *i*) des nanoparticules (par précipitation suivie d'une cristallisation hydrothermale), *ii*) des structures allongées de type nanofils (par le procédé « Kasuga ») et *iii*) des matériaux nanostructurés de type aérogels et xérogels. Les plus originales d'entre elles ont été dopées selon des procédés de la littérature, soit par voie cationique (nanofils dopés au Vanadium), soit par voie anionique (aérogels et xérogels dopés à l'azote). Les nanomatériaux les plus prometteurs ont été évalués en suspension, avec ou sans dépôt de platine, vis-à-vis de la photogénération. Il ressort de cette étude que les nanofils et les aérogels sont très pertinents pour l'application visée. Dans les conditions expérimentales suivies, les aérogels présentent notamment des taux de conversion nettement supérieurs à ceux du photocatalyseur de référence (i.e. un mélange de poudres d'anatase et de rutile).

**Mots clés :** nanoparticules, nanotubes, aérogel, dioxyde de titane, dopage, photocatalyse, hydrogène.

## **Title : Elaboration and study of TiO<sub>2</sub> nanostructures for hydrogen generation via photolysis of water**

**ABSTRACT :** Hydrogen is considered as an energy carrier of high potentiality to face problems related to the climate change and the depletion of fossil resources. Among the necessary improvements, its production through clean processes is still a big challenge. The water photolysis process under sun irradiation is one of the most relevant ones (usage of renewable energy, abundant and cheap catalyst, room temperature...). The energetic efficiency is however still too low. The objective of this thesis is to study the impact of the morphology and the nanostructure of the reference semiconductor – titanium dioxide (TiO<sub>2</sub>) – on its performance for water splitting. To this end, three types of radically different anatase nanostructures have been prepared and finely characterized: *i*) nanoparticles (precipitation followed by hydrothermal crystallisation), *ii*) elongated nanowire-like structures ("Kasuga" process) and *iii*) aerogels and xerogels like nanostructured materials. The most original ones have been doped following literature processes in order to get vanadium doped nanowires and nitrogen doped aerogels and xerogels. Slurries of the most promising materials have then been evaluated for hydrogen evolution, with or without platinum co-catalyst. It came out from this study that the nanowires and the aerogels were relevant for the foreseen application. Under the chosen experimental conditions, aerogels showed a conversion activity clearly higher than that of the reference photocatalyst (a mixture of anatase and rutile).

**Keywords :** nanoparticles, nanotubes, aerogel, titanium dioxyde, doping, photocatalysis, hydrogen.